DEFENSE MINISTERY
BRAZILIAN ARMY
SCIENCE AND TECHNOLOGY DEPARTMENT
MILITARY INSTITUTE OF ENGINEERING
GRADUATE PROGRAM IN MATERIALS SCIENCE AND ENGINEERING

LUCAS DE MENDONÇA NEUBA

BALLISTIC EVALUATION AND CHARACTERIZATION OF EPOXY COMPOSITE REINFORCED BY ALKALI TREATED SEVEN-ISLANDS SEDGE AND COATED BY GRAPHENE OXIDE

RIO DE JANEIRO
2024

LUCAS DE MENDONÇA NEUBA

BALLISTIC EVALUATION AND CHARACTERIZATION OF EPOXY COMPOSITE REINFORCED BY ALKALI TREATED SEVEN-ISLANDS SEDGE AND COATED BY GRAPHENE OXIDE

Dissertation presented to Military Institute of Engineering, in partial satisfaction of the requirements for the degree of Doctor of Science in Materials Science and Engineering.

Advisor(s): Sergio Neves Monteiro, Ph.D.
Marc André Meyers, Ph.D.

Rio de Janeiro

2024

MILITARY INSTITUTE OF ENGINEERING
General Tibúrcio Square, 80 – Vermelha Beach
Rio de Janeiro – RJ ZIP: 22290-270

Neuba, Lucas de Mendonça.
BALLISTIC EVALUATION AND CHARACTERIZATION OF EPOXY COMPOSITE REINFORCED BY ALKALI TREATED SEVEN-ISLANDS SEDGE AND COATED BY GRAPHENE OXIDE / Lucas de Mendonça Neuba. – Rio de Janeiro, 2024.
258 f.

Advisor(s): Sergio Neves Monteiro and Marc André Meyers.

Dissertation (doctorate) – Military Institute of Engineering, Materials Science and Engineering, 2024.

1. Natural Lignocellulosic Fibers; Dynamic Mechanical Analysis; Residual Velocity;*Cyperus malaccensis*; Analysis of Variance. i. Neves Monteiro, Sergio (Advis.) ii. André Meyers, Marc (Advis.) iii. Title

LUCAS DE MENDONÇA NEUBA

BALLISTIC EVALUATION AND CHARACTERIZATION OF EPOXY COMPOSITE REINFORCED BY ALKALI TREATED SEVEN-ISLANDS SEDGE AND COATED BY GRAPHENE OXIDE

Dissertation presented to Military Institute of Engineering, in partial satisfaction of the requirements for the degree of Doctor of Science in Materials Science and Engineering.
Advisor(s): Sergio Neves Monteiro and Marc André Meyers.

Approved at Rio de Janeiro, August 20, 2024, by the committee in charge:

Prof. **Sergio Neves Monteiro** - Ph.D.- IME - Chair

Prof. **Marc André Meyers** - Ph.D. - UCSD

Prof. **André Ben-Hur da Silva Figueiredo** - D.Sc. - IME

Prof. **Talita Gama de Sousa** - D.Sc. - IME

Prof. **Alexandre Alvarenga Palmeira** - D.Sc. - UERJ

Prof. **Maria de Fátima Vieira Marques** - D.Sc. - UFRJ-IMA

Rio de Janeiro
2024

"Somewhere, something incredible is waiting to be known."
Carl Sagan

ACKNOWLEDGEMENTS

To my beloved father, André, for all the support, advice, and affection they provided me during the entire period of graduate studies and life, as well as the strength and courage he gave me to pursue this particular dream.

To my dear grandmother Vera Lúcia for all the care and support during this journey.

To Raquel, my future wife, for all the support, love and encouragement throughout this trajectory of my life!

To my civilian and military friends I made during the master's and doctoral programs, for the good times we shared and experiences we went through together, especially to Raí, Isaque, Vanessa, Sabrina, Andressa, Magno, Pedro, Matheus, Hugo, Douglas, Lucas Reis and Aragão.

To the friends from the natural fibers laboratory: Artur, Fernanda, Michelle, Wendell, Ulisses, Thuane, Raphael, Fábio, and Matheus.

To the professors of the Materials Science Graduate Program at IME, for the teachings and knowledge imparted.

To Sheron and Prof. Meyers for all the support on the extra embira fibers research we worked on.

To IME, CAPES, Prof. Sergio and Meyers for making it possible my visit student program in UCSD

To prof. Sergio Neves at IME for all the academic advices and support. A special thanks to Prof. Meyers who was my advisor in the UCSD and for all the support he gave me in the United States. At last, a special thanks to Prof. Artur Camposo at UFOP that was my second advisor and for all the advice and support on original papers discussion and analysis we have done so far.

To UENF for enabling the Charpy, Izod Impact and DMA tests. Special thanks to Prof. Noan Tonini for all the willingness, researcher and postdoctoral fellow, for all the willingness and assistance, and to the doctoral student Maria Eduarda Ribeiro. Also, to COPPE for allowing perform DMA tests. Thank you very much.

To IPQM for enabling the thermal, physical and chemical characterization analyses of epoxy composite materials reinforced with fibers.

To Danilo, Pedro Poubel, Sheron, Benjamin Lazarus, Noan Tonini and Ulisses Oliveira for analyzing all the SEM images of the composites in this work. Thank you very

much!

To CAPES (Coordination of Improvement of Higher Education Personnel) for the support and financial assistance for the development of this work.

"A scientist in their laboratory is not merely a technician, they are also a child placed before natural phenomena that impress them as if they were a fairy tale."
(Marie Curie)

RESUMO

Muitos setores da indústria como a automotiva e aeroespacial buscam desenvolver materiais mais resistentes e leves como uma forma de aprimorar o desempenho mecânico. Compósitos, principalmente os que possuem uma matriz polimérica reforçada com fibras se enquadram bem nessas necessidades devido a sua alta capacidade de unir um material de baixa densidade e alta resistência mecânica. Portanto, muitas pesquisas estão sendo desenvolvidas com esse objetivo para diversas aplicações de engenharia e até como um material utilizado na proteção balística pessoal. Além disso, existe uma preocupação da comunidade científica em desenvolver novos materiais ambientalmente favoráveis. Esse esforço resultou em diversos trabalhos voltados a incorporação de fibras naturais lignocelulósicas (FNLs) em matrizes poliméricas. O uso dessas fibras como material de engenharia pode contribuir no desenvolvimento econômico de certas regiões ribeirinhas e rurais no Brasil se for empregada em uma escala maior, sendo um fator relevante. Sendo assim, o presente estudo, sugere o uso de fibras de junco-sete-ilhas (*Cyperus malaccensis Lam.*), aqui chamadas de fibras de junco (SF), como reforço em matriz de epóxi. De forma inédita na literatura científica, foi investigado o efeito do tratamento de mercerização e funcionalização das fibras com óxido de grafeno (GO), e SF que reforça uma matriz epóxi incorporada com GO. O trabalho tratou os SFs com diferentes concentrações de solução de NaOH de 3%, 5% e 10% com períodos de 24, 48 e 72 h. Os SFs tratados apresentaram parâmetros que podem ser aplicados para obter melhores propriedades dos SFs que reforçam os compósitos de epóxi. Além disso, esse trabalho avaliou o efeito do revestimento de GO na superfície das fibras de junco (SFGO). A concentração de GO usada foi equivalente a 0,1% em peso de SFs e matriz epóxi. Além disso, será feito pela primeira vez uma investigação do material compósito em um sistema de blindagem multicamadas (SBMs). A caracterização química, térmica e mecânica das fibras que irão sofrer tratamento e os respectivos compósitos serão realizadas. Dentre as técnicas sugeridas pode-se citar a análise termogravimétrica (TGA), calorimetria diferencial de varredura (DSC), análise termomecânica (TMA), difração de raios X (DRX), espectroscopia do infravermelho por transformada de Fourier (FTIR), microscopia eletrônica de varredura (MEV). Em relação aos ensaios mecânicos propostos vale destacar os ensaios de tração, impacto Izod e Charpy, ensaios de flexão e análise dinâmico-mecânica (DMA). A avaliação balística será investigada empregando o ensaio de velocidades residual com uma munição de calibre 7,62 mm e o ensaio com o SBM unido a um material que simula a densidade do corpo humano. Por último, os resultados serão tratados estatisticamente através da análise de variância (ANOVA), teste Tukey e análise de Weibull. Além disso, para todos os tratamentos alcalinos de diferentes concentrações e tempos, o desaparecimento da banda de 1731 cm^{-1} se destacou em comparação com a fibra não tratada. A análise de DMA referente a 30 SFGO/EP revelou que o módulo atingiu um pico máximo de 128 MPa, indicando que o GO agiu restringindo mais fortemente o movimento das macromoléculas da matriz. Tan δ de 30 SFM/EP foi de aproximadamente 0,39, muito semelhante à 30 SFGO/EP (0,41), indicando que o tratamento alcalino produziu um compósito com forte interação. Por fim, os compósitos avaliados possuem potencial em aplicações aeroespaciais e automotivas.

Palavras-chave: Natural Lignocellulosic Fibers; Dynamic Mechanical Analysis; Residual Velocity; *Cyperus malaccensis*; Analysis of Variance.

ABSTRACT

Several industry sectors such as automotive and aerospace seek to develop stronger and lighter materials as a way to improve mechanical performance. Composite, especially those with a fiber used as a reinforcement for polymer matrix, fit well into these demands due to their high capacity to unite a low density material and a high mechanical strength. Therefore, many researchers are making an effort to develop composites that can be applied on a variety of engineering applications, even as a material used in personal ballistic protection. In addition, there is a concern from the scientific community to develop new environmentally friendly materials. This effort resulted in several works focused on the incorporation of natural lignocellulosic fibers (NLFs) in polymeric matrices. The use of NLFs as engineering material can aid the economic development of certain riverside and rural regions in Brazil if used on a larger scale. Therefore, the present dissertation uses the seven-island-sedge fibers (*Cyperus malaccensis Lam.*), here denoted as sedge fibers (SF), for short, as reinforcement to epoxy matrix. For the first time it is investigated in the scientific literature, the effect of the alkali treatment and functionalization of the SFs with graphene oxide (GO), as well as the SF reinforcing an epoxy matrix incorporated with GO. The work treated SFs with different NaOH solution concentrations of 3%, 5%, and 10% with periods of 24, 48, and 72 h. The treated SFs presented parameters that can be applied for obtaining better properties of the SFs reinforcing epoxy composites. Furthermore, this work evaluated the GO coating effect on the surface of sedge fibers (SFGO). The GO concentration used was equivalent to 0.1 wt.% of SFs and epoxy matrix. Moreover, an investigation of the composite material in a multilayer armor system (MAS) was carried out for the first time. The chemical, thermal and mechanical characterization of the SFs and their epoxy composites were performed. Among the utilized techniques, is worth mentioning the thermogravimetric analysis (TGA), differential scanning calorimetry (DSC), thermomechanical analysis (TMA), X-ray diffraction (XRD), Fourier transform infrared spectroscopy (FTIR), electron scanning microscopy (SEM). Regarding the proposed mechanical tests, it is worth mentioning the tensile tests, Izod and Charpy impact tests, bending tests and dynamic-mechanical analysis (DMA). The ballistic evaluation was investigated using the residual velocity test with a 7.62 mm caliber ammunition and the test with the MAS attached to a material that simulates the density of a human body. Experimental results were statistically treated using the methods of analysis of variance (ANOVA), Tukey test and Weibull analysis. Furthermore, for all alkali treatments of different concentrations and times, the disappearance of the 1731 cm^{-1} band stood out in comparison with the untreated fiber. DMA analys regarding the 30 SFGO/EP nanocomposite revealed the modulus reached a maximum peak of 128 MPa, indicating that the GO acted more strongly restricting the movement of the matrix macromolecules. Whereas, The Tan δ value of 30 SFM/EP was approximately 0.39, very similar to 30 SFGO/EP (0.41), indicating that the present alkaline treatment produced a composite with a strong interfacial interaction. The results of 30 SFGO/EP, the projectile stopped by it has a mean speed of 172 m/s. At last the present composites are suitable for aerospace and automotive applications.

Keywords: Natural lignocellulosic fibers; Dynamic mechanical analysis; Residual velocity *Cyperus malaccensis*; Analysis of variance.

LIST OF FIGURES

LIST OF TABLES

LIST OF ABBREVIATIONS AND ACRONYMS

ABNT	Brazilian Association of Technical Standards (*Associação Brasileira de Normas Técnicas*)
AFM	Atomic Force Microscopy
aGO	Solution of Graphene Oxide in Alcohol
A_2lO_3	Alumina
AlN	Aluminum Nitride
ANOVA	Analysis of Variance
ASTM	American Society for Testing of Materials
BFS	Backface Signature
B_4C	Boron Carbide
C	Effective coefficient
CAEx	Army Evaluation Center (*Centro de Avaliações do Exército*)
CBMM	Brazilian Metallurgy and Mining Company (*Companhia Brasileira de Metalurgia e Mineração*)
CI	Crystallinity index
CH4	Methane
CNLFs	Composites Reinforced with Natural Fiber
C NMR	Carbon-13 Nuclear Magnetic Resonance
CS	Crystallite Size
DGEBA	Diglycidyl Ether of Bisphenol A
DMA	Dynamic Mechanical Analysis
DSC	Differential Scanning Calorimetry
DTG	Derivative Thermogravimetry
E'	Storage Modulus

E"	Loss Modulus
EDS	Energy Dispersive Spectroscopy
FEM	Finite Element Method
FTIR	Fourier Transform Infrared
GO	Graphene Oxide
HSD	Honestly significant Difference
H_2SO_4	Sulfuric Acid
H_2O_2	Hydrogen Peroxide
HPI	High-Pressure Instrumentation
IME	Military Institute of Engineering (*Instituto Militar de Engenharia*)
INT	National Institute of Technology (*Instituto Nacional de Tecnologia*)
IPqM	Naval Research Institute (*Instituto de Pesquisas da Marinha*)
KBr	Potassium Bromide
KNO_3	Potassium Nitrate
$KMnO_4$	Potassium Permanganate
LbL	Layer-by-Layer Deposition
MAS	Multilayered Armor Systems
MFA	Microfibrillar Angle
NaOH	Sodium Hydroxide
NBR	Brazilian Standard (*Norma Brasileira*)
Nb_2O_5	Niobium Pentoxide
NIJ	National Istitute of Justice
NLFs	Natural Lignocellulosic Fibers (*Fibras Naturais Lignocelulósicas*)
PA	Polyamide
PE	Polyethylene
PEG	Polyethylene Glycol

PP	Polypropylene
PS	Polystyrene
PVC	Polyvinyl Chloride
QMR	Residual Mean Square (*Quadrado Médio do Resíduo*)
s_3N_4	Silicon Nitride
SE	Secondary Electrons
SEM	Scanning Electron Microscopy
SiC	Silicon Carbide
TEM	Transmission Electron Microscope
TETA	Triethylene Tetramine
TGA	Thermogravimetric Analysis
TMA	Thermomechanical Analysis
UCSD	University of California San Diego
UENF	State University of the North Fluminense Darcy Ribeiro (*Universidade Estadual do Norte Fluminense*)
UFF	Federal Fluminense University
UHMWPE	Ultra High Molecular Weight Polyethylene
UV	Ultraviolet Light
XPS	X-ray Photoelectron Spectroscopy
XRD	X-ray Diffraction

LIST OF SYMBOLS

d	Fiber Diameter
E	Elastic Modulus
$\mathrm{E_{comp}}$	Composite Elastic Modulus
E_m	Matrix Elastic Modulus
E_f	Fiber Elastic Modulus
V	Volume
V_c	Composite Volume Fraction
V_m	Matrix Volume Fraction
V_f	Fiber Volume Fraction
σ	Tensile Strength
$\sigma_{\mathrm{máx}}$	Maximum Engineering Stress
τ	Shear Yield Stress of the Matrix
σ_f	Maximum Fiber Tensile Strength
ϵ	Engineering Strain
$\mathrm{d}\sigma_f/\mathrm{d}\epsilon$	Slope of the Stress-Strain Curve
ρ	Specific Density
l_c	Critical Fiber Length
t	Time
P	Pressure
S	Material State Equation Constant
C_o	Velocity
C	Speed of Sound in the Material
U_p	Particle Velocity
U_S	Shock Wave Velocity

V_{50}	Ballistic Limit
V_p	Plastic Wave Velocity
V_E	Elastic Wave Velocity
V_S	Projectile Shock Velocity
V_L	Limit Velocity
V_r	Residual Velocity
V_i	Impact Velocity
E_{abs}	Absorbed Energy
I_c	Crystallinity Index
I_1	Minimum Diffraction Intensity
I_2	Maximum Diffraction Intensity
q	Total Amplitude
r	Number of Treatment Repetitions
GL	Degrees of Freedom
Θ	Characteristic Unit
β	Weibull Modulus
$\beta\ ln(\theta)$	Linear Coefficient
R^2	Linear Fit
T_g	Glass Transition Temperature
e_{verde}	Green Body Thickness
$e_{sinterizado}$	Sintered Sample Thickness
$\rho_{sinterizado}$	Specific Mass of the Sintered Ceramic Body
C	Carbon
g	Gram
h	Hour
J	Joule

m	Meter
mg	Milligram
ml	Milliliter
mm	Millimeters
m/s	Meters per Second
N	Newton
O	Oxygen
MPa	Mega Pascal
q	Total Amplitude
r	Number of Treatment Repetitions

SUMÁRIO

1 INTRODUCTION

Since the dawn of human civilization, the scenario of armed conflicts worldwide has been marked by the constant evolution of weapons and armor. Today, new materials are being studied and developed by researchers to offer protection not only against single high-velocity projectiles but also against multiple shots, explosive devices, and explosive fragments (LIU; STRANO, 2016). However, increasing the protective capacity of a monolithic armor usually causes an increase in its weight. This is an important issue for protecting the military, for whom mobility is a basic requirement, demanding lighter and more flexible materials. Therefore, studies are being carried out to develop lighter armor by joining different materials to create what is known as a multi-layered armor system (MAS), which can offer even greater protection (LUZ et al., 2020; KUMAR et al., 2021).

Thus, MAS is being investigated and applied as plates in vests for personal ballistic protection against the threat of high-velocity ammunition (>800 m/s) (MONTEIRO et al., 2018; BHAT et al., 2021; SCAZZOSI et al., 2022). A typical MAS has a fragile front ceramic layer, which is hard enough to erode the projectile. Since this projectile, like the NIJ level III 7.62 mm(JUSTICE, 2000), hits the ceramic front, a compressive shock wave travels through the material and is reflected as a tensile wave that shatters the brittle ceramic, absorbing more than 50% of the impact energy. A second layer is selected in search of a lighter material capable of reflecting the traction wave and reducing even more the impact energy, capturing the ceramic's debris and the projectile. A ductile metal plate can be used as the third layer of the MAS. The system's ballistic efficiency is evaluated by positioning the target onto a clay witness that simulates the density of the human body (REIS et al., 2021).

According to Medvedovski (2006), different ceramics are being used as the front layer, mainly alumina (Al_2O_3), but also non-oxide compounds such as boron carbide (B_4C), silicon carbide (SiC), silicon nitride (S_3N_4) and aluminum nitride (AlN), and others. Regarding the intermediate layer, synthetic laminates based on aramid fiber, such as Kevlar^{TM} and Twaron^{TM}. Furthermore, it is also used ultra-high molecular weight polyethylene (UHMWPE), as Dyneema^{TM} and Spectra (LUZ et al., 2020).

In a recent review, Benzait e Trabzon (2018) stated that the advent of new materials with excellent rigidity and resistance, low density, and high energy absorption positions them as future choices for ballistic armor materials. Additionally, they highlighted another trend identified in recent research (NURAZZI et al., 2021; NAYAK et al., 2020), where polymer matrix composites reinforced with natural fibers are explored as alternatives to replace Kevlar in MASs. Although significantly weaker than aramid fiber, the investigated composites (FILHO et al., 2020a; PEREIRA et al., 2020; FILHO et al., 2021), when used

as a second layer, exhibit ballistic performance comparable to Kevlar of the same thickness. This performance is assessed by the trauma inflicted on clay witness. As suggested by standards, the back-face signature (BFS), also known as recoil, must be less than 44 mm. The unexpected ballistic performance of natural fiber composites is attributed to the second layer's role in dissipating impact energy, relying on the fiber's ability to capture ceramic fragments rather than the fiber's strength (MONTEIRO et al., 2019).

Additionally, the use of lignocellulosic natural fibers (NLFs) is encouraged due to their low cost, which can be up to 70 times cheaper than Dyneema, a material commonly used in ballistic vests (LUZ et al., 2020). Thus, along with other advantages such as low environmental impact and abundant availability, makes natural fiber-based composites a promising alternative to replace synthetic fibers (PICKERING; EFENDY; LE, 2016; GÜVEN et al., 2016).

As most NLFs applied in polymeric composites (COSTA et al., 2019; JUNIO et al., 2020; SOUZA et al., 2020), seven-island sedge fiber also exhibits low interfacial adhesion (NEUBA et al., 2020). This is attributed to the amorphous hemicellulose and lignin, which act as a natural hydrophilic wax, absorbing water on the fiber's surface. Consequently, a weak bond is expected between the fiber surface and the hydrophobic polymer. This impacts the composite's performance as the second layer of MASs for ballistic protection. In fact, the impact of a high-velocity projectile on an MAS with a seven-island sedge composite results in various fracture mechanisms, including delamination, rupture, and fiber pullout (BRAGA et al., 2017b; BRAGA et al., 2017a). Some of these mechanisms are crucial for absorbing impact energy. However, others, such as delamination, may compromise the integrity of the MAS after an initial ballistic shot. This leads to the loss of its capability to provide protection against multiple shots, as required by standard regulations (JUSTICE, 2000).

Despite ballistic performance in comparison to a synthetic material as Kevlar^{TM}, the integrity of a composite reinforced with NLFs is always questionable. Lower amounts, usually below 30% by volume of fiber, have resulted in its rupture (ASSIS et al., 2018; NASCIMENTO et al., 2017). Even a composite with 30% volume fraction can be broken due to delamination, allowing easy penetration of a projectile in the case of a subsequent shot.

The surface modification of NLFs has been widely applied to enhance the adhesion between the matrix and the fiber (LATIF et al., 2019; REDDY; YOGANANDAM; MOHANAVEL, 2020), providing an effective way to prevent delamination. Consequently, to increase the effectiveness of interfacial bonding, the fiber's surface needs to be modified with different chemicals products, as chemical treatment exposes more reactive groups on the fiber surface, facilitating efficient coupling with matrices. As a result, improved mechanical properties of the composites can be achieved (JENA; MOHANTY; NAYAK,

2020).

Recently, some researchers have focused their efforts on coating NLFs with graphene oxide (GO) (LUZ et al., 2021; COSTA et al., 2021; PEREIRA et al., 2022). This approach allows the improvement of interfacial adhesion between the fiber and matrix, enhancing both mechanical and ballistic properties.

Therefore, the focus of this work is to investigate how alkaline treatment and GO functionalization influence the mechanical, chemical, and thermal properties of fibers from the plant *Cyperus malaccensis Lam.* Additionally, it aims to explore the use of epoxy matrix composites reinforced with seven-island sedge fiber as a secondary layer in MASs, as well as other potential future applications for this material. It is worth noting that these studies are currently absent in the literature, making the investigation of these aforementioned fiber treatments and tests essential, based on their significant contribution to scientific knowledge.

1.1 MOTIVATION

The present work was developed taking into consideration the global concern for producing new environmentally sustainable materials capable of exhibiting performance similar to commercially employed ones, along with a reduced environmental impact and lower material cost. Furthermore, studies investigating the development of new materials applied to personal ballistic protection are relevant for the Brazilian Army. Consequently, the Materials Engineering Department at the Military Institute of Engineering (IME) invests resources in research related to this type of application. According to the literature, composite materials reinforced with NLFs have shown promising results in terms of ballistic performance, associated with lower costs and reduced weight. Thus, this work aims to characterize chemically treated and graphene oxide (GO) functionalized seven-island sedge fibers to investigate if there is an enhancement in their properties and ballistic applications when compared to *in natura* fibers incorporated as reinforcement in epoxy resins. The goal is to increase the use of domestic raw materials and support the development of economically less privileged regions. Additionally, the characterization of the proposed material can be applied to investigate other possible conventional or structural applications, providing original contributions to the state of the art in the field of composite materials.

1.2 RESEARCH OBJECTIVES

1.2.1 GENERAL OBJECTIVE

The purpose of this study is to characterize mechanically, structurally, and thermally the *in natura*, alkali treated, and GO functionalized seven-island sedge fibers by

investigating and analyzing the resulting properties after their incorporation into epoxy resin-based composites. The alkaline and functionalization treatments aim to enhance the compatibility of the matrix-fiber interface. Additionally, the effectiveness of ballistic performance will be verified when different groups of composites reinforced with seven-island sedge fibers are incorporated as an intermediate layer of MASs. The evaluation will be conducted by measuring the depth of indentation (trauma) caused in clay witness. Measurements of kinetic energies absorbed by the composite plates in various groups and compositions will be investigated. Furthermore, it will be emphasized the mechanisms and fracture surfaces revealed through destructive tests and observed in the microstructures of the specimens by Scanning Electron Microscopy (SEM).

1.2.2 SPECIFIC OBJECTIVES

In pursuit of achieving the general objective, the following specific objectives have been outlined:

- Seven-island sedge fibers characterization

1) Evaluate the effectiveness of alkaline treatment on seven-island sedge fibers and the increase in crystallinity at concentrations of 3%, 5%, and 10% NaOH, with immersion times of 24h and 72h, without agitation. Analysis using X-ray diffraction (XRD) of the fibers will be conducted. Additionally, the material's microstructure will be assessed with the aid of SEM;

2) Analyze the efficiency of GO functionalization of seven-island sedge fibers concerning the increase in crystallinity by XRD analysis and verify the material's microstructure using SEM analyses;

3) Analyze the chemical composition of alkali treated and GO-functionalized fibers by Fourier-transform infrared spectroscopy (FTIR) analyses;

4) Evaluate the thermal properties of alkali treated and GO-functionalized fibers through thermogravimetric analysis (TGA) and differential scanning calorimetry (DSC) tests.

- Composites reinforced with seven-island sedge fibers characterization

5) Calculate the glass transition temperature (T_g) of composites reinforced with 0%, 10%, 20%, and 30% of sedge fibers volume using DMA curves. This includes groups of composites reinforced with 30% of alkali treated fibers, GO coated fibers, and epoxy matrix incorporated with GO. Evaluate storage modulus (E'), loss modulus (E"), and tangent delta (Tanδ);

6) Examine the thermal properties of composites reinforced with 30% of alkali treated fibers, GO coated fibers, and epoxy matrix incorporated with GO by TMA, DSC,

and TGA analyses;

7) Verify the chemical composition of composites reinforced with 30% by volume of alkali treated fibers, GO coated fibers, and epoxy matrix incorporated with GO by FTIR spectroscopy analysis;

8) Verify the influence of alkaline treatment and coated fibers by GO, as well as epoxy matrix functionalized with GO, regarding impact energy through Izod and Charpy impact tests. The manufactured groups will consist of epoxy matrix composites reinforced with 30% of seven-island sedge fibers. In addition, perform other mechanical tests such as tensile, bending, and compression tests. Furthermore, analyze the microstructure of fracture surfaces using SEM and conduct an ANOVA analysis.

• Ballistic performance evaluation of composites reinforced with seven-island sedge fibers

9) Determine if composites reinforced with seven-island sedge fibers, tested as an intermediate layer in MASs, meet the requirements of the international standard NIJ 0101.04 (2000) for level III protection;

10) Compare the ballistic performance of composites reinforced with seven-island sedge fibers with other composites used as a intermediate layer in MASs. Additionally, investigate the fracture surfaces of the composites after ballistic tests to examine the energy absorption mechanisms through SEM;

11) Compare the individual performance of epoxy composites reinforced with seven-island sedge fibers based on the limit velocity (V_L) and absorbed energy (E_{abs}). Examine physical integrity and analyze fracture surfaces of the composites after ballistic tests to identify energy absorption mechanisms through SEM;

12) Compare the individual performance of epoxy composites reinforced with 30% of alkali treated fibers and epoxy fibers functionalized with GO based on the limit velocity (V_L) and absorbed energy (E_{abs}). Examine physical integrity and analyze fracture surfaces of the composites after ballistic tests to identify energy absorption mechanisms through SEM.

2 LITERATURE REVIEW

2.1 NATURAL FIBERS

Natural fibers are considered a renewable resource and have been extensively used for millennia through materials derived from these fibers, such as mats, ropes, and baskets. They are obtained from various sources, including animal, mineral, and plant origins (BLEDZKI; GASSAN, 1999). Plant fibers contain components such as cellulose, hemicellulose, lignin, and pectin. Animal fibers made of proteins are less robust than plant fibers. Mineral fibers consist of a group of minerals, including asbestos and basalt. Unfortunately, the use of mineral fibers leads to health issues, and therefore, they are not extensively used (KANNAN; THANGARAJU, 2021).

In recent years, the gradual concern regarding non-renewable resources has become increasingly relevant, associated with the scientific community's interest in investigating environmentally friendly and sustainable materials. This has led to scientists making efforts towards the development and use of natural fibers derived from plants, especially lignocellulosic natural fibers (NLFs), as reinforcement in composites used in many engineering applications (SAHEB; JOG, 1999; KU et al., 2011; THAKUR; SINGHA; THAKUR, 2013; SABA et al., 2016b; GÜVEN et al., 2016; LOTFI et al., 2019).

When compared to composites reinforced with synthetic fibers, natural fiber-based composites exhibit low cost, lightweight, biodegradability, abundance, high specific mechanical strength, specific stiffness, and require minimal technology for extraction. However, they present some disadvantages such as low thermal resistance, low thermal stability, and moisture absorption, leading to poor surface adhesion between the fiber and matrix. Nevertheless, through physical and chemical treatments and an appropriate fiber extraction method, efforts are made to enhance the mechanical properties and improve the interfacial adhesion between the fiber and matrix. In this way, the study of various NLFs becomes relevant and feasible (BLEDZKI; GASSAN, 1999; PICKERING; EFENDY; LE, 2016; SANJAY et al., 2018; PEÇAS et al., 2018; LOTFI et al., 2019).

Brazil is in a prominent position regarding the production of natural fibers, since a wide variety of these fibers are possible to obtain. Due to its vast territory, biodiversity, and favorable climatic conditions, Brazil has the capacity to provide materials that can be used in engineering and the textile industry (SATYANARAYANA; GUIMARÃES; WYPYCH, 2007).

2.2 NATURAL LIGNOCELLULOSIC FIBERS (NLFs)

Fibers obtained from plants are also known as lignocellulosic fibers. This term used in the literature suggests the predominance of cellulose and lignin in their structure. Another important aspect of fibers is directly related to the fact that they are complex natural composites. As shown in FIG. 2.1, natural fibers are highly heterogeneous, depending on the type of harvest, soil, fertilizers used, leaves, fruits, or stems of the plants (JOHN; THOMAS, 2008; MONTEIRO et al., 2011).

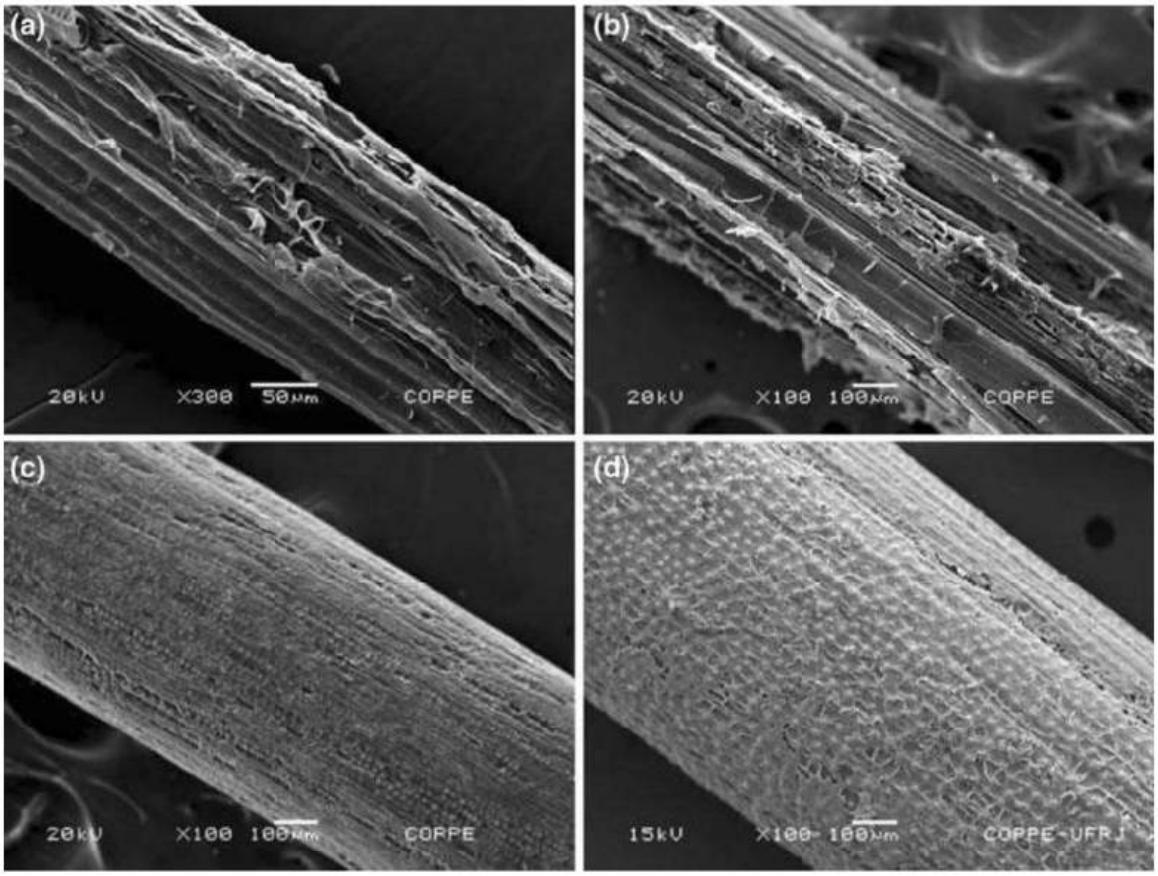

Figura 2.1 – SEM of the surface of NLFs: (a) Sisal, (b) Bamboo, (c) Coir, and (d) Piassava.

Source – Adapted from Monteiro et al. (2011).

The characteristic properties of natural fibers vary considerably due to factors such as the age of the plant and where they were extracted, for example, stem, leaf, or seed. Furthermore, properties of a single fiber depend on the shape, size, crystallinity, orientation, and thickness of the cell wall. In contrast, synthetic fibers as aramid, glass, or carbon fibers are engineered with preset properties. On the other hand, inherent properties of natural fibers fluctuate considerably. Fibers are categorized as shown in TAB. 2.1 (GHOLAMPOUR; OZBAKKALOGLU, 2020).

Tabela 2.1 – Origin of some well-known NLFs.

Origin	Fibers
Leaf	sisal, curaua, piassava
Seed	cotton
Fruit	coir
Stem	flax, jute, malva and ramie.
Wood	eucalyptus and pine
Grasses	bamboo, sugarcane bagasse.

Source – (Adapted from JOHN; THOMAS, 2008).

The chemical composition of plant fibers, when moisture content is eliminated, consists primarily of cellulose, hemicellulose, and lignin. Consequently, these fibers are classified as natural composites, where cellulose microfibrils surround and reinforce a matrix composed of hemicellulose and lignin. The chemical composition varies according to the type of plant, as evident in TAB. 2.2, which outlines the main chemical constituents for some distinct fibers (MOHANTY; MISRA; DRZAL, 2002; FARUK et al., 2012; SOOD; DWIVEDI, 2018).

Tabela 2.2 – Chemical composition of some NLFs.

Fiber	Cellulose (%)	Hemicellulose (%)	Lignin (%)	Waxes (%)
Bagasse	55.2	16.8	25.3	-
Bamboo	26-43	30	21-31	-
Flax	71	18.6-20.6	2.2	1.5
Kenaf	72	20.3	9	-
Jute	61-71	14-20	12-13	0.5
Hemp	68	15	10	0.8
Ramie	68.6-76.2	13-16	0.6-0.7	0.3

Source – (adapted from FARUK, 2012).

The cell wall in a fiber is not a homogeneous membrane. Each fibril presents a complex layered structure consisting of a primary layer, secondary layer, and a central void known as the lumen. While the first layer has a very thin wall, deposited during cell growth that surrounds a secondary layer, the second layer is composed of three sub-layers, and the mechanical properties of the fibers are determined by the thickness of the middle layer. The middle layer contains a series of helically wound cellulose microfibrils conceived along a chain of cellulose molecules. The angle between the fibril axis and the microfibril is referred to as the microfibrillar angle (MFA). The specific value of this parameter varies from one fiber to another (BLEDZKI; GASSAN, 1999; JOHN; THOMAS, 2008; OUSHABI, 2019). FIG. 2.2 illustrates the microstructure of a natural fiber.

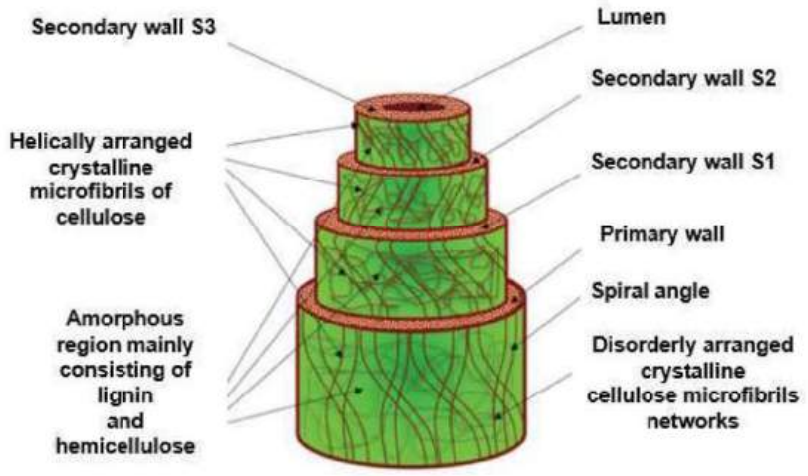

Figura 2.2 – Natural lignocellulosic fiber's microstructure.

Source – Adapted from Kannan e Thangaraju (2021).

Cellulose is a hydrophilic glucan polymer consisting of a linear chain linked by β-1,4-glycosidic bonds that have alcoholic hydroxyl groups. These groups establish intramolecular hydrogen bonds within the macromolecule itself and between other cellulose macromolecules, as well as with hydroxyl groups from the surroundings. Therefore, all lignocellulosic fibers exhibit hydrophilic nature (MOHANTY et al., 2000). FIG. 2.3 depicts the structure of the cellulose chain.

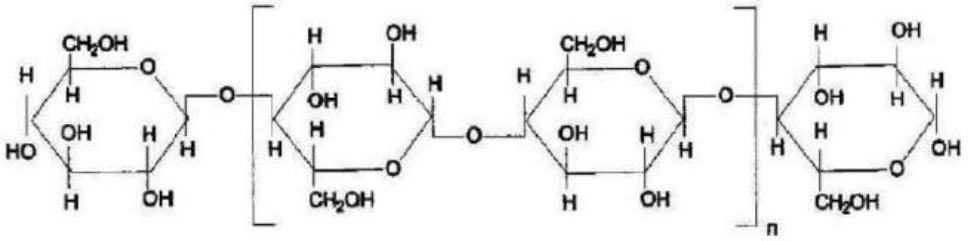

Figura 2.3 – Structure of the cellulose chain.

Source – Adapted from John e Thomas (2008).

.

Hemicellulose is a polysaccharide with a structure similar to that of cellulose. However, it exhibits distinct features such as a high degree of cross-linking, a lower degree of polymerization, and is formed by different sugars as opposed to cellulose (MOHANTY; MISRA; DRZAL, 2002).

Lignin is a biochemical polymer that acts as a material for structural support in plants. Lignin fills the spaces between polysaccharide fibers, connecting them. The lignification process leads to the hardening of the cell wall and is the most thermally

stable component. The structure of lignin is depicted in FIG. 2.4 (THAKUR; THAKUR; GUPTA, 2014).

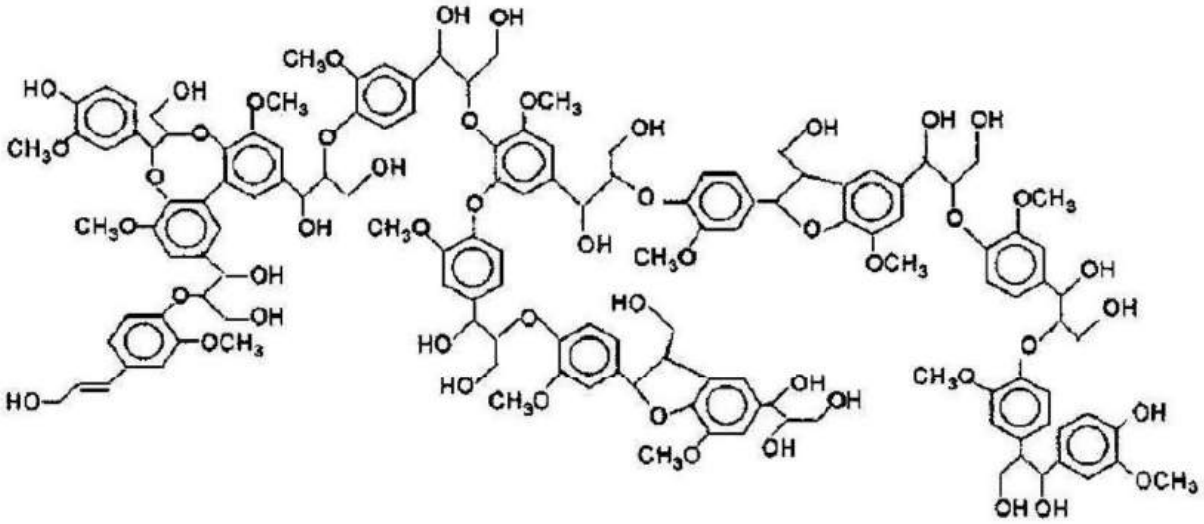

Figura 2.4 – Structure of lignin chain.

Source – Adapted from Mohanty, Misra e Drzal (2005).

When synthetic fibers are compared to certain lignocellulosic fibers, it can be observed that plant fibers exhibit good mechanical properties. TAB. 2.3 displays some properties of specific NLFs compared to synthetic fibers. It is noted that NLFs, in general, have low density compared to synthetic fibers. The option to use them as reinforcement in composite materials provides new materials with significantly low weight and superior properties due to the unique characteristics of these fibers (MONTEIRO et al., 2011; SHAH, 2013).

In TAB. 2.3, there is an extensive variation in the values of NLF properties. This variation is due to the configuration of each fiber being affected by the conditions that govern the process and the growth of the complex structure monitored through the plant cell metabolism. These factors are linked to the amount of light in the environment, soil composition, water abundance, and even the genetic variation of each plant. Consequently, mechanical and physical properties vary from one fiber to another (ELANCHEZHIAN et al., 2018).

Tabela 2.3 – A comparison of density (ρ), microfibrillar angle (MFA), diameter, elastic modulus (E) and tensile strength (σ) between NLFs and synthetic fibers properties.

Fiber	ρ **(g/cm^3)**	**"σ" (MPa)**	**"E" (GPa)**	**MFA (°)**	**Diameter (μm)**
Carbon	1.78 - 1.81	2500 - 6350	230 - 400	-	-
E-Glass	2.5 - 2.58	2000 - 3450	70 - 73	-	-
Aramide	1.44	3000 – 4100	63 – 131	-	-
Cotton	1.55	300 - 700	6 - 10	20 - 30	11.5 - 17
Bamboo	1.50	575	27	-	10 - 40
Flax	1.40 - 1.50	500-900	50-70	5	17.80-21.60
Hemp	1.40- 1.50	310-750	30-60	6,20	17-23
Jute	1.20 - 1.50	200-450	20-55	8.10	15.90-20.70
Ramie	1.55	915	23	-	28.10-35
Abaca	1.50	12	41	-	17-21.40
Banana	1.30 - 1.35	529 - 914	27 - 32	11 - 12	-
Pineapple leaf fiber	1.44 - 1.56	413-1627	60-82	6-14	20-80
Sisal	1.30 - 1.50	80 - 840	9-22	10-22	18.30 - 23.70
Coir	1.15 - 1.35	106-175	6	39-49	16.20 - 19.50
Guaruman	-	614	21	7.30-8.20	7-27

Source – Adapted from Monteiro et al. (2011), Jha et al. (2019), Reis et al. (2020).

There is a trend of increasing mechanical properties in certain NLFs associated with the inverse of the diameter of these fibers. This occurs due to the presence of fewer defects in thinner fibers compared to thicker ones. Thus, fibers found within smaller diameter ranges exhibit higher strength. FIG.2.5 illustrates, based on experimental data of the average tensile strength of specific NLFs, graphs as a function of the mean diameter (MOHANTY et al., 2000; SATYANARAYANA; GUIMARÃES; WYPYCH, 2007; JHA et al., 2019).

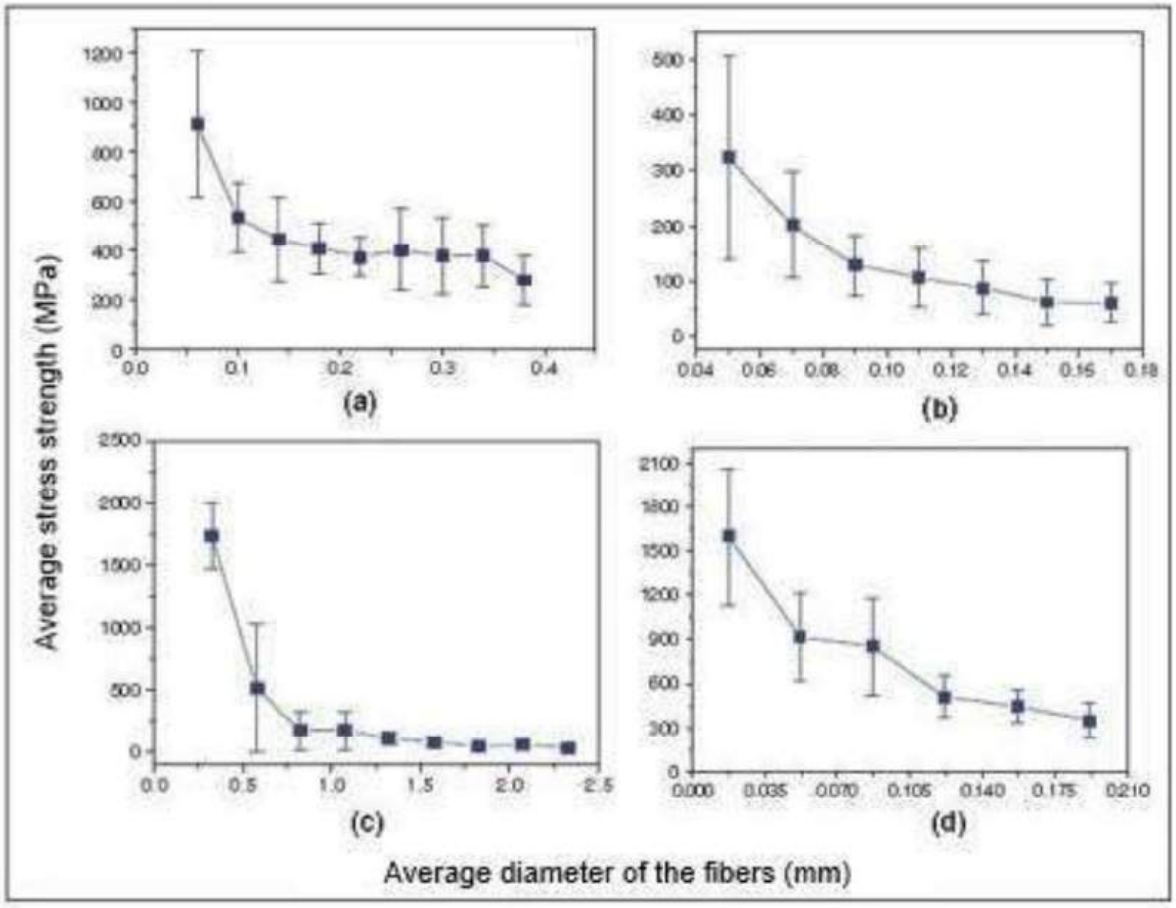

Figura 2.5 – Average tensile strength as a function of the diameter of sisal fibers (a), jute fibers (b), piassava fibers (c), and (d) ramie fibers.

Source – Adapted from Monteiro et al. (2011).

.

Furthermore, according to the literature, the crystallinity index and microfibrillar angle of NLFs have a direct relationship with mechanical properties such as mechanical strength and modulus of elasticity. Thus, the higher the cellulose content and the lower the MFA value, the better the mechanical properties. Despite other factors, with surface treatment being one of them, influencing directly the reduction or enhancement of these properties (TELI; TEREGA, 2019; HASSANI et al., 2020; REIS et al., 2020).

2.3 SURFACE MODIFICATION ON NATURAL LIGNOCELLULOSIC FIBERS (NLFs)

NLFs are generally hydrophilic by nature. Additionally, they possess certain properties that affect compatibility with hydrophobic matrices, resulting in poor interfacial adhesion. These properties include low thermal stability, low dimensional stability, and high

moisture absorption (ALHIJAZI et al., 2020; AMIANDAMHEN; MEINCKEN; TYHODA, 2020; KHAN; SRIVASTAVA; GUPTA, 2018).

The surface modification treatment of natural fibers directly influences their physical and chemical properties (BLEDZKI; REIHMANE; GASSAN, 1996; VALASEK; MUELLER; SLEGER, 2017). Therefore, various surface modification techniques are being addressed in numerous citations in the literature (OUSHABI, 2019; OUSHABI et al., 2017; ZHOU; CHENG; JIANG, 2014; MOKALOBA; BATANE, 2014), aiming to improve the interfacial performance of composites reinforced with this type of material.

Among physical modification treatments, one can mention treatments such as corona, laser, plasma, etc. On the other hand, chemical treatments are known as alkaline treatment, silanization, acetylation, among others. Chemical treatments are recognized as a more cost-effective method than physical treatments. Alkaline treatment (NaOH), in particular, is known as the cheapest and extensively used chemical modification technique (MANALO et al., 2015).

The chemical modification of NLFs actually amounts to altering the percentage of cellulose, representing the major constituent of these fibers. According to Mwaikambo e Ansell (2002), the spatial conformation of cellulose controls its physical and chemical properties. Moreover, the amorphous region is much more accessible to the attack of reagents than the crystalline region.

2.3.1 ALKALINE TREATMENT

This treatment consists of immersing lignocellulosic fibers in an aqueous NaOH solution, previously establishing the concentration and the immersion time. The objective is removing part of the lignin, pectins, waxy substances, and natural and artificial impurities covering the external surface of the fiber cell wall. Additionally, alkaline treatment leads to fiber fibrillation, meaning it breaks down the composite fiber bundle into smaller fibers, increasing the effective surface area available for contact with a wet matrix. It should be noted that sodium hydroxide (NaOH) is the most commonly used chemical in this type of treatment (OUSHABI, 2019). Nevertheless, a high alkaline concentration or period of exposure excessively increases NLFs delignification, which leads to weaker or damaged fibers, as well as diminishing their mechanical performance (LOGANATHAN et al., 2020). For this reason, achieving an optimum value between the two parameters is essential to enhance fibers' properties and consequently composites.

Furthermore, alkaline treatment minimizes the fiber diameter, thereby increasing the aspect ratio. Additionally, it results in an increased surface roughness of the fiber, improving the adhesion between the fiber and the matrix (JAAFAR et al., 2019). The treatment further promotes the conversion of hydroxyl groups into cellulose alkoxides and

reduces the hydroxyl group present on the fiber surface. This conversion enhances the hydrophobicity of the fibers (KANNAN; THANGARAJU, 2021).

Another important point is related to the removal of surface impurities, which can be an advantage for fiber-matrix adhesion as it can facilitate both mechanical interlocking and bonding reactions due to the exposure of hydroxyl groups to chemicals such as resins. In recent years, much research has been conducted on the relationship between alkaline treatment and changes in the crystallinity index and tensile strength properties of fibers (OUSHABI, 2019).

It is important to emphasize that the optimization of parameters influences the treatment efficiency, such as solution concentration, temperature, and treatment time, contributing to the improvement of the mechanical properties of NLFs and composite materials (OUSHABI, 2019). However, the treatment operation results in additional costs and reduces the economic competitiveness of natural fibers compared to synthetic fibers (BLEDZKI; GASSAN, 1999; MONTEIRO et al., 2009; SATYANARAYANA; ARIZAGA; WYPYCH, 2009; FARUK et al., 2014; KOOHESTANI et al., 2019).

Several studies have related that chemical treatments, including alkaline, induce a decrease in the tensile strength of fibers. This might be assigned to damage present on the cell wall and the exceeding removal of lignin and hemicellulose that act as a matrix phase in NLFs structures (SALIH; ZULKIFLI; AZHARI, 2020; LI; TABIL; PANIGRAHI, 2007; JACOB; THOMAS; VARUGHESE, 2004). Nonetheless, the thermal stability of fibers is significantly improved, as in the case of *Luffa cylindrica* which was immersed in a 2% NaOH alkaline solution or even the sisal (MISHRA et al., 2003). It also reduces the moisture absorption for composites reinforced by NLFs; for example, jute fibers could considerably reduce water absorption, when they were treated with 5%, 10%, and 15% of NaOH (KALIA; KAITH; KAUR, 2009). Thus, it enables the use of these composites in several applications due to the fact that fibers develop a higher hydrophobicity. As a consequence, the interface of the composites is not affected, improving the performance of the composites (RAJESH; PRASAD; GUPTA, 2018; OHIJEAGBON et al., 2021).

2.4 SEVEN-ISLANDS SEDGE (*Cyperus Malaccensis Lam.*)

The seven-islands sedge (*Cyperus malaccensis Lam.*; Order, Cyperales; Family, Cyperaceae, commonly named due to its native habitat in the region of seven islands. It has an erect stature, ranging from 1.5 to 1.8 meters in height, and its stem is used in the production of mats, pillows, sandals, insoles, curtains, bags, ties, coarse hats, and serves as raw material for papermaking. Among the characteristics of *Cyperus malaccensis*, it is worth highlighting the absence of nodes in its sharp stem, which is long and triangular with 2 to 3 leaves at the top of the stem (HIROCE; JÚNIOR; FEITOSA, 1988; SHIOYA

et al., 2019).

The Ribeira Valley, located in the southern state of São Paulo, has currently become the sole producer of this type of sedge in the Americas, with approximately 50 hectares of cultivated area in flooded lowlands. This plant is likely native to Seven Islands, Japan, and was introduced by the immigrant Shigeru Yoshimura in 1931. Due to local ecological conditions, the sedge cultivation has an advantage in its production, as the excess heat and humidity allow for harvesting three times a year, as opposed to Japan where it occurs only once (HIROCE; JÚNIOR; FEITOSA, 1988; SCIFONI, 2008). FIG. 2.6 depicts the seven-islands sedge plant in its cultivation zone.

Figura 2.6 – (a) cultivation area of the plant *Cyperus malaccensis Lam.* (b) stem with roots of the plant after harvest.

Source – Adapted from Shioya et al. (2019).

The process of making mats begins with a defibering machine, where the stem is split into two, becoming thinner. Then they are spread on the ground to dry, acquiring a brownish hue. FIG. 2.7 illustrates the processing and manufacturing process (SCIFONI, 2008).

Figura 2.7 – Manufacturing process.

Source – Adapted from Michelleti (2021).

.

In addition, studies have been conducted in different countries over the last decade, focusing on researching the seven-islands sedge in areas such as biology, agronomy, and environmental sciences. FIG. 2.8 shows a graph indicating published works in different areas and the percentage of studies in each individual area related to the term "*Cyperus malaccensis Lam.*", according to the Scopus database.

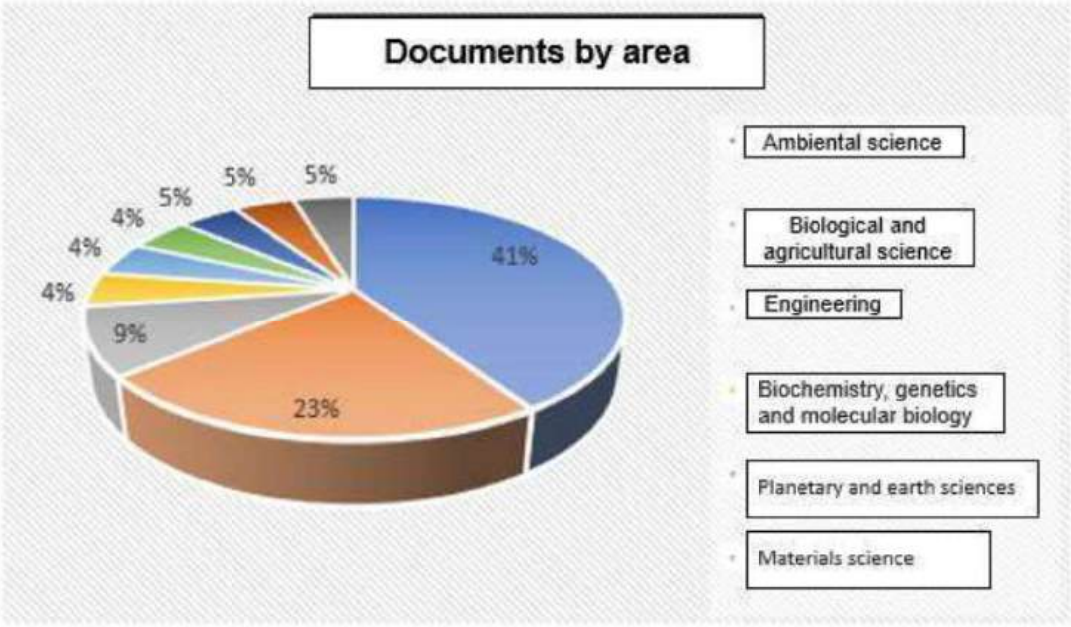

Figura 2.8 – Chart representing areas of interest related to the term "*Cyperus malaccensis Lam.*"in the Scopus database.

In recent years, a limited number of studies have focused on studying the *cyperus malaccensis* plant. Some are directed towards regions where they are cultivated (YANG et al., 2019). Research on the accumulation of heavy metals, which cause various environmental

problems due to their toxicity, in cultivation areas of this plant is considered important in the literature. Additionally, there are works related to the preparation of mats in the rural economy of Sundarbans (MANNA; MUKHERJEE; ROY, 2016; SUN et al., 2019; LI et al., 2020).

Other studies on biological topics, such as the decomposition pattern of *Cyperus malaccensis* with a cluster of fungi in the cultivation region, have been conducted. Furthermore, works involving the effects of tidal inundation and how it can influence the biogeochemical cycle of iron in sedge plantation sediments are present in the literature. Additionally, research related to nutrient concentration and how different species interact in the same region is relevant in this field (SRIDHAR; KARAMCHAND; SUMATHI, 2010; WANG et al., 2015; LUO et al., 2016).

Only in 2019, Shioya and colleagues developed a study dedicated to the investigation of properties of seven-islands sedge stems, where they were the first to determine the natural frequency, damping coefficient, and flexural stiffness using the finite element method. FIG. 2.9 displays a triangular profile of the cross-sectional structure of the stem of this plant (SHIOYA et al., 2019).

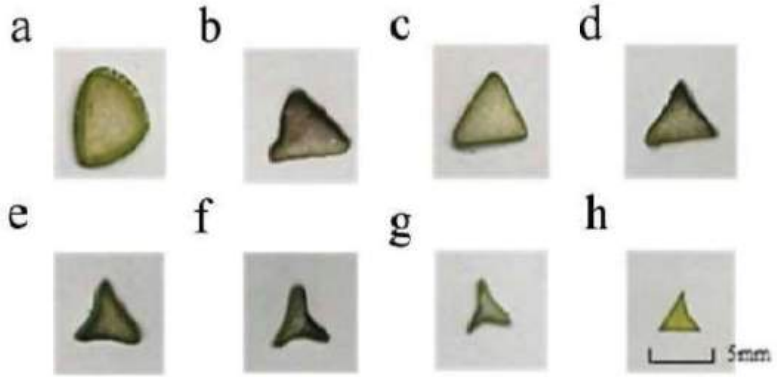

Figura 2.9 – Cross-section of the stem of *Cyperus malaccensis*. (a) indicates the region near the root; (b-g) indicates the position at multiple increments of 15 cm from position a; (h) indicates the top of the stem where the leaves grow.

Source – Adapted from Shioya et al. (2019).

According to the Scopus database (SCOPUS, 2024), a couple of researches have been published investigating the incorporation of fibers extracted from the Seven-islands sedge plant to reinforce a polymeric matrix. According to Neuba et al. (2020), the impact resistance result improved the absorbed energy by 181% for the group containing 30% fiber by volume compared to the control group. However, the tensile strength results were lower than the control group. As the authors observed, the low interfacial strength resulted in larger fracture surfaces and caused the improvement of impact properties. On the other hand, Neuba et al. (2022a) investigated basic properties of sedge fibers were investigated

with possible application in reinforcing composite materials. A dimensional distribution and the effect of fiber diameter on density were investigated using gas pycnometry. The Weibull method, used to statistically analyze the acquired data from the diameter intervals, indicated an inverse dependence, where the thinnest fibers had the highest density values. The morphology of the fibers was obtained through scanning electron microscopy (SEM), in which a lower presence of defects was revealed in the thinner fibers, corroborating the inverse density dependence. In addition, the sedge fiber was characterized by differential scanning calorimetry and thermogravimetric analysis, which indicate an initial thermal degradation at around 241°C. These results revealed for the first time that thinner sedge fibers might be promising reinforcement for polymer composites with a limit in temperature application. Additionally, Neuba et al. (2022b) have characterized the fibers extracted from sedge plant by X-ray diffraction (XRD) to calculate the crystallinity index and the microfibrillar angle (MFA). Also, an evaluation of the ultimate tensile strength by diameter intervals has been investigated and statistically analyzed by both the Weibull method and the analysis of variance (ANOVA). Moreover, the maximum deformation and tensile modulus have been found from the data acquired. Pullout tests have been conducted to investigate the critical length and interfacial strength when sedge fibers, are incorporated into epoxy resin matrix. Microstructure analysis by scanning electron microscopy (SEM) was performed to observe the mechanism responsible for causing rupture of the fiber as well as the effective fiber interfacial adhesion to the epoxy matrix.

The following investigations already published in scientific journals are results acquired, statistically treated and analyzed proposed for this dissertation. Neuba et al. (2023) have investigated alkali treated sedge fibers, aiming to enhance the fiber-matrix interface. The group conditions were divided into three NaOH concentrations (3%, 5%, and 10%), as well as the three periods of immersion (24, 48, and 72 h). Therefore, nine different conditions were investigated in terms of their thermal behaviors, chemical structures, physical structures, and morphological aspects. Based on TGA curves, it could be noticed that treatments related to 3% NaOH for 24 h and 48 h exhibited better thermal stability properties. For the time of 48 h, better thermal stability with for a decay of the thermal DSC curve was shown for all treatment conditions. The FTIR spectra has shown a reduction of waxes for higher NaOH concentrations. The XRD diffractogram exhibited an increase in the crystallinity index only for 5% NaOH and an immersion time of 48 h. The morphological aspects of fibers treated with 5% and 10% of NaOH have shown that the treatments have damaged the fiber, which highlighted the crystallinity index reductions. Moreover, Neuba et al. (2023b) proposed a ballistic investigation of an epoxy matrix composite owning a novel *Cyperus malaccensis* (CM) fibers as a reinforcement is proposed. The tests explored the limit and residual velocity of composites in three different conditions, 10, 20, and 30 vol%. Afterwards, fractured surfaces were analyzed in a scanning electron microscopy (SEM) for a deeper investigation of the failure mechanism. From the tests, it could be observed

that the plates condition of 20 vol% of CM fibers attained the highest value of energy absorption (222.11 J) and limit velocity (231.34 m/s), although the ones reinforced with 30 vol% showed a more complete physical integrity. For this group, the SEM micrographs presented the mechanisms of failure related to delamination and fiber rupture. The 10 and 20 vol% reinforced plates presented a slight difference in residual velocity (810.27 and 808.37 m/s, respectively). At last, Neuba et al. (2023a) investigated a complementary research work extends the previous study to dynamic mechanical analysis (DMA) and thermal mechanical analysis (TMA) for GO-incorporated epoxy matrix nanocomposites incorporated with 30 vol.% of CM sedge fibers. In comparison to basic epoxy (control sample) the damping factor (tan δ), as the ratio between DMA loss and storage moduli, is significantly increased from 0.45 to 0.75 for 30 vol.% CM fiber composite. TMA findings disclosed only slight variations in the glass transition temperature (119– 241°C) as well as in the thermal expansion coefficient (168 x 10^{-6} to 220 x 10^{-6}/°C). These DMA and TMA results confirms the promising CM sedge fiber reinforcing effect on GO-incorporated epoxy nanocomposites and its mechanical/thermal viscoelastic contribution.

The botanical genus *Cyperus* belongs to the *Cyperaceae* family and comprises between 650 to 700 species spread around the world. Some existing species are used in the manufacturing of mats, specifically *C. articulatus*, *C. corymbosus*, *C. iria*, *C. pangorei*, and *C. malaccensis* (BENAZIR et al., 2010). Some species of this botanical genus have been studied as potential engineering materials. Among these species, *Cyperus pangorei* has been extensively researched regarding its physical, chemical, and structural properties, as well as its application in polyester matrix composites and a hybrid epoxy matrix composite (BENAZIR et al., 2010; MAYANDI et al., 2016; VIJAY; SINGARAVELU, 2018). Another fiber that was investigated as reinforcement in a polypropylene matrix was *Cyperus esculentus* in a study focusing on exploring the thermal and mechanical properties of this composite (BABU et al., 2020).

According to the Gbif website (2020), responsible for disseminating information about various plant species worldwide, *Cyperus malaccensis Lam.* is found in various countries such as Japan, China, Australia, Indonesia, India, the Philippines, and Thailand. However, it does not provide any data regarding the occurrence of this species in Brazil. This is observed in FIG. 2.10.

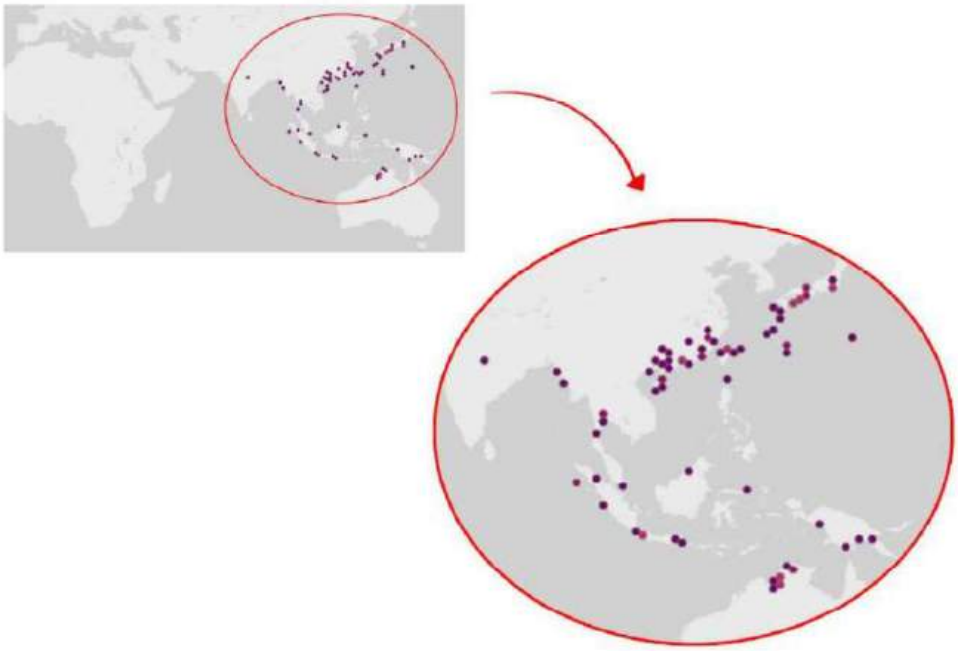

Figura 2.10 – Locations where the plant species *Cyperus malaccensis* is present.

Source – Adapted from Gbif (2020).

2.5 POLYMER RESINS

Humanity has used natural polymers over the course of centuries. However, technological development, through research, has facilitated the investigation and subsequent synthesis of complex structures. Widely employed today due to the need for low-cost materials with good performance, driven by the growth in global consumption, this has led to the development of high-performance polymeric resins that are extensively utilized (BRYDSON, 1966; JR; RETHWISCH, 2020).

That said, polymers can be synthetic or natural. Among various natural polymers, cellulose, silk, lignin, wool, and natural latex can be mentioned. On the other hand, commonly known synthetic polymers include nylon and silicone. Polymerization is referred to as the chemical reaction responsible for guiding the formation of large molecules (polymers) from small molecules classified as monomers (PAOLI, 2009).

A common way to classify polymers is based on their mechanical behavior, chemical structure, and technological characteristics. According to the chemical structure of the polymer chain, polymers are divided into groups such as polyester, polyurethanes, polyacetals, and polyamides. Regarding mechanical behavior, polymers are classified as elastomers, fibers, plastics, or rubbers (MANO, 2001).

Considering the technological characteristics of fusibility, polymers are segmented

into thermosetting and thermoplastic. Thermosetting polymers are cross-linked network polymers, exhibiting covalent bonds between adjacent chains, requiring extremely high energy to break these bonds through heating at high temperatures, leading to polymer degradation. Through thermal processes, these bonds encircle the chains, thus demonstrating good resistance to high temperatures, vibration, and rotational movements of the structure. In light of these facts, thermosetting polymers become more resistant and rigid when compared to thermoplastics, in addition to having better dimensional stability. The functional groups of polymers associated with thermosetting include: amines, epoxies, silicones, phenolics, and polyesters (ASKELAND; PHULÉ, 2008; JR; RETHWISCH, 2020).

On the other hand, thermoplastics have branched or linear structures. Additionally, the bonds between atoms in different chains are relatively weak, mainly due to Van der Waals forces. As a result of the strength of these bonds, thermoplastics soften when heated and harden when cooled. Thermoplastics widely used in commercial and industrial applications include polyethylene (PE), polyvinyl chloride (PVC), polypropylene (PP), polystyrene (PS), polyamide (PA), among others (JR; RETHWISCH, 2020).

2.5.1 EPOXY RESIN

"Epoxy"originates from the Greek "EP"(between or upon) and the English "OXI"(oxygen), literally meaning oxygen between carbons. In essence, it refers to a group formed by an oxygen atom bonded to two carbon atoms. Epoxy resins have been known since the 1940s and are used in various industries, thanks to their good resistance and low cost when compared to other resins commercially available. Epoxies are classified in the class of thermosetting polymers; these molecules undergo polymerization to form chains and, consequently, react chemically with curing agents to initiate the cross-linking process (ASKELAND; PHULÉ, 2008).

Epoxy resins are one of the most important classes of thermosetting polymers, given their use in various structural applications or as coatings and adhesives. This is due to their easy processing, good electrical properties, thermal resistance, chemical resistance, and high tensile strength. However, they have a significant drawback in certain applications due to low fracture resistance (PIRES et al., 2005).

These resins feature glycidyl groups in their molecules and have a three-dimensional structure created through a reaction of the glycidyl group with a hardener (cross-linking agent). The component containing the epoxy group is epichlorohydrin, responsible for reacting with chemical species that have active hydrogen atoms. Bisphenol A is the most common species in terms of possessing active hydrogens. The chemical structure of the epoxy resin, diglycidyl ether of bisphenol A (DGEBA), is depicted in FIG. 2.11 (ASKELAND; PHULÉ, 2008).

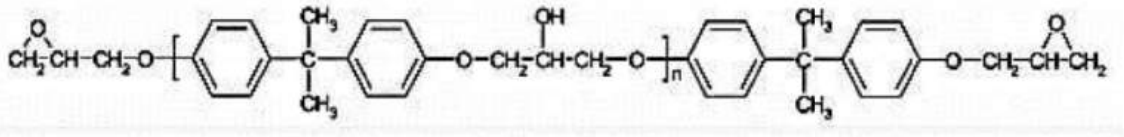

Figura 2.11 – Chemical structure of the DGEBA.

Source – Adapted from Boutin et al. (2020).

.

The excellent adhesion exhibited by these polymers is due to the polarity of ether groups and aliphatic hydroxyls, typically forming the initial resin chain and the cured system network. The polarity of these groups serves to generate interaction forces between the adjacent surface and the epoxy molecule, establishing its application as a coating and adhesive. Regarding their use in composites, the presence of these polar groups minimizes inherent issues in the reinforcement/matrix interface (RUSHING; THOMPSON; CASSIDY, 1994).

The epoxy resin (DGEBA) is one of the most widely used epoxy resins due to its higher chemical resistance, good thermal properties, effective adhesion, corrosion resistance, dimensional stability, and high resistance to bonding with various substrates. Consequently, these properties enable various applications in diverse fields such as coating, adhesive, painting, automotive components, and other engineering applications. Some mechanical properties are shown in TAB. 2.4 (KUMAR et al., 2019).

Tabela 2.4 – Mechanical and physical properties of epoxy resin, such as: density (ρ), elongation, elastic modulus (E), tensile strength (σ) and fracture toughness (K_{IC}).

E (GPa)	**σ (MPa)**	**Elongation (%)**	**ρ (g/cm^3)**	**K_{IC} (MPa.m$^{1/2}$)**
2.41	27.60 a 90	3-6	1.10-1.40	0.60

Source – Adapted from Jr e Rethwisch (2020)

Immediately after the addition of a hardener, curing agents, epoxy resins transform into thermosetting polymers, undergoing what is commonly known as the curing reaction. This process can occur at both elevated temperatures and room temperatures, depending solely on the desired end properties or the initial products employed. On average, epoxy systems exhibit small contraction values of around 2% after curing, indicating the requirement for a low degree of molecular rearrangement to form the cured system. Regarding chemical stability, epoxy is one of the most inert thermosets and demonstrates good dimensional stability in service (ASKELAND; PHULÉ, 2008; JR; RETHWISCH, 2020). FIG. 2.12 depicts the production reaction of the DGEBA epoxy resin.

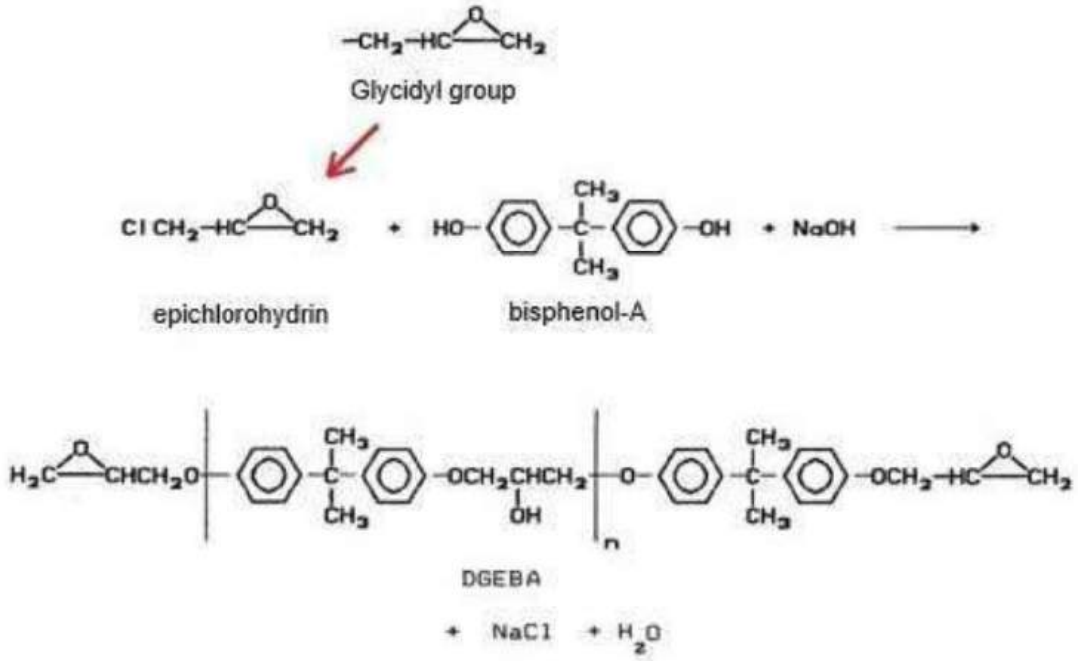

Figura 2.12 – Production reaction of the epoxy resin.

Source – Adapted from Bezerra (2020).

2.6 COMPOSITE MATERIALS

This class of materials can be defined as a compound composed of at least two materials from the major material groups: polymers, ceramics, and metals. By combining these phases to create a composite material, a new material with unique properties emerges, distinct from the original materials. These phases must exhibit minimally favorable chemical compatibility to form an interface. Therefore, composite materials can be produced and are used worldwide to address various engineering requirements. Typically, when creating a composite material, one or more phases, known as the reinforcing phase, are dispersed in a matrix phase so that the reinforcement enhances certain properties of the matrix. The reinforcement bears the applied load, while the matrix bonds the reinforcing materials and distributes the load among them (CHAWLA, 2012; JR; RETHWISCH, 2020; SHEKAR; RAMACHANDRA, 2018).

There are various types of composites, and examples of possible configurations with different reinforcement patterns are shown in FIG. 2.13. The matrix material can be metallic, ceramic, or polymeric. However, the majority of composites in the industry are based on polymers (CLYNE; HULL, 2019).

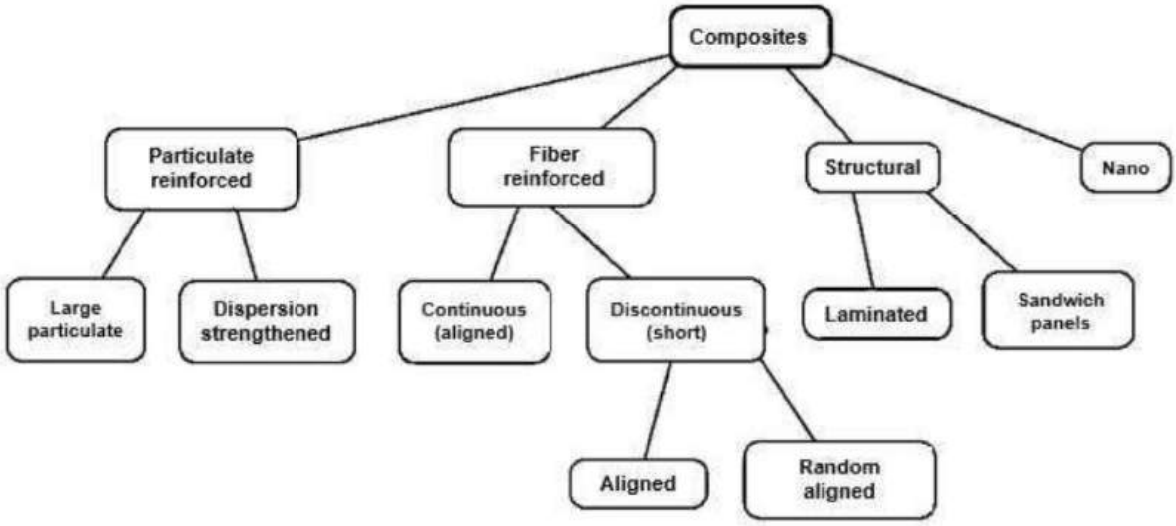

Figura 2.13 – Classification of composite materials.

Source – Adapted from Jr e Rethwisch (2016).

.

Composites have defined properties according to specific requirements following the rule of mixtures, considering that the material property is attributed by the weighted average of the properties of the existing phases. Deviations from this rule usually occur due to the consideration of ideal conditions, such as a perfect interface. However, it can be used as an approximation of interface properties, serving as an estimate of composite properties or for comparison. The rule of mixtures is expressed in Eq. 2.1 (JR; RETHWISCH, 2020).

$$E_{\text{comp}} = E_m.V_m + E_f.V_f \tag{2.1}$$

Where:

E_{comp} – elastic modulus of the composites;

E_m– elastic modulus of the matrix;

V_m – fiber volume fraction of the matrix;

E_f – elastic modulus of the fiber;

V_f – fiber volume fraction of the fiber.

Fiber-reinforced composites belong to the most relevant group due to the ability to develop materials with high specific strength and high elastic modulus, allowing for various technological applications. The dispersed phase in this composite is in the form of fibers. The final properties of the material depend on the interfacial bond between the matrix and the fiber. Thus, reinforcement requires the fiber to have an interface with good

adhesion and a certain critical length (l_c), directly influenced by the shear yield strength of the matrix, the diameter, and the tensile strength limit of the fiber. Fibers that have a length 15 times greater than the critical length are known as continuous, while those shorter are considered as short or discontinuous fibers (JR; RETHWISCH, 2020). Eq. 2.2 expresses the relationship between the parameters that determine the critical length of the fiber.

$$l_c = \frac{(\sigma_f.d)}{(2.\tau)} \tag{2.2}$$

Where:

l_c – critical length of the fiber;

σ_f – maximum tensile strength of the fiber;

d – fiber's diameter;

τ – fiber/matrix interfacial bond strength.

2.6.1 POLYMERIC MATRICES REINFORCED BY NATURAL FIBERS

Currently, there is a growing interest in the use of natural fiber-reinforced polymer matrix composites, as evidenced by FIG. 2.14, which demonstrates the increasing evolution of the number of publications over the past years. These composites do not require much energy for processing and have low costs. Moreover, the production of natural fibers requires less energy when compared to synthetic fibers like glass fibers. Each species and type of lignocellulosic fibers have specific morphological characteristics on their surface, influencing the mechanical behavior of composites in various ways and having the potential to enhance their mechanical properties satisfactorily. The use of these fibers in composite materials is highly promising, aiming for a future that embraces environmentally friendly, strong, and cost-effective materials (SUMMERSCALES et al., 2010; ZINI; SCANDOLA, 2011; BALLA et al., 2019).

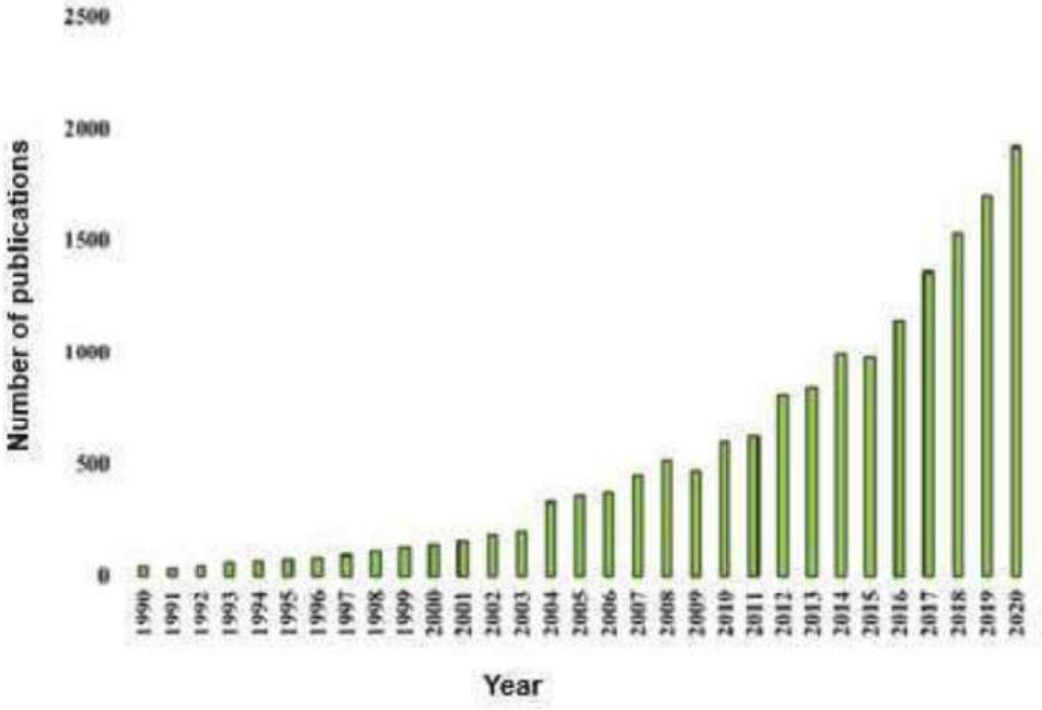

Figura 2.14 – Number of articles published in the field of natural fiber-reinforced composites.

Source – Adapted from Kannan e Thangaraju (2021).

Polymeric composites are developed with a thermosetting or thermoplastic matrix, playing a role in correctly accommodating the dispersed phase and transferring the imposed stress to it. In the case of structural applications, thermosetting polymers are most commonly used, forming products with high strength. One of the most commonly used resins as a matrix in composites is epoxy resin, as it imparts low material shrinkage rates during curing and provides excellent adhesion to the fiber (MONTEIRO et al., 2009). It has been observed that composites reinforced with natural fibers exhibit better electrical resistances, high fracture resistance, good mechanical properties, and good thermal properties (SANJAY et al., 2018). Some composites reinforced with lignocellulosic fibers (CNLF) are presented in TAB. 2.5.

Tabela 2.5 – Mechanical properties for different CFNLs, such as: elastic modulus (E), tensiles strength(σ) and flexural strength (σ_{flexural}).

Matrix	**Fiber**	Vf **(%)**	σ **(Mpa)**	σ_{flexural}**(Mpa)**	**E (GPa)**
Epoxy	Sisal	37-77	183-410	290-320	6-20
Epoxy	Flax	46-54	280-279	-	35-39
polylactic acid	Ramie	30	66.8	-	-
Polypropylene	Jute	30	47.9	-	5.8
Polypropylene	Flax	30	29.1	-	5

Source – Adapted from BALLA, 2019.

The most commonly used and technologically relevant composites are those with the reinforcing phase in the form of fibers. Their main purpose is to combine high stiffness and strength with low density for both the fiber and matrix (JR; RETHWISCH, 2020).

The quality of the fiber/matrix interface is essential and crucial for the use of natural fibers as reinforcement for plastic materials. It has the potential to directly impact the final mechanical behavior of a composite material. Moreover, the adhesion between the matrix and the fiber is a function of various factors, such as the level of roughness present between the contact surfaces (BLEDZKI; GASSAN, 1999; PARK et al., 2006).

The fiber/matrix interface is primarily responsible for transferring the load from the matrix to the reinforcement; these properties, in turn, become specific to each system. Strong fibers with high rupture strain elevate the level of energy involved in the fracture of composites. Additionally, the stress-strain behavior of the fibers directly influences the toughness of composites reinforced by them (JR; RETHWISCH, 2016).

Consequently, it is plausible to state that certain factors such as maturity, careful selection of fibers, processing methods used for fiber extraction, and the need for surface treatment become fundamental for acquiring high-performance composites. Thus, the quality of natural fibers and a significant portion of the mechanical and tribological properties of composite behavior depend on these factors (SANJAY et al., 2019).

The weight fraction of fibers directly influences the properties related to the tensile and flexural strength of natural fiber-reinforced composites. These properties gradually increase and then decrease after reaching a peak value corresponding to an ideal weight fraction for the fiber. However, this value is not definitive and varies from one fiber to another (KHAN; SRIVASTAVA; GUPTA, 2018).

Several mechanisms are responsible for the energy absorption of fibrous composites exposed to impact loads, such as the elastic strain of the composite, shearing of the layers, delamination between the layers, and fracture stress of the fibers. Delamination is the separation of phases in composites and occurs due to certain factors such as low wettability

of the fibers or transverse direction and the presence of reinforcing fibers with a high degree of impurity (GHASEMNEJAD et al., 2012).

2.7 CERAMIC MATERIALS

Ceramic materials are excellent materials used in the manufacture of ballistic armour, because they have characteristics that make them great for their application, such as low density, high hardness, and a good set of mechanical properties, being better than other classes of materials used for this purpose (BENITEZ; GÓMEZ, ; SILVEIRA et al., 2021).

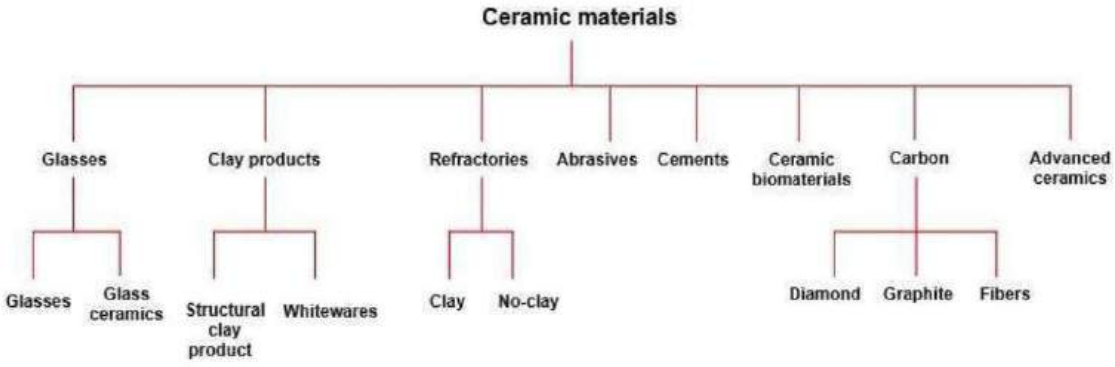

Figura 2.15 – Classification of ceramic materials based on their application.

Source – Adapted from Jr e Rethwisch (2020).

The most used ceramics in ballistic applications today are silicon carbide (SiC), boron carbide (B_4C), alumina (Al_2O_3) (DRESCH et al., 2021). From a commercial point of view, alumina is the most cost-effective of these materials (SILVEIRA et al., 2020).

2.7.1 ALUMINA (Al_2O_3)

Alumina is one of the first advanced ceramics to be developed. Currently, it is one of the most studied among engineering ceramics, for its low cost, ease of obtaining and processing, besides good mechanical, electrical, thermal, and chemical properties. Alumina is the shielding material that presents the most beneficial price relations among advanced ceramics: high elasticity modulus, high refractoriness, high hardness, and commercial viability (SILVEIRA et al., 2021).

The properties of alumina vary widely, making them dependent on the refinement of processing parameters such as sintering temperature and atmosphere, impurities, and grain size. The multilayer armor with alumina layers are cost-effective and have good ballistic perfomance. The high density of alumina (approximately 3.9 g/cm^3) compared to SiC

(approximately 3.2 g/cm^3) and B_4C (approximately 2.6 g/cm^3) brings the disadvantage of making the armors heavier, limiting the user's movement, besides low fracture toughness, that limits ballistic performance against higher caliber weapons (SILVEIRA et al., 2021).

Alumina has low fracture toughness when compared to SiC and B_4C, so during the production of this material, additives composed of other oxide materials (ZrO_2, MgO, Y_2O_3, Nb_2O_5, etc.) can be added in small fractions to improve the original properties of alumina (SILVEIRA et al., 2021).

2.7.2 ALUMINA (Al_2O_3) ADDITIVATED WITH NIOBIUM (Nb_2O_5)

The use of additives improves the properties of ceramic material and lowers the sintering temperature by forming a second phase in its microstructure. Niobium pentoxide or niobia (Nb_2O_5) is the most commonly adopted for this purpose (SILVEIRA et al., 2021).

Gomes, Louro e Costa (2006) added 4% by weight of Nb_2O_5 to alumina, causing a decrease in the sintering temperature from 1600 to 1400 °C, while maintaining high toughness and densification and generating significant energy savings in the process. Furthermore, the addition of niobium for alumina sintering allows for the growth of the grain in the final microstructure. The observed growth increases with the niobium concentration (MORAIS et al., 2017).

2.7.3 CERAMIC PROCESSING

Desired properties in a specific application are directly linked to each stage of the processing. It can be said that ceramic processing is defined as a sequence of indispensable steps to obtain a sintered ceramic product. In addition to the manufacturing process, the chemical composition, sintering temperature, quantity of components, and average particle size define the final properties of ceramic bodies (LAKHDAR et al., 2021). FIG. 2.16 illustrates the stages of ceramic processing.

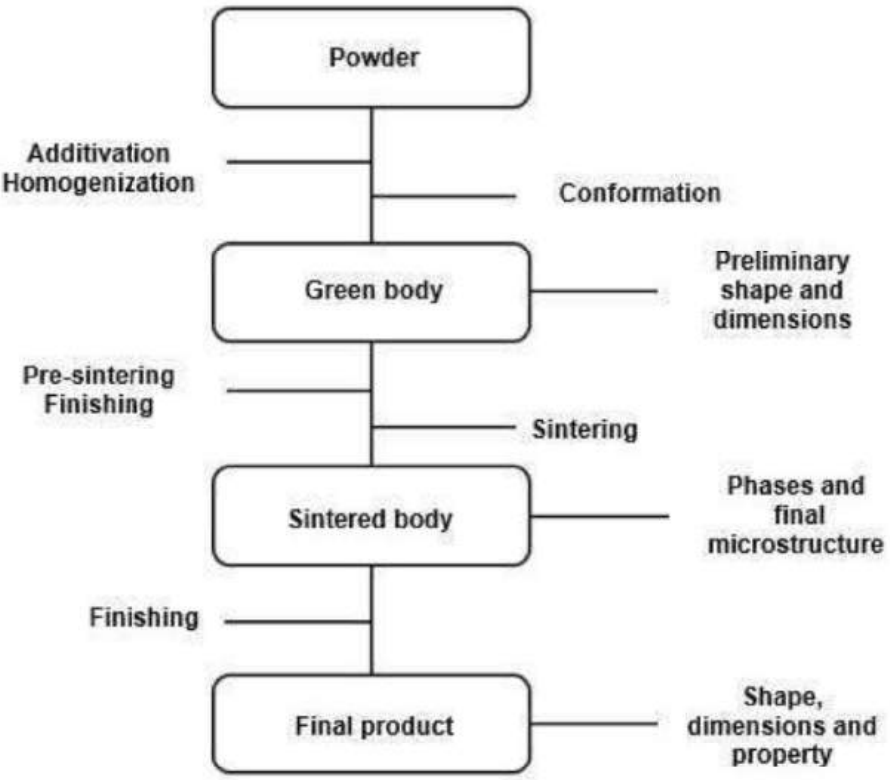

Figura 2.16 – Steps for ceramic processing.

The additive operation involves the presence of niobium and other additives with the purpose of improving the mechanical properties of the ceramic material. Additionally, a molecular binder is used in this stage to provide the bonding of ceramic particles. Thus, milling is performed to homogenize the mixture, contribute to a more spherical shape, and reduce the average particle size (YIN; ZHU; ZENG, 2010; RICHERSON; LEE, 2018). Generally, the applied binder is known as PEG (polyethylene glycol), which is a polymeric ethylene oxide with the structure HO - [CH2 - CH2 - O]$_n$ - H. PEG binders are water-soluble and have limited solubility in a wide range of solvents. Moreover, they are commercially available with a molecular weight range varying from 200 to 8000 g/mol (REED, 1995).

In the forming stage, the creation of the "green body"takes place, providing a preform to the desired product. Among the possible forming processes, uniaxial pressing, hot pressing, isostatic pressing, and slip casting can be mentioned (SAM; JOJITH; RADHIKA, 2021).

After obtaining the green body, meaning the ceramic body with preliminary shape and dimensions and possessing mechanical properties below the expected value, sintering is performed, known as the main stage of ceramic processing. In this process, the compacted powder transforms into a dense and robust ceramic body through heating. Requiring time and temperature, as it is a thermally activated process, it occurs in three stages with the

following characteristics:

Initial stage - formation of "necks", densification of 60 to 65%, occurring on the surface and at lower temperatures;

Intermediate stage - development of continuous porous channels, densification of 65 to 90%, consolidation occurs, meaning particles throughout the material come together, creating an aggregate and acquiring greater mechanical strength;

Final stage - grain growth and cooling until reaching room temperature. In this stage, the pores become isolated (REED, 1995).

Finishing stages may exist with the aim of obtaining the final product, characterized in terms of its shape, dimensions, and properties.

2.8 GRAPHENE OXIDE (GO)

An important member of the family of materials derived from graphene is GO, in which this material has carbon sheets containing functional groups, especially carboxyl, carbonyl, epoxide and hydroxyl groups. The most common groups in GO are epoxides and hydroxyls, which are distributed on the basal plane, while carboxyl, carbonyl and possible other groups tend to be on the edges (STOBINSKI et al., 2014).

Graphene oxide has sp^2 or sp^3 hybridization and can be considered a electrically insulating material compared to graphene (YASIN et al., 2015). For sp^3 hybridization, the deterioration in electrical conductivity is due to the extensive presence of C-C bonds that behave like defects, causing the deviation of the layer (LI et al., 2019), limiting the use of GO in conductive materials. The electrical properties of GO can be altered by varying the oxygen content (JEONG et al., 2009), of impurities (HUANG et al., 2013) or partially returning the sp^2 (LI et al., 2019). The presence of oxygen groups affects the mechanical and electrochemical properties of GO when compared to graphene. However, the functional groups present in its structure give it an amphiphilic character, improving the resistance of the interface between the polymer matrix and the natural lignocellulosic fibers (NLFs), (COSTA et al., 2019; SARKER et al., 2018; TISSERA et al., 2015). The use of functional groups facilitates the excellent dispersion of GO in water and different solvents, allowing for the easy preparation of polymer nanocomposites and for the production of GO in abundance (PAPAGEORGIOU; KINLOCH; YOUNG, 2017).

2.8.1 GO PROPERTIES

With regard to the mechanical properties of GO, the first report was published by DIKIN et al. (2007) on a graphene oxide paper assembled from individual sheets of GO. The stress distribution in the sample was homogeneous, and the stiffness found was up to

40 GPa, while the strength was only 120 MPa. Various adjustments have subsequently been proposed in the literature to improve the mechanical properties of similar materials (PARK et al., 2008; LEE et al., 2013; STANKOVICH et al., 2010; TIAN et al., 2013; COMPTON et al., 2012), did not significantly exceed the initial values of DIKIN et al. (2007).

SUK et al. obtained the effective Young's modulus of the GO monolayer (thickness 0.7 nm) with a combination of atomic force microscopy (AFM) contact mode and finite element method (FEM) in the order of 208 ± 23 GPa. WANG et al. (2013) studied the strain of a GO sheet using in situ AFM in vacuum and air. The tensile strength of the GO sheets was lower under vacuum, as these conditions promote the removal of water between the layers, leading to poor stress transfer and lower tensile strength properties. As with graphene, Raman spectroscopy was also used to evaluate the mechanical properties of GO by observing band changes with increasing stress (LI; KINLOCH; YOUNG, 2016; CORRO; TARAVILLO; BAONZA, 2012). For the thermal conductivity of GO, since in the work by MU et al. (2014), the presence of oxygen, even at a percentage as low as 5%, reduces the thermal conductivity by around 90%. On the other hand, GO has excellent photoluminescence (LOH et al., 2010), an important characteristic for application in biosensors or photoelectronics.

2.8.2 GO CHARACTERZATION

With regard to the morphological characterization of GO, in addition to AFM being used to evaluate the mechanical properties, it can also be used to evaluate the exfoliation of the material in different solvents with the thickness of the flakes produced (STANKOVICH et al., 2006). Transmission electron microscopy (TEM) revealed no obvious differences with graphene in its structure and electron diffraction pattern (WILSON et al., 2009). Using a scanning electron microscopy (SEM) it is possible to show the disintegrated and randomly aggregated nature (STANKOVICH et al., 2007).

The structure of GO can be characterized by various spectroscopic techniques such as X-ray photoelectron spectroscopy (XPS), Fourier transform infrared spectroscopy (FTIR), Raman spectroscopy, carbon-13 nuclear magnetic resonance (^{13}C NMR) and UV-VIS spectroscopy (PAPAGEORGIOU; KINLOCH; YOUNG, 2017).

In the specific case of the Raman spectrum of GO, it proves to be different from graphene, since a strong D band that is not present in graphene can be observed in the spectrum belonging to GO, indicating the formation of sp^3 bonds. There is also broadening of the G band compared to graphene. The relative intensities of the G and D bands can be used to assess the defects that form during GO reduction (KUDIN et al., 2008). X-ray diffraction (XRD) analysis can be used to monitor the transformation of graphite into GO due to the intense Bragg peak of the peak at $2\theta = 26°$, which disappears after the

conversion procedure and a new peak appears at lower angles. In addition, the distance between layers can be calculated using Bragg's law, usually ranging from 0.6 to 1.0 nm, depending on the preparation method. Thermogravimetric analysis (TGA) is also useful, since the presence of functionalities in GO allows the material to decompose at lower temperatures in three stages. The first stage corresponds to the removal of moisture, the second to the pyrolysis of oxygen-containing groups and the third and final stage to the decomposition of more stable oxygen functionalities such as carbonyls and phenols (LERF et al., 1998).

2.8.3 GO SYNTHESIS

The oxidation of graphite was first proposed by Brodie in 1859, using nitric acid and potassium chloride. Later, Staudenmaier in 1898 added the use of sulfuric acid to the process. In 1958, the Hummers and Hoffman method was developed, usually just called the Hummers method. Currently, GO production is mostly done using the Hummers method or a variation of this method (MUZYKA et al., 2017). The Hummers method consists of using a concentrated solution of sulfuric acid (originally with a concentration of 63%; however, today higher concentrations are used), sodium nitrate, potassium permanganate, a small amount of hydrogen peroxide and water as a dispersant (JR; OFFEMAN, 1958).

When producing GO, regardless of the method used, there is a large variation in sheet sizes. As the dimensions of the sheets significantly affect the properties of GO, techniques have been developed to separate them by size, such as: centrifugation at high speeds, which removes the smallest sheets from the supernatant; ultrasonic shaking techniques, which break up sheets to make them smaller, and high shear techniques (CAI et al., 2017). FIG. 2.17 shows the formation mechanism of the GO.

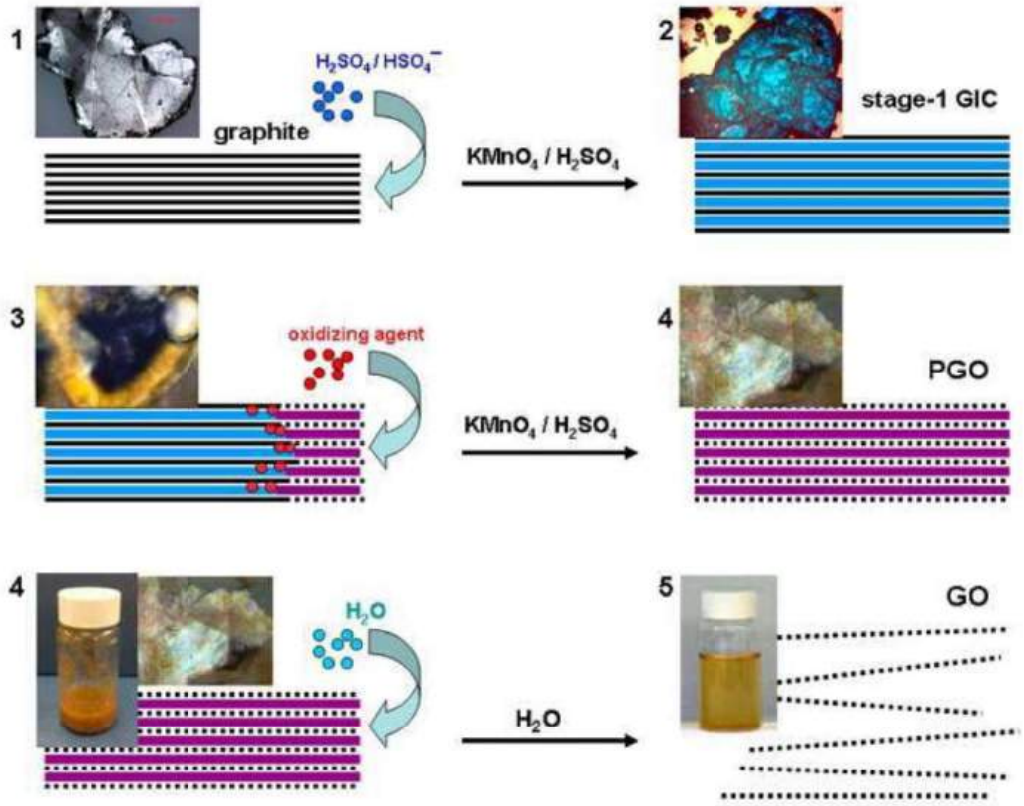

Figura 2.17 – GO formation mechanism.

Source – Adapted from Dimiev e Tour (2014).

2.9 NANOCOMPOSITES INCORPORATING GRAPHENE-BASED MATERIALS

The discovery of graphene has led to the emergence of new opportunities for the development of new lightweight, high-performance nanocomposites, allowing their application in diverse fields, from electronics to aerospace. In fact, a low filler content of this material or its derivatives can significantly improve the mechanical, thermal and physical properties (TIAN et al., 2014; RAY, 2015; ELMARAKBI; AZOTI, 2018; JI et al., 2016; HU et al., 2014; PANZAVOLTA et al., 2014; RAFIEE et al., 2010; VECA et al., 2009; XU; GAO, 2010; ZHANG; PARK; CHOI, 2010). The final properties of graphene-based polymer composites can be affected by several factors, including the type of graphene used and the method used to produce the composite (ELMARAKBI; AZOTI, 2018).

The most important objective during the fabrication of polymer nanocomposites reinforced with graphene-based materials is to ensure that the reinforcing phase can properly disperse in the matrix. A homogeneous dispersion will provide the best mechanical reinforcement for the matrix, providing better mechanical properties to the new material. The nature of the interface between graphene and the polymer matrix, with the aspect

ratio of the filler, are key aspects for the design of polymer nanocomposites. Manufacturing techniques have been used to produce graphene-based nanocomposites. Among these techniques, the processes of melt blending, solution compounding, in situ polymerization, layer by layer assembly and coating are the most common (JI et al., 2016; DONA et al., 2012).

The scheme illustrated in FIG. 2.18 presents the main components derived from graphene and the processing techniques presented previously. However, it is reported in the literature that methods such as melt mixing are not applicable for thermoset polymers, as they leave residual solvent, which can be detrimental to the mechanical properties of the final product (KIM; ABDALA; MACOSKO, 2010) or cause irreversible hardening (curing) of the polymer matrix. In situ polymerization methods can also produce high-quality compounds. For thermosetting resins, in situ polymerization is the only viable option (HE et al., 2017b).

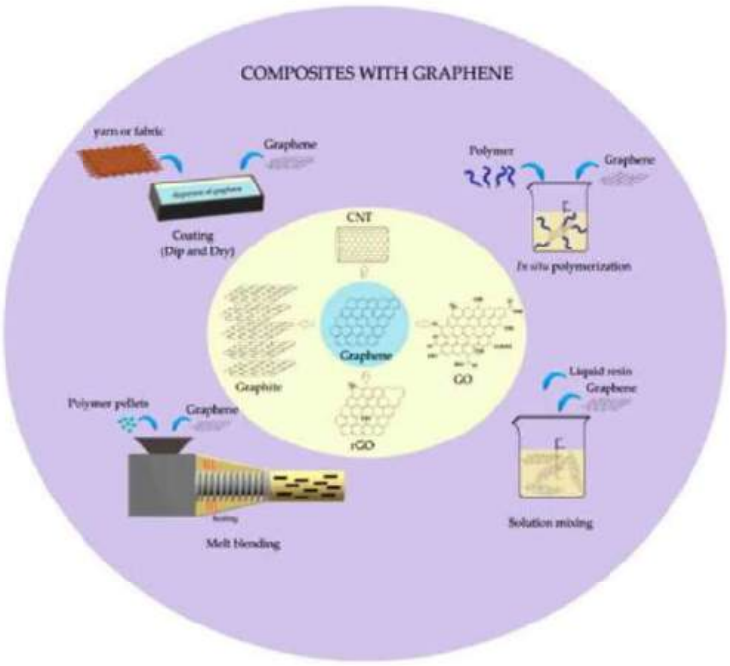

Figura 2.18 – Summary of the main manufacturing processes for graphene-based materials for nanocomposites.

Source – Adapted from Luz et al. (2020).

The solution mixing method involves mixing a graphene-based suspension with a polymer that is already in solution or will be combined with the graphene suspension (provided it is compatible with the solvent) by simple mixing, by shearing or ultrasonication. In general, solution mixing provides adequate dispersion of the flakes and is quite versatile, as different solvents can be used to dissolve the matrix and disperse the filler. Furthermore, it is a quick and easy procedure, allowing for wide exploration (PANDELE et al., 2014; SHEN et al., 2013; LIAO et al., 2013). This strategy, however, is not without drawbacks.

Some of the problems involve the use of toxic solvents, the total elimination of solvents in the final product and the possible re-aggregation of the filler during one of the preparation steps.

During in situ polymerization, graphene flakes are initially mixed with monomers or prepolymers and the polymer. In other words, graphene derivatives are added and dispersed before the curing step. The polymerization procedure carried out subsequently leads to the production of composites with good dispersion and strong interactions between the matrix and the flakes. (XU; GAO, 2010; POTTS et al., 2011; FABBRI et al., 2012). This allows payload to be added, with or without functionalization, to increase compatibility between system components. Some difficulties are associated with the increase in viscosity during the polymerization process, which limits the filler fraction and processing of the composites (VERDEJO et al., 2011). In some cases, a solvent is added to avoid this deficiency. Furthermore, the oxygen-containing groups present in graphene oxide provide sufficient active sites to form bonds with the matrix or a second secondary filler that can improve the final properties of the composites. It has been demonstrated that GO can be thermally reduced during the polymerization procedure (XU; GAO, 2010).

The melt mixing process is the most used procedure in the industry for the production of thermoplastic nanocomposites as it is fast, cheap and relatively simple. This method consists of melting the polymer at high temperatures and mixing the graphene flakes (in powder form) using a single, double, triple or even quadruple screw extruder. Several graphene-based nanocomposites have been prepared using this technique (ISTRATE et al., 2014; ACHABY et al., 2012). The results show that melt mixing produces nanocomposites with an adequate degree of dispersion, however care must be taken during preparation at mixing temperatures, as high temperatures can cause polymer degradation. The high shear loads that are sometimes necessary for efficient mixing of the polymer with the flakes can cause strain or breakage of the graphene sheets, occurring when viscosity increases with high filler contents in the composite (DONA et al., 2012). In general, melt mixing generally leads to poorer dispersion than in situ polymerization or solution mixing (MAHMOUD, 2011). Another point to be highlighted is that this technique is free of toxic solvents, making it environmentally friendly (JI et al., 2016).

The layer-by-layer (LbL) deposition process consists of a versatile technique that has been continuously explored in recent years for the production of graphene-based composites. In LbL assembly, various nanomaterials with desired nanoarchitectures can be combined to produce multilayer thin films of specific thickness or hierarchical nanostructures by alternating anionic and cationic phases on a substrate. By tuning the deposition sequence, new functional materials can be prepared for a wide variety of applications, including lithium-ion batteries, membranes, field-effect transistors and supercapacitors. Furthermore, GO with the various hydroxyl and epoxy groups on the basal plane and carboxyl and

carbonyl groups on the edges can enhance the electrostatic attractive interactions and hydrogen bonding during LbL assembly (XIAO et al., 2016).

To improve fiber properties, coating method is normally used. This can be done by either immersing in a graphene-based dispersion or spraying the graphene dispersion directly onto the fiber. The first method, the most common, is also known as dip and dry, and can be followed by a reduction or washing process (JI et al., 2016). The coating method is applied to electronic textiles, as it promotes electrical conductivity, without compromising its flexibility and extensibility (AFROJ et al., 2020).

2.10 DYNAMIC BEHAVIOR OF MATERIALS

When a material is subjected to slightly oscillating loads, it can differ significantly from a material subjected to quasi-static or static conditions (MEYERS, 1994).

A process is termed dynamic or static depending on the rate of application of an external load on the material. Dynamic behavior is acquired at a high rate of strain, where loading becomes a localized phenomenon propagating through the material as a stress wave. In contrast, for slow strain rates, static behavior is defined as a loading phenomenon supported throughout the material (ZUKAS, 1980; MEYERS, 1994).

Understanding dynamic strain involves the propagation of waves varying from section to section of the body. In this context, internally existing stress and strain are transferred atom by atom at a specific velocity, not transmitted immediately, and can be calculated with an appropriate estimate. On the other hand, quasi-static strain occurs in a succession of equilibrium states, as the time is sufficient for the relaxation of the entire structure (ZUKAS, 1980; MEYERS, 1994).

When a projectile impacts a material, the interaction occurs at high rates of strain, and this dynamic response can be understood as the ballistic behavior of the material. The waves formed due to external loading on a material can be provided in the form of plastic, elastic, and shock waves (MEYERS, 1994).

The pulse created is identified as an elastic wave as long as the applied external load does not exceed the material's yield stress, and its velocity (C_o) can be obtained through Equation 2.3 (MEYERS, 1994).

$$C_o = \sqrt{\frac{E}{\rho}} \tag{2.3}$$

E = elastic modulus;

ρ = density of the material.

The speed of elastic waves extensively varies its value depending on the medium through which they are propagating, as shown in TAB. 2.6.

Tabela 2.6 – Velocity of elastic waves.

Materials	V_E (m/s)	V_{shear} (m/s)
Air	340	-
Aluminum	6100	3100
Iron	5800	3100
Lead	2200	700
Beryllium	10000	-
Glass	6800	3300
Polystyrene	2300	1200

Source – Adapted from MEYERS,1994.

In ductile materials, when the applied external stress exceeds the material's yield stress, plastic strain occurs, and the stress pulse generated that surpasses the elastic regime dissociates into an elastic wave and a plastic wave. The speed of the plastic wave (V_p) can be obtained using Equation 2.4.

$$V_p = \sqrt{\frac{\frac{d\sigma_f}{d\epsilon}}{\rho}} \tag{2.4}$$

Where:

$d\sigma/d\epsilon$ = slope of stress curve (σ) versus strain (ϵ) at the plastic and elastic portion;

ρ = Density of the material.

The stress-strain curve for a ductile material is shown in FIG. 2.19, where it can be observed that the slope of the curve in the elastic regime is equal to the material's modulus of elasticity (E). In the elastic regime, the slope of the curve is constant, while in the plastic regime, the slope of the curve is variable. It is also noted that $d\sigma/d\epsilon$ is higher in the elastic regime, indicating that the speed of elastic waves exceeds that of plastic waves (MEYERS, 1994).

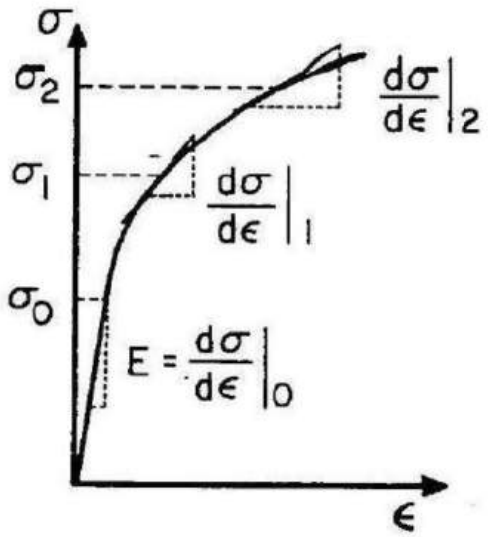

Figura 2.19 – Stress-strain curve for a ductile material.

Source – Adapted from Meyers (1994).

Regarding the amplitude of a stress wave being higher than the dynamic yield strength of the material, shear stresses can be neglected, and in this situation, fluid dynamics can be applied. In this scenario, the waves are transmitted in a single shock front with a speed exceeding the elastic wave and are referred to as shock waves. In FIG. 2.20, a simple model of a cylinder with a compressible fluid and a piston is presented to aid in understanding the concept of shock waves and the included conservation equations (MEYERS, 1994).

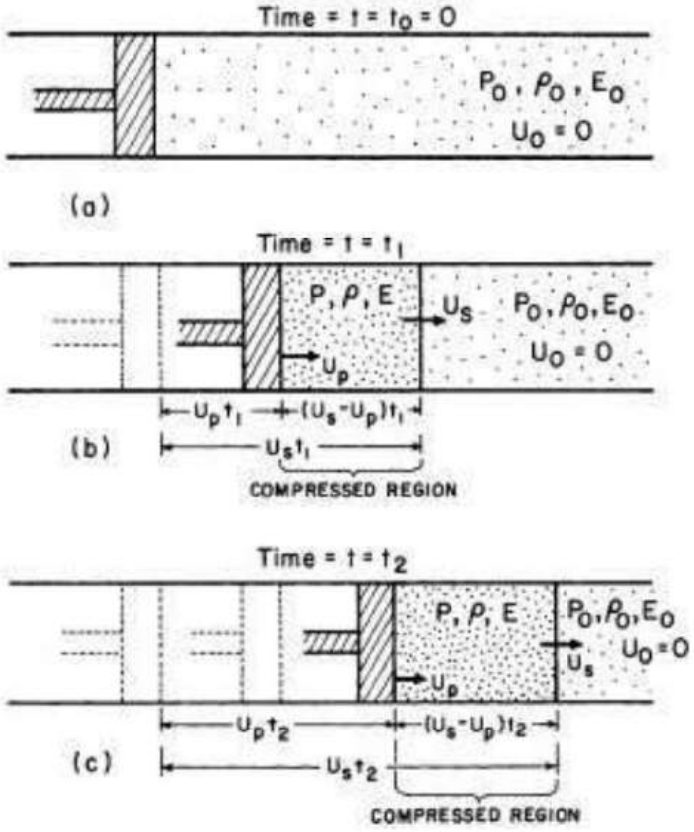

Figura 2.20 – Physical model of shock wave propagation: (a) before the shock; (b) after a time t_1; (c) after a time $t_2 > t_1$.

Source – Adapted from Meyers (1994).

.

The shock front can be analyzed as a plane dividing the compressed region from the stationary region and has a speed U_s. It can be seen in FIG. 2.20 that the shock wave front advances the compressible material with a speed greater than the piston speed ($U_s > U_p$), and in the compressed region, the density and pressure are changed to higher values ($P > P_o$ and $\rho > \rho_o$). A region of larger amplitude of the shock wave propagates at a higher speed than that of smaller amplitude, creating a disturbance leading to a discontinuity in pressure, density, and temperature (MEYERS, 1994).

The Rankine-Hugoniot conservation relationships involve the movement of the piston and the compressed region of the fluid, and they can be applied to a shock wave propagating in gas, solid, or liquid. The equations are displayed by EQ. 2.5 to EQ. 2.7.

- Energy conservation:

$$(E - E_o).2 = (P - P_o).(V - V_o) \tag{2.5}$$

Where:

E = internal energy of the material during the passage of the wave;

E_o = internal energy of the material before the passage of the wave;

P = pressure during the passage of the wave;

P_o = pressure before the passage of the wave;

V = volume during the passage of the wave;

V_o = specific volume of the material before the passage of the wave.

• Mass conservation:

$$\rho_o.U_s = \rho.(U_s - U_p) \tag{2.6}$$

Where:

ρ = density of the material during the passage of the wave;

ρ_o = density of the material before the passage of the wave;

U_s = velocity of the shock wave propagation;

U_p =particle velocity.

• Momentum conservation:

$$P - P_o = \rho_o.U_s.U_p \tag{2.7}$$

Where:

P = pressure during the passage of the wave;

P_o = pressure before the passage of the wave;

ρ_o = density of the material before the passage of the wave;

U_s = velocity of the shock wave propagation;

U_p = particle velocity.

In the equations presented, there are five variables: P (pressure), particle velocity (U_p), energy (E), density (ρ) e shock wave propagation velocity (U_s). Therefore, a fourth equation (EQ) is essential to obtain all parameters. This is called the material equation of state (EOS). This equation shows an experimentally derived relationship between U_s e U_p, using an empirical relation and involving the parameters S_1 e S_2. This results in EQ. 2.8:

$$U_s = C_o + S_1.U_p + S_2.U_{p2} + \cdots \tag{2.8}$$

Where:

S_1, S_2 = empirical parameters;;

C_o = speed of sound in the material at zero relative pressure (P).

For the majority of materials, higher-order empirical parameters are zero. Therefore, EQ. 2.9 is limited to:

$$U_s = C_o + S_1 U_p \tag{2.9}$$

EQ. 2.9 depicts a linear relationship between particle velocity and shock propagation velocity, accurately demonstrating the shock response of non-porous materials that have not undergone a phase transformation. The values of S_1 and C_o are commonly tabulated and found in the literature (MEYERS, 1994). The Rankine-Hugoniot conservation relations can be applied exclusively according to the circumstances:

a) The material undergoes no phase transformation;

b) The shock front is a surface with no apparent thickness and is discontinuous;

c) Heat conduction in the shock front and external forces such as gravitational forces are considered negligible;

d) Absence of elastic-plastic behavior;

e) When the material behaves as a fluid, the shear modulus of the material is nonexistent.

2.10.1 INTERACTION AND REFLECTION OF SHOCK WAVES

Since the moment a shock wave travels through an interface between materials, a pressure is generated at a certain particle velocity U_p and can be measured through a parameter known as shock impedance (MEYERS, 1994).

Concerning the joining of different materials used for shielding applications, interfaces are created between them, and the interaction of a shock wave at these interfaces can be investigated using the impedance matching method (MEYERS, 1994).

Shock impedance can be understood as the product of the shock wave velocity (U_s) and density (ρ_o), If the value of U_s is not available, it is possible to use an approximation of shock impedance using the sonic velocity of the wave (C_o) instead of the shock wave. FIG. 2.21 demonstrates the sequence of ballistic impact events between the projectile and the target.

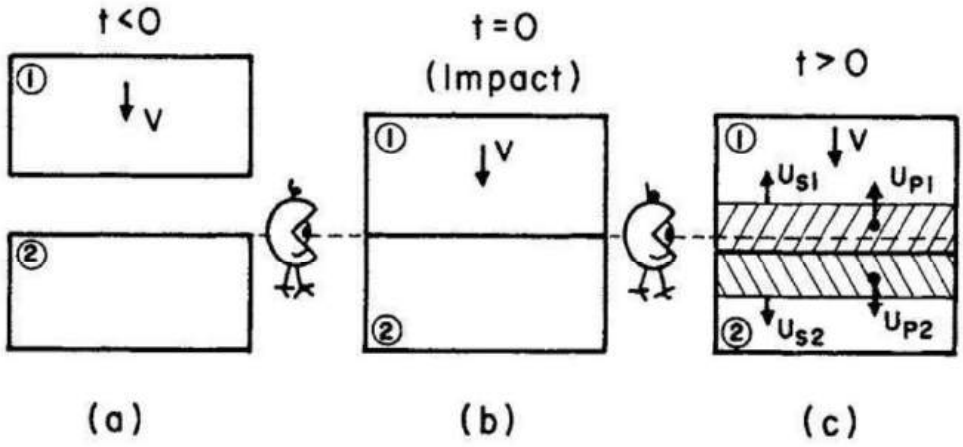

Figura 2.21 – Sequence of events during ballistic impact: (a) before impact; (b) at the moment of impact; (c) after impact.

Source – Adapted from Meyers (1994).

Before the impact occurs, the target (2) is at rest, and the projectile (1) is in motion with a velocity V. After the impact, two compressive waves are generated, one acquiring a velocity U_{s1} that moves within the projectile (1), and another with a velocity U_{s1} traveling into the target (2). The uncompressed part remains at rest, while the uncompressed portion of the projectile is in motion with a velocity V. The impedance matching method is most suitable for elucidating the transfer of a wave from medium A to medium B between materials with high impedance. For the method to be effective, it is necessary for the material to be continuous at the impact interface, meaning that the particle velocity in the compressed region corresponds ($U_{p1} = U_{p2}$) and the pressure is likewise (P_1=P_2). If the particle velocities were not equal, the creation of either very dense regions or voids would occur, and if the pressures were not corresponding, the development of another pulse would occur (MEYERS, 1994).

a) Transfer of a shock wave from a material with high impedance (A) to a material with low impedance (B): This circumstance depicts a situation in which the outer layer (material A) is denser than the intermediate layer (material B), as shown in FIG. 2.22. Thus, pressure P_1 is greater than pressure P_2, and at time t_4 (FIG. b), a tensile pulse is formed, propagating in both directions, i.e., both into material A and into material B. This leads to the fragmentation of the material in the case where the tensile wave has a sufficiently high amplitude (MEYERS, 1994).

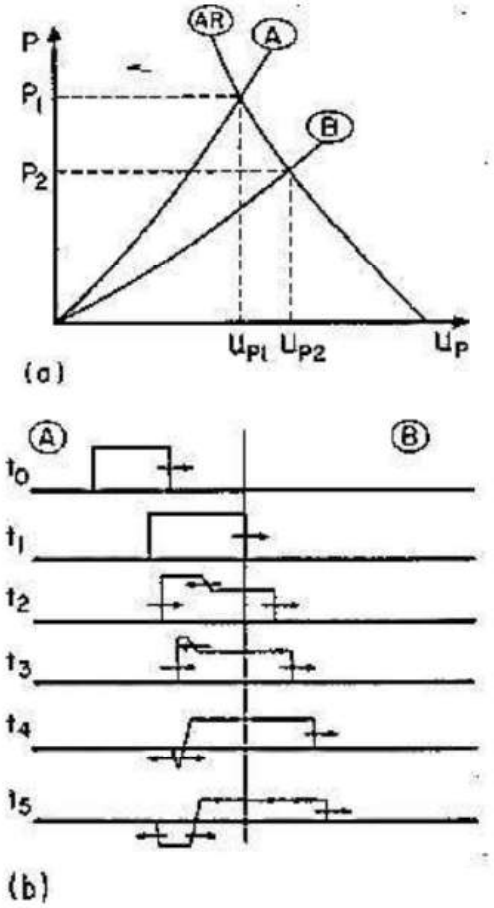

Figura 2.22 – Transfer of the shock wave from a medium with high impedance to a medium with low impedance: (a) pressure versus particle velocity graph; (b) pressure profiles.

Source – Adapted from Meyers (1994).

Transfer of a shock wave from a material with low impedance (A) to a material with high impedance (B): The transfer occurs when an outer layer material (A) has lower density than the material with an intermediate layer (B). FIG. 2.23 (a) shows a pressure variation with particle velocity for materials A and B. The shock impedance is indicated by the slope of the dashed line at pressure P_1, demonstrating the discontinuity in pressure or density during impact. The curve AR describes the inversion of curve A, where the point (U_{p1}, P_1) is common between curves AR and A. On the other hand, the point (U_{p1}, P_1) is common between curves AR and B. FIG. 2.23 (B) displays pressure profiles as they reach the interface, revealing that to maintain balance between pressures, the pressure P_1 of the shock front rises discontinuously to P_2. From this point onward, the shock wave splits into two waves: one propagates in material A in the opposite direction, and the other propagates in material B. At t_3 and t_4, ahead of pressure P_1, the remaining shock wave encounters and drops to $P_2 - P_1$. Particle velocity U_{p2} remains constant in the high-pressure region in A and B, supporting the continuity of particle velocity and

pressure (MEYERS, 1994).

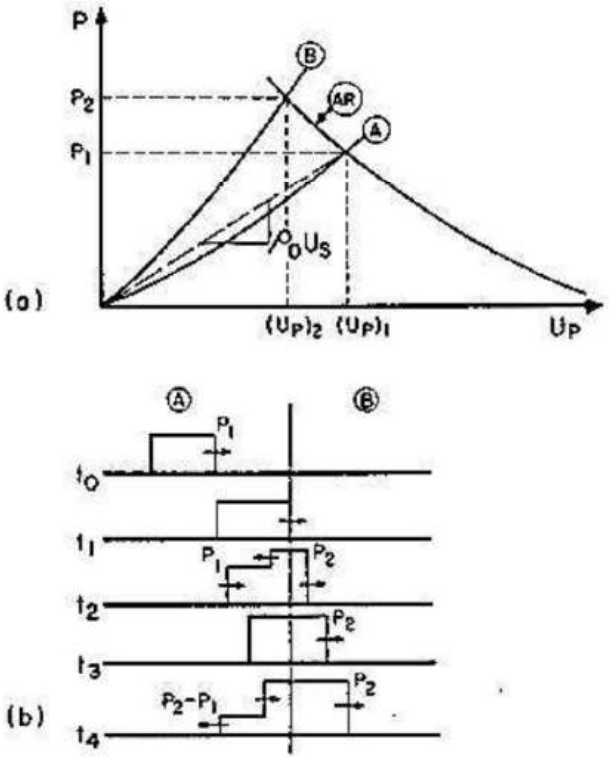

Figura 2.23 – Transfer of a shock wave from a medium with low impedance to a medium with high impedance: (a) pressure versus particle velocity graph; (b) pressure profiles.

Source – Adapted from Meyers (1994).

2.11 BALLISTIC ARMOR

Ballistic armor can be defined as a protective barrier designed to resist the penetration of projectiles from firearms (STANDARD, ; ABNT, 2005).

Currently, the Brazilian Army and Auxiliary Forces adhere to standards provided by the United States National Institute of Justice (STANDARD, ; (OLES); AMERICA, 2008) and the Brazilian Association of Technical Standards (ABNT, 2005), aiming to assess the performance of ballistic shields. These regulations specify shields at different protection levels based on minimum velocity, projectile mass, and caliber. Table 2.7 presents the classification of various protection levels according to the previously mentioned parameters.

Tabela 2.7 – Classification of protection levels in ballistic shielding.

Level	Caliber	Mass (g)	Projectile minimum velocity (m/s)	Energy (J)
	.22 LR	2.6	310	125
I				
	.38 SPL	10.2.	239	291
	9 mm	8	320	410
II-A				
	357 Mag	10.2	369	694
	9 mm	8	343	471
II				
	357 mag	10.2	410	857
	9 mm	8	411	676
III-A				
	44 Mag	15.6	411	318
III	7.62 x 51	9.7	823	3285
IV	.30-06	10.8	853	3929

Source – Adapted from NIJ 0101.04., 2000.

According to the NIJ 0101.06 standard (2008), concerning the determination of the effectiveness of the multilayer armor system, the simplest method involves checking for an indentation (trauma) directly in the clay witness after conducting a ballistic test with a 7.62 mm ammunition. The maximum level of indentation in the standard material is 44 mm for test validation; if it exceeds this limit, the damage caused by the impact is considered fatal to the human body. The use of clay witness as the standard material is justified because it is similar to modeling clay, resembling the material that constitutes the human body (MONTEIRO et al., 2016; (OLES); AMERICA, 2008). FIG. 2.24 illustrates the evaluation method of the reference material (clay witness) before and after the projectile impact.

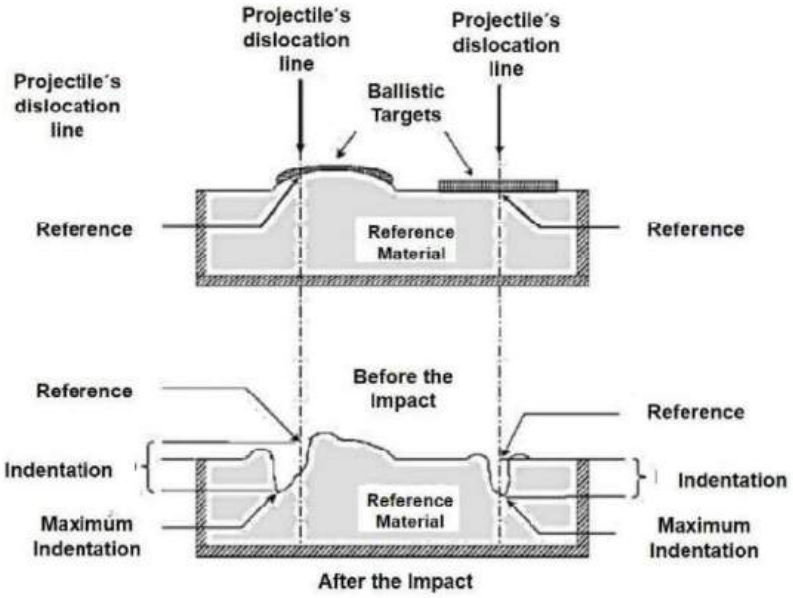

Figura 2.24 – Projectile trauma assessed by indentation in the reference material (clay witness).

Source – Adapted from braga (2015), (OLES) e America (2008).

The calculation of the limit velocity (V_L), represents another method for evaluating the efficiency of a shielding and is based on determining the velocity of a projectile upon hitting the MAS. This velocity is known as the minimum velocity required for the target to be penetrated. The primary parameter for estimation (V_{50}), designated as the ballistic limit, establishes the velocity at which the probability of penetration would be 50%. However, the calculation using the V_{50} parameter in conditions where the velocity is above 800 m/s, as is the case with 7.62 mm ammunition, becomes impractical; it would be essential to have at least 3 shots that do not penetrate the target. The objective would be to produce an average of the impacts to calculate the ballistic limit (ZUKAS, 1980; SILVA et al., 2014; WANG et al., 2014).

Consequently, an analytical model is substantial for gauging the limit velocity (V_L) without occurrence of shield penetration and is based on the absorbed energy (MORYE et al., 2000). The projectile's velocity was measured immediately before (V_i) and after (V_R) the impact. The kinetic energy variation was related to the energy absorbed by the target (E_{abs}) and used for comparison between the tested materials, exposed in EQ. 2.10, where m is the mass of the projectile.

$$E_{\text{abs}} = \frac{m.(V_i^2 - V_R^2)}{2} \tag{2.10}$$

Another calculation was performed for the V_L, which is an estimate of the velocity at which the target would be able to stop the projectile, V_R is considered zero. That is, as soon as the shielding system completely absorbs the kinetic energy resulting from the

projectile, it becomes feasible to consider the value of the limit velocity according to EQ. 2.11.

$$V_L = \sqrt{\frac{2E_{\text{abs}}}{M}} \tag{2.11}$$

3 MATERIALS AND METHODS

The focus of the work consisted of characterizing the alkaline treatment and functionalization with GO coating of seven-island sedge fibers, aiming to improve the fiber-matrix interface. Consequently, enhancing the mechanical and thermal properties of the composites. Additionally, this research proposes to conduct MAS ballistic test evaluations, having composite plates reinforced with seven-island sedge fibers as an intermediate layer. Therefore, several steps need to be carried out, as outlined in FIG. 3.1. According to the presented, the first step was perform an alkaline treatment with 3, 5, and 10% (w/v) of NaOH. Additionally, functionalization of GO on the fibers and epoxy matrix were carried out.

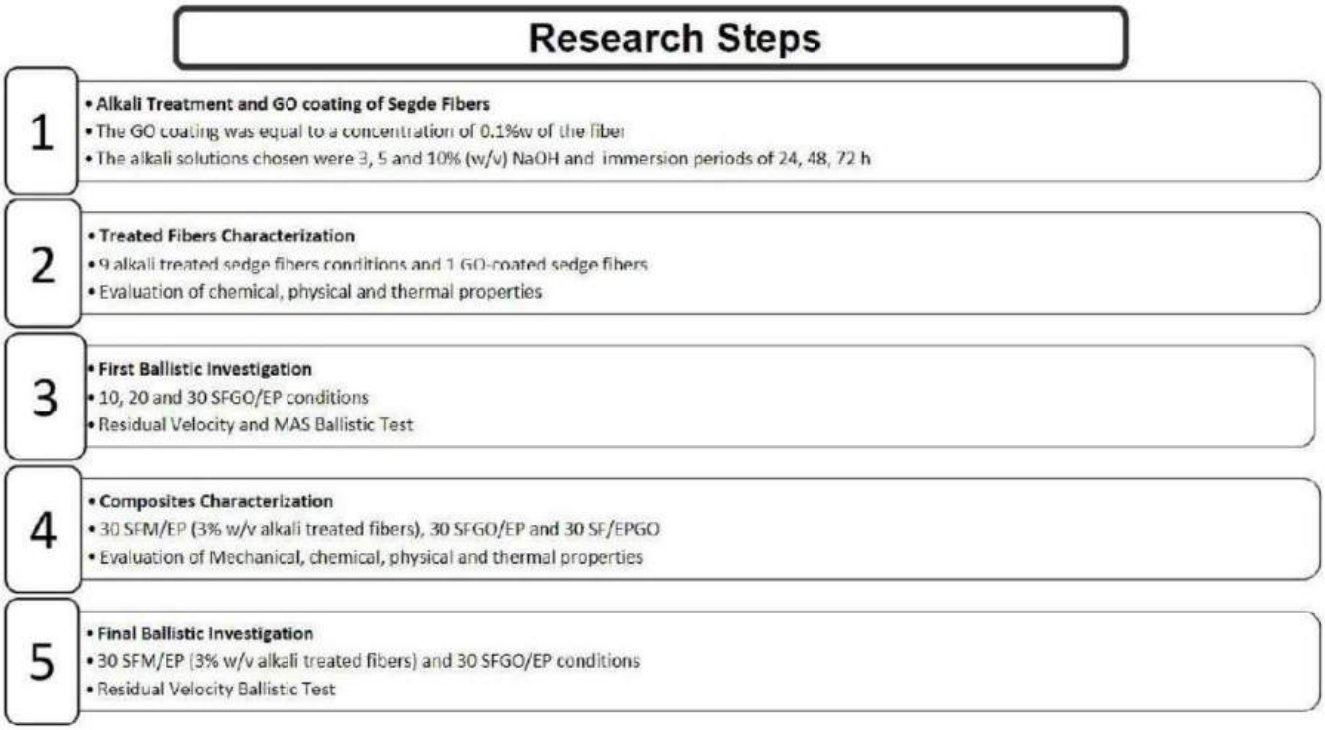

Figura 3.1 – Research steps proposed for this research project.

Chemical, thermal, and morphological characterizations were carried out for all treatments applied to the fibers, allowing an understanding of how the treatments influenced the intrinsic characteristics of the fiber and its physical properties. The third stage involved manufacturing composite plates reinforced with 10, 20, and 30% of seven-island sedge fibers volume to conduct MAS clay witness tests. Ceramic plates were produced, and aramid fabrics were cut to appropriate dimensions to produce MASs specimens reinforced with the mentioned fiber percentages. After assembling the system, the trauma inflicted on the plastiline were verified.

The fourth stage was related to the manufacture of composite plates reinforced with 30% of fibers functionalized with GO and the group that demonstrates the best results from the alkaline treatment. Subsequently, tests related to mechanical, thermal, chemical, and physical properties were investigated and compared with composites reinforced with untreated seven-island sedge fibers.

The final stage focused on investigating the residual velocity ballistic evaluation of composite plates reinforced with 30% of functionalized with GO and alkaline treated seven-island sedge fibers.

3.1 MATERIALS

3.1.1 SEDGE FIBERS

Sedge fibers were extracted from as-received stalks, commercially supplied by the company Artevale. These *Cyperus malaccensis* (CM) sedges, found in the Brazilian southeast region of the Vale do Ribeira, are illustrated in FIG.3.2. A CM mat was acquired from the company Artevale, São Paulo, Brazil. The extracted fibers were manually cleaned, immersed in water for 24 h, 3.2a, shredded, 3.2b, cut to a 150 mm length, FIG. 3.2, and then dried at 70 °C for 24 h. These fibers were not subjected to any chemical treatment. FIG. 3.3 demonstrates the fibers after they were dried. Moreover, the fibers will be subjected to an alkaline treatment and functionalization with GO.

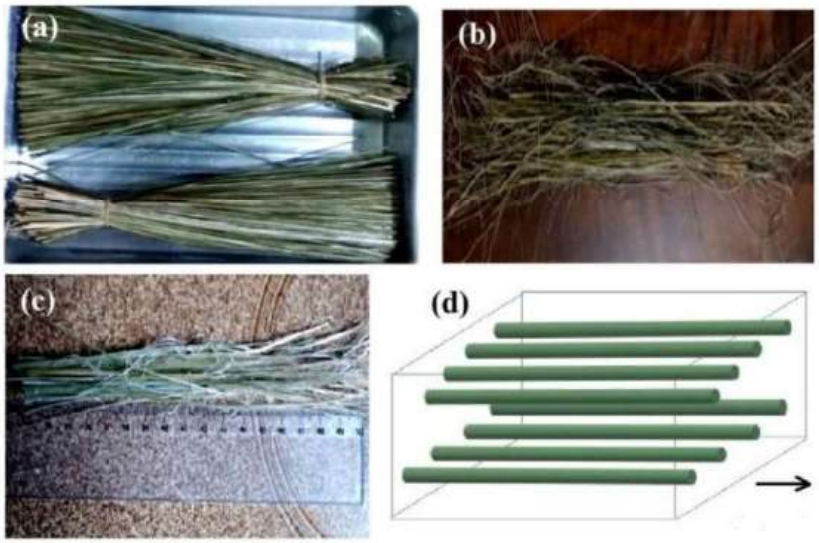

Figura 3.2 – The extraction process of the fibers: (a) *Cyperus malaccensis* (CM) sedge immersed in water for a period of 24 h; (b) shredded fibers; (c) fibers already cut 150 mm in length; (d) schematic diagram of the aligned arrangement of the fibers in the composite.

Source – Adapted from Neuba et al. (2020).

The immersion technique was adopted for providing greater flexibility and thus contributing to making the defibration process easier. Cutting tools helped in the process, assisting the removal of continuous fibers without sudden rupture, making it possible to obtain fibers with a larger length and quantity. FIG. 3.2 depicts the extraction process of the fibers.

Figura 3.3 – Dried sedge fibers.

3.1.2 EPOXY RESIN

A commercial epoxy resin, diglycidyl ether of bisphenol A (DGEBA)-type, hardened with triethylene tetramine (TETA) in a 13 phr stoichiometric ratio, was used as a polymeric matrix. It was fabricated by the company Dow Chemical, São Paulo, Brazil, and distributed by the company Resinpoxy Ltda, Rio de Janeiro, Brazil.

3.1.3 ARAMID FABRIC

The aramid fiber used in fabric form, produced by Teijin Aramid, was employed as the third layer of the MASs. The mechanical, physical properties, and its characteristics are represented in TAB. 3.1. Additionally, in TAB. 3.2, the technical characteristics of the aramid yarn can be viewed.

Tabela 3.1 – Characteristics of aramid fabric.

Model	Linear Density	Twaron Type	Areal Density (g/m^2)	Thickness (mm)	Minimum Ultimate stress (N/5cm x 1000) Fabric
T 750	3360	1000	460	0.65	17.4

Source – Adapted from TEIJIN (2019).

Tabela 3.2 – Characteristics of aramid yarn.

Linear Densities	Twaron Type	Number of Filament yarn	Ultimate Strain %	Ultimate stress (N)
3360	1000	2000	3.70	688

Source – Adapted from TEIJIN (2019).

3.1.4 ALUMINA

The alumina employed in this study was the APC 11-SG product from the manufacturer Alcoa. The manufacturer provides the average particle size of the material in the order of 3 μm. The purity content of the product and the chemical composition according to the manufacturer are presented in TAB. 3.3

Tabela 3.3 – Alumina specifications.

Element	Quantity (%)	Specification (%)
Al_2O_3	99.4	Min. 99.1
SiO_2	0.04	Máx. 0.06
Fe_2O_3	0.04	Máx. 0.06
Na_2O	0.11	Máx. 0.15
Moisture at 300 °C	0.20	Máx. 0.50

Source – Adapted from the manufacturer's catalog.

3.1.5 NIOBIA

Utilized as a sintering additive and acquired from the Brazilian Company of Metallurgy and Mining (CBMM). The commercial composition of niobia, as presented by CBMM, is detailed in TAB. 3.4.

Tabela 3.4 – Niobia specifications.

Element	Quantity (%)
Nb_2O_5 (%)	99.5
Ta (ppm)	745
Ti (ppm)	240
Fe (ppm)	136
Sn (ppm)	95
Si (ppm)	66

Source – Adapted from the manufacturer's catalog.

3.1.6 POLYETHYLENEGLYCOL (PEG)

An organic additive used as a binder for ceramic powders, PEG 400 model from the manufacturer Synth. It imparts minimum mechanical strength to the green body for handling between green body shaping and sintering stages. During the sintering process, the evaporation of PEG from the ceramic system occured. Specific information about PEG 400 is provided in TAB. 3.5.

Tabela 3.5 – Polyethyleneglycol specifications.

Specifications	
PH sol. 5% / 25 °C	4.5 - 7.5
average molecular weight	380 - 420
viscosity	6.8 - 8 cst
solution color	Transparent
ethylene glycol and diethylene glycol	0.25 %
heavy metals	5 ppm
ethylene oxide and 1.4 dioxane free	10 ppm
Ignition residue	0.1%

Source – Adapted from the manufacturer's catalog.

3.2 EXPERIMENTAL PROCEDURE

3.2.1 ALKALINE TREATMENT

In addition to the use of untreated seven-island sedge fibers *in natura*, chemical alkaline treatment were performed using NaOH, combining the following parameters:

1 – Agitation or non-agitation of the solution;

2 – Immersion period.

3 – NaOH concentration;

A total of 09 treatment combinations were conducted, in addition to the control group, which consisted of untreated seven-island sedge fibers. The purpose of the alkaline treatment was to increase the crystallinity of the fibers, enhance their mechanical properties, and promote better adhesion between the fibers and the polymeric matrix by increasing interfacial roughness. TAB. 3.6 highlights the types of samples produced by varying alkaline treatment parameters.

Tabela 3.6 – Alkali conditions based on the time and NaOH concentration.

Parameters			
NaOH Concentration	**Immersion period**		
-	24 h	48 h	72 h
3%	group 1	group 4	group 7
5%	group 2	group 5	group 8
10%	group 3	group 6	group 9

After the previously mentioned procedure, approximately 10 g of seven-island sedge fibers *in natura* were subjected to alkaline treatment to enhance fiber crystallinity for the production of composite plates. Alkali solutions of 3%, 5%, and 10% (w/v) NaOH were prepared using distilled water. Initially, the clean and dried sedge fibers were immersed in an alkali solution at room temperature for specified durations without stirring. After 24, 48, or 72 h, the sedge fibers were washed multiple times with distilled water to neutralize residual NaOH on the fiber surface and then dried at 80 °C in an oven for 24 h. The pH was monitored using pH strips and later a pH meter until reaching values close to 7 after the washing procedure. The fibers, which were subjected to a 24 h alkaline treatment, are depicted in FIG. 3.4.

Figura 3.4 – Alkali treated fiber bundle after 24 h.

3.2.2 GRAPHENE OXIDE (GO) SYNTHESIS

The graphene oxide (GO) used in this work was produced by the Hummers Offeman method (WILLIAM et al., 1958), modified by Rourke et al. (2011) as depicted in FIG. 3.6, with concentration calculated in 12 mg/ml. Then, it was diluted to 0.56 mg/mL GO solution corresponding to 0.1 wt.% of the resin and fiber. The GO use in this research is presented in FIG. 3.5.

Figura 3.5 – Graphene Oxide.

The procedure involved mixing 5 g of graphite from Nacional de Grafite 99550, 4.5 g of potassium nitrate (KNO_3), and 169 ml of sulfuric acid (H_2SO_4) under magnetic stirring for 2 h, thus beginning the intercalation stage. The oxidation step started with the addition of 22.5 g of potassium permanganate ($KMnO_4$) in twelve equal portions over 2 h, with continuous magnetic stirring and cooling with ice. Subsequently, the exfoliation stage commenced with the dropwise addition of 605 ml of 5% (H_2SO_4) solution over 1 h, followed by magnetic stirring for an additional 3 h. The oxidation was then completed by incorporating 16.5 g of 30% hydrogen peroxide (H_2O_2) with continued stirring for 2 h.

The exfoliation stage continued with solution washing, adding 3% H_2SO_4 and 0.5% H_2O_2 (15.8 ml of H_2SO_4, 7.8 ml of H_2O_2, and 476.4 ml of deionized water), where the mixture remained under magnetic stirring for 12 h. Subsequently, 12 washes with additions of 3% H_2SO_4 and 0.5% H_2O_2 solution were performed in the Hettich Centrifugen rotina 420R centrifuge at 9300 rpm, using 4 tubes of 250 ml, at the National Institute of Technology (INT). Another 5 washes with deionized water were carried out in the same centrifuge. Therefore, the product obtained was the dispersion of graphene oxide (GO).

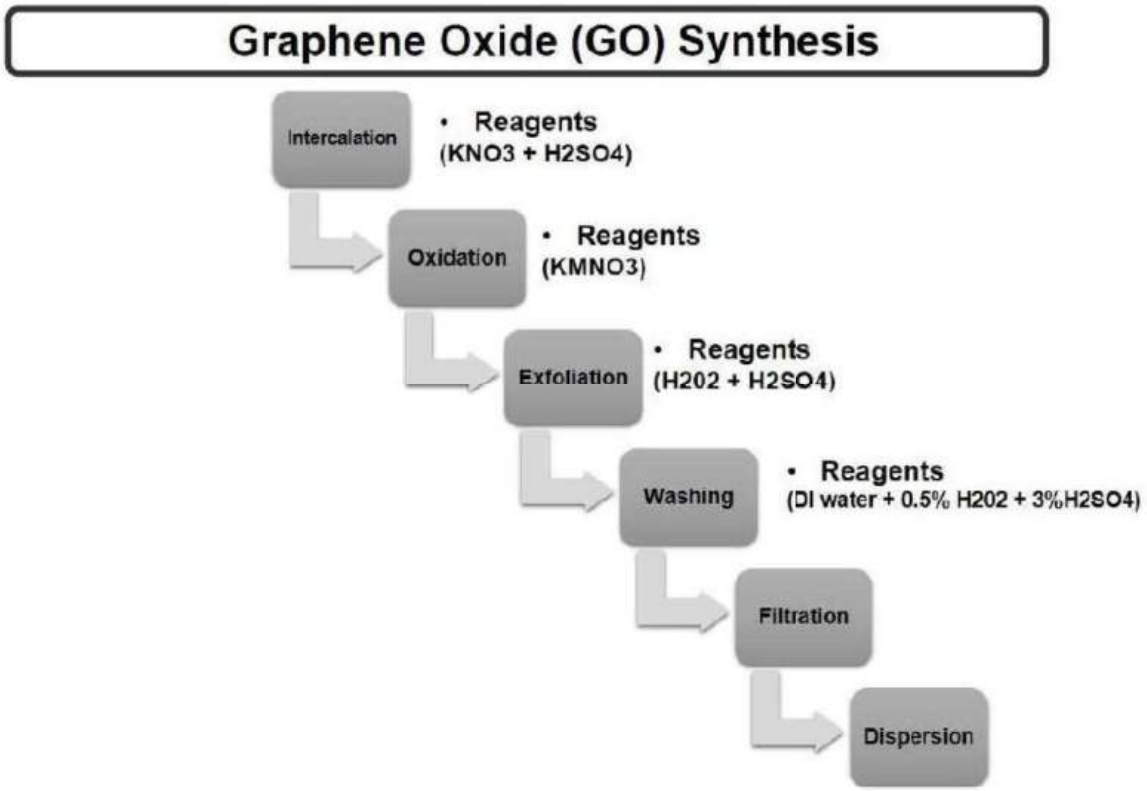

Figura 3.6 – Flowchart of the steps taken to obtain the GO, as well as the reagents used in each step.

3.2.3 SEDGE FIBERS FUNCIONALIZATION

Besides, GO applied as a coating, for the sedge fiber, was acquired from GOgraphene company (commercial name of William Blythe). The nanomaterial possess a concentration of 1%, equivalent to 10 mg/mL, variable sheet size and a pH superior to 2. The already dried sedge fibers were then immersed in a 0.56 mg/mL GO solution, with alcohol isoprophilic, corresponding to 0.1 wt.% of the fiber and kept under agitation for a period of 30 min in a universal mechanical shaker, in order to guarantee and optimize the contact of the GO with the fiber. Later, the sedge fibers soaked with GO were inserted in an oven at 80 °C for 24 h, obtaining the final sedge fiber coated with GO (SFGO)

3.2.4 EPOXY MATRIX FUNCTIONALIZATION

For the GO incorporation into the epoxy resin, it was used the nanomaterial produced at the INT. A 25 ml of GO suspension was dried, corresponding to a concentration of 0.1 wt.% of the resin, for the complete water removal. Then, dried GO suspension was mixed with 50 ml de isopropyl alcohol, obtaining an homogeneous solution of GO in alcohol (aGO), with this, 100 g of DGEBA resin was added. The DGEBA/aGO system is mixed in a a universal mechanical shaker, in order to guarantee and optimize the contact of the GO with the fibers. Thereafter it was placed in a stove at 80 °C for 24 h order to evaporate the isopropyl alcohol, remaining only the resin and GO (DGEBA/GO). This eliminates the chances to form air voids during the curing process caused by the alcohol evolution. Then, the hardener was added to the DGEBA/GO suspension and the material used as matrix for the composites was produced. The epoxy matrix functionalized by GO has been produced in order to be investigated in the University of California San Diego (UCSD).

3.2.5 CERAMIC PROCESSING

The preparation began with the groups separation and samples weighing on the Gehaka AG 200 digital balance, with an accuracy of 0.0001 g. The powders of alumina (700 g – 94.5 wt.%), niobia (29.15 g – 3.94 wt.%), and the liquid binder PEG (11.3 g – 1.53 wt.%) were added. The ceramic powders were then mixed in the previously investigated ratio that yielded the best results in ballistic tests (COSTA et al., 2019; OLIVEIRA et al., 2021; REIS et al., 2021). PEG was heated to 70 °C in order to assist the mixing of components. The milling and homogenization process were carried out using an alumina ball mill, model MA 500, for a period of 8 h.

Following the milling and homogenization process, the mixture was placed in an ELKA brand oven at 70 °C for 48 h. The ceramic mass obtained was macerated using a mortar and pestle. After maceration, the mixture was sieved using a stack of mesh sieves until reaching the sieve with an opening of 0.355 mm (42 Mesh).

After the sieving process, the ceramic mixture was subjected to a compressing process to obtain the "green body."A set consisting of two punches and a floating die was employed. 100 g of the ceramic mass was weighed for each test specimen. Additionally, a 30-ton motorized hydraulic press from the NOWAK brand was used for the pressing process. A load of 12 tons, corresponding to 30 MPa, was applied.

The final step in the ceramic processing involved the sintering process, where the "green body"transformed into a sintered ceramic body with the desired mechanical properties for ballistic applications. The sintering route employed aligns with previous works in the literature focused on producing materials for ballistic protection (COSTA

et al., 2019; REIS et al., 2021). An INTI furnace, model FE 1700, was used to conduct the sintering stage of the ceramic processing, according to FIG. 3.7 and the following conditions:

1 – Heating from 25 °C to 158 °C, using a rate of 1 °C/min;

2 – Heating plateau at 158 °C for 1 h;

3 – Heating from 158 °C to 375 °C using a rate of 1 °C/min;

4 – Heating from 375 °C to 1000 °C using a rate of 8 °C/min;

5 – Heating from 1000 °C to 1400 °C using a rate of 5 °C/min;

6 – Sintering plateau at 1400 °C for 3 h;

7 – Cooling from 1400 °C to 1000 °C using a rate of 5 °C/min;

8 – Cooling from 1000 °C to 700 °C using a rate of 3 °C/min;

9 – Cooling from 700 °C to 25 °C through furnace inertia after shutdown.

The first three stages were slower and aimed at the evaporation of the organic binder; after that, the material composition converted to 96% alumina and 4% niobium. In this study, 35 ceramic bodies were produced and sintered for various MASs that have been investigated.

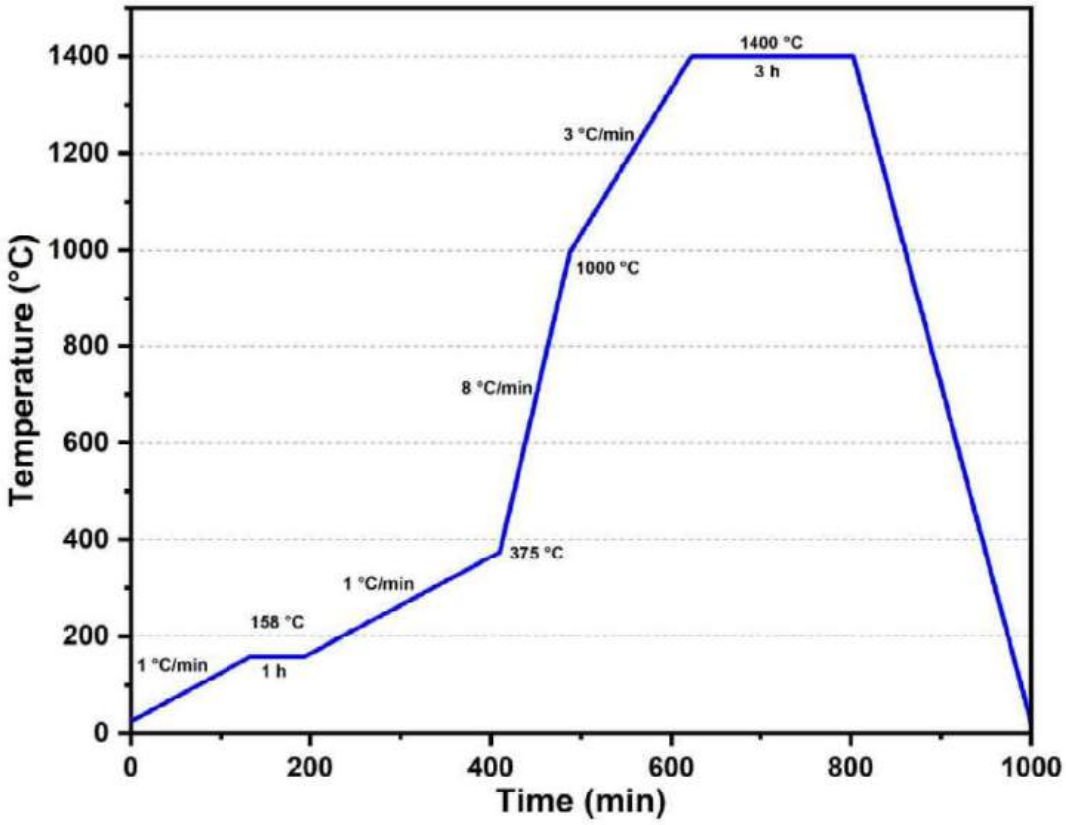

Figura 3.7 – Flowchart of the sintering steps carried out to obtain the ceramic samples.

3.2.6 CHARACTERIZATION OF CERAMIC BODIES

The specific mass of the ceramic bodies was determined according to the calculation of the mass/volume ratio (Eq. 3.1) and densification (Eq. 3.2), expressed as a percentage relative to the theoretical specific mass of the mixture (Al_2O_3 + Nb_2O_5). The theoretical specific mass was calculated using the rule of mixtures, which takes into account the fraction of each component present in the mixture.

$$\rho_{\text{sinterized}} = \frac{m}{v} \tag{3.1}$$

$$Densification = (\frac{\rho_{\text{sinterized}}}{\rho})x100\% \tag{3.2}$$

Where:

ρ – theoretical density;

ρ_{sintered} – density of the sintered ceramic body;

m - mass of the sample (g);

V - volume of the sample (cm^3).

As the most critical dimension is the thickness of the ceramic body, the calculation of linear shrinkage (R_L) was performed only in this dimension and in accordance with EQ 3.3.

$$R_{\text{L}} = \frac{e_{\text{green body}} - e_{\text{sinterized}}}{e_{\text{green body}}}x100\% \tag{3.3}$$

Where:

$e_{\text{green body}}$ – thickness of the green body;

$e_{\text{sinterized}}$ – thickness of the sintered sample.

The ceramic bodies resulting from this processing employed raw materials from the same suppliers and had been previously characterized in the literature by other authors (COSTA et al., 2019; REIS et al., 2021). They exhibited an average densification of 88.1% during sintering and an average density of the sintered material of 3.53 g/cm^3.

3.2.7 COMPOSITE PROCESSING

The composites reinforced with untreated, functionalized, and alkaline treated seven-island sedge fibers were subjected to mechanical tests, ballistic tests, FTIR analyses, and thermal analyses for the 10%, 20%, and 30% volume fiber groups. The adopted density corresponds to the average linear geometric density obtained from previous literature. To

produce the composite plates, a metal mold with dimensions of 15 x 12 x 1.19 cm and an internal volume of 214.2 cm^3 was used. Plates were fabricated using a 15-ton SKAY press. Details regarding fiber percentages, the number of plates to be fabricated, and objectives are presented in TAB. 3.7.

The steps taken to obtain the plates were:

1 - Cleaning the internal and external surfaces of the matrix components, including the upper punch, lower punch, and fixed sleeve;;

2 - Coating the matrix surfaces with Epoxyfiber-EX300 silicone lubricant. Followed by weighing the raw materials according to their required mass fractions of resin, catalyst, and fibers;

3 - Inserting the matrix into the press with the lower punch, fixed sleeve, and shims placed on the fixed sleeve, essential for obtaining plates with the required thickness;

4 - The aligned fibers were carefully accommodated inside the mold's cavity, schematically illustrated in FIG. 3.2d, and the resin-hardener mix was poured into the mold in a previously calculated fiber/resin ratio;

5 - The mixture was kept under a pressure of 5 tons for 24 hours to assist the curing process;

6 - Demolding the plate.

Tabela 3.7 – all proposed conditions of sedge fiber reinforced epoxy composites. The number and dimensions of the composite's plates were highlighted.

Conditions	**N° of plates**	**Tests**	**Dimensions of the plate (mm)**
0% 10% 20% 30% 30% (alkaline treatment) 30% (functionalization with GO) 30% (epoxy functionalized with GO)	7	DMA TMA DSC FTIR TGA/DTG	150 x 120 x 11.9
	7	Bending	150 x 120 x 4
	3	Tensile	150 x 120 x 4
	7	Charpy	150 x 120 x 11.9
	3	Izod	150 x 120 x 11.9
	7	Quasi-static compression	150 x 120 x 11.9
Total	**34**	**10**	**-**

FIG. 3.8 represents the equipment required for the fabrication of composite plates. For the epoxy resin, the density value of 1.1 g/cm^3 was taken from the literature (JR; RETHWISCH, 2016). Fibers oriented preferentially in the longitudinal direction were manually inserted into the matrix and evenly distributed throughout the mold after being wetted with the resin, divided into three different groups based on their volume percentages of 10, 20, and 30%. Additionally, the different composite groups were referenced with specific nomenclatures during the results discussion chapter. TAB. 3.8 displays the adopted nomenclatures.

Tabela 3.8 – Groups set up for the ballistics test.

Nomenclature	Composition
EP or control group	pure epoxy resin without sedge fiber reinforcement
10 SF/EP	10% by volume of sedge reinforcing an untreated epoxy matrix
20 SF/EP	20% by volume of sedge reinforcing an untreated epoxy matrix
30 SF/EP	30% by volume of sedge reinforcing an untreated epoxy matrix
30 SF/EP-GO	30% by volume of edge reinforcing a GO functionalized epoxy matrix
30 SFGO/EP	30% by volume of sedge coated with GO reinforcing an untreated epoxy matrix
30 SFM/EP	30% by volume of sedge treated with the best alkali treated group reinforcing an untreated epoxy matrix

Figura 3.8 – Equipment that assisted in the manufacture of the composite plates, such as the parts that composed the steel matrix.

3.2.8 ASSEMBLY OF MULTILAYER ARMOR SYSTEM (MAS)

The assembly of the test specimens for the multilayer shielding were carried out by combining the ceramic material as a front layer, followed by the seven-island sedge fiber-reinforced epoxy composite, and finally, the last layer composed of aramid fabric. In order to bond each component, a layer of polyurethane-based adhesive, ULTRAFLEX brand, was used. According to previous works, the adhesive did not influence or interfere with ballistic results (COSTA et al., 2019; REIS et al., 2021). The number of produced plates is shown in TAB. 3.9.

Tabela 3.9 – Composite and ceramic plates manufactured.

Conditions	**N° of composites plates**	**N° of ceramic plates**	**Tests**
10% 20% 30% 30% (alkaline treatment) 30% (functionalization with GO)	10	-	Residual velocity
	18	18	MAS
Total	**28**	**18**	**2**

3.3 BALLISTIC TEST

In order to assess the kinetic energy absorption capacity of a moving projectile by a MAS or materials applied in isolated ballistic protection, ballistic tests were conducted. In this study, two types of ballistic tests were employed. In the first one, the MAS is placed over a 50 mm thick clay witness (CORFIX^{TM}), which has a similar consistency to a human body and a specific mass of approximately 1.7 g/cm^3. An illustrative scheme of this ballistic test is presented in FIG. 3.9. The objective is to measure the trauma, also known as backface signature (indentation), caused by the impact of 7.62 mm caliber ammunition on the MAS target. According to the NIJ 0101.04 standard (JUSTICE, 2008), a ballistic armor was deemed effective if the indentation caused in the clay witness is equal to or less than 44 mm. Measurements were performed with a Q4X Banner digital laser sensor. The tests were carried out at the Brazilian Army Assessment Center (CAEx), Rio de Janeiro.

To verify that the density of the clay witness is in accordance with the standard, it was inserted into a hot chamber (WEISS) for approximately 2 h. Then, the clay is removed, and its density is checked following the procedure specified in section 5.7.5 of the NIJ 0101.04 standard (JUSTICE, 2000), verifying the depth of the indentation caused by a steel sphere. The tests were divided into groups according to the composite material of the intermediate layer. TAB. 3.10 lists the groups that were prepared for this test.

Tabela 3.10 – Groups set up for the ballistics test.

Group	intermediate layer	Number of plates
1	Epoxy resin reinforced with 10% of seven-island sedge fibers	6
2	Epoxy resin reinforced with 20% of seven-island sedge fibers	6
3	Epoxy resin reinforced with 30% of seven-island sedge fibers	6

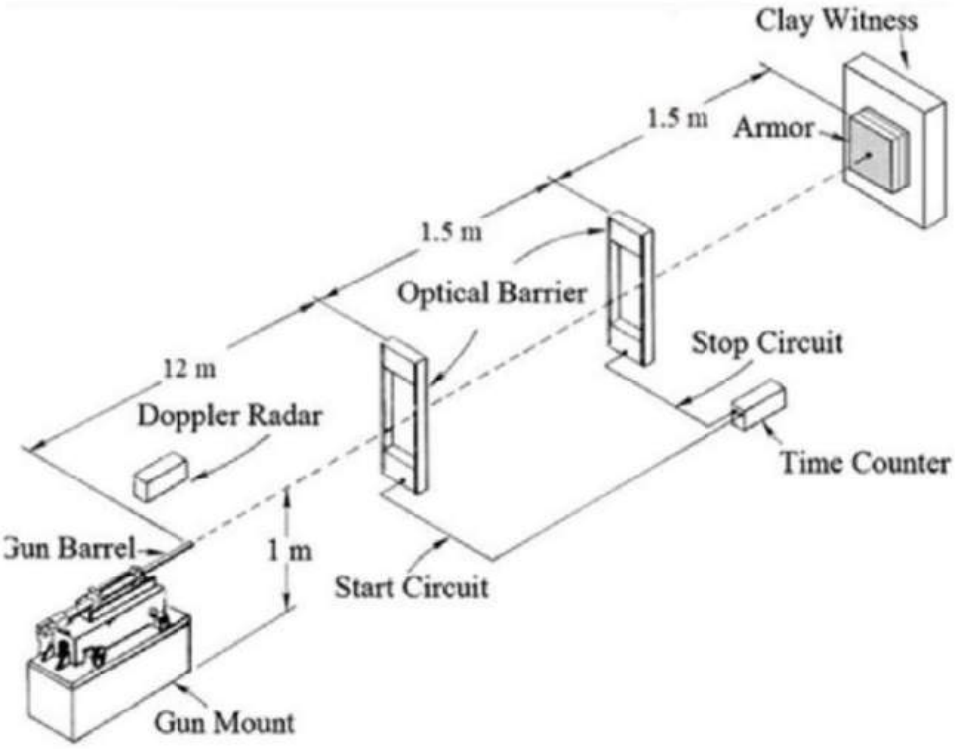

Figura 3.9 – Schematic illustration for the ballistic test of the MAS groups.

Source – Adapted from Pereira e Assis (2019).

The second ballistic test aims to measure the energy absorbed by the composite (intermediate layer of the armor). To measure the projectile velocity before and after the ballistic impact, a model SL-520 P Weibel Doppler radar from Denmark (Fixed-Head Doppler Radar Systems) was used, along with Windopp software for processing the raw data. The ballistic test schematic is illustrated in FIG. 3.10. The limit velocity can be calculated using the data acquired by the Doppler radar and the equations mentioned in the literature review chapter. A total of 8 shots were fired in each group for the evaluation of residual velocity. TAB. 3.11 shows the groups prepared for this test.

Tabela 3.11 – Groups manufactured for the ballistic residual velocity test.

Group	intermediate layer	Number of plates
1	Epoxy resin reinforced with 10% of seven-island sedge fibers	8
2	Epoxy resin reinforced with 20% of seven-island sedge fibers	8
3	Epoxy resin reinforced with 30% of seven-island sedge fibers	8
4	Epoxy resin reinforced with 30% of seven-island sedge fibers alkaline treated	8
5	Epoxy resin reinforced with 30% of seven-island sedge fibers functionalized with GO	8

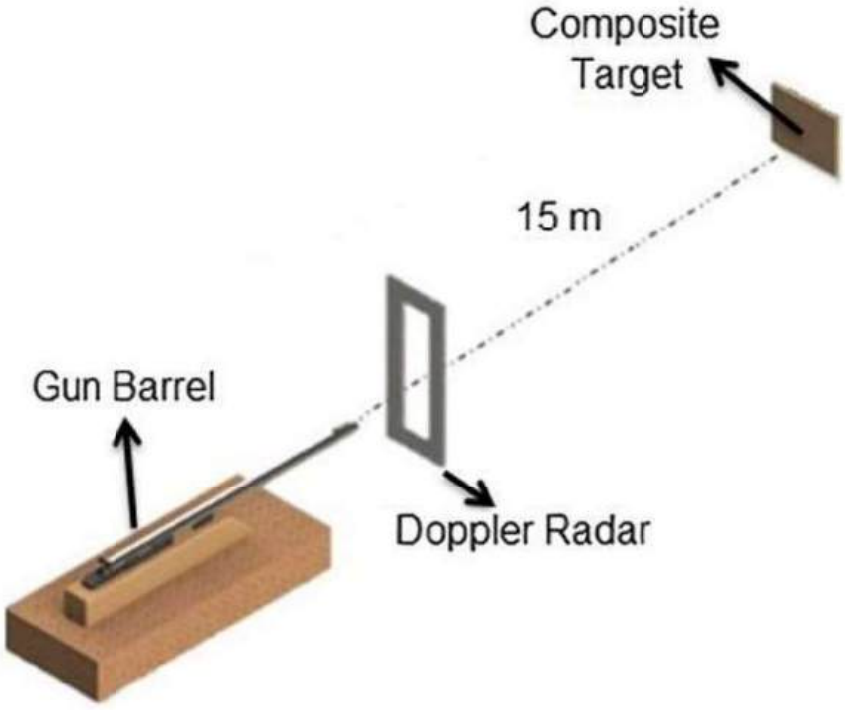

Figura 3.10 – Schematic illustration of the ballistic residual velocity test.

Source – Adapted from Filho et al. (2020a).

The adopted conditions for the ballistic tests were:

Ammunition: 7.62 mm M1 caliber, as commercially provided to the Army. It has a mass of 9.7 g;

Device: Target fixture device and test specimen produced by High-Pressure Instrumentation (HPI) for a 7.62 x 51 mm gun barrel caliber;

Target distance: 15 meters, according to the NIJ 0101.06 standard for 7.62 mm ammunition;

Angle of incidence on the target: 90°;

Number of shots for each type of ballistic test: 7 shots per group for the trauma verification in the clay and 8 shots per group for residual velocity measurement;

Location: Brazilian Army Assessment Center (CAEx), located on Marambaia in Rio de Janeiro.

3.4 MECHANICAL TESTS

Knowledge of the mechanical properties of a material is crucial for determining its use, application, and selection in any engineering projects. Therefore, tensile, quasi-static compression, flexural, Charpy impact, and Izod impact tests were conducted.

3.4.1 IZOD IMPACT TEST

The preparation for the fabrication of test specimens (TSs) involved using fibers cut to a length of 120 mm to accommodate them within the rectangular steel mold. Additionally, the fibers were placed in an oven at 70 °C for 24 h before the plate fabrication. The total number of plates manufactured was based on the treated conditions of 30 SF/EP-GO, 30 SFGO/EP, 30 SFM/EP with random diameter and uniformly aligned.

After this process, the plates were cut using a saw to obtain a total of 7 to 10 samples with dimensions of 60.25 x 12.7 x 10 mm for each group, following the ASTM-D256 standard. It was necessary to sand down the samples with sandpaper of various grits, aiming to eliminate possible surface defects and achieve the required dimensions in accordance with the standard, for specimens that exceeded the required values. A notch was made using a single-tooth manual notcher from the Pantec Iz/Ch-50 brand, performed individually for each specimen following the standard, with a radius of curvature of 0.25 mm $\pm$ 0.05 mm, an angle of 45 ° $\pm$ 1 °, and a 2.54 mm deep V-notch. In order to calculate the energy absorbed per unit length, it was necessary to measure the dimensions of all specimens.

The tests were carried out in the Natural Fibers Laboratory at the North Fluminense State University Darcy Ribeiro (UENF) in Campos dos Goytacazes. The equipment used was a Pantec model XC-50, employing a 22J hammer. The results of the absorbed energy were statistically analyzed.

3.4.2 CHARPY IMPACT TEST

The preparation for the fabrication of TSs involved using fibers cut to a length of 120 mm, allowing them to fit inside the rectangular steel mold. Additionally, the fibers were placed in an oven at 70 °C for 24 h before plate fabrication. The total number of plates manufactured was based on the treated conditions of 30 SF/EP-GO, 30 SFGO/EP, 30 SFM/EP with random diameter and uniformly aligned.

After this process, the plates were cut using a saw to obtain a total of 7 to 10 samples with dimensions of 127 x 12.7 x 10 mm for each group, following the ASTM-D6110 standard. It was necessary to sand down the samples with sandpaper of various grits, aiming to eliminate possible surface defects and achieve the required dimensions in accordance with the standard, for specimens that exceeded the required values. A notch was made using a single-tooth manual notcher from the Pantec Iz/Ch-50 brand, performed individually for each specimen following the standard, with a radius of curvature of 0.25 mm ± 0.05 mm, an angle of 45 ° ± 1 °, and a depth of 2.54 mm. In order to calculate the energy absorbed per unit length, it was necessary to measure the dimensions of all specimens.

The tests were conducted in the Natural Fibers Laboratory at the North Fluminense State University Darcy Ribeiro (UENF) in Campos dos Goytacazes. The equipment used was a Pantec model XC-50, employing a 22J hammer. The results of the absorbed energy were statistically analyzed.

3.4.3 TENSILE TEST

For the fabrication of the test specimens, the fibers were cut to a length of 150 mm and inserted into an oven for 24 hours prior to the plate fabrication. A total of 3 plates were produced, one for each group: 30 SF/EP-GO, 30 SFGO/EP, 30 SFM/EP. Two additional shims were required inside the mold as the necessary thickness for the plate was 6 mm, according to the ASTM-D3039 standard. The plates were later sanded to remove burrs and improve surface finish, then cut with the assistance of a saw to dimensions of 150 x 15 x 6 mm.

The tensile tests were performed on an Instron universal mechanical testing machine at the Applied Mechanics Laboratory of the University of California San Diego (UCSD), in San Diego. The EMIC Series 23 equipment with a load capacity of 20 kN was used. Additionally, the tests were also conducted on a universal machine from EMIC, at the Applied Mechanics Laboratory at the Federal Fluminense University (UFF), with a load cell of 10 kN. A total of 5 samples were tested for the 30 SF/EP-GO condition, and 7 to 10 for the conditions of 30 SFGO/EP and 30 SFM/EP. The tests were conducted with a crosshead speed of 2 mm/min and a gauge length of 90 mm. By measuring the

cross-sectional area of the specimens, it was possible to calculate the maximum stress values, enabling a statistical analysis of the results. The maximum tensile stress values were obtained using Eq. 3.4.

$$\sigma_{\max} = \frac{F_{\max}}{A_o} \tag{3.4}$$

Where:

$\sigma_{\max}$ - Ultimate tensile strenght;

$F_{\max}$ - maximum load;

A_o - initial cross-sectional area of the test specimen.

Additionally, in order to determine the values of the modulus of elasticity, Eq. 3.5 was used.

$$E = \frac{\sigma_1 - \sigma_2}{\epsilon_1 - \epsilon_2} \tag{3.5}$$

Where:

E - elastic modulus (GPa);

σ_1 e σ_2 - tensile stress (MPa);

ϵ_1 e ϵ_2 - engineering strain (mm/mm).

3.4.4 BENDING TEST

The three-point bending test was conducted using a universal Instron mechanical testing machine, located in the laboratory of the Department of Mechanical and Aerospace Engineering at UCSD. The tests were also performed on a universal EMIC machine in the Applied Mechanics Laboratory at the Federal Fluminense University (UFF), with a 10 kN load cell. A total of 7 to 10 samples were tested for the condition of 30 SF/EP-GO, and 10 samples for the conditions of 30 SFGO/EP and 30 SFM/EP. The parameters used comply with the ASTM-D790 standard. The test specimens were produced from composite plates with dimensions of 120 x 15 x 6 mm, with a crosshead speed of 2 mm/min, and a support span of 96 mm. The maximum stress ($\sigma_{máx}$) and the flexural modulus (E) were calculated according to EQs. 3.6 and 3.7.

$$\sigma_{\max} = \frac{3LQ_{\mathrm{m}}}{2bd^2} \tag{3.6}$$

$$\sigma_{\max} = \frac{Q_{\mathrm{m}}L^3}{4bd^3\Delta_{\mathrm{y}}} \tag{3.7}$$

Where: Q_m - maximum load; L - distance between supports; b - width; d - thickness; Δy - deflection.

From the results, it was possible to statistically analyze the outcomes. In terms of plate fabrication, a total of 7 plates were produced, one for each group: EP, 10 SF/EP, 20 SF/EP, 30 SF/EP, 30 SF/EP-GO, 30 SFGO/EP, and 30 SFM/EP.

3.4.5 QUASI STATIC COMPRESSION TEST

The quasi-static uniaxial compression test was conducted on an universal Instron mechanical testing machine located in the laboratory of the Department of Mechanical and Aerospace Engineering at UCSD. The parameters used comply with the ISO-604 standard. The test specimens were produced from 30 SF/EP-GO composite plates, from which 10 samples were created. The tests were also performed on a universal EMIC machine in the Applied Mechanics Laboratory at the Federal Fluminense University (UFF), with a 10 kN load cell. A total of 7 to 10 samples were used for the conditions of 10 to 30 SF/EP, 30 SF//EPGO, 30 SFGO/EP and 30 SFM/EP.

To obtain the cylindrical test specimen, a drill coupled with a diamond hole saw with a diameter of 14 mm was used. This approach allowed for the creation of specimens with diameters equivalent to 10.5 mm and a height of 10.5 mm. Regarding the parameters used during the test, a crosshead speed of 2 mm/min was employed. The effective length adopted was equivalent to 10 mm. The calculations followed EQs. 3.4 and 3.5, enabling a statistical analysis of the results.

3.4.6 DYNAMIC MECHANICAL ANALYSIS (DMA)

Dynamic Mechanical Analysis (DMA) was carried out to identify parameters such as storage modulus (E'), loss modulus (E"), and tangent delta (Tan δ) related to the viscoelastic behavior of the material, as well as crucial parameters like the glass transition temperature of the composites. The samples used included EP and composites under the conditions of 10 SF/EP, 20 SF/EP, 30 SF/EP, 30 SF/EP-GO, 30 SFGO/EP, and 30 SFM/EP. The entire procedure was conducted following the ASTM D4065-01 standard on rectangular samples with dimensions of 11 x 38 x 4 mm.

The equipment, a Q800 model (TA Instruments, New Castle, USA), owned by UENF, was employed. It operated at a frequency of 1 Hz, with a heating rate of 3 ° C/min, a temperature range from -50 to 200 °C, static load of 0.1 N, and amplitude of 20 μm under a nitrogen atmosphere. The samples were subjected to a three-point bending test.

3.5 THERMAL ANALYSIS

Thermal analyses were employed to investigate at which temperature the treated fibers and epoxy composites reinforced with seven-island sedge fibers experience a maximum limit of moisture loss. Additionally, the analyses aimed to identify the specific temperatures at which the degradation of the fiber and composite microstructures occurs.

3.5.1 THERMOGRAVIMETRIC ANALYSIS (TGA/DTG)

For thermogravimetric analysis (TGA), treated seven-island sedge fibers were comminuted and placed into a platinum crucible. The same procedure was followed for composite samples of 30 SF/EP-GO, 30 SFGO/EP, and 30 SFM/EP, totaling 13 samples. Samples were heated from 25 to 600 °C at a rate of 10 °C/min under a nitrogen atmosphere and a gas flow of 50 mL/min. The test was conducted at the Naval Research Institute (IPQM) using a DTG-60H model (Shimadzu, Tokyo, Japan). Temperatures associated with various degradation stages of the materials, such as structural component degradation of fibers and moisture loss, were identified during the analysis. After obtaining the data, they were processed using *Software Origin Pro.*

3.5.2 DIFFERENTIAL SCANNING CALORIMETRY (DSC)

The preparation of the specimens for DSC analysis followed the same standards as the TGA analysis; the 13 samples were comminuted and placed in a platinum crucible. The tests were conducted at the Naval Research Institute (IPQM) using a DTG-60H model (Shimadzu, Tokyo, Japan). The parameters established for the test were: a heating rate of 10 °C/min, starting at 30 up to 600 °C, under a nitrogen atmosphere, with a gas flow of 50 mL/min. From the data obtained, it was possible to generate graphs using the *Origin Pro.*

3.5.3 THERMOMECHANICAL ANALYSIS (DMA)

Through this analysis, measurements of the linear thermal expansion coefficient of EP and composites (SF/EP, 20 SF/EP, 30 SF/EP, 30 SF/EP-GO, 30 SFGO/EP, and 30 SFM/EP) made from seven-island sedge fibers were carried out using the TMA-60 (Shimadzu, Tokyo, Japan) owned by IPQM. The test was conducted according to the ASTM E831 standard, under a nitrogen atmosphere with a temperature ranging from 10 to 250 °C, a gas flow rate of 50 ml/min, and a compression load of 10 gf. The samples were produced from composite plates with dimensions of 10 x 5 x 10 mm.

3.6 FOURIER TRANSFORM INFRARED SPECTROSCOPY (FTIR)

In order to perform the analysis, the alkaline treated and GO-coated samples of seven-island sedge fiber and the composites 30 SF/EP, 30 SF/EP-GO, 30 SFGO/EP, and 30 SFM/EP were ground into the required powder condition. The preparation of the specimens involves pressing the previously mixed powder to produce the KBr sample. The analyses were conducted in the laboratory of the Navy Research Institute (IPQM) on a model IRPrestige-21 (Shimadzu, Tokyo, Japan). The samples were scanned from 4000 to 400 cm^{-1}, with 32 scans.

The reason for choosing the chemical analysis of the composites was to investigate the chemical interaction between the reinforcement phase and the matrix, while the analyses in the different groups of treated seven-island sedge fibers examined the vibrations and stretches of the effective fiber bonds. The generated data were processed using the *Software Origin Pro*, generating the respective spectra of percentage transmittance (%) by wavenumber (cm^{-1}).

3.7 X-RAY DIFFRACTION (XRD)

The crystallinity index (Ic) and the crystallite size (CS) of the SFGO, SFM, 30 SFGO/EP, 30 SF/EP-GO and 30 SFM/EP were calculated from the diffractogram obtained by XRD analysis. In order to calculate the fiber Ic, the proposed method by (SEGAL et al., 1959) was used according to the EQ. 3.8, in which the crystallinity is given by the difference of the peak relative to the (0 0 2) plane, by the amorphous halo in the diffractogram:

$$I_c = 1 - \frac{I_1}{I_2} \tag{3.8}$$

Where:

I_1 – intensity of the diffraction minimum (amorphous region);

I_2– intensity of the diffraction maximum (crystalline region).

For the calculation of the crystallite size (CS), the method used was established by Scherer's relations as expressed by the EQ. 3.9 below.

$$CS_{002} = 1 - \frac{0.89\lambda}{\beta_{002} cos\theta} \tag{3.9}$$

Where:

K - constant 0.89;

λ - intensity of radiation;

β - full-width at half-maximum (FWHM);

θ - Bragg's angle.

The PANalytical X'pert Pro MRD diffractometer and a Pixcel detector, with a cobalt anode, were used with the following parameters to obtain the diffractogram: a scan rate of 0.05 (2θ/s), scan from 5° to 75°, 40 mA, 40 kV, and Kα (1.789 A) radiation. Through this test, it was possible to obtain a diffractogram for SFM, SFGO, 30 SFGO/EP, 30 SF/EP-GO and 30 SFM/EP conditions. The samples were prepared using dried fibers after 24 hours at 70°C, cut to a length equivalent to 30 mm, and placed in parallel on a monocrystalline silicon wafer until reaching 30 mm in width. The acquired data was processed using the Origin Pro software, enabling the generation of the diffraction profile.

3.8 SCANNING ELECTRON MICROSCOPY (SEM)

The morphological analysis of seven-island sedge fibers was conducted through SEM, aiming to investigate details of the cross-section, surface, microfibrils, lumen, and any morphological modifications resulting from specific treatments, types of tests, or analyses. Similarly, morphological analyses of composites reinforced with seven-island sedge fibers was performed to examine fracture surfaces after conducting the tests. Since the samples are polymeric material, it was necessary to metallize them in the electron microscopy laboratory at IME, using a platinum-coated and gold-coated film deposition equipment from LEICA, model EM ACE600, under high vacuum conditions.

The surfaces were analyzed using a Quanta FEG 250 FEI equipment (Hillsboro, OR, USA) at the IME laboratory. Additionally, a model FEI Apreo FESEM equipment (Waltham, Massachusetts, USA) from the NE-MRC laboratory at UCSD was employed. The equipment operated with a secondary electron detector at an acceleration voltage between 9 and 10 kV, a spot size of 4.5, and a working distance of 10 mm, using the secondary electron (SE) analysis mode. FIG. 3.11 shows some samples after the gold coating has been applied.

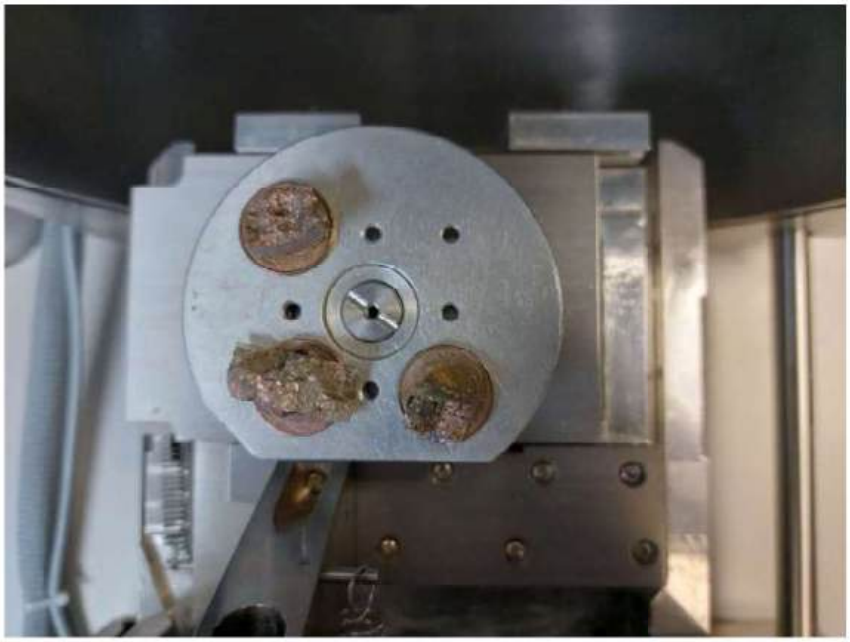

Figura 3.11 – Metallized test specimens.

3.9 STATISTICAL TREATMENT

In an attempt to ensure reliability of the results and to check for significant differences among the sample groups, the mechanical test results were analyzed using the Weibull method, ANOVA, and Tukey's test.

3.9.1 WEIBULL

The Weibull distribution is a statistically robust method extensively employed for reliability and engineering calculations, capable of adapting to various cases through the adjustment of a few parameters (ABERNETHY et al., 1983; O'CONNOR; KLEYNER, 2012).

The Weibull cumulative distribution function is expressed in EQ. 3.10.

$$F(x) = 1 - exp[-(\frac{x}{\Theta})^{\beta}] \tag{3.10}$$

Where:

Θ – characteristic unit or scale parameter;

β - Weibull modulus or shape parameter.

Manipulating Eq. 3.10 mathematically, we get Eq. 3.11:

$$\ln[\ln(\frac{1}{1-F(x)})] = \beta \ln(x) - [\beta \ln[\theta)] \tag{3.11}$$

EQ. 3.11 represents a linear equation, where:

β - angular coefficient;

$\beta\ ln(\theta)$ - linear slope.

Ordered and sorted data presented in ascending order enable the acquisition of Weibull parameters through graphical methods (O'CONNOR; KLEYNER, 2012).

3.9.2 ANOVA

With the aim of comparing the properties obtained from tests associated with different volumetric fractions of reinforcement, analysis of variance (ANOVA) and Tukey's test were employed to compare mean values. This test is also known as an honestly significant difference (HSD) and allows investigating the equality within treatments or the absence in different sample groups through a hypothesis test. Considering the test results, the hypothesis of equality between the means of the properties can be either rejected or not, depending on the HSD, as determined by EQ. 3.12.

$$HSD = q.\sqrt{(\frac{MSE}{r})} \tag{3.12}$$

Where:

HSD – mean square error;

r – number of replicates of each treatment;

q – total range.

Analysis of variance was performed on the data from the test results to determine whether there is a significant difference between the values of the evaluated properties for samples from different groups. In case of significant variation, the Tukey's test was employed. Thus, it is possible to conclude quantitatively and qualitatively which configuration represents the most suitable results for the acquired properties.

4 RESULTS AND DISCUSSION

4.1 SEDGE FIBERS COATED BY GRAPHENE OXIDE (GO)

4.1.1 THERMOGRAVIMETRIC ANALYSIS (TGA/DTG)

FIG. 4.1 and TAB. 4.1 illustrate the results of TGA and the first-order derivative (DTG) of the SFGO. It could be observed a mass loss of 11.84% up to 200 °C, due to the evaporation of moisture content present on the surface of the fibers, resulting in dehydration. When compared to SF, equal to 13.23%, the current results revealed a slightly lesser percentage of moisture content. Moreover, the DTG curve exhibits a peak concerning the mass loss drop occasioned by the molecular structures' moisture desorption.

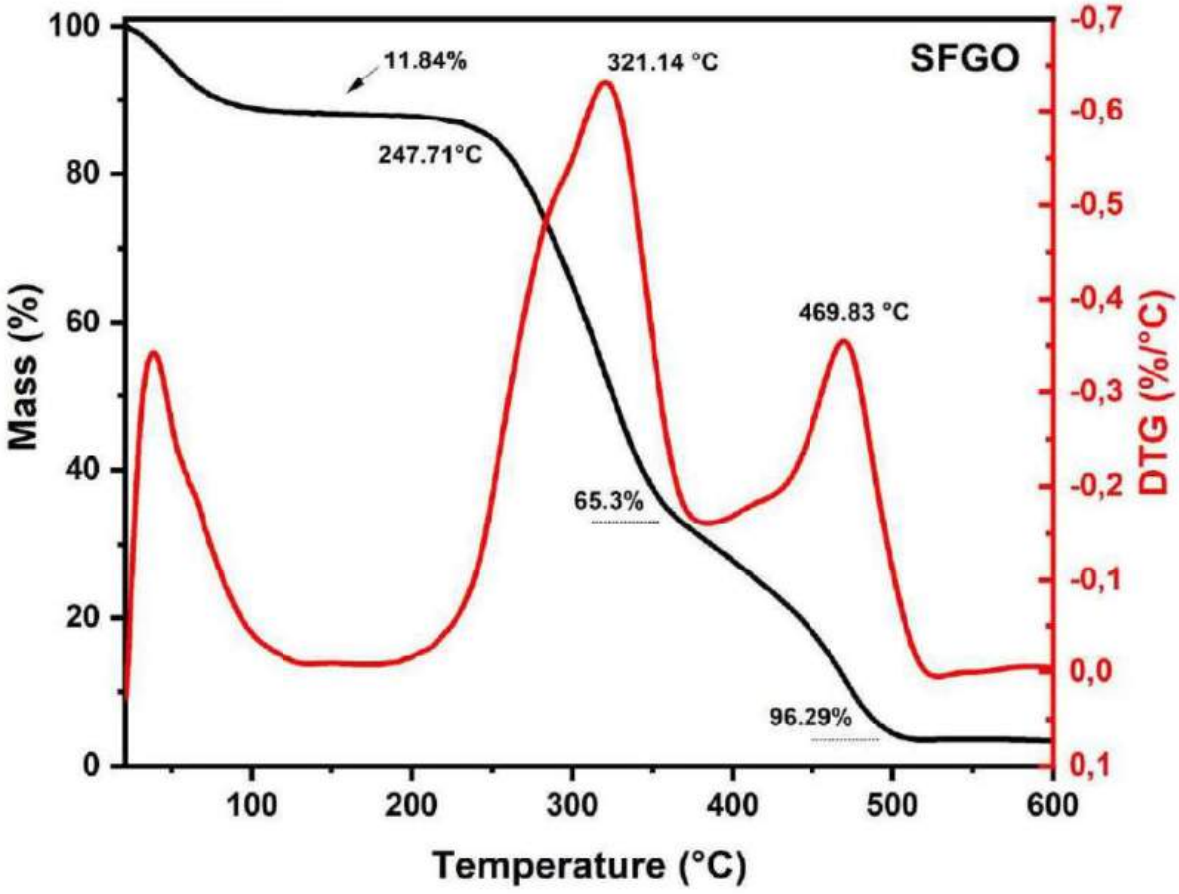

Figura 4.1 – TGA and DTG curves for the sedge fiber coated with GO (SFGO).

However, the T_{onset} for the SF is slightly higher than that of SFGO, and a sudden mass drop is observed from 227 to 357 °C. These temperatures are considered the first limit for the thermal stability of NLFs (FERREIRA et al., 2017; MORIANA et al., 2014; ASYRAF et al., 2021). The maximum degradation rate at 321.14 °C is also related to the

structural components of the fibers, such as lignin and hemicellulose. (SPINACÉ et al., 2009; SANTOS et al., 2007).

Tabela 4.1 – Thermogravimetric parameters for the sedge and piassava fiber coated by GO, as well as the untreated sedge condition.

Functionalization	**M. L. up to 200 °C (%)**	**T $_{onset}$ (°C)**	**T. M. D. R. (°C)**	**M. L. S. S. (%)**	**M. L. at 600 °C (%)**	**References**
SFGO	11.84	247.71	321.14	65.3	65.3	PT*
SF	13.23	255.68	300.95	63.07	66.3	Neuba et al. (2022a)
Piassava	7.3	-	317	-	-	Filho et al. (2020b)

PT = present work; M.L. = Mass Loss; T. = Temperature; D.R. = Degradation Rate; S. S. = Second Stage; M = Maximum

Compared to the SFGO with 321.14 °C, the maximum degradation rate of SF occurs at 300.95 °C. Thus, GO coating improved the maximum rate by around 6.3%, exhibiting higher thermal stability at higher temperatures. It is even higher than the GO coating used in piassava fibers, reported by (FILHO et al., 2020b). Moreover, according to (SARKER et al., 2018), this occurs due to a formation of a carbonaceous shield of GO onto the SF surface. Thus, delaying the degradation and enhancing the thermal stability (OUSHABI et al., 2017; KANNAN; THANGARAJU, 2022; AMIANDAMHEN; MEINCKEN; TYHODA, 2020). Furthermore, the second stage presented a final mass loss equal to 65.3%. Whereas, on the temperature variation between 351 and 512 °C the SFGO presented a mass loss of 96.04%. A DTG peak, in this stage is associated with the lignin decomposition. After this stage, no mass loss and decomposition occured until 600 °C. Remaining only ash.

4.1.2 DIFFERENTIAL SCANNING CALORIMETRY (DSC)

FIG. 4.2 shows the result of the DSC analysis for the SF and SFGO. In this figure, mass loss and heat dissipation start at room temperature (RT). An endothermic peak at 80°C is associated with the GO water desorption and moisture loss of sedge fibers. Thus, confirming that the thermal behavior observed for the TGA is similar, presenting moisture removal until 100 °C. While for the SF condition the peak is observed at 97°C. The peak shift to the left might indicate that the SFGO absorbed less moisture at RT. Therefore, this represents an advantage for the GO functionalization, since the moisture can seriously damage the fiber-matrix interface (CHEN; MIAO; DING, 2009).

It is also observed two exothermic peaks probably associated with the degradation of NLFs constituents. The first at 135 °C might be related to the beginning of lignin

decomposition and part of the cellulose I degradation (BOURMAUD et al., 2018; MANIMARAN et al., 2021; SHAPCHENKOVA et al., 2022). The peak observed at 342°C can be due to the degradation of α cellulose and hemicellulose (SEKI et al., 2013). A last one at 466 °C, not shown in FIG. 4.2, is reported to be associated with the lignin decomposition and part of cellulose I decomposition (NARAYANASAMY et al., 2020). Beyond 400 °C, the curve continues to travel in the endothermal region due to the volatilization of lignin and wax (FU; SONG; LIU, 2017).

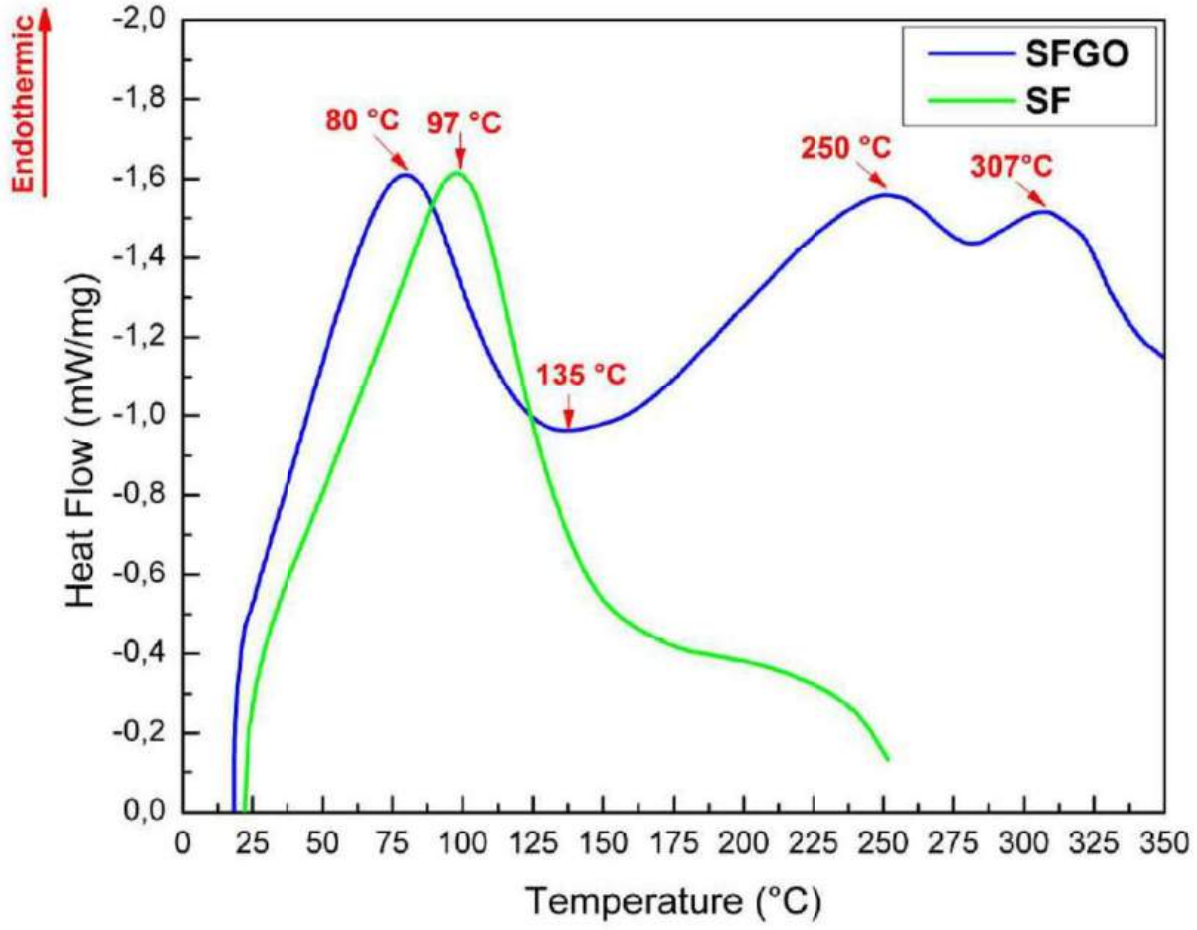

Figura 4.2 – DSC curve for unfunctionalized sedge fiber (SF) and GO functionalized sedge fiber (SFGO).

4.1.3 FOURIER TRANSFORM INFRARED SPECTROSCOPY (FTIR)

The FTIR spectrum of the SFGO is shown in FIG. 4.3, while typical functional groups and IR signals with possible sources are listed in TAB. 4.2. It was possible to observe the changes in the spectra, even at a low concentration of the GO coating. Furthermore, some intensities between some bands are not the same for the SF spectra. This might be associated with the GO molecule linkage to the functional groups of the fiber, changing the intensities of the spectrum. An absorption band appears at 3430 cm^{-1}, which is attributed to the axial vibration of hydroxyl groups of the cellulose (NEUBA et al., 2020)

and functional groups present in the GO nanosheet structures (CHAIYAKUN et al., 2012). Besides, the presence of GO in SF induced an increase in the intensity of this band, due to the stretch that GO also presents. While the band found at 2923 cm^{-1} for the SF is now absent and refers to the vibration of CH2 and CH3 molecules of the organic structure of NLFs. According to (NEUBA et al., 2020), the small amplitude of this band might justify a low interfacial interaction with polymer matrices. However, the band at 2361 cm^{-1} is assigned to the stretching vibration of CO2 (LI et al., 2020). The band at 1637 cm^{-1} is related to C=O. The band at 1368 cm^{-1} belong to CH curvature of polysaccharides (LIU et al., 2012). Whereas, the band at 1254 cm^{-1} to the C-O and C-C bonds. There is the C-O-C asymmetrical stretching at 1119 cm^{-1} (LIU et al., 2012) The bands at 1030 and 446 cm^{-1} to C-O and C-C strain of the respective covalent bonds. At last, these bands confirm that there is an abundance of oxygen-containing groups available for GO.

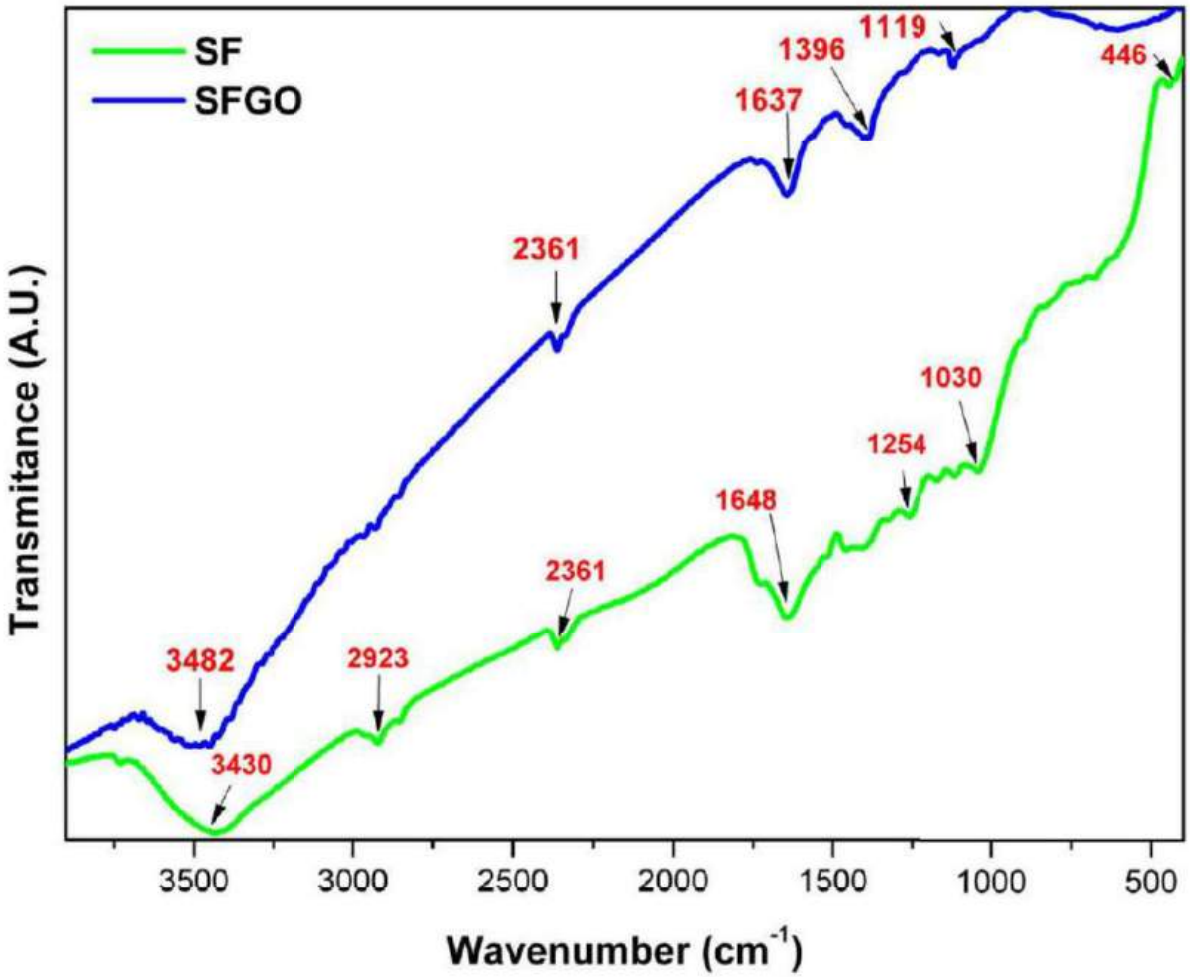

Figura 4.3 – FTIR spectra of unfunctionalized sedge fiber (SF) and GO functionalized sedge fiber (SFGO).

Tabela 4.2 – Bands with vibrational modes assigned to the FTIR spectrum of SFGO and SF

Sample	Wavenumber (cm^{-1})	Vibration Type
SF	3430	- Axial vibration of O-H
	2923	- CH2 and CH3
	2361	- CO2 stretching
	1648	- C=O
	1254	- C-O and C-C
	1030	- C-O
	446	- C-C
SFGO	3482	- Axial vibration of O-H
	2361	- CO2 stretching
	1637	- C=O
	1119	- C-O-C asymmetrical stretching

4.1.4 X-RAY DIFFRACTION (XRD)

The diffractogram plot for the SFGO is present in FIG. 4.4, while TAB. 4.3 highlights the peaks, crystallite size and crystallinity index of SFGO. As reported in the literature (LIU et al., 2012), one might expect that the presence of GO on the surface of the sedge fibers reduces the crystallinity index due to the amorphous character of GO. Furthermore, it is possible to observe a peak at 16.13° related to cellulose I which has not been found previously in the literature (NEUBA et al., 2020) for the SF. At last, an increase in the CS of SFGO was noticed, which favors the resistance to moisture absorption and chemical reactivity of the fiber (ARTHANARIESWARAN; KUMARAVEL; SARAVANAKUMAR, 2015).

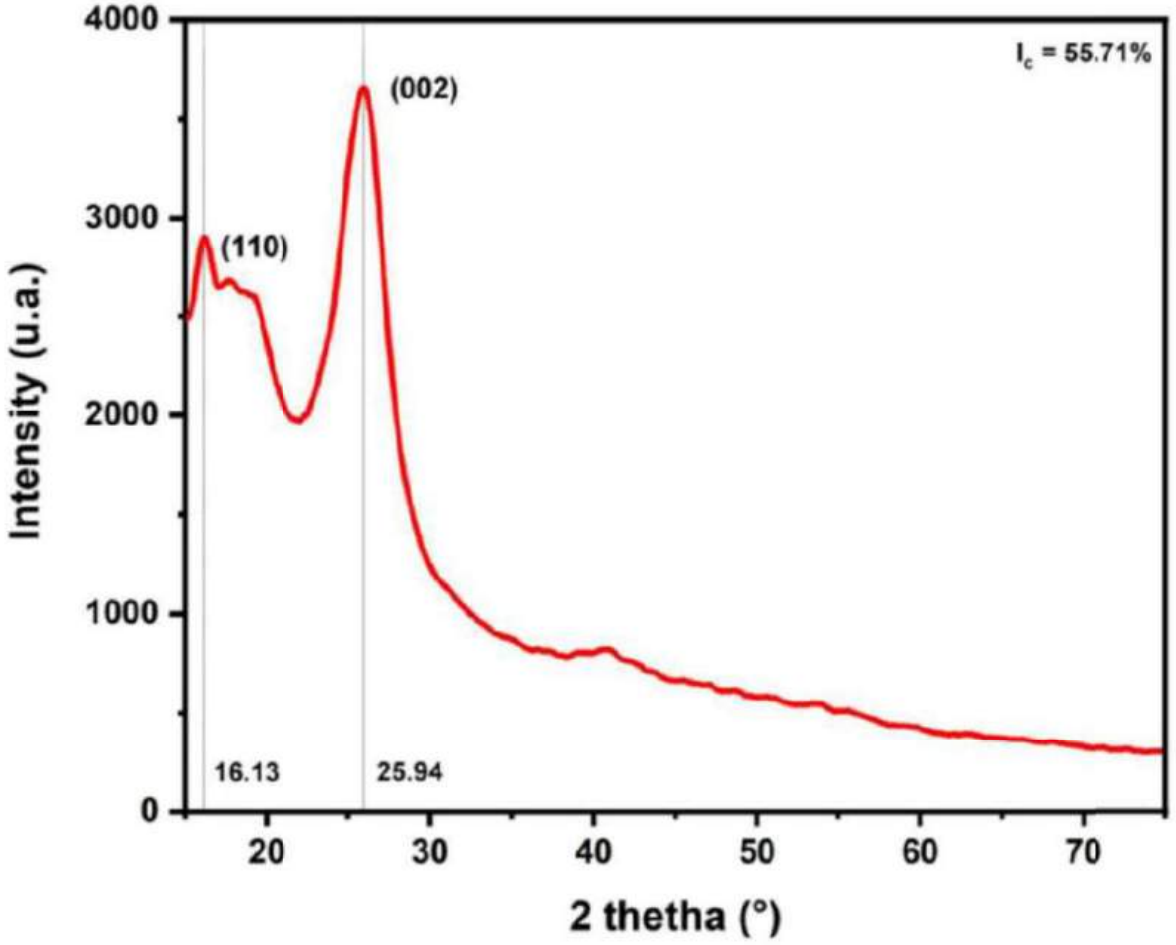

Figura 4.4 – XRD diffractogram pattern of GO functionalized sedge fiber (SFGO).

Tabela 4.3 – Crystallite size (CS), crystallinity index (CI) and peaks of the untreated and coated by GO sedge fibers.

Treatments	**Cellulose I peak (2θ)**	**Amorphous halo (2θ)**	**Cellulose IV peak (2θ)**	**CI (%)**	**CS (nm)**	**References**
SJGO	16.13	18.10	25.63	62.47	3.36	PT*
SF	-	17.95	25.94	55.71	2.56	Neuba et al. (2020)

PT = Present Work.

4.1.5 SCANNING ELECTRON MICROSCOPY (SEM)

FIG. 4.5 shows SEM images of SFGO (FIG. 4.5 d to f) and SF (FIG. 4.5 a to c). The thinner presence of GO coating on the surface of the sedge fibers was able to reduce the roughness. Although, according to (CHEN et al., 2018) the GO sheets attached on the surface of the natural fiber have led to an increase in the surface roughness, which is useful to improve the interfacial adhesion. Indeed, the aspect of the GO flakes were agglomerated

and wrinkled, diverging from the present plain nor agglomerated aspect observed. On the other hand (SILVEIRA et al., 2022; LUZ et al., 2022) have presented morphological evidences that the GO coating was similar to the SFGO, showing a more uniform and evenly coated fiber surface. Therefore, may be due to chemical bonding provided by the functional groups of GO.

Moreover, at greater magnifications it could be seen some cracks in the GO coating which are not observed on the surface of plain sedge fibers, as depicted in FIG. 4.5. Confirms the presence of the GO coating. In FIG. 4.5, it could be observed that the amorphous content present on the fiber is not removed. Actually, the removal only occurs with chemical treatments, such as alkali. Whereas, in FIG. 4.5 its possible to observe an agglomeration of the nanomaterial.

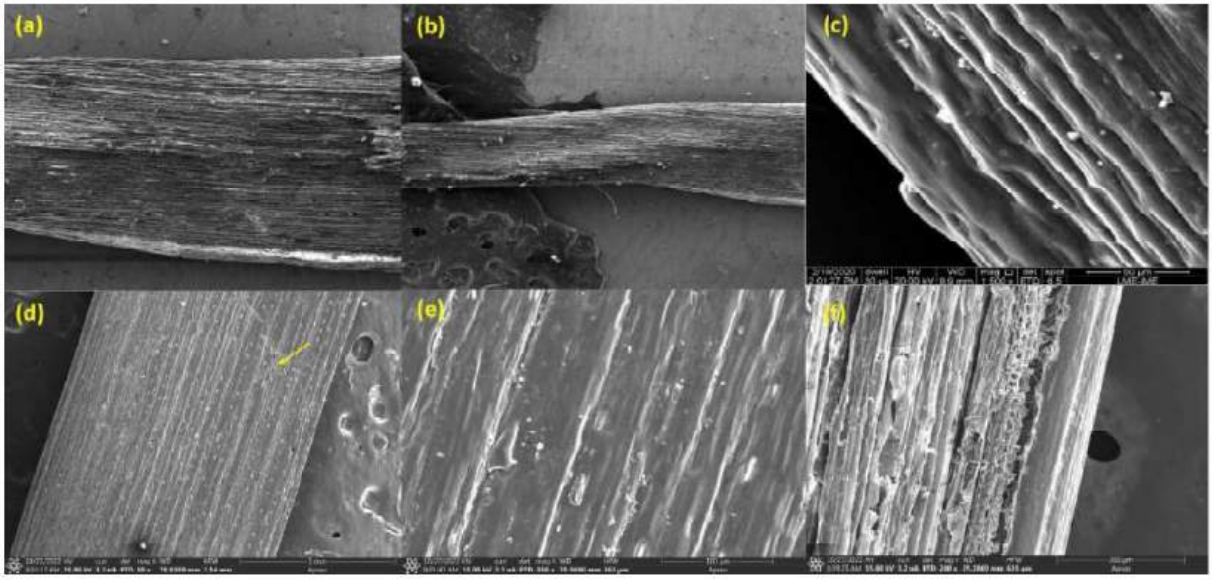

Figura 4.5 – SEM images of: untreated sedge fibers (a) to (c); (d) to (f) sedge fibers coated by GO.

4.2 ALKALIZED SEDGE FIBERS

4.2.1 THERMOGRAVIMETRIC ANALYSIS (TGA/DTG)

FIG. 4.6 to 4.8 and TAB.4.4 depict the results of TGA and first-order derivative analysis (DTG) for the sedge fibers treated with NaOH concentrations of 3%, 5%, and 10% for 24, 48, and 72 h.

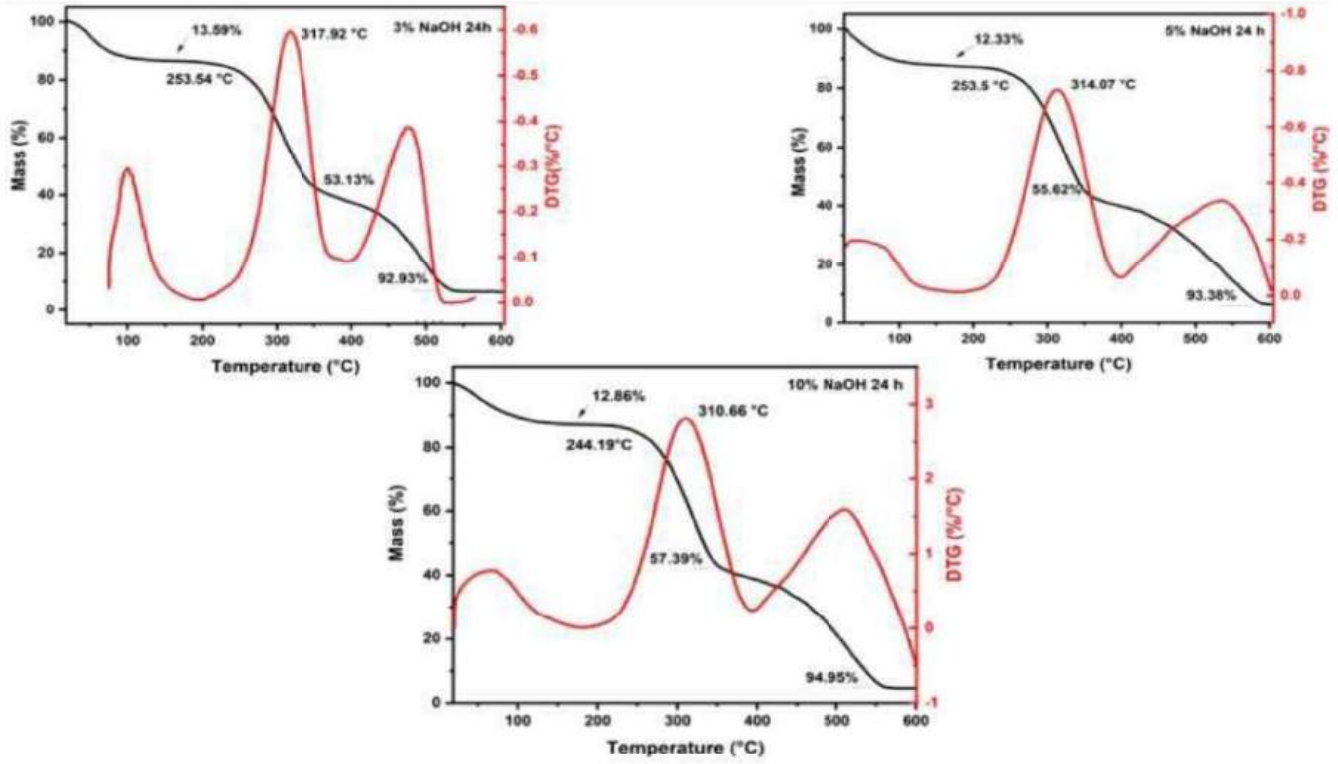

Figura 4.6 – TGA and DTG curves for all the concentrations immersed in a NaOH solution for 24 h.

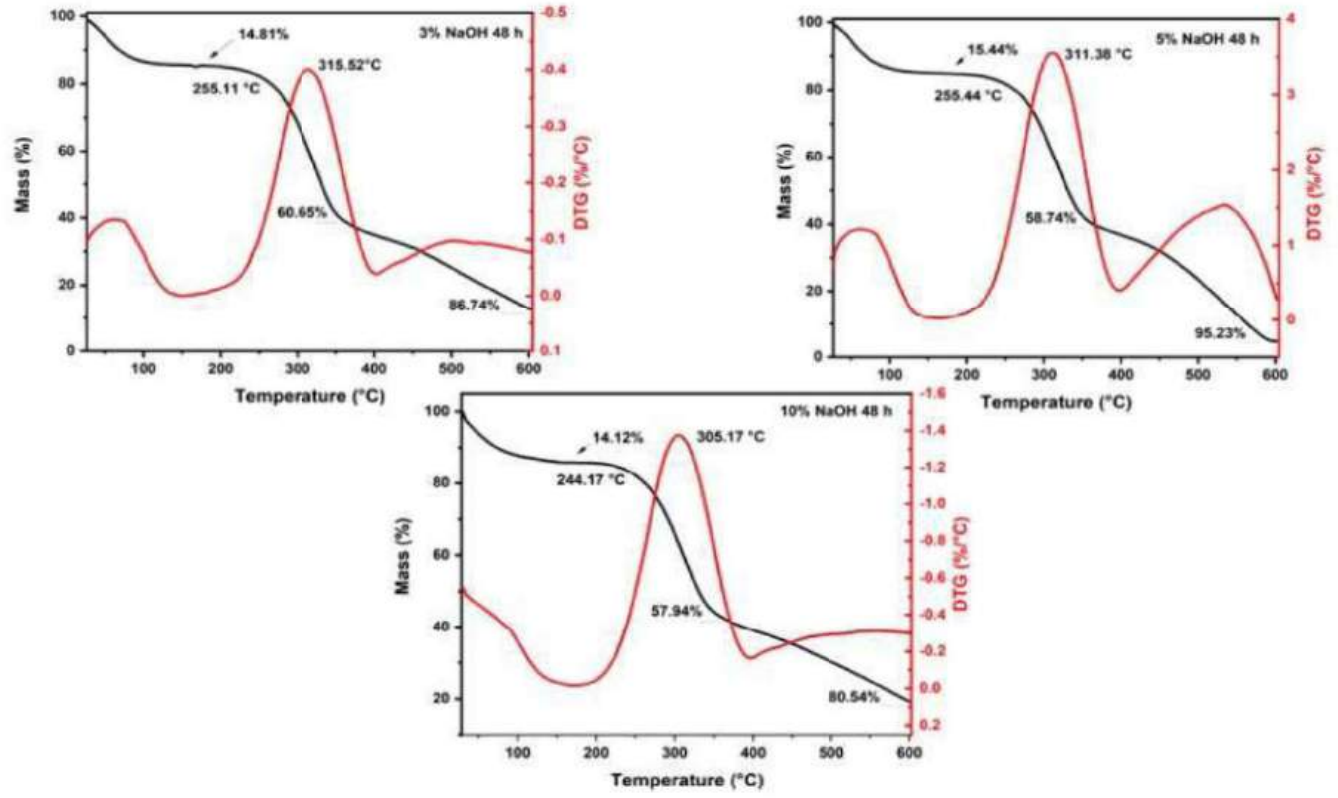

Figura 4.7 – TGA and DTG curves for all the concentrations immersed in a NaOH solution for 48 h.

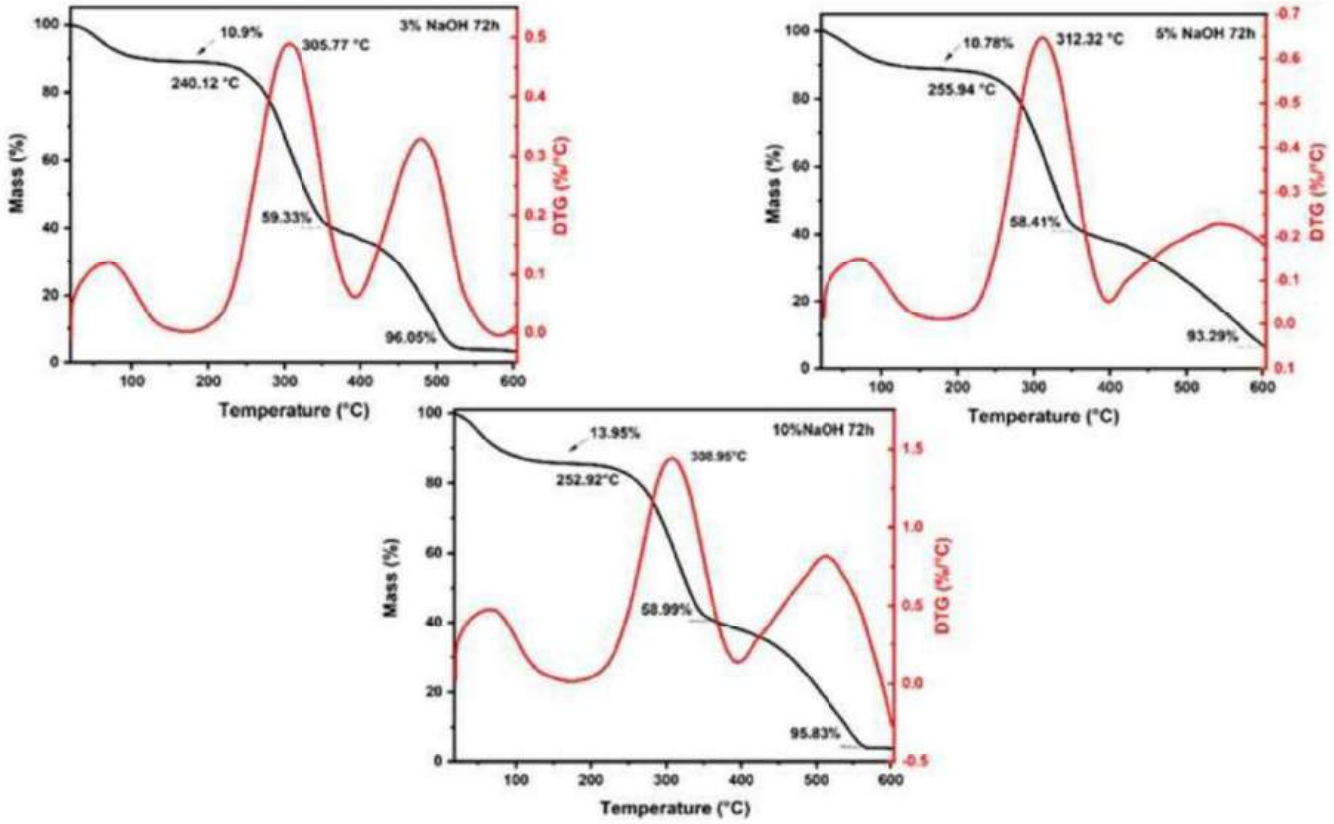

Figura 4.8 – TGA and DTG curves for all the concentrations immersed in a NaOH solution for 72 h.

Tabela 4.4 – Thermogravimetric parameters for all the concentrations immersed in a NaOH solution for 24, 48, and 72 h.

Conditions		Mass Loss			Initial Degradation (°C)	Maximum Degration Rate (°C)
		Up to 200 °C (%)	At the end of the Second Stage (%)	At 600 °C (%)		
24 h	3%	13.59	53.13	92.93	253.54	317.92
	5%	12.33	55.62	93.38	253.5	314.07
	10%	12.86	57.39	94.95	244.19	310.66
48 h	3%	14.81	60.65	86.74	255.11	315.52
	5%	15.44	58.74	95.23	255.44	311.38
	10%	14.12	57.94	80.54	244.17	305.17
72 h	3%	10.9	59.33	96.05	240.12	305.77
	5%	10.78	58.41	93.29	255.94	312.32
	10%	13.95	58.99	95.83	252.92	308.95
∗ Untreated		13.23	63.07	96.04	255.68	300.95

∗(NEUBA et al., 2022a).

It could be observed that the fiber mass losses for all treatments at temperatures up to 200 °C were around 12%, due to the evaporation of the moisture content on the surface of the fibers. The untreated sedge fibers have shown a mass loss of 13.23% (NEUBA et al., 2022a), which was higher than the mass losses of the fibers treated with 5% and 10% of NaOH for 24 h, lower than the mass loss of the fibers treated with all three NaOH concentrations for 48 h, and only slightly lower than the mass loss of the fibers treated with 10% NaOH for 72 h. This can be associated with a higher percentage of the hemicellulose content that allows the fibers to retain more moisture (ISMAIL et al., 2021). The alkali treatment eliminated some proportion of hemicellulose and lignin; thus, the fibers tended to absorb less moisture on their surface (KATHIRSELVAM et al., 2019).

The T_{onset} values found for 24, 48 and 72 h of the sedge-treated fibers were slightly lower when compared to those of the untreated fibers. As for the maximum rate, all treatments presented to be slightly higher, indicating higher thermal stability at higher temperatures. Furthermore, it could be observed that in all treated fiber concentrations the hemicellulose content was decomposed within a range of 240–360 °C. This behavior is in accordance with other reports in the literature (ISMAIL et al., 2021).

The sudden mass drop starting at the T_{onset} region resulted in mass losses around 58% for all NaOH concentrations of 3%, 5%, and 10%. The untreated sedge fiber showed a slightly higher mass loss, indicating that the treated fibers presented better thermal stability at higher temperatures. The third stage ranged from 300 to 590 °C for all the treated sedge fibers and resulted in a total mass loss around 95% for the 3%, 5%, and 10% NaOH concentrations. The final mass loss occurred at higher temperatures for the treated fibers when compared to that found for the untreated sedge fibers at 496 °C. Further, after this range, no degradation and mass loss occurred until the end of the test at 600 °C, due to the ash content present.

It is extensively known that the final stage of degradation is directly associated with the elimination of lignin, within a range of 560–580 °C for all conditions. Observing all the treatments for different durations of time, it can be noted that the treatments related to 3% NaOH for 24 h and 48 h exhibited better thermal stability properties. Furthermore, the group treated with 3% NaOH for 48 h showed that the lignin present did not fully decompose. For this reason, it can be selected for its use as a reinforcement for composites. Furthermore, previous results incorporating untreated sedge as a reinforcement for an epoxy matrix showed that the composites disclosed poor thermal stability when compared to the neat epoxy (NEUBA et al., 2020). This reason is due to the fact that natural fibers present a lower thermal stability and influence the thermal behavior of the composites. Therefore, it is expected that the novel composites reinforced by alkali-treated sedge present a higher thermal stability.

4.2.2 DIFFERENTIAL SCANNING CALORIMETRY (DSC)

DSC plots of treated sedge fibers shown in FIG.4.9 helped to support the degradation of cellulose compound previously witnessed in TGA curves. The endothermic peak noticed ranging from 69 to 75 °C is related to the thermal energy required for the vaporization content present in the fiber surface (KATHIRSELVAM et al., 2019). Then, it was observed that the exothermic peak ranging from 334 to 334 °C relates to the degradation of α cellulose and hemicellulose. Further, the curves continued to travel in the endothermal region beyond 400 °C due to the volatilization of lignin and wax. As usual, the lignin compound in fiber started to decompose at a temperature range of 280 to 520 °C (FU; SONG; LIU, 2017), which was observed in this thermal event on the endothermal regions of the curves. At temperatures beyond 600 °C, the curves continued to swing toward the exothermic region due to the breakdown of some chemical compounds in hemicellulose and lignin deposits (KATHIRSELVAM et al., 2019).

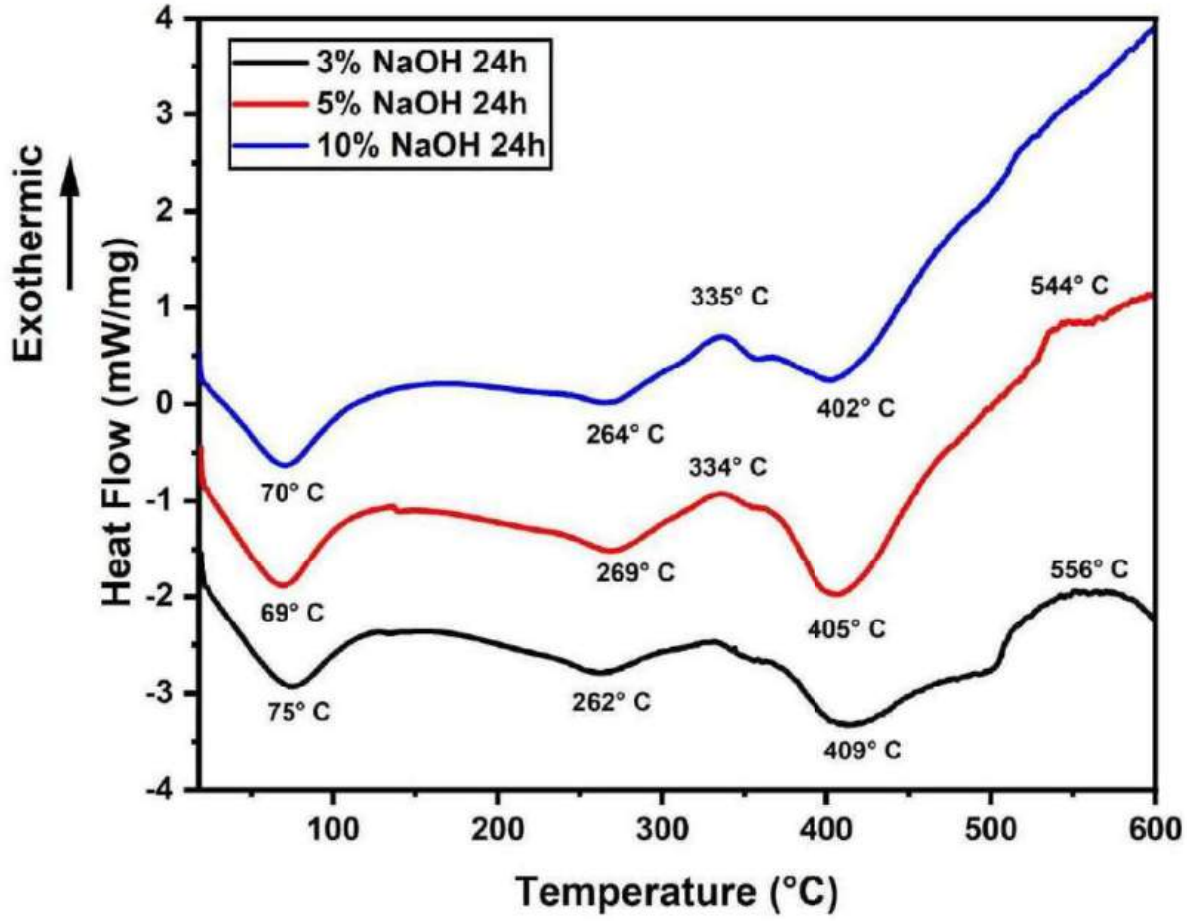

Figura 4.9 – DSC curves for all the concentrations immersed in a NaOH solution for 24 h.

The endothermic peak noticed ranging from 81 to 92 °C in FIG.4.10 is related to the thermal energy required for the vaporization content present in the fiber surface (KATHIRSELVAM et al., 2019). Further, the curves continued to travel in the endothermal

region up to the temperature range of 256 to 86 °C due to the volatilization of lignin and wax. Then, it was observed that the exothermic peak ranging from 338 to 354 °C related to the degradation of α cellulose and hemicellulose (SEKI et al., 2013). At temperatures beyond 400 °C, only the curve under a 10% NaOH solution condition continued to swing toward the exothermic region due to the breakdown of some chemical compounds in hemicellulose and lignin (KATHIRSELVAM et al., 2019).

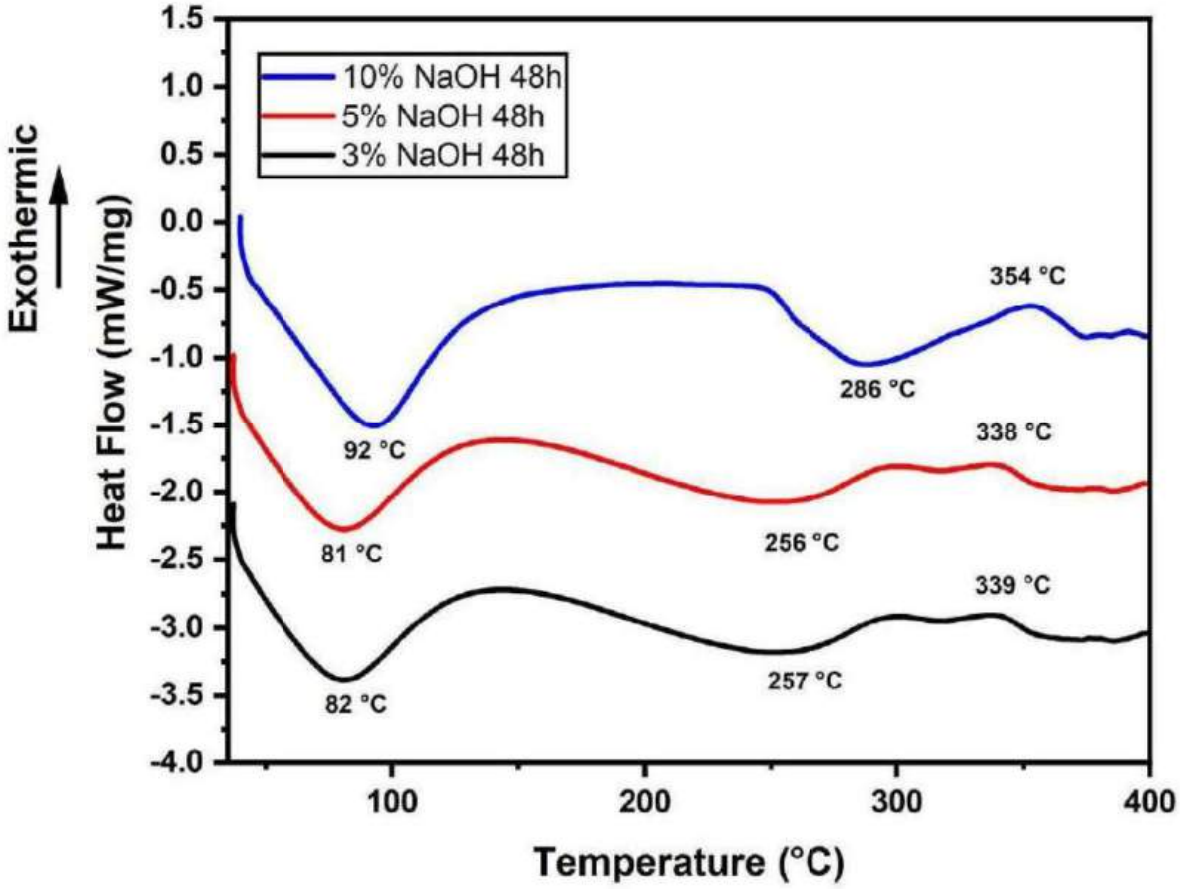

Figura 4.10 – DSC curves for all the concentrations immersed in a NaOH solution for 48 h.

The endothermic peak noticed ranging from 69 to 72 °C in FIG.4.11 is related to the thermal energy required for the vaporization content present in the fiber surface (KATHIRSELVAM et al., 2019). Further, the curves continued to travel in the endothermal region up to the temperature range of 261–274 °C due to the volatilization of lignin and wax. Then, it was observed that the exothermic peak ranging from 331 to 362 °C related to the degradation of α cellulose and hemicellulose (SEKI et al., 2013). At temperatures beyond 400 °C, the curves continued to swing toward the exothermic region due to the breakdown of some chemical compounds in hemicellulose and lignin deposits (KATHIRSELVAM et al., 2019).

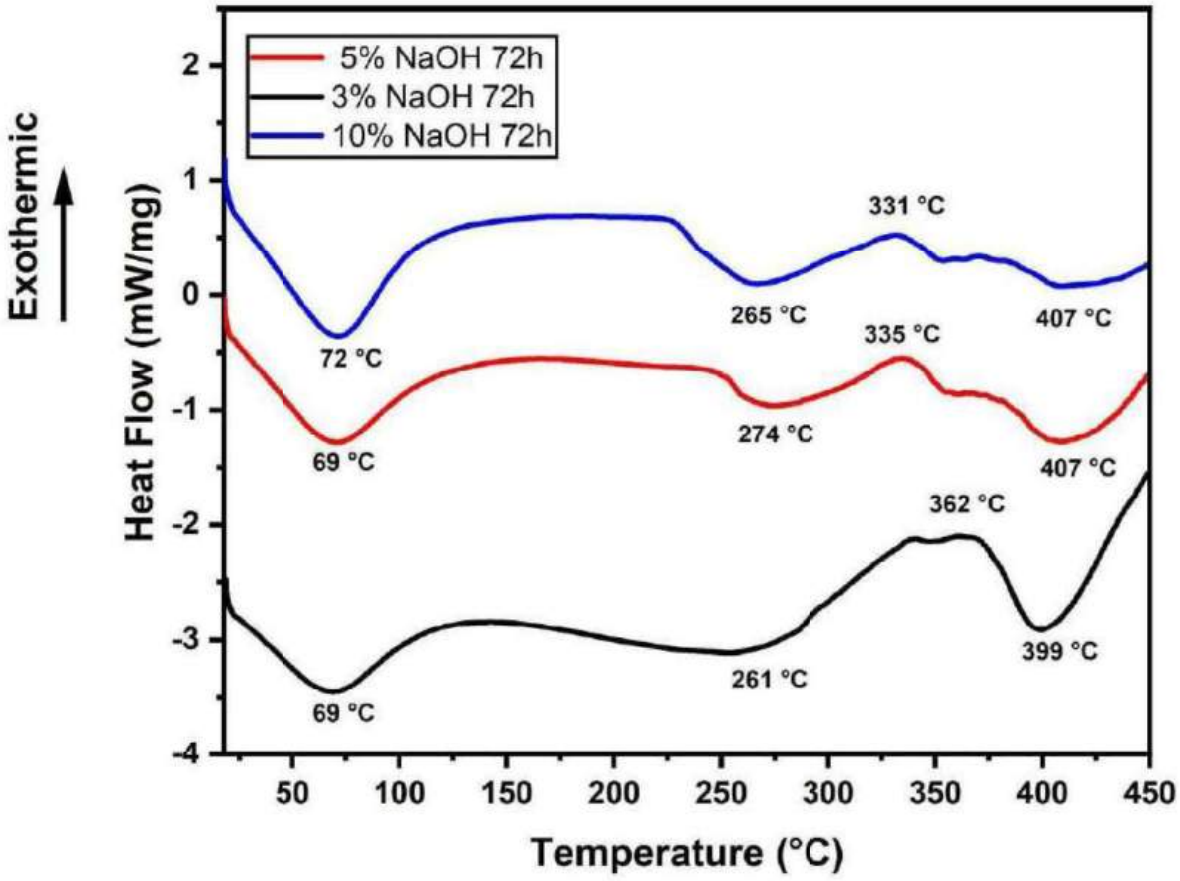

Figura 4.11 – DSC curves for all the concentrations immersed in a NaOH solution for 72 h.

Comparing all the tests, the sedge fibers treated with NaOH at a concentration of 3% obtained low values of the thermal curves when compared with those treated with 5% and 10% NaOH. In addition, the untreated fibers showed lower values than those with the 3% NaOH treatment (NEUBA et al., 2022a). Under the time of 48 h, better thermal stability with a decay of the thermal curves was shown for all treatment conditions.

4.2.3 FOURIER TRANSFORM INFRARED SPECTROSCOPY (FTIR)

FIG. 4.12 illustrate the FTIR spectra of NaOH treated sedge fibers within the range of 4000 to 400 cm^{-1}. The region at 3453 to 3489 cm^{-1} indicates bands of O-H functional groups in cellulose. The band at 2915 to 2915 cm^{-1} is identified as the C-H stretching of cellulose (VENUGOPAL; BOOMINATHAN, 2022), and the peak at 2366 cm^{-1} is assigned to the bond between organic molecules and wax compounds in the fiber surface (KATHIRSELVAM et al., 2019). The common peak under all conditions at 1641 cm^{-1} is related to C=O aromatic groups in the lignin component present in the sedge fibers (CHEN et al., 2021). The band at 1381 to 1381 cm^{-1} can be related to the CH_3 symmetric bending according to (D'APUZZO et al., 2021). The band at 1119 cm^{-1} is

associated with C-O stretching vibrations, and the band at 674 cm^{-1} is related to C-C stretching. It could be stated that the treatment in the conditions investigated was not enough to reduce the content of hemicellulose and lignin, although the peak related to wax content was absent at the 10% NaOH treatment.

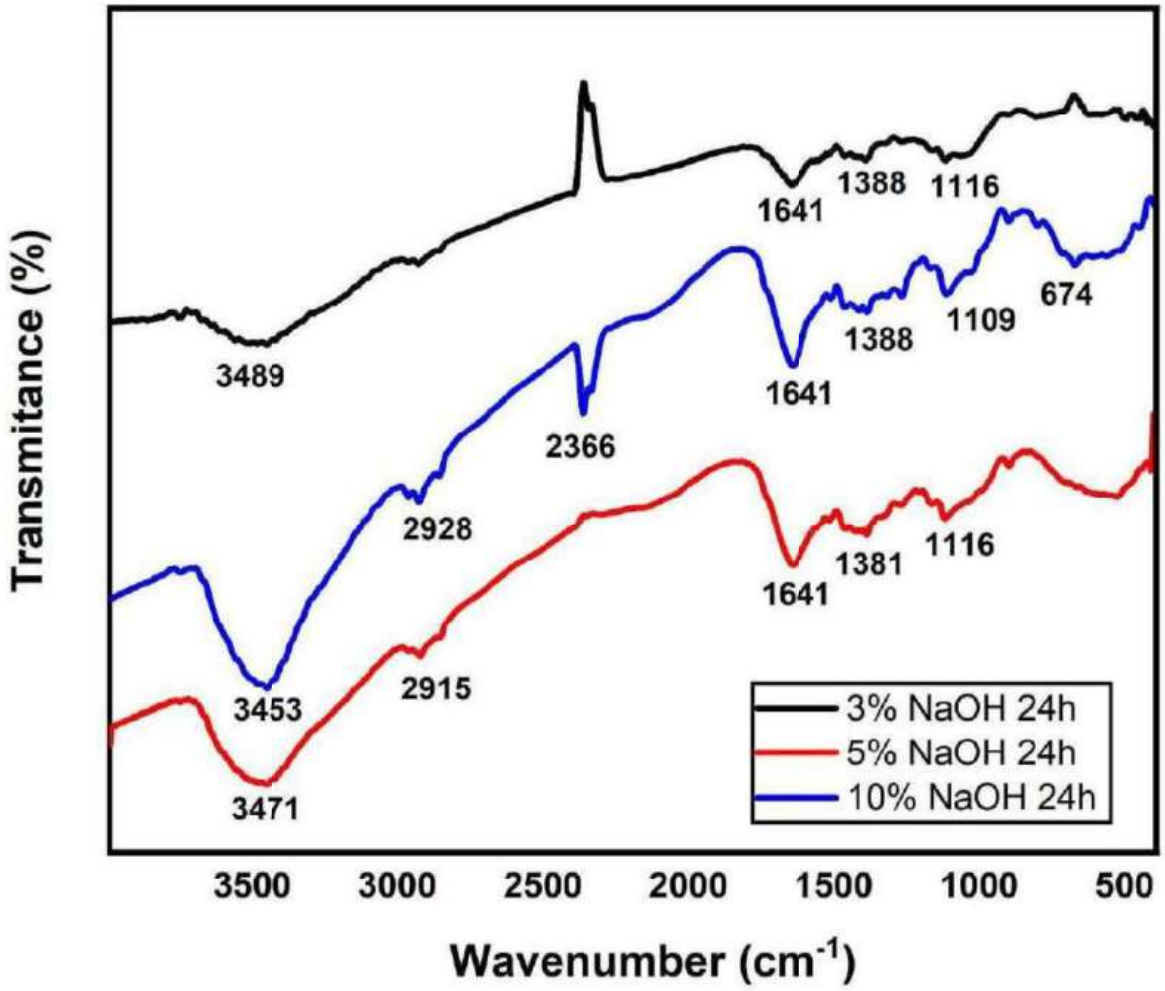

Figura 4.12 – FTIR spectra for all the concentrations immersed in a NaOH solution for 24 h.

In FIG.4.13, the region at 3452 to 3482 cm^{-1} indicated bands of O-H functional groups in cellulose. The band at 2361 to 2367 cm^{-1} is assigned to the bond between organic molecules and wax compounds in the fiber surface, which is almost absent for the 5% NaOH condition (KATHIRSELVAM et al., 2019). The peak at 1638 to 1649 cm^{-1} is related to C=O aromatic groups in lignin and hemicellulose components present in the sedge fibers (CHEN et al., 2021). It can be noted that the treatment for 24 h resulted in a strong presence of lignin and hemicellulose, which was shown in lower NaOH concentrations for 48 h. The band at 1384 to 1390 cm^{-1} can be related to the CH_3 symmetric bending according to (D'APUZZO et al., 2021). The band at 1119 to 1125 cm^{-1} is associated with C-O stretching vibrations, and the band at 664 to 955 cm^{-1} is related to the C-C

stretching. It could be stated that the treatment in the conditions investigated was not enough to reduce the content of hemicellulose and lignin, although the conditions of 24 h presented stronger peaks related to the C=O aromatic groups.

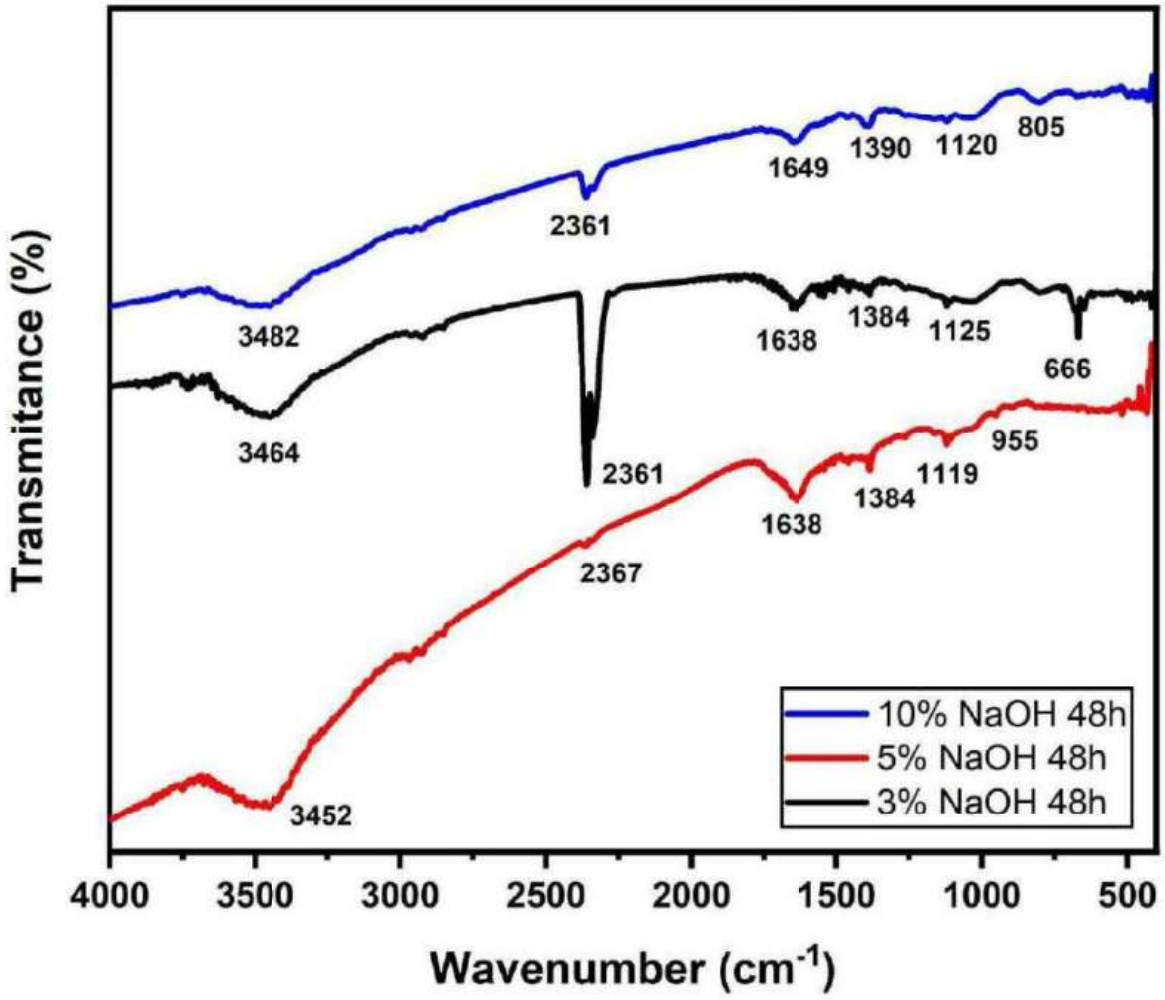

Figura 4.13 – FTIR spectra for all the concentrations immersed in a NaOH solution for 48 h.

In FIG.4.14, the region at 3456 to 3483 cm^{-1} indicated bands of O-H functional groups in cellulose. The band at 2921 to 2927 cm^{-1} is identified as the C-H stretching of cellulose (KATHIRSELVAM et al., 2019), and the peak at 2360 cm^{-1} is assigned to the bond between organic molecules and wax compounds in the fiber surface (KATHIRSELVAM et al., 2019). The peak at 1644 cm^{-1} is related to C=O aromatic groups in lignin and hemicellulose components present in the sedge fibers (CHEN et al., 2021). It can be noted that the conditions treated for 24 h had a strong presence of lignin and hemicellulose, which was shown in lower concentrations for 72 h. The band at 1381 to 1386 cm^{-1} can be related to the CH_3 symmetric bending according to d'Apuzzo et al. (2021). The bands at 1111 to 1117 cm^{-1} and 1034 cm^{-1} are associated with C-O stretching vibrations, and the band at 664 to 955 cm^{-1} is related to the C-C stretching. It could be stated that

the treatment in the conditions investigated was not enough to reduce the content of hemicellulose and lignin, although the conditions of 24 h presented stronger peaks related to the C=O aromatic groups.

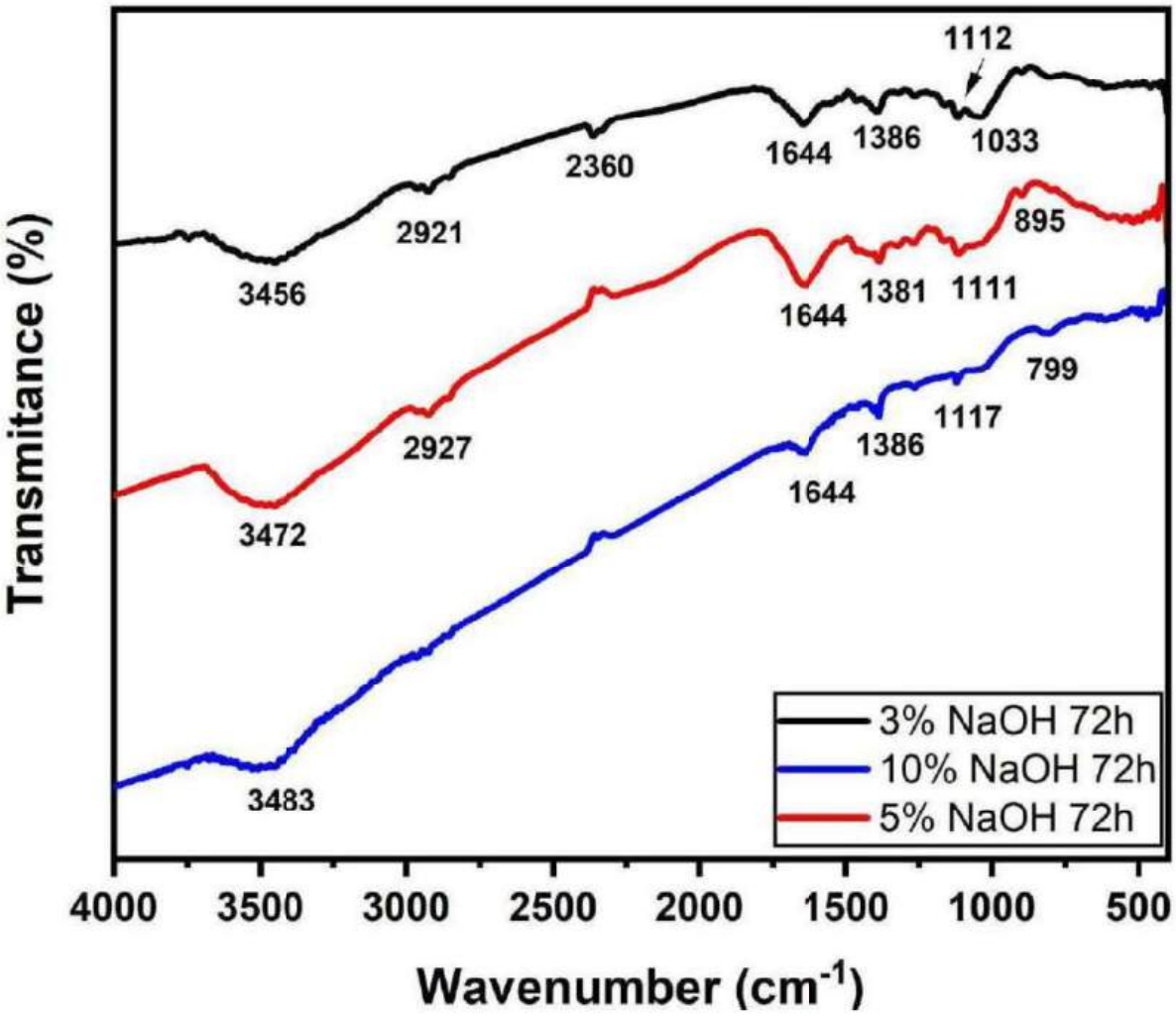

Figura 4.14 – FTIR spectrum for all the concentrations immersed in a NaOH solution for 72 h.

For all treatments of different percentages and times, the disappearance of the 1731 cm^{-1} band stood out in comparison with the untreated fiber (NEUBA et al., 2020). This band is associated with the stretching of ester and carboxyl groups (C-O compound) present in hemicellulose; this band vanished during the NaOH treatment, indicating the removal of hemicellulose (KATHIRSELVAM et al., 2019).

4.2.4 X-RAY DIFFRACTION (XRD)

In TAB.4.5 highlights the peaks, the crystallite sizes, and the crystallinity indices of the untreated and treated sedge fibers. The peak (1 1 0) is attributed to a reflection of the crystalline structure in cellulose I, while the halo of (1 0 1) reflection is associated with

the amorphous region composed of lignin and hemicellulose structures (KATHIRSELVAM et al., 2019). The reflection of (0 0 2) is related to the cellulose IV fraction (VENUGOPAL; BOOMINATHAN, 2022). After the alkali treatment, it can be noticed that for some conditions the peak at (1 1 0) appeared. However, the amorphous halo was present. This might indicate that a significant amount of lignin and hemicellulose remained, although they were partially removed. In addition, this condition was the only one presenting an increase in the fraction of crystalline cellulose, as shown in the diffractogram in FIG.4.15, due to the removal of low-molecular-weight hemicellulose, wax, and lignin compounds as a result of NaOH treatment (VENUGOPAL; BOOMINATHAN, 2022). On the other hand, under all conditions, an increase in the crystallite size was presented, which was caused by the swelling of the cellulose chain with Na. It also penetrated the crystal lattice and reacted with the OH group after breaking the hydrogen bonds and producing the cellulose alkali complex (KUNUSA et al., 2018). Although the increase in crystallite size favored resistance to moisture absorption and chemical reactivity of sedge fibers (KATHIRSELVAM et al., 2019), a higher concentration of NaOH could lower the content of α cellulose since strong degradation occurred by intracrystalline swelling (KUNUSA et al., 2018). This could be the reason why most conditions had a lower crystallinity index. The results in TAB.4.5 were in contrast with this hypothesis, because all the other NLFs presented an increase in the crystallinity index as a function of crystallite size. Possibly in the case of the sedge fibers, the treatment might be too strong, so it damaged the microstructure.

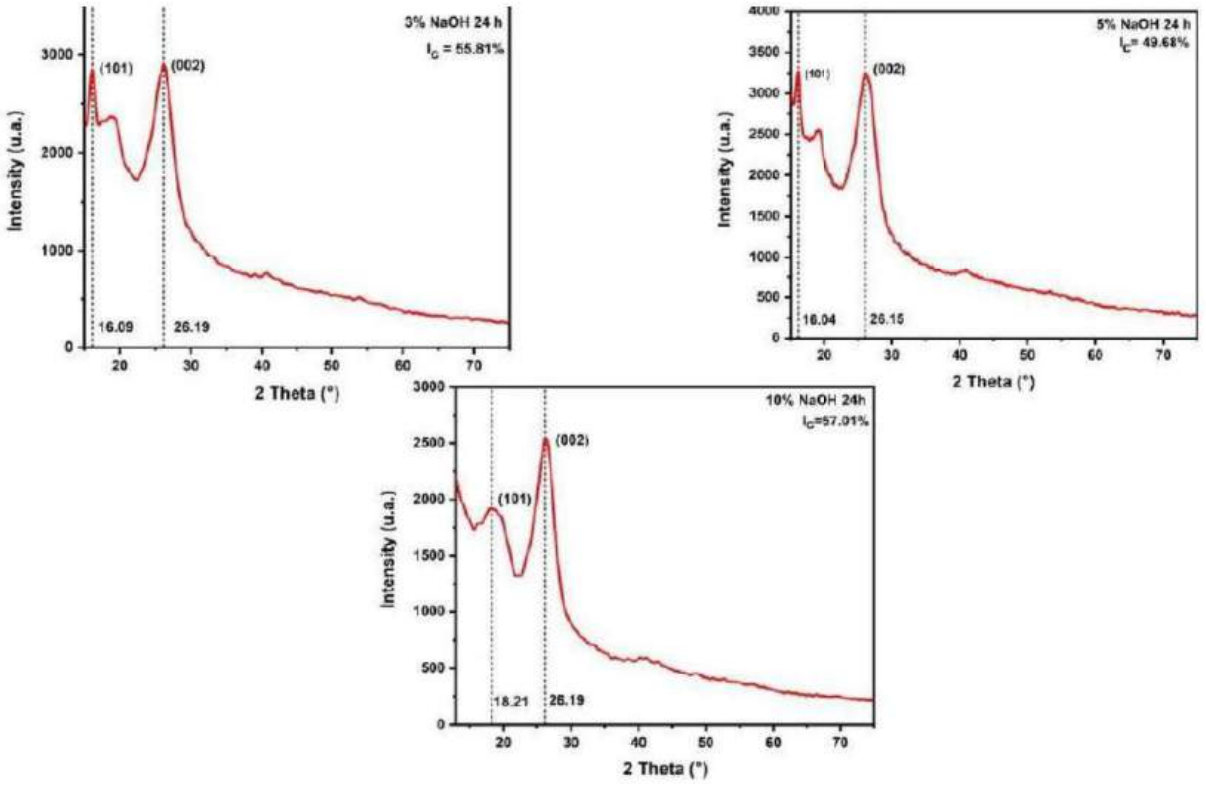

Figura 4.15 – XRD diffractograms regarding a concentration immersed in a 3% NaOH solution for all periods of time.

Tabela 4.5 – Crystallite sizes (CS) and crystallinity index (CI) of the untreated and alkali-treated sedge fibers, as well as other NLFs.

Treatments	**CI (%)**	**CS (nm)**	**References**
Raw *Pongamia pinnata L.*	45.31	5.43	(UMASHANKARAN; GOPALAKRISHNAN, 2021)
Alkalized *Pongamia pinnata L.*	52.43	8.43	(UMASHANKARAN; GOPALAKRISHNAN, 2021)
Raw banyan Fiber	72.47	6.28	(GANAPATHY et al., 2019)
Alkalized banyan banyan fiber	76.35	7.74	(GANAPATHY et al., 2019)
Raw ACF	27.5	4.17	(VENUGOPAL; BOOMINATHAN, 2022)
Alkalized ACF	35.6	6.43	(VENUGOPAL; BOOMINATHAN, 2022)
Untreated sedge fibers	62.47	2.56	(NEUBA et al., 2022b)
Alkali Treatments	**CI (%)**	**CS (nm)**	**References**
24 h 3%	55.81	3.75	PT
24 h 5%	49.68	3.43	
24 h 10%	57.01	3.44	
48 h 3%	66.50	10.66	
48 h 5%	51.24	4.09	
48 h 10%	39.40	6.84	
72 h 3%	57.21	3.66	
72 h 5%	52.71	3.68	
72 h 10%	56.40	3.89	

PT = present work

4.2.5 SCANNING ELECTRON MICROSCOPY (SEM)

SEM images for the alkali-treated fibers are shown in FIG.4.16 eand FIG.4.17. FIG.4.16 depicts the untreated and treated fibers with 3% NaOH in different periods of time. It is clear that not much hemicellulose, wax, impurities, and lignin existed in FIG.4.16a,b. These contents impaired the interfacial bonding characteristics of the fiber during composite formation. In contrast, in micrographs in FIG.4.16d–f, it is possible to visualize the amorphous content on the surface of the fibers. Additionally, lignin and hemicellulose were bonded as glues on a microfibril in FIG.4.16e. In other words, this

amorphous content played a role of a matrix phase for this natural (MONTEIRO et al., 2011). Another evidence that the alkali treatment modified the fibers is the void present in FIG.4.16b. It was occasioned by the removal of the amorphous phase, indicating the strength of the fibers might reduce significantly.

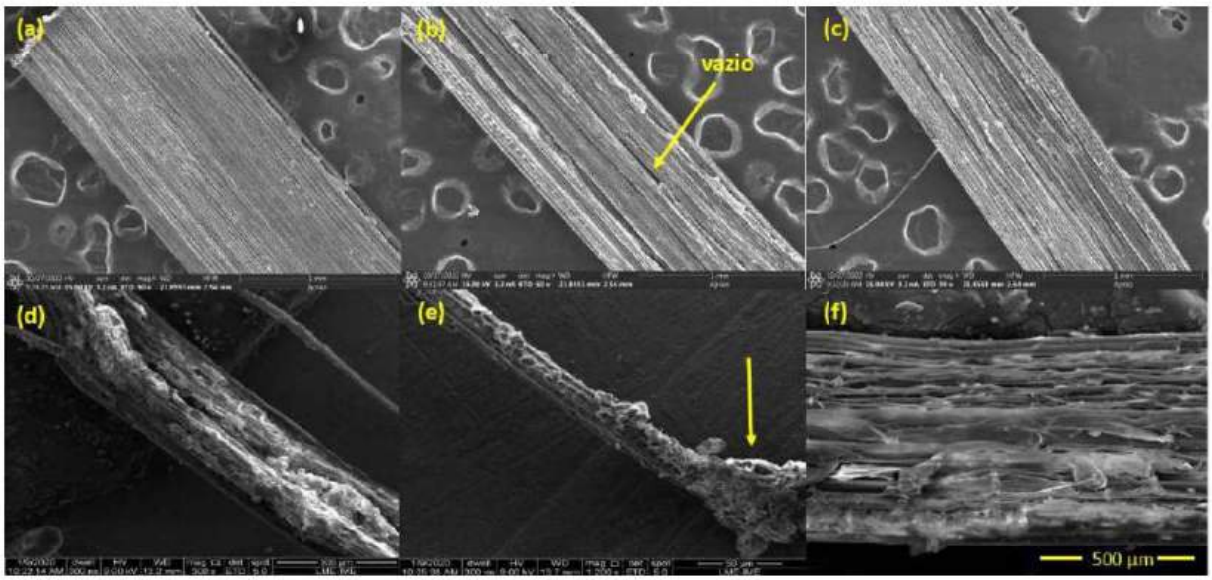

Figura 4.16 – SEM images of alkali-treated fibers in a NaOH concentration of 3% for 24 h (a), 48 h (b), and 72 h (c) immersion periods; SEM images of untreated sedge fibers for 24 h (d), 48 h (e), and 72 h (f) immersion periods.

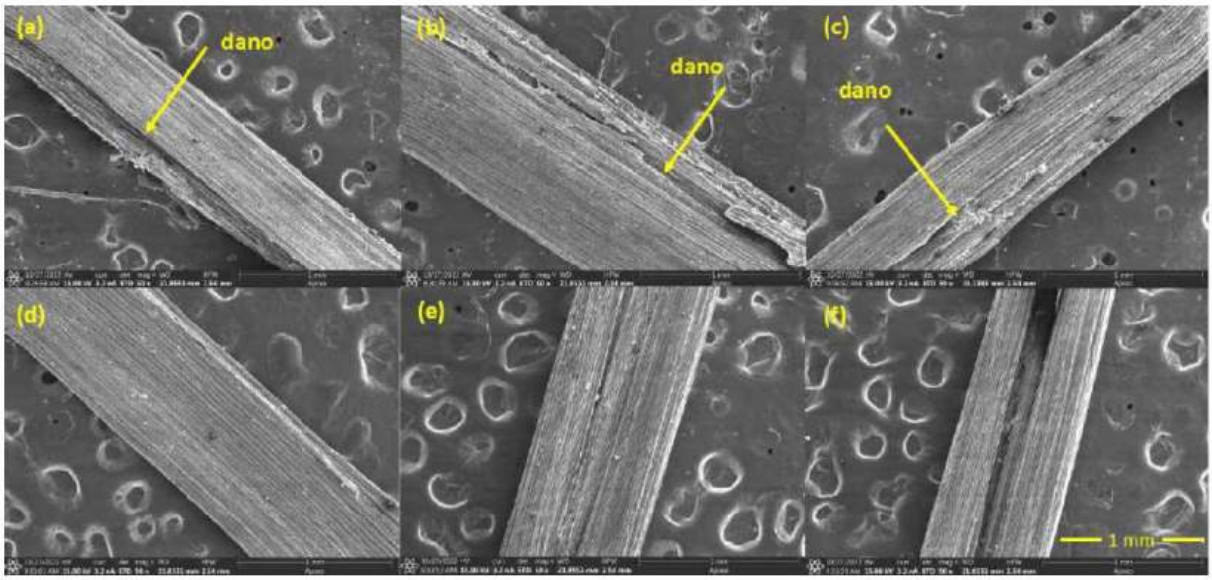

Figura 4.17 – SEM images of alkali-treated fibers in a concentration of 5% NaOH for the immersion periods of 24 h (a), 48 h (b), and 72 h (c); SEM images of alkali-treated fibers in a concentration of 10% NaOH for the immersion times of 24 h (d), 48 h (e), and 72 h (f).

FIG.4.17 is related to all 5% and 10% alkali-treated sedge fibers surface. Fibers treated with 72, 48, and 24 h of the immersion time presented some degradation aspects on

their surface, proving that the treatment was so strong that it damaged the fiber structure. This might reduce their mechanical properties and negatively impact the performance of the composites. Surprisingly, the conditions related to a 10% NaOH did not follow the same degradation behavior. Despite that, the fibers showed hollow spaces along their longitudinal length. Once again, it may be assigned to a greater removal extent in comparison to the condition presented in FIG.4.16. Therefore, under these conditions of 5% and 10% NaOH, damages on the surface of the fiber and greater extension of voids were present. This could reduce the mechanical performance when acting as a reinforcement phase. For this reason, the lowest (3%) NaOH concentration could lead to a possible enhancement for composites reinforced by this fiber.

4.3 SEDGE FIBER REINFORCED GRAPHENE OXIDE (GO) - INCORPORATED EPOXY NANOCOMPOSITES

4.3.1 DYNAMIC MECHANICAL ANALYSIS (DMA)

Storage modulus (E') or dynamic modulus describes a material's stiffness and elastic behavior (SHRIVASTAVA, 2018; HARIS et al., 2022). In other words, it indicates the material's capacity to store and release energy during a cyclical process of loading and unloading for an applied loads. The modulus E' is usually used to determine the elastic properties of the material (MURALIDHAR et al., 2020). While the variation in E' as a function of temperature acquired during the tests can be used to determine the stiffness of the material. It is determined by various parameters such as the interfacial interaction of the fiber-matrix, molecular weight or degree of cross-linking (MATHAPATI et al., 2022).

FIG. 4.18 shows the E' curves as a function of temperature from -50 to 200 °C for EP, all SF/EP and 30 SF/EP-GO conditions. It can be inferred that an increase in temperature induced a drop in E' for all conditions, occurring from 50 to 150 °C. The increase in the percentage volume of sedge fiber caused a downward trend in the E' of all the composites. Whereas, the fall of the E' curve began in 73 °C for EP, 75 °C in 30 SF/EP-GO, 78 °C for 30 and 10 SF/EP and around 80 °C for 20 SF/EP condition. As previously reported (NEUBA et al., 2020), the SF/EP interface is relatively weak, causing a reduction in the storage modulus. In the case of condition 30 SF/EP-GO, the high loss in the E' value may be associated with the effect of GO on the viscoelastic behavior of the matrix, which can reduce the E'.

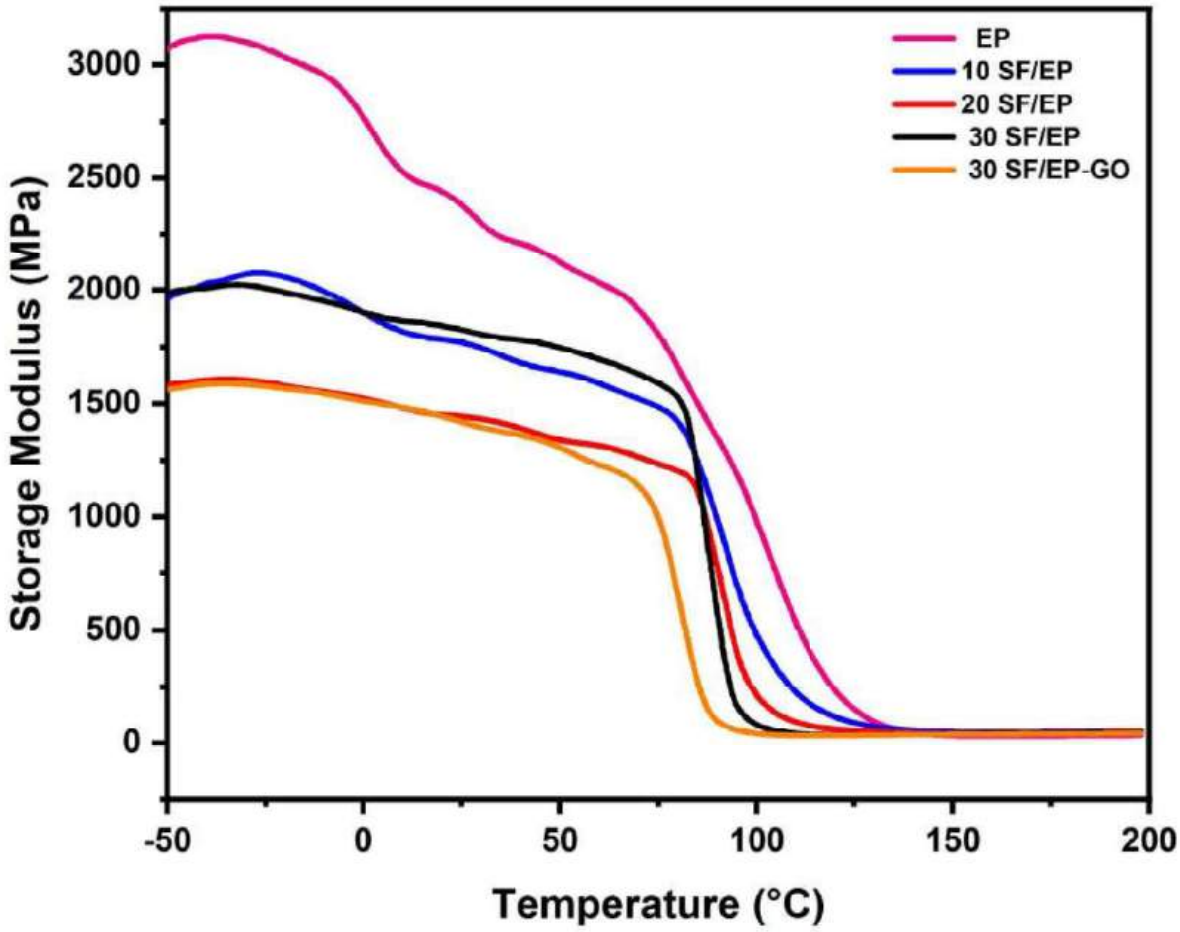

Figura 4.18 – Storage modulus variation with temperature for the basic epoxy (EP) as well as 10 to 30 SF/EP composite and 30 SF/GO-EP nanocomposite.

The significant drop in E' values, in FIG. 4.18, is related to the end of the glassy condition of polymers. In fact, the glass transition region (T_g) is one of the main applications of DMA analysis and its beginning can be determined by the *onset* of the drops in the E' curves (PAULA et al., 2019). The E' curves can be divided into three stages: (i) the first is situated below the T_g and can be named as the glassy region where the movement of the polymer chain is restricted due to the low mobility of the compacted and frozen molecular arrangement. Consequently, E' has a higher value; (ii) region of the T_g, occurring when the temperature rises and the compacted molecular arrangement begins to collapse, causing a high molecular mobility reached by the polymeric chains. As a result, E' is drastically reduced; (iii) the rubbery or viscoelastic region reaches a plateau at the value of E' (RAJA et al., 2022). Moreover, TAB. 4.6 illustrates the values for E', loss modulus (E") and Tan δ.

Tabela 4.6 – Main Parameters for DMA storage modulus (E'), loss modulus (E") and tangent delta (Tan δ) for the investigated materials.

Conditions	**E' at -50 °C (MPa)**	**E' at 25 °C (MPa)**	**E" (MPa)**	**Tan δ**	**T_g (°C)**
EP	3066	2380	200	0.458	129
10 SF/EP	1956	1766	188.5	0.579	117
20 SF/EP	1579	1441	168	0.602	106.5
30 SF/EP	1967	1832	201	0.737	99
30 SF/EP-GO	1563	1414	145	0.606	89

E"or dynamic modulus is a measure of the viscous response of a material, indicating the energy lost as heat or dissipated during a single loading cycle of a sinusoidal strain. The value of E"is usually associated with the internal friction of the material. In addition, the viscoelastic response of a polymeric material is still considered and is mainly affected by the molecular arrangement, heterogeneities and phase transition processes (MATHAPATI et al., 2022; MURALIDHAR et al., 2020; SABA et al., 2016a). In addition, a high loss modulus shows a greater ability to dissipate energy. Therefore, it better indicates the damping properties to reduce damaging loads induced by mechanical energy (CHEE et al., 2021). FIG. 4.19 shows the E"curves as a function of temperature for EP, all SF/EP and SF/EP-GO conditions.

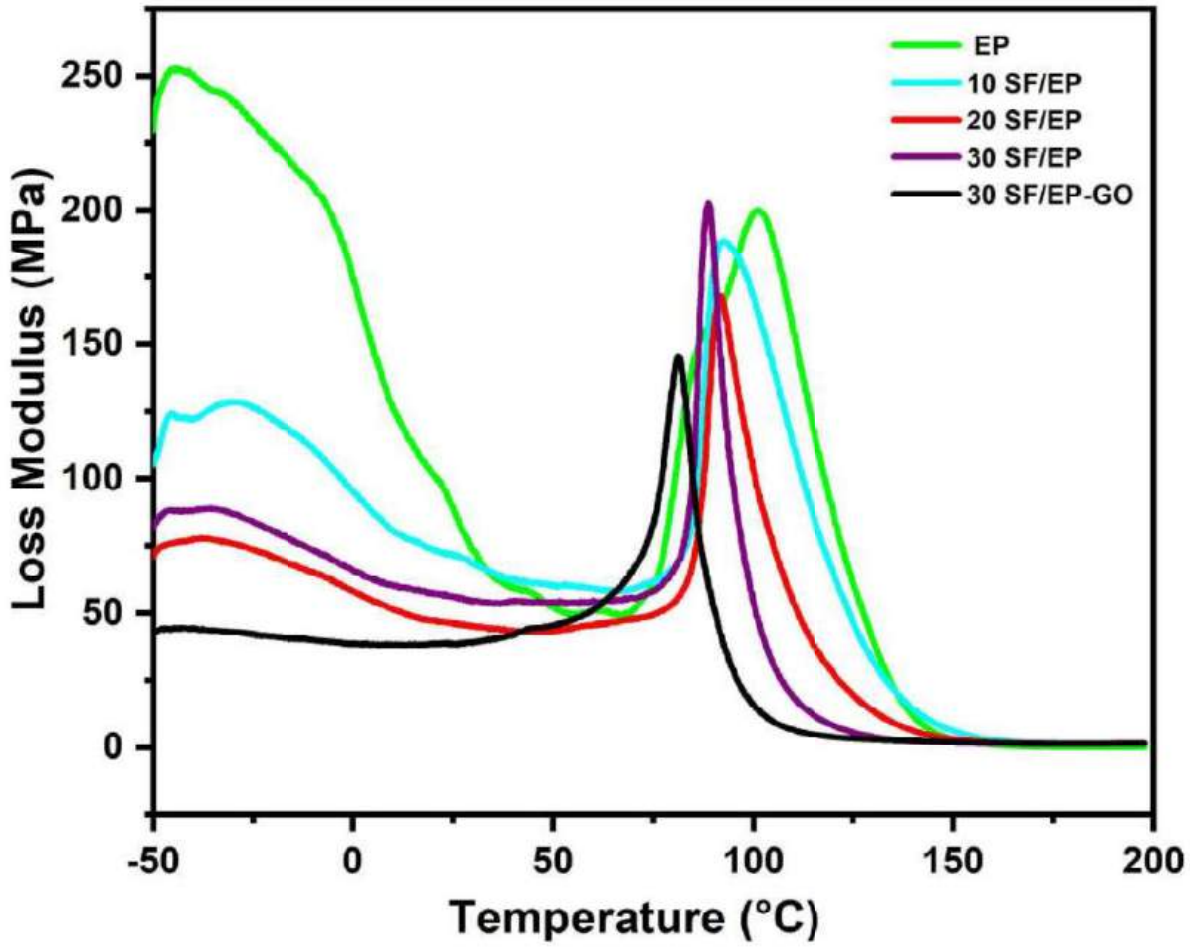

Figura 4.19 – Loss modulus variation with temperature for the basic epoxy (EP) as well as the 10 to 30 SF/EP composite and 30 SF/GO-EP nanocomposite.

It can be seen in the E"curves that all the groups tested reached a maximum peak in the T_g region, varying from 80-100 °C. Additionally, it can be seen that the T_g regions start around 72 °C. Therefore, in this region the material is hard and rigid, consequently the loss modulus is low and constant. However, when it passes through the T_g region, changing from the glassy to the rubbery state, the viscous behavior of the material increases dramatically. This can mainly be explained by the molecular movement of the polymer chain in convergence with mechanical strain, developing high internal friction and non-elastic strain (CHEE et al., 2019; JESUAROCKIAM et al., 2019). This results in high energy dissipation, with the module reaching a maximum peak, denoted as the temperature T_g of the system. After reaching this peak, the molecules are in a more relaxed state and reduce internal friction, thus resulting in a drop in E". The 30 SF/EP-GO condition has the lowest E"value (145 MPa), whereas the 10 and 20 SF/EP conditions exhibit a lower value when compared to EP (200 MPa). Only the 30 SF/EP condition has a similar value to the control group. It can be deduced that, as with E", the GO structure acted as a filler, restricting molecular movement and reducing the viscoelastic friction capacity of the matrix.

The damping factor (Tan δ), or also known as Tan delta, expresses the coefficient of the loss and storage modulus (E"/E') and describes the material's resistance to strain (EBNESAJJAD; KHALADKAR, 2018). In a polymeric structure, the damping properties of the material are responsible for maintaining a balance between the viscous and non-viscous phases (GOLISZEK et al., 2020). For fiber-reinforced polymer composites, a greater interfacial bond between fiber and matrix results in a higher Tan δ value. This is mainly due to lower energy loss due to internal molecular movement, as the movement of the interconnected molecular structures is restricted. (GOLISZEK et al., 2020; SABA et al., 2016b; RAHMAN, 2021).

Therefore, FIG.4.20 illustrates the behavior of SF when added as a reinforcing phase for EP and EP-GO. The variation in damping properties as a function of temperature can be seen. All the Tan δ values of the composites (0.55-0.75) are higher compared to EP (0.46). This shows that the composites have a higher damping factor, associated with greater non-elastic strain and energy dissipation. However, the reduced peak height of the EP condition can be attributed to a polymer chain with restricted movement (JESUAROCKIAM et al., 2019). Indicating that the composites do not have a strong interfacial interaction, resulting in greater energy dissipation at the interface (HAZARIKA; MANDAL; MAJI, 2014; NAVEEN et al., 2019). Furthermore, it can be seen that Tan δ decreased when GO was incorporated into the 30 SF/EP condition from 0.75 to 0.55. This may be related to the fact that the GO acted as nanoparticles interfering with the movement of the EP molecules, as proposed for the E' (FIG.4.18) and E"(FIG.4.19) results. Moreover, the final T_g intervaled occured in a lower temperature range (89 °C) in comparison to 30 SF/EP (98 °C) and EP (131 °C).

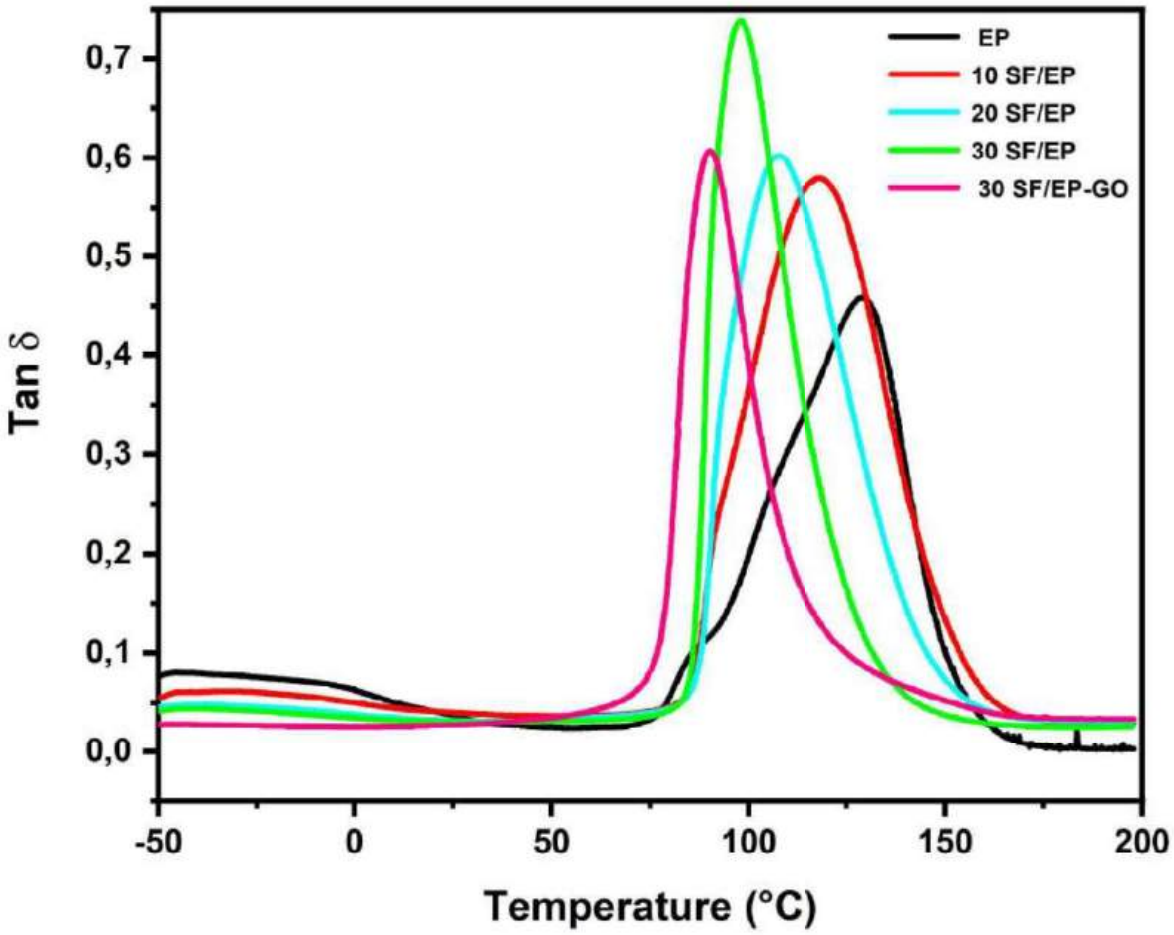

Figura 4.20 – Tan δ variation with temperature for the basic epoxy (EP) as well as the 10 to 30 SF/EP composite and the 30 SF/GO-EP nanocomposite.

The correlation between the E"and E' modules can be interpreted by the Cole-Cole graph (DEVI; BHAGAWAN; THOMAS, 2010; SILVA et al., 2022), containing curves showing a semicircular pattern for homogeneous polymeric systems. This pattern is associated with effects present at the interface and heterogeneous dispersions or phases (PANAITESCU et al., 2020). Therefore, FIG. 4.21 illustrates irregular curves for all the conditions analyzed, decreasing for higher volumes of SF reinforcement. It can be inferred that the curves of the composites show greater heterogeneous dispersions compared to EP due to the presence of the reinforcements in the polymer structure. In particular, the effect of GO promotes a comparatively greater distortion in the aspect of the semicircle for the 30 SF/EP Cole-Cole curve, which can be attributed to the heterogeneous dispersions within the matrix.

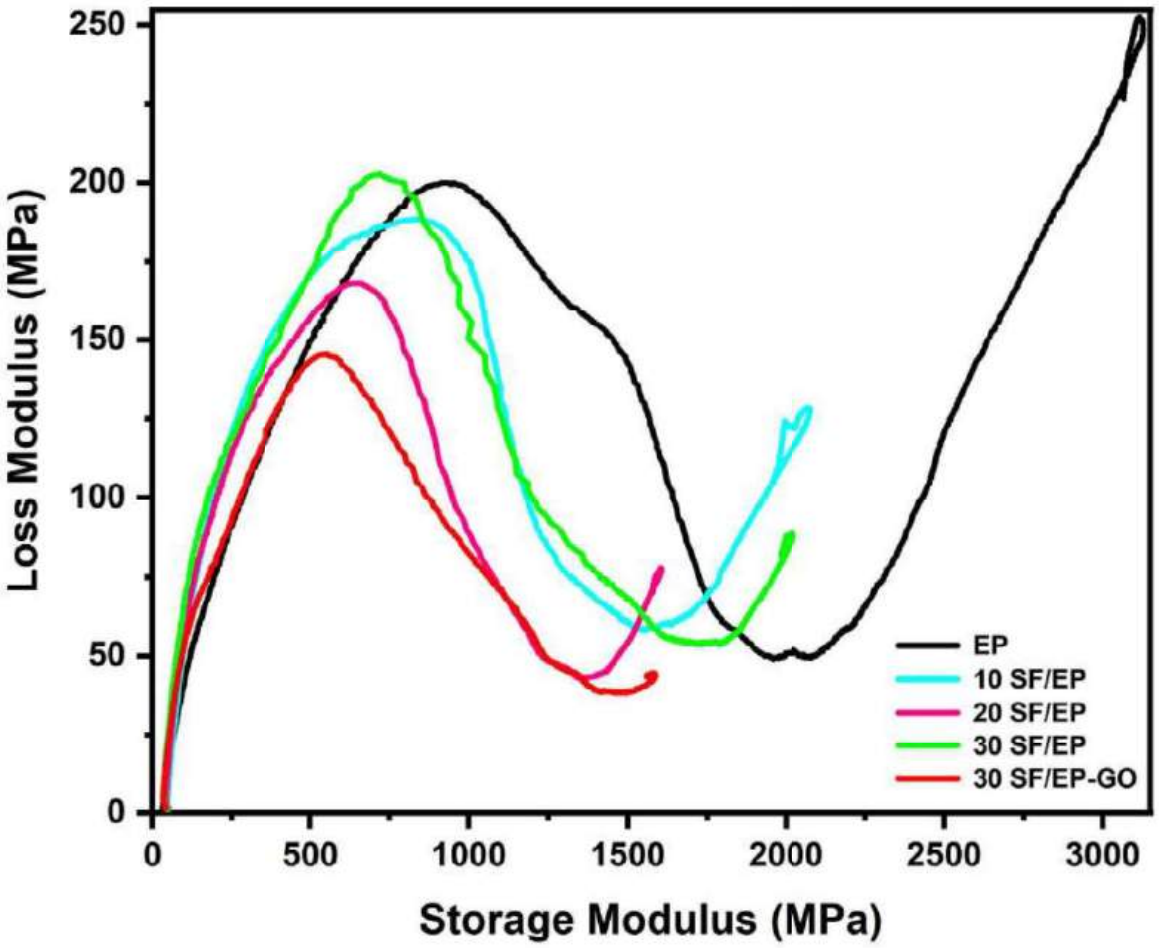

Figura 4.21 – Cole-Cole curves for the basic epoxy (EP) as well as the 30 SF/EP composite, and 10 to 30 SF/GO-EP nanocomposite.

In order to clarify the mechanisms of SF reinforcement and interfacial adhesion of GO to the EP matrix, the effectiveness coefficient can be used (PANAITESCU et al., 2020). This coefficient highlights the contribution of SF and GO in the transition from the glassy to the rubbery state and is determined by:

$$C = \frac{(\frac{E'g}{E'r})composite}{(\frac{E'g}{E'r})matrix} \tag{4.1}$$

Where E'_g and E'_r are the storage modulus values in the glassy and rubbery region for the composites and the matrix. The E' values at 25 and 165 °C were used for E'_g and E'_r, respectively. The value of the effectiveness coefficient is an indication of the contributions of SF and GO in the transition from the glassy to the rubbery state. A lower value corresponds to high effectiveness (PANAITESCU et al., 2020). As can be seen in TAB. 4.7, lower values were obtained for the 20 SF/EP and 30 SF/EP-GO conditions, showing greater reinforcement efficiency. The fiber-matrix interface has a strong influence on reinforcement effectiveness, and may indicate that the 30 SF/EP condition has a

relatively stronger interface than for 30 SF/EP (PANAITESCU et al., 2017).

Tabela 4.7 – Effective coefficient (C) for EP, 10 to 30 SF/EP composite and the 30 SF/GO-EP nanocomposite

Composites	Tan δ (25 °C)	E' glassy (25 °C)	E"rubbery (165 °C)	C
EP	0.03707	2380	31	-
10 SF/EP	0.04020	1766	48	0.479
20 SF/EP	0.03188	1441	45	0.417
30 SF/EP	0.03077	1832	44	0.542
30 SF/EP-GO	0.02736	1414	41	0.453

4.3.2 THERMOMECHANICAL ANALYSIS (TMA)

FIG. 4.22 shows the TMA curves for the EP, 10 to 30 SF/EP and 30 SF/EP-GO conditions, as well as the temperatures of T_g.

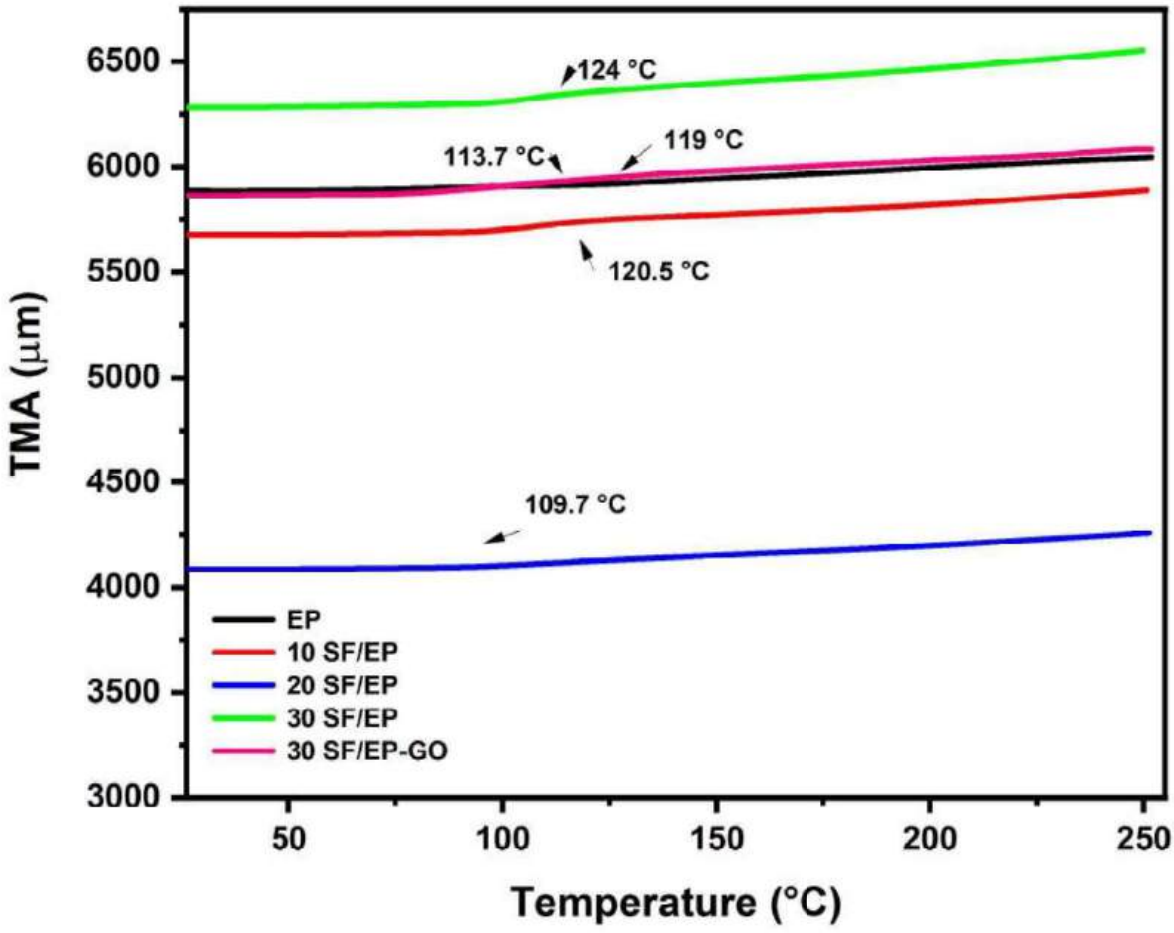

Figura 4.22 – Temperature dependence of the thermomechanical analysis for the basic epoxy (EP) as well as 10 to 30 SF/EP composite and the 30 SF/GO-EP nanocomposite.

The T_g value determined by the TMA curves in FIG. 4.22 was 119 °C for 30 SF/EP-GO and 113 °C for EP. While the values for conditions 10 to 30 SF/EP were, respectively: 120.5, 109.7 and 124 °C. The difference between these values is caused by various factors, such as the addition of fillers and chemical composition that affect the molecular mobility of the material and consequently the T_g range (MUTHUKUMAR et al., 2022). In the case of SF, adding it as a reinforcement led to a restriction in macromolecular mobility. Surprisingly, the T_g found in the TMA for 30 SF/EP was higher than EP in contrast to that found for the DMA in TAB.4.6. This can be attributed to thermal expansion.

In TMA experiments, the material were subjected to thermal expansion as the temperature increases. The linear thermal expansion coefficient (TEC) found in this research for EP was 168.03 x 10^{-6}/°C and 248.95 x 10^{-6}/°C for 30 SF/EP-GO. Whereas, the conditions of 10 to 30 SF/EP were, respectively: 156.19, 220.23 and 208.52 x 10^{-6}/°C. The increase in TEC is due to a low interfacial adhesion of the SF, there is no restriction of the molecular mobility of the matrix at high temperatures (MUTHUKUMAR et al., 2022). This could justify a relatively higher TMA level for 30 SF/EP-GO in FIG. 4.22 and consequently the inflection associated with the T_g. In contrast, the level of 30 SF/EP-GO is very similar to EP.

4.3.3 THERMOGRAVIMETRIC ANALYSIS (TGA/DTG)

The thermogravimetric (TG) and its derivatives (DTG) curves are presented in FIG.4.23, for the 30 SF/GO-EP nanocomposite. The TG curve in this figure highlights that a small mass loss (5.37%) occurred at low temperatures, until 200 °C, which is related to moisture desorption. Mass loss at this stage was slightly higher than for the EP and sedge composites previously obtained in another study (NEUBA et al., 2020), according to TAB. 4.8 demonstrates. This was due to a greater moisture absorption capacity on the part of the SF and a possible contribution from the GO now present in the structure of the composite. In addition, the parameters associated with the main thermogravimetric events, such as the temperature and mass loss of all the conditions previously studied (NEUBA et al., 2020), as well as the 30 SF/EP-GO nanocomposite are present in the TAB. 4.8.

Tabela 4.8 – TGA parameters for the present investigated 30 SF/GO-EP nanocomposite and previous results of EP and up to 30 SF/EP composite.

Conditions	M.L. up to 200 °C (%)	T_{onset} (°C)	T. M. D.R. (°C)	M.L. at 2° stage (%)	M.L. at 600 °C (%)	Ref.
EP	1.63	344.7	388.5	70.6	80.4	Neuba et al. (2020)
10 SF/EP	4.23	300.5	341.6	62.4	79.3	Neuba et al. (2020)
20 SF/EP	4.18	287.1	362.1	48.7	77.6	Neuba et al. (2020)
30 SF/EP	3.23	292	334.2	56.3	77.4	Neuba et al. (2020)
30 SF/EP-GO	5.37	290.6	325.6	52.7	86.7	PT*

PT= Present work; Ref.= Reference; T. = temperature; M.L. = Mass Loss; M. = Maximum; D.R. = Degradation Rate

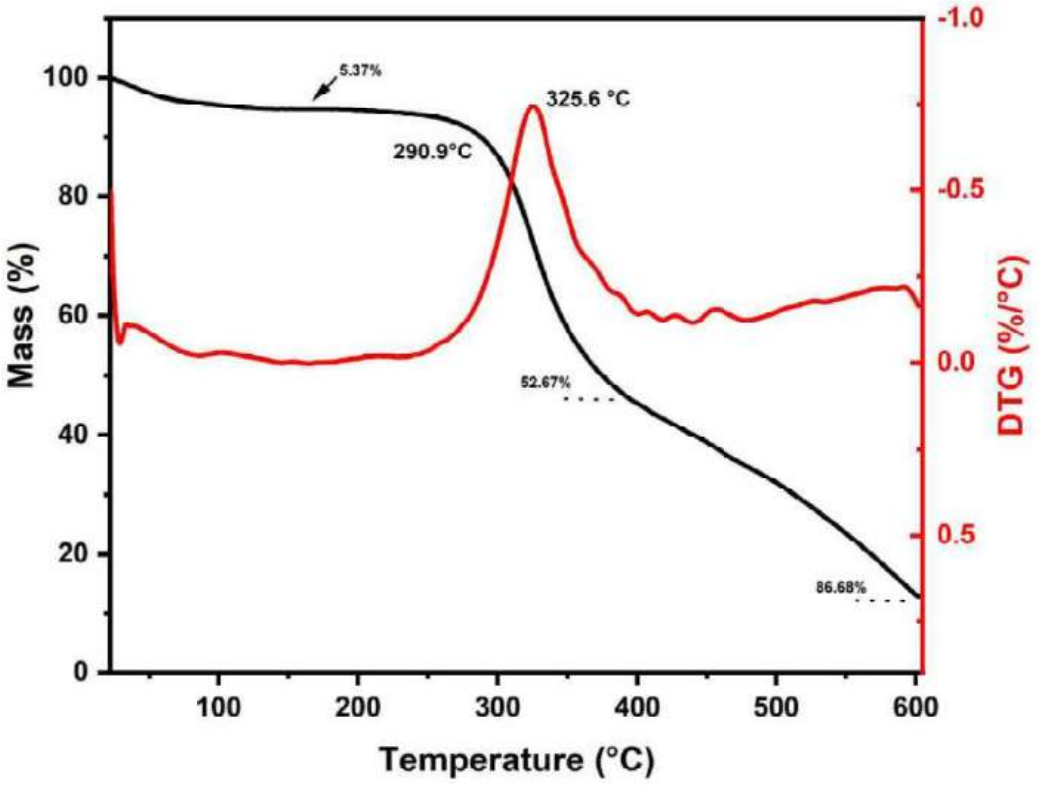

Figura 4.23 – Thermogravimetric curves for the present investigated 30 SF/GO-EP nanocomposite.

Observing high temperatures, the rupture and degradation of the polymer chains can be seen, with a severe loss of mass. Occurring from T_{onset} (290.6 °C) and maximum rate at 325.6 °C, as a result 52.67% was the mass loss at the end of the second stage. Whereas the final stage, occurring between 400 and 600 °C and resulted in a final ash content equivalent to 13.32% of the initial mass. However, for the EP and SF/EP conditions reported by (NEUBA et al., 2020) degradation occurred at higher temperatures. In addition, all T_{onset}

exhibited higher values. This is indicative of the first thermal stability limit for these conditions. However, the 30 SF/EP-GO condition showed a slightly lower value than 30 SF/EP condition. This indicates that although GO is present in EP microstructure, it was not possible to increase the thermal stability of the composites as a whole. The same can be said about the maximum degradation temperature range when compared to previously reported results (NEUBA et al., 2020). Furthermore, one study reported that GO when incorporated into an epoxy resin reduced the initial degradation temperature as well as the maximum degradation rate (ZHI et al., 2019). According to the authors, the worse thermal stability may be caused by the GO reinforcement decreasing the cross-link density of the epoxy.

4.3.4 DIFFERENTIAL SCANNING CALORIMETRY (DSC)

FIG. 4.24 depicts the DSC curve obtained for the 30 SF/EP-GO. It is possible to observe an endothermic peak at 63 °C, probably associated with the glass transition temperature (T_g) and the release of moisture present in the sedge fibers surface. The following exothermic peak might be related to the post curing process. As observed by (NEUBA et al., 2020), the SF/EP composites conditions have presented a higher T_g and post curing temperature. The same phenomena was observed in other studies (XUE et al., 2019; UMER et al., 2015). According to the authors, this occurred due to hidroxyl groups on the EP-GO basal plane participate in the opening of epoxy rings as a curing agent. Then, acting as a catalyst and accelerating the curing reaction (UMER et al., 2015; ACOCELLA et al., 2016). It is also observed two exothermic peaks, probably associated with the degradation of NLFs constituents. The first exothermic peak is observed at 342 °C and can be related to the degradation of α cellulose (SEKI et al., 2013). The second peak at 466 °C, is associated to the lignin decomposition and part of cellulose I decomposition (NARAYANASAMY et al., 2020; VRINCEANU et al., 2013).

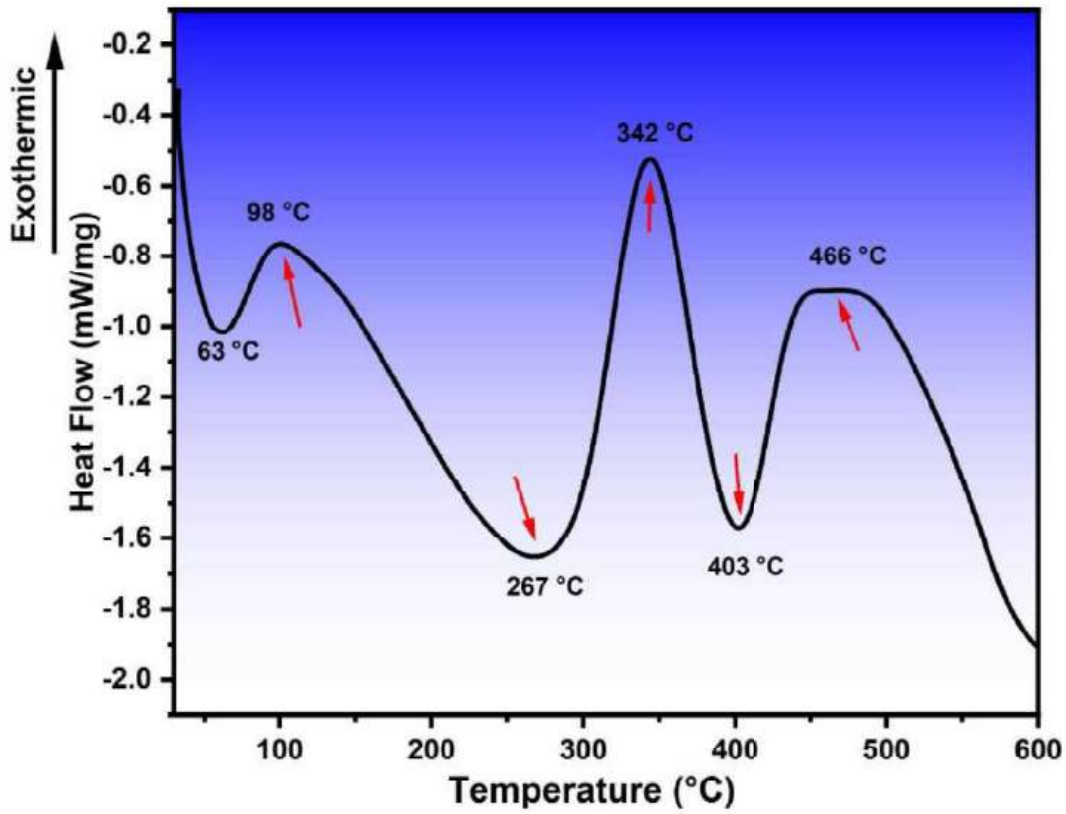

Figura 4.24 – DSC curve for the 30 SF/EP-GO nanocomposite.

4.3.5 FOURIER TRANSFORM INFRARED SPECTROSCOPY (FTIR)

FIG. 4.25 depicts the FTIR spectra of 30 SF/EP-GO composite condition. The O-H stretching and functional groups present in the GO can be observed on 3433 cm^{-1}, while the C-H stretching can be seen at 2956 cm^{-1}. The peak observed at 2354 cm^{-1} is assigned to the bond between organic molecules. As for the C=O aromatic groups, the peak is associated with the 1618 cm^{-1} and is present the GO nanostructure and the composites. The aromatic rings appeared at 1513 cm^{-1}, which indicated that did not occurred any chemical interaction between sedge fibers and the aromatic ring. According to (CECEN et al., 2008), the vibration at 1447 cm^{-1} is related to the asymmetric bending of methyl group. Further, the band at 1255 cm^{-1} can be attributed to the CH_2 torsion vibration and the stretching of C-O occurred at 1032 cm^{-1}, the last peak is also associated to the GO nanosheets. The peak at 559 cm^{-1} is associated to the C-C stretching. At last, any expressive change was observed on the composites FTIR spectra.

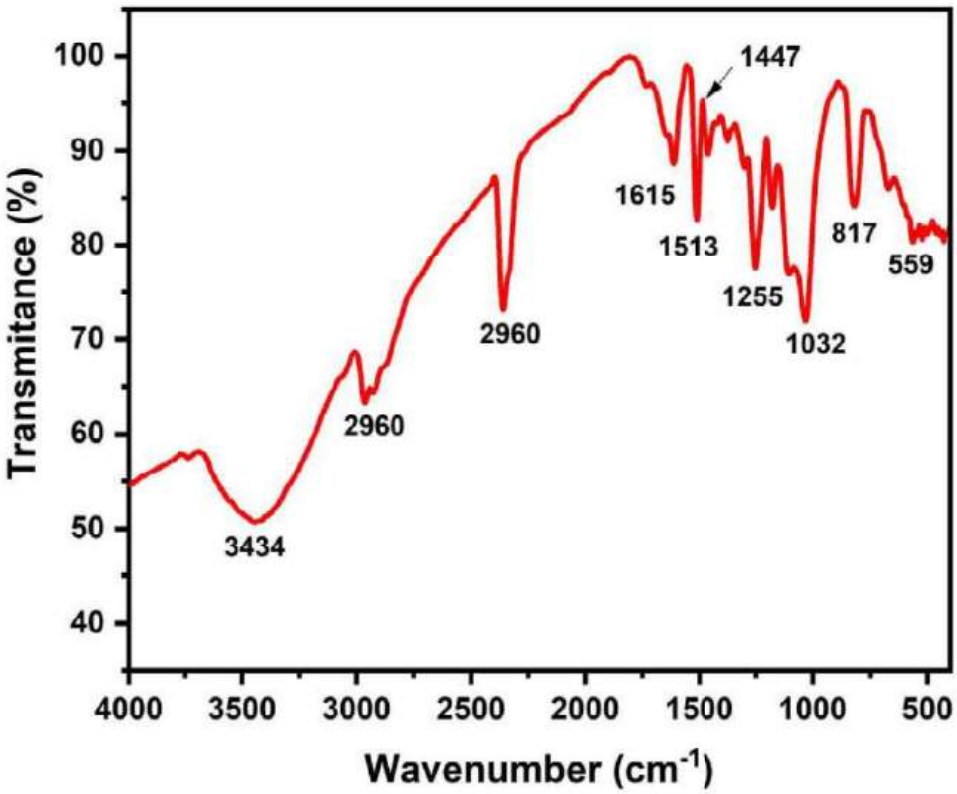

Figura 4.25 – FTIR spectra for the 30 SF/EP-GO nanocomposite.

4.3.6 CHARPY IMPACT TEST

The results acquired from the Charpy impact test of EP, 10 to 30 SF/EP and 30 SF/EP-GO conditions are presented in TAB. 4.9. The nanocomposite disclosed a higher energy absorption when compared to EP and SF/EP conditions.

Tabela 4.9 – Charpy impact energy for the following conditions: EP, 10 to 30 SF/EP and 30 SF/EP-GO.

Charpy Impact Energy (J/m)					
Samples	**EP**	**10 SF/EP**	**20 SF/EP**	**30 SF/EP**	**30 SF/EP-GO**
1	7.89	19.39	59.41	109.43	135.96
2	13.27	22.26	66.12	86.79	180.55
3	9.61	16.91	35.71	64.81	186.83
4	10.54	27.42	85.48	94.21	83.49
5	12.15	54.25	41.39	58.72	113.09
6	-	41.25	59.95	92.73	156,.49
7	-	27.88	67.45	113.41	137.74
Mean	**10.69 ± 1.88**	**29.93 ± 0.13**	**60.17 ± 13.77**	**89.63 ± 18.10**	**139.17 ± 30.63**

The results can be better visualized by the graph FIG. 4.26. A tendency of increasing

impact energy with increasing filler content was observed. The effect of incorporating GO nanofillers, developing a hybrid nanocomposite, was remarkable and has shown a 1202% increase compared to the value obtained for the neat epoxy resin. While a 55.27% increase has been found when comparing the hybrid nanocomposite to 30 SF/EP condition.

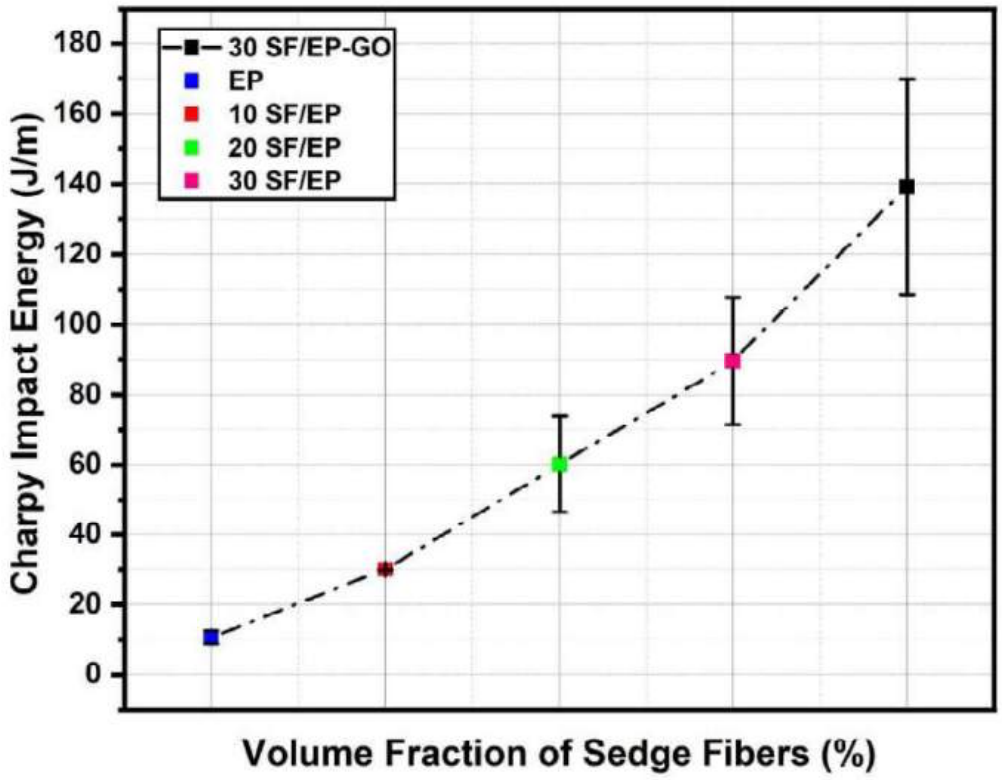

Figura 4.26 – Charpy impact Energy for the EP, 10 to 30 SF/EP and 30 SF/EP-GO conditions.

The samples, totally fractured, are exhibited in FIG.4.27. The complete rupture justifies the test validation. According to the macroscopic aspect, it is possible to observe the existence of a brittle fracture in the EP condition. On the other hand, the other conditions showed a ductile-fragile transition.

Figura 4.27 – Samples after the Charpy impact test.

It is also possible to see the fibers rupture macroscopically, representing one of the fracture mechanisms present in the composites and nanocomposites. Micrographs were observed in order to investigate other mechanisms involved in the fracture process of the specimens more clearly. FIG. 4.28 illustrates some micrographs of the fracture surface of the materials.

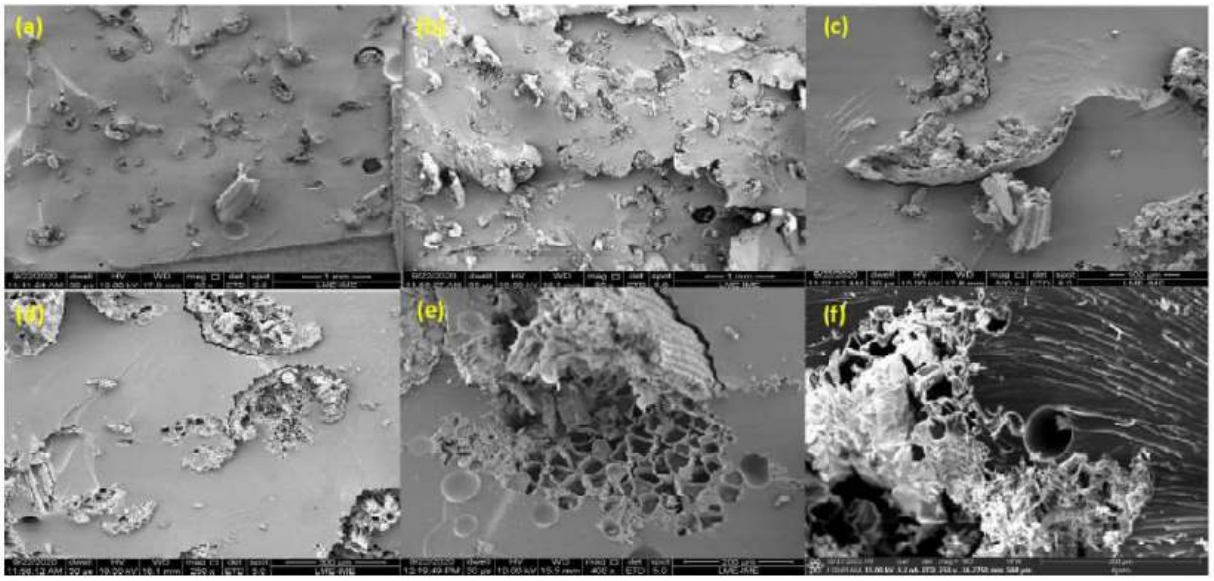

Figura 4.28 – SEM micrographs for the charpy impact samples surface.

FIG. 4.28 (a) and (b), represent the 10 and 30 SF/EP conditions, respectively. Both micrographs show the fracture mechanisms that contributed to the increase in impact energy, such as fiber rupture, *pullout* and river marks. However, the major difference between these images is the fiber content present, as several articles have pointed out

(NASCIMENTO et al., 2018; CANDIDO et al., 2017; PEREIRA et al., 2017) a higher fiber content combined with the the failure mechanisms will lead to an increase in the absorption of impact energy. However, as seen in (c) to (e), there is a great deal of detachment of the fiber from the matrix. This mechanism is known as delamination and is detrimental to the mechanical properties, contributing negatively to the performance of the composite material. (HEIDARY; KARIMI; MINAK, 2018; ZHANG et al., 2021). Delamination is caused by a poor fiber-matrix interface, occurring mainly due to the difference in the hydrophilic character of the fiber and the hydrophobic nature of the matrix. However, in (f), it can be seen that delamination has not occurred, although many river marks are present near the interface region. This is because the GO has been incorporated into the EP matrix and has groups such as hydroxyl and carboxyl obtained during the oxidation process (LUZ et al., 2020). These groups can improve the interaction between the fiber and the polymer matrix, resulting in higher interfacial resistance.

Analysis of variance (ANOVA) was carried out to determine whether there was a significant difference between the results obtained for the Charpy impact energy between the EP, 10 to 30 SF/EP and 30 SF/EP-GO conditions. Therefore, TAB. 4.10 shows the results obtained.

Tabela 4.10 – Analysis of variance of Charpy impact energy for the conditions of 10 to 30 SF/EP, EP and nanocomposite 30 SF/EP-GO.

Causes of Variation	**Sums of squares**	**Degrees of freedom**	**Mean Square**	**F (calculated)**	**Fc (tabulated)**
Treatments	53399.07	4	13349.77	**46.86**	**3.05**
Residue	4272.75	15	284.5		
Total	57671.82	19			

According to the results obtained by ANOVA, the hypothesis that the means are equal was rejected at a significance level of 5%, because according to the statistics, the F calculated (46.86) is higher than the F tabulated (3.05). Therefore, the effects of the percentage of the different fiber conditions and the GO in the composites develop different effects for the Charpy impact energy. In addition, the Tukey's test was used to compare the means, applying a confidence level of 95%, in order to ascertain which condition provides the best results. the Tukey's honestly significant difference (HSD) was found at 22.12 J/m. TAB. 4.11 displays the results for the differences between the mean impact energy values between the conditions investigated.

Tabela 4.11 – Results for the differences between the mean values of the Charpy impact energy after applying Tukey's test.

Conditions	EP	10 SF/EP	20 SF/EP	30 SF/EP	30 SF/EP-GO
EP	0	17.35	**46.93**	**72.09**	**144.82**
10 SF/EP	17.35	0	**29.57**	**54.74**	**127.47**
20 SF/EP	**46.93**	**29.57**	0	**25.17**	**97.89**
30 SF/EP	**72.09**	**54.74**	**25.17**	0	**72.72**
30 SF/EP-GO	**144.82**	**127.47**	**97.89**	**72.72**	0

Based on the results of Tukey's test with a confidence level of 5%, the condition 30 SF/EP-GO showed the best performance. There was a significant difference between the EP and SF/EP conditions, as the values were higher than the HSD of 22.12.

4.3.7 IZOD IMPACT TEST

The results obtained for the Izod impact test of condition 30 SF/EP-GO are shown in TAB. 4.12. This condition provided comparatively higher energy absorption compared to the EP and SF/EP conditions (NEUBA et al., 2020).

Tabela 4.12 – Izod impact test results for the 30 SF/EP-GO nanocomposite.

Izod impact energy (J/m)	
Samples	**30 SF/EP-GO**
1	100
2	112.36
3	157.41
4	100.46
5	83.49
6	52.17
7	93.81
8	97.13
9	130.11
10	158.08
Mean	**108.5 ± 31**

FIG. 4.29 shows a comparative graph of the average impact energy for each condition, as well as the standard deviation. The upward trend can be seen more clearly as the reinforcement content increases. 30 SF/GO-EP group showed a promising increase of 384.37% against the control group. In addition, an increase of 72.22% was found when comparing with the 30 SF/EP composite.

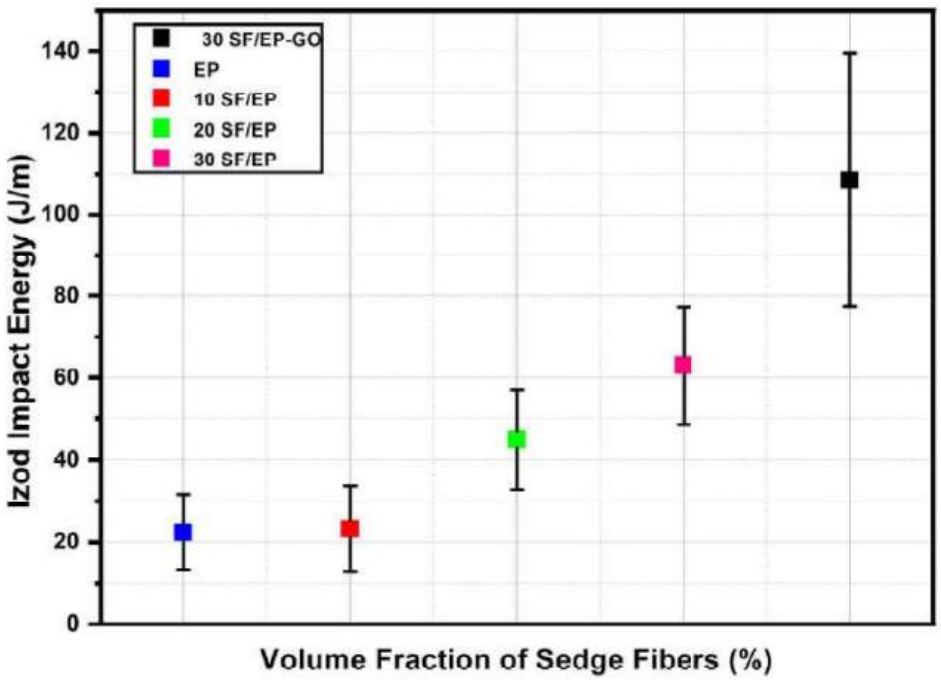

Figura 4.29 – Izod impact energy for the present nanocomposite 30 SF/EP-GO investigated and the other conditions previously reported.

The test samples were completely fractured, justifying the validity of the results obtained, as illustrated by FIG. 4.30. Besides, the fracture mechanism related to fiber breakage is observed macroscopically.

Figura 4.30 – Fracture of the samples 30 SF/EP-GO after the IZOD impact test.

Izod impact properties were altered due to EP-GO functionalization, adding a new phase. Thus, new fracture mechanism events are present, contributing to increased energy

absorption. Therefore, in order to understand these events more clearly, microscopies were acquired. FIG. 4.31 shows some micrographs related to the fracture mechanisms. As previously observed for the Charpy test, the fiber-matrix interface has been considerably improved.

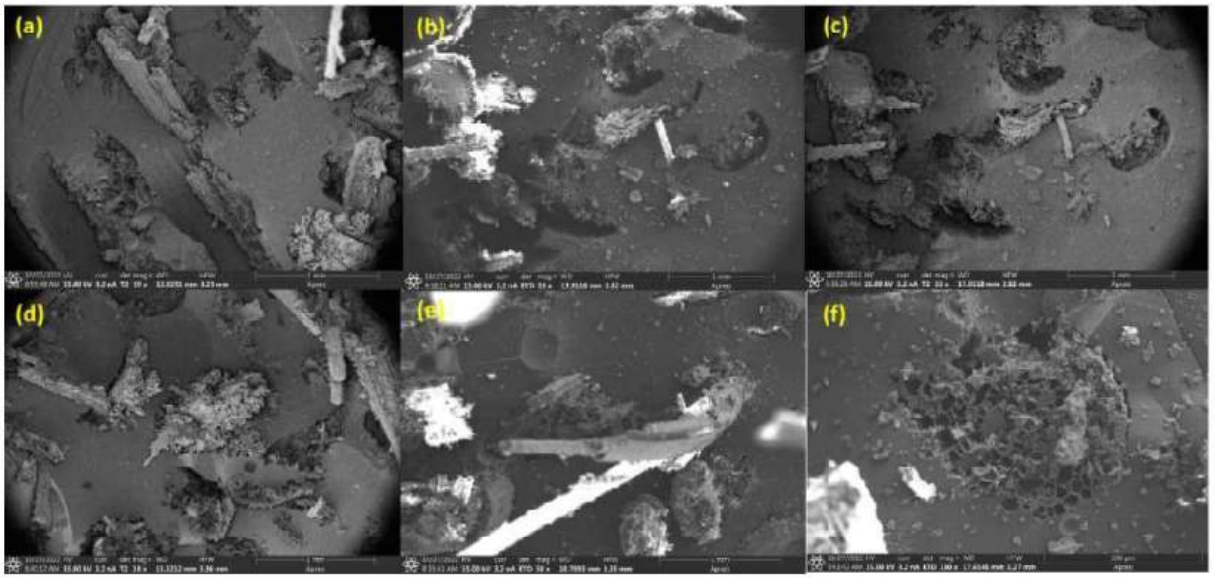

Figura 4.31 – Fracture mechanisms observed microscopically for the 30 SF/EP-GO nanocomposite.

In all the micrographs it is possible to clearly see an improvement between the fiber-matrix interface, with a low content of the delamination fracture mechanism. A large predominance of delamination was observed in the SF/EP composites, as seen in the discussion of the Charpy impact results. This delamination is caused by poor fiber adhesion as a result of the difference in hydrophobic and hydrophilic nature.(AL-MAHARMA; AL-HUNITI, 2019). On the other hand, GO has an amphiphilic character and can act as a coupling between the matrix and the fiber (MCCOY et al., 2019; HOU et al., 2021; LIU et al., 2022; TISSERA et al., 2015). Moreover, many studies reported in the literature state that the presence of the GO nanofiller increases the toughness of the material and the mechanical properties in general, and may be another factor responsible for the increase in Izod impact energy. In addition, other fracture mechanisms are present, such as fiber tearing and fiber pullout. The latter is widely known in the literature as pullout and is identified by the imprint of the fiber on the surface of the matrix (FIG.4.31 (a)) and hollows (FIG.4.31 (b)).

ANOVA was carried out in order to determine whether there was a significant difference between the results acquired for the Izod impact energy between the EP, 10 to 30 SF/EP and 30 SF/EP-GO conditions. TAB. 4.13 displays the results obtained.

Tabela 4.13 – Analysis of variance of Izod impact energy for the conditions 10 to 30 SF/EP, EP and nanocomposite 30 SF/EP-GO.

Causes of Variation	Sums of squares	Degrees of freedom	Mean Square	F (calculated)	Fc (tabulated)
Treatments	44452.83	4	11113.21	**29.29**	**2.61**
Residue	15172.61	40	379.32		
Total	59625.47	44			

In view of the results obtained by the ANOVA analysis, the hypothesis of equality between the means was rejected at a significance level of 5%. According to the F statistic, the F calculated value (29.29) is higher than the F tabulated (2.61). Thus, the GO reinforcement and the percentage of sedge fibers had different effects on the impact energy. Tukey's test was therefore applied to compare the means using a confidence level of 95% to check which condition gave the best results. The HSD found was 18.19 J/m. The results of Tukey's test for the difference between the mean values of the Izod impact energy are shown in TAB. 4.14.

Tabela 4.14 – Results for the differences between the mean Izod impact energy values after applying Tukey's test.

Conditions	EP	10 SF/EP	20 SF/EP	30 SF/EP	30 SF/EP-GO
EP	0	1.97	**35.03**	**54.29**	**115.12**
10 SF/EP	1.97	0	**33.06**	**52.32**	**113.15**
20 SF/EP	**35.03**	**33.06**	0	**19.27**	**80.09**
30 SF/EP	**54.29**	**52.32**	**19.27**	0	**60.83**
30 SF/EP-GO	**115.12**	**113.15**	**80.09**	**60.83**	0

Based on the results with a significance level of 5%, condition 30 SF/EP-GO performed best, as it had an average Izod impact energy value of 108.5. Therefore, there was a difference between all the conditions. This was because the differences found were greater than the value of 18.19 J/m. In addition, it was observed that there was no significant average difference between the EP and 10 SF/EP conditions, due to the low percentage of sedge fibers in this condition. This behavior follows the same trend as other previous studies (RAFIQ et al., 2017; CAMINERO et al., 2018; KARTHIKEYAN; BALAMURUGAN; KALPANA, 2013).

4.3.8 BENDING TEST

TAB.4.15 presents the means, together with the standard deviation, of the mechanical properties acquired in the 3-point bending test for the EP, composites up to 30 SF/EP

and the 30 SF/EP-GO nanocomposite. Researchers in the literature have reported that the bending properties increased as the volume fraction of NLFs incorporated increased (KHALID; ARIF; RASHID, 2022; HEMNATH et al., 2021). The present study showed an upward trend up to 30 SF/EP-GO, as FIG. 4.32 illustrates. However, the EP condition showed better mechanical performance, in terms of flexural strength and modulus of elasticity, than all the conditions investigated. The reason for the reduced mechanical performance may be linked to the sedge fibers acting as a filler rather than a reinforcement. Furthermore, a poor interface between the matrix and the fiber could still be an indication. Finally, a possible development of voids between the fibers due to the resin not being able to wet all the fiber content could be an indication of possible regions that could act as stress concentrators. This would again be linked to poor adhesion of the matrix coating the fiber due to the difference in nature.

Tabela 4.15 – Flexural strength properties of the samples of the EP, 10 to 30 SF/EP and 30 SF/EP-GO conditions.

Conditions	**Flexural Strength (MPa)**	**Total Strain (%)**	**Elastic Modulus (GPa)**
EP	41.38 ± 7.02	2.75 ± 0.19	1.19 ± 0.14
10 SF/EP	22.27 ± 6.02	3.02 ± 0.62	0.68 ± 0.18
20 SF/EP	20.78 ± 5.06	2.86 ± 0.56	0.66 ± 0.09
30 SF/EP	24.63 ± 6.75	3.1 ± 0.35	0.83 ± 0.24
30 SF/EP-GO	29.03 ± 4.78	3.95 ± 0.56	0.87 ± 0.22

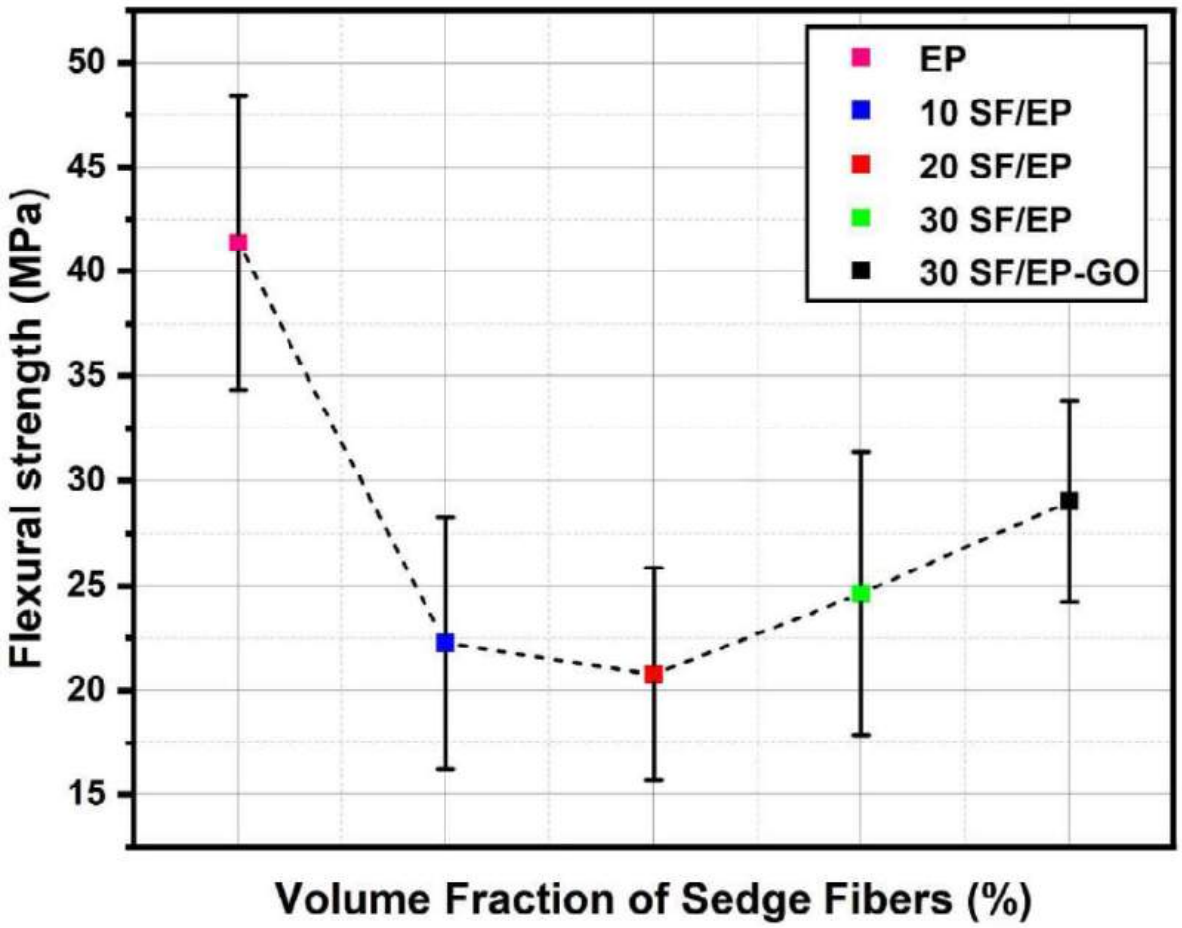

Figura 4.32 – Graphical comparison of the flexural strength of the EP, 10 to 30 SF/EP and 30 SF/EP-GO conditions.

The total strain behavior, shown in the graph of FIG.4.33 and TAB. 4.15. The results show that the EP condition presents a totally brittle behavior, while the composites show an increase in total strain, which is associated with the effect of fiber reinforcement and GO nanoreinforcements in improving the toughness of the new material made. Many authors point out that this is due to a ductile-fragile transition presented by these composites (KERN et al., 2016; SELEZNEVA et al., 2018; HAN et al., 2019; CHEN et al., 2023). Whilst for the elastic modulus, presented for all composite conditions, there was an upward trend up to 30 SF/EP-GO. It can be inferred that this must be related to the action of GO, contributing to an increase in the material's hardness. However, this is still below the average achieved by the control group.

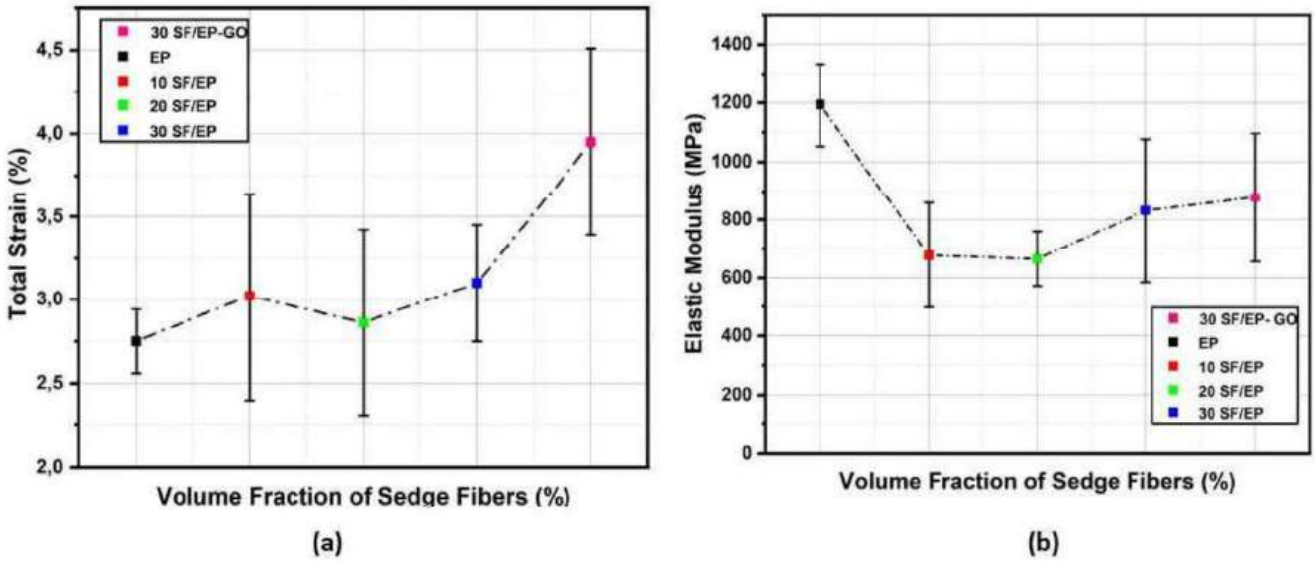

Figura 4.33 – Graphical comparison of the: (a) total strain and (b) elastic modulus shown by the bending test of the EP, 10 to 30 SF/EP and 30 SF/EP-GO conditions.

In search to better understand the fracture mechanisms that contribute to the increase in reinforcement under the conditions investigated, SEM micrographs were acquired according to FIG.4.34. It can be seen that item (a) related to the EP condition has a predominantly fragile fracture mechanism with only river marks present. Item (b) refers to condition 10 SF/EP. In this case it can be seen that in addition to the brittle fracture mechanism, i.e. river marks, fiber ruptures are present. The concentration of fiber-related fracture mechanisms increases under conditions of 20 SF/EP, in (c), and 30 SF/EP, in micrographs (d) and (E). These micrographs show the mechanisms mentioned above, as well as pullout and delamination. The latter appears less frequently and may be an indication of a good interface between the fiber and the matrix. It was also possible to verify the size of the lumen cross-section of a sedge fiber, corresponding to a value of 178.5 μm. Finally, micrograph (f) shows the effect of GO on the epoxy matrix for the 30 SF/EP-GO condition. The arrow indicates an agglomeration of the nanofiller, which directly interferes with the propagation of the river marks, acting as an obstacle. In general, as already mentioned in the literature, the agglomeration of GO impairs mechanical properties. Therefore, although there was an increase in properties, the performance could have been even better if it had been evenly distributed. In addition, it can be seen that the GO functionalizing the matrix acted positively to obtain a stronger interface between the matrix phase and the reinforcement.

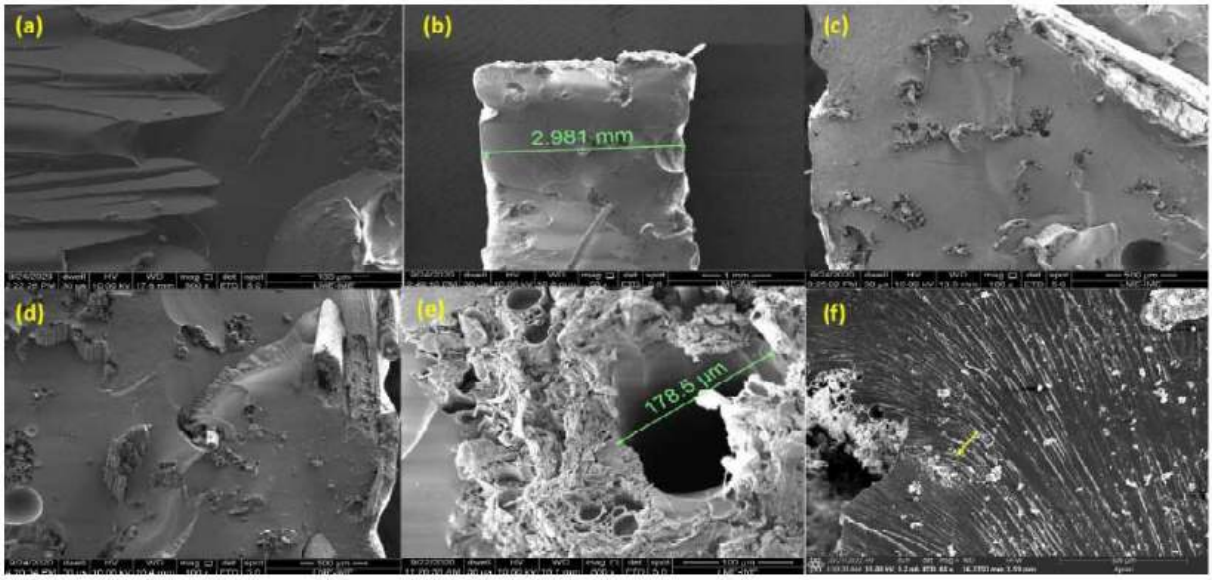

Figura 4.34 – Fracture mechanisms observed microscopically for the 30 SF/EP-GO nanocomposite, EP, and composite up to 30 SF/EP.

In order to ascertain whether there is in fact a significant difference between the bending properties for the different groups, an ANOVA analysis was carried out. In TAB. 4.16 it can be seen that the hypothesis that the means are equivalent was rejected, once again, with a confidence level of 5%. This is due to the F calculated being greater than the F_c tabulated. Therefore, it was confirmed that there is a significant difference between the flexural strength property for the different reinforcement conditions.

Tabela 4.16 – Analysis of variance of flexural strength for the composites 10 to 30 SF/EP, EP and nanocomposite 30 SF/EP-GO.

Causes of Variation	**Sums of squares**	**Degrees of freedom**	**Mean Square**	**F (calculated)**	**Fc (tabulated)**
Treatments	1124.78	4	281.19	**29.29**	**2.61**
Residue	807.83	25	32.31		
Total	1932.62	29			

TAB.4.17 shows the comparison of the means obtained by applying the Tukey test, based on the HSD the value found was 6.62 MPa, so differences greater than the HSD were considered significant. These values are highlighted and showed that the EP condition was better than all the other groups tested. In addition, it was observed that the 30 SF/EP-GO group is different from the other fiber-reinforced composite groups, slightly improving flexural strength. However, all the groups under performed in the EP condition.

Tabela 4.17 – Results for the differences between the mean flexural strength values after applying Tukey's test.

Conditions	EP	10 SF/EP	20 SF/EP	30 SF/EP	30 SF/EP-GO
EP	0	**15.76**	**21.41**	**19.72**	**8.8**
10 SF/EP	**15.76**	0	3.65	1.97	**8.95**
20 SF/EP	**21.41**	3.65	0	1.68	**12.6**
30 SF/EP	**19.72**	1.97	1.68	0	**10.92**
30 SF/EP-GO	**8.8**	**8.95**	**12.6**	**10.92**	0

4.3.9 TENSILE TEST

TAB.4.18 depicts a comparison of the present condition investigated and the average values of all the conditions previously studied (NEUBA et al., 2020).

Tabela 4.18 – Comparison of the mechanical properties of the EP, 10 to 30 SF/EP and 30 SF/EP-GO conditions.

Conditions	Tensile Strength (MPa)	Total Strain (%)	Elastic Modulus (GPa)	References
EP	34.00 ± 4.2	3.0 ± 1.0	1.7 ± 0.5	Neuba et al. (2020)
10 SF/EP	7.0 ± 3.1	4.0 ± 1.2	0.6 ± 0.2	Neuba et al. (2020)
20 SF/EP	12.4 ± 5.5	4.3 ± 0,6	1.3 ± 0.4	Neuba et al. (2020)
30 SF/EP	15.2 ± 3.6	4.7 ± 1.1	3.8 ± 0.1	Neuba et al. (2020)
30 SF/EP-GO	18 ± 3.7	3.3 ± 2.1	0.8 ± 0.4	Present Work

The new hybrid nanocomposite exhibited a higher tensile strength value compared to the other SF/EP conditions. This may be related to a more homogeneous dispersion of the GO within the epoxy matrix and stronger interfacial interaction. Due to hydrogen bonding and ionic interaction in both components (BORA et al., 2013). However, 30 SF/EP-GO condition showed a lower tensile strength value when compared to EP. This is possibly associated with the fact that the fibers did not act as reinforcement when tensile stresses were applied to the material (NEUBA et al., 2020). For this reason, the fibers probably acted as defects for the structure of the material and the fiber-matrix interface was affected.

The results can be better visualized by graphs of FIG. 4.35 and FIG. 4.36. Although there was a tendency for tensile strength to increase with increasing reinforcement, it was still significantly low compared to EP. This behavior is the opposite of that observed for the Charpy and Izod impact properties, but similar to the bending test. A low interfacial resistance can be associated with this performance, resulting in a larger fracture surface.

In addition, an agglomeration of GO can contribute to poor material performance (CHEN et al., 2022; BHAWAL et al., 2018; LI et al., 2017).

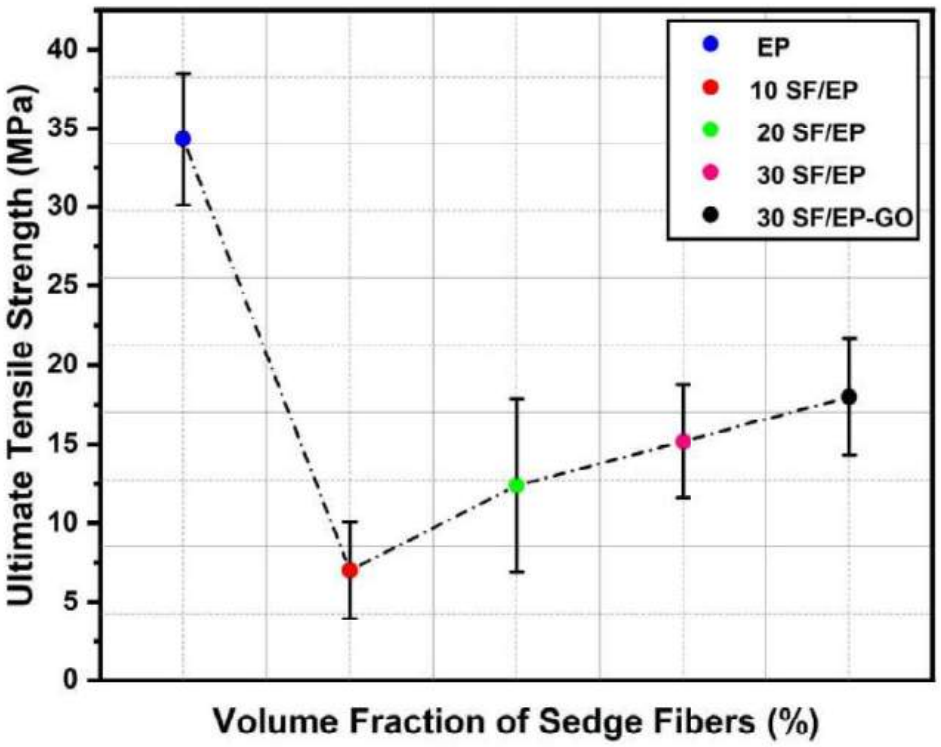

Figura 4.35 – Tensile strength for the present nanocomposite 30 SF/EP-GO investigated and the other conditions previously reported.

FIG. 4.36 illustrates a tendency for the modulus of elasticity to increase as the reinforcement content increases. This is probably related to the stiffness provided by the fibers. In the case of 30 SF/EP-GO, there was a decrease in the modulus of elasticity. This could be due to the GO reducing the movement of the polymer chain and the high aspect ratio of the nanomaterial. Similar observations were reported for other polymer nanocomposites reinforced with GO (KONG et al., 2012; ZHAO et al., 2010; GAFSI et al., 2021). Thus, only the condition that exceeded the EP was 30 SF/EP-GO. With regard to the total strain graph, the reinforcements did not vary significantly within the standard deviation range. However, there was a tendency for the average values to increase.

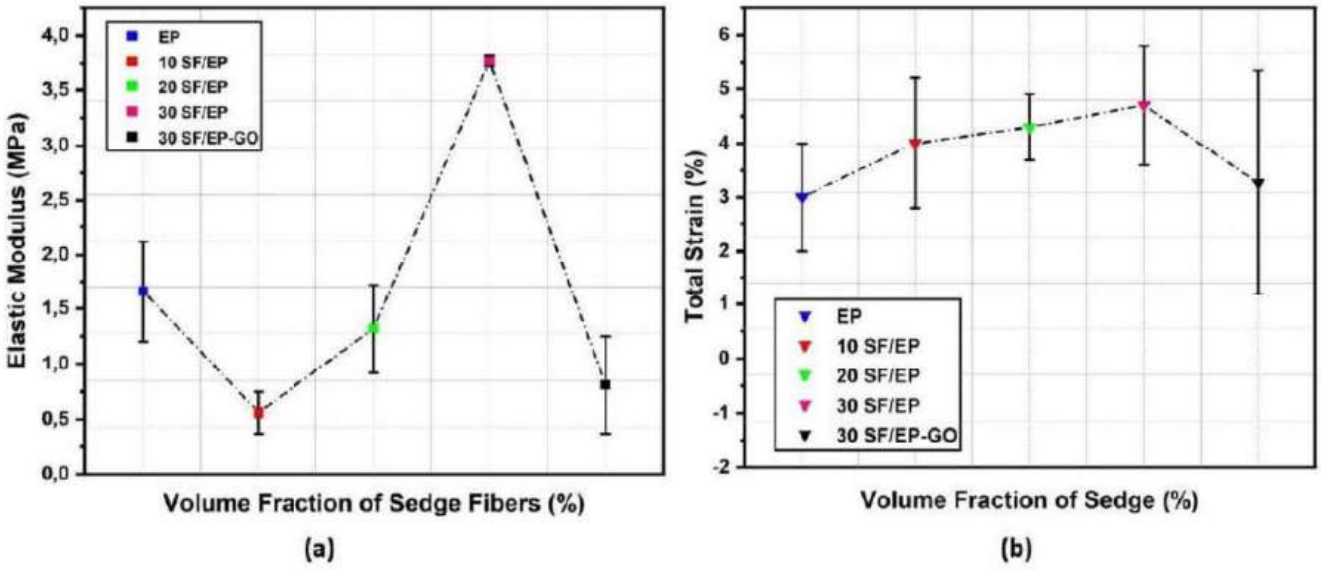

Figura 4.36 – (a) elastic modulus and (b) strain of EP, 10 to 30 SF/EP, and 30 SF/EP-GO conditions.

The fracture mechanisms that arose during the process can be clearly seen in the micrographs present in FIG. 4.37. According to FIG. 4.37 (a), it is possible to observe an agglomeration of GO nanosheets with some re-stacking which may affect the improvement in mechanical properties. In addition, in (b) it is possible to observe the presence of river marks, which is indicative of the existence of a brittle fracture mechanism. While in (c) the pullout mechanism occurs, in addition to the presence of broken fibers and an absence of the delamination mechanism. This absence is also observed in (d) to (f), indicating that hydrogen bonds and even ionic interactions contribute to a stronger interfacial resistance. Moreover, in (f) it is still possible to see a crack in the matrix. All these fracture mechanisms, especially the absence of delamination mechanisms, contribute to an increase in tensile strength compared to the other conditions.

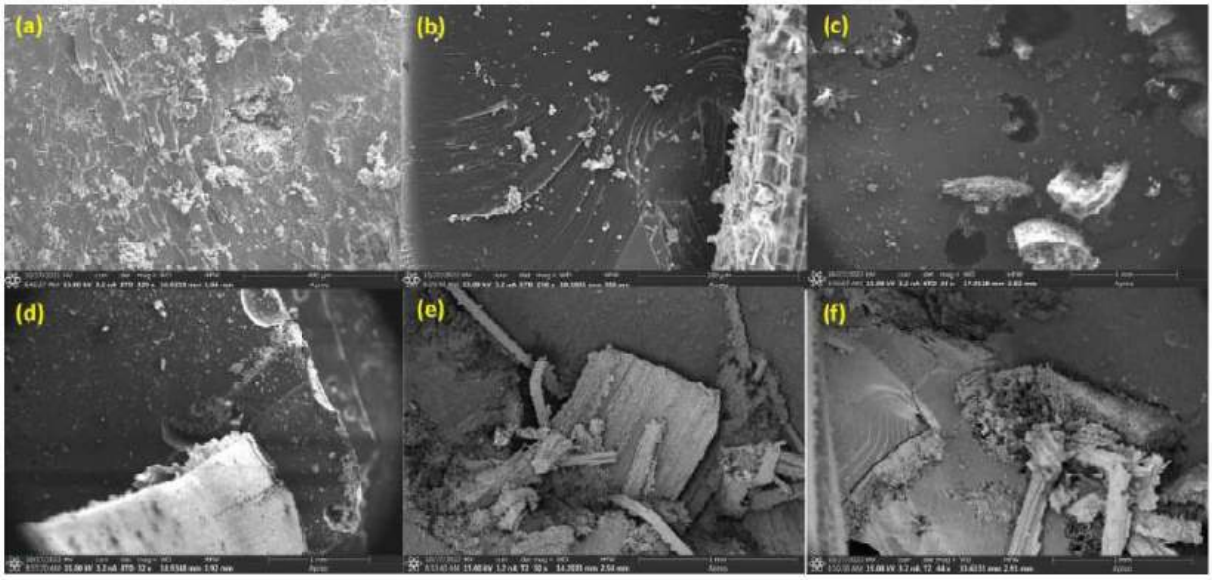

Figura 4.37 – Micrographs of the fracture surfaces after the Tensile Test.

TAB. 4.19 displays ANOVA for the tensile strength of the conditions investigated to check if there is a significant difference between the results.

Tabela 4.19 – Analysis of variance of the ultimate tensile strength for the composites 10 to 30 SF/EP, EP and 30 SF/EP-GO.

Causes of Variation	Sums of squares	Degrees of freedom	Mean Square	F (calculated)	Fc (tabulated)
Treatments	3	453.3	151.10	**9.56**	**3.24**
Residue	16	252.88	15.8		
Total	19	706.19			

This analysis shows that the hypothesis that the means are equal at a significance level of 5% is rejected, because the F calculated (9.56) is greater than the F tabulated (3.24). It is therefore possible to state that the different reinforcement contents of the composites have different effects on the performance of the materials when subjected to tensile stress. The Tukey's test was used to compare the means, applying a confidence level of 95% in order to verify which conditions provided the best behavior. The value found for HSD was 4.71 MPa and TAB. 4.20 depicts these results.

Tabela 4.20 – Results for the differences between the mean values of the ultimate tensile strength after applying the Tukey's test.

Conditions	10 SF/EP	20 SF/EP	30 SF/EP	30 SF/EP-GO
10 SF/EP	0	4.35	**10.54**	**11.75**
20 SF/EP	4.35	0	**6.19**	**7.39**
30 SF/EP	**10.54**	**6.19**	0	**1.21**
30 SF/EP-GO	**11.75**	**7.40**	1.21	0

As shown, the 30 SF/EP-GO and 30 SF/EP conditions showed significant differences compared to 10 and 20 SF/EP. However, there was no superior difference between the 10 and 20 groups and between 30 SF/EP and 30 SF/EP-GO. Therefore, even though GO contributed to an improvement in mechanical performance, it was not enough in the 0.1 wt.% condition. Thus, it did not contribute to a significant improvement in properties related to the tensile test.

4.3.10 COMPRESSION TEST

TAB. 4.21 shows the results of the compressive stress and average maximum strain for the specimens tested. In addition, FIG. 4.38 displays a comparison of the compressive stress of the different reinforcement conditions. It can be seen that the condition that suffered the greatest percentage strain was 30 SF/EP-GO, followed by 10 SF/EP. According to the graph and table, there is a tendency for the percentage of reinforcement to increase. However, the improvement was not as significant, including the nanocomposite. Compared to the tensile and flexural strength results, all showed little increase in the mechanical properties of the composites compared to the 30 SF/EP condition.

Tabela 4.21 – Mean percentage strain and compression strength obtained by the compression test of the EP, 10 to 30 SF/EP and 30 SF/EP-GO conditions.

Conditions	Compression strength (MPa)	Total Strain (%)
10 SF/EP	18.51 ± 1.50	25.71 ± 10.36
20 SF/EP	20.44 ± 2.49	13.81 ± 4.45
30 SF/EP	21.21 ± 1.45	15.19 ± 4.69
30 SF/EP-GO	25.55 ± 2.82	37.58 ± 10.53

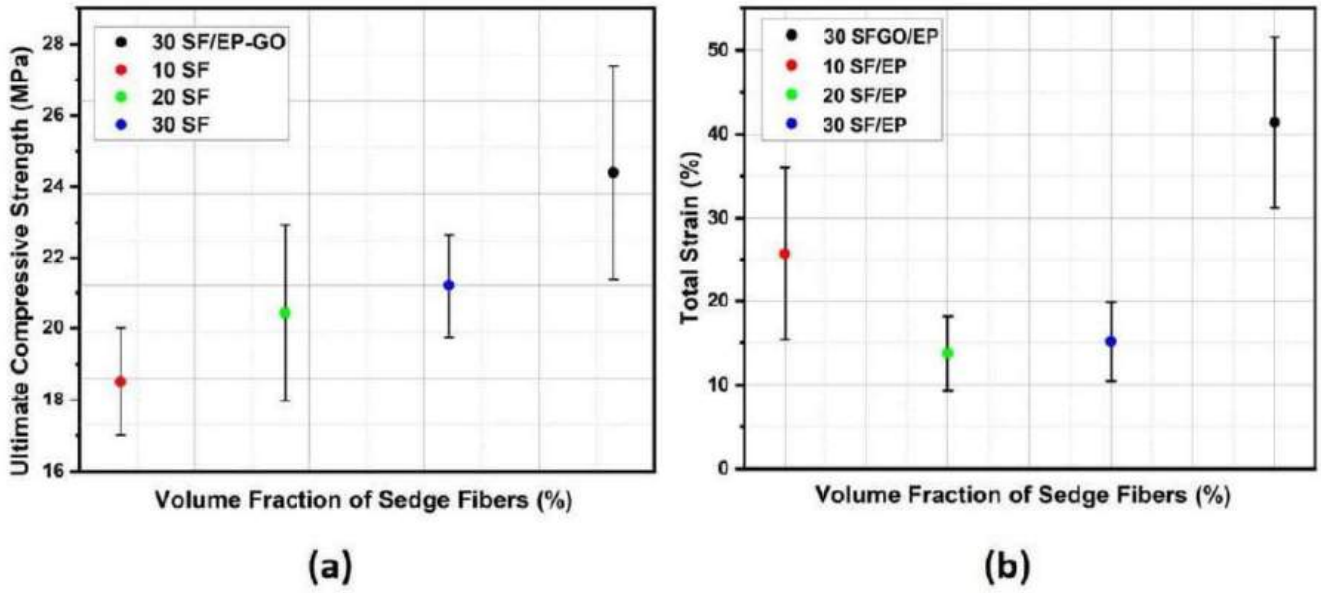

Figura 4.38 – (a) compressive strength and (b) total strain for the EP, 10 to 30 SF/EP, and 30 SF/EP-GO conditions.

In order to investigate the fracture mechanisms present after the compression test, micrographs were analyzed according to FIG.4.39. From micrograph (a), it can be seen that there has been a detachment of the epoxy matrix along with the presence of good adhesion between the fiber/matrix interface. Likewise, items (b) and (c) show good interfacial adhesion, which may be an indication that the addition of GO was beneficial to the composite material. In addition, item (b) shows another type of epoxy matrix mechanism related to crack propagation without preferential direction. While in (c) it can be seen that the pullout mechanism has occurred. Micrograph (d) shows bending at the ends of the sedge fiber. In addition, (e) and (f) the fracture mechanisms present refer to the breaking of the sedge fibers. Finally, (f) indicates a propagation of cracks in the fiber, which is a possible mechanism for initiating fiber breakage. Both FIGs. show again detachment from the matrix.

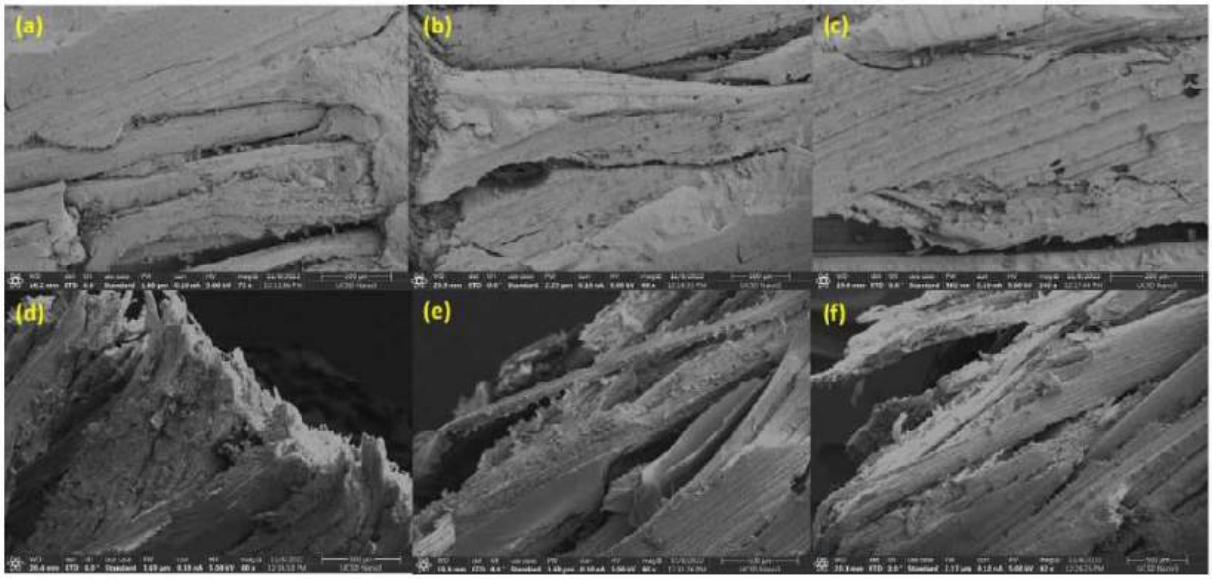

Figura 4.39 – Micrographs of the fracture surfaces after the compression test.

TAB. 4.22 displays ANOVA for the compressive stress of the conditions investigated to see if there is a significant difference between the results.

Tabela 4.22 – Analysis of variance of ultimate compressive stress for EP, 10 to 30 SF/EP and 30 SF/EP-GO.

Causes of Variation	**Sums of squares**	**Degrees of freedom**	**Mean Square**	**F (calculated)**	**Fc (tabulated)**
Treatment	3	155.06	51.69	**10.22**	**3.24**
Residue	16	80.94	5.06		
Total	19	236.00			

This analysis shows that the hypothesis that the means are equal at a significance level of 5% is rejected, since the F calculated (10.22) is greater than the F tabulated (3.24). It is therefore possible to state that the different conditions investigated have different effects on the performance of the materials when subjected to tensile stress. The Tukey's test was used to compare the means, applying a confidence level of 95% in order to verify which conditions provided the best behavior. The value found for HSD was 2.97 MPa and TAB. 4.23 depicts these results.

Tabela 4.23 – Results for the differences between the mean values of the ultimate compressive strength after applying Tukey's test.

Conditions	10 SF/EP	20 SF/EP	30 SF/EP	30 SF/EP-GO
10 SF/EP	0	1.13	2.24	**7.29**
20 SF/EP	1.13	0	1.10	**6.15**
30 SF/EP	2.24	1.10	0	**5.05**
30 SF/EP-GO	**7.29**	**6.15**	5.05	0

According to the above, the 30 SF/EP condition is the only one to show a significant difference compared to the other conditions. This indicates that the GO effectively contributed to a significant improvement in performance for the properties related to the compression test. Thus, the only mechanical test in which the nanocomposite failed to effectively show a significant difference between the 30 SF/EP condition was in the tensile test. However, only the impact tests were able to outperform the control group.

It has been pointed out extensively in the literature that poor dispersion of the nanomaterial can be solved by some chemical modifications in order to improve the particle-matrix bond. It is therefore an excellent alternative for improving the mechanical performance of nanocomposites. Some authors in the literature use different nomenclatures to refer to the functionalization of GO, i.e. the addition of functional groups through chemical synthesis. of functional groups through chemical synthesis. These GO nomenclatures can be found in the literature as modified graphene oxide (mGO) (HE et al., 2017b; HE et al., 2019; LIU et al., 2019; MCCREARY et al., 2019), GO derivatives (HE et al., 2017a) and functionalized graphene oxide (f-GO) (DIVAKARAN et al., 2020; HAZARIKA et al., 2018). In general, they have a higher mechanical performance than GO, without the need to add more percentage. This makes the modification economically viable, as well as avoiding undesirable agglomerations.

4.4 EPOXY MATRIX REINFORCED WITH SEDGE FIBERS COATED BY GRAPHENE OXIDE (GO)

4.4.1 DYNAMIC MECHANICAL ANALYSIS (DMA)

FIG. 4.40 shows the E' curve as a function of ambient temperature up to 200 °C for the 30 SFGO/EP condition. It can be inferred that an increase in temperature led to a decrease in E', occurring from 50 to 150 °C. While the drop in the E' curve began at 79 °C for the 30 SFGO/EP condition, it was very similar to the behavior exhibited by 30 SF/EP-GO and 10 to 30 SF/EP. Therefore, it can be inferred that the investigated new treatment condition did not show a significant change in the E' value. Furthermore, TAB.

4.24 illustrates values for E', loss modulus (E"), and Tan δ for the 30 SFGO/EP condition compared to the EP, 10 to 30 SF/EP conditions.

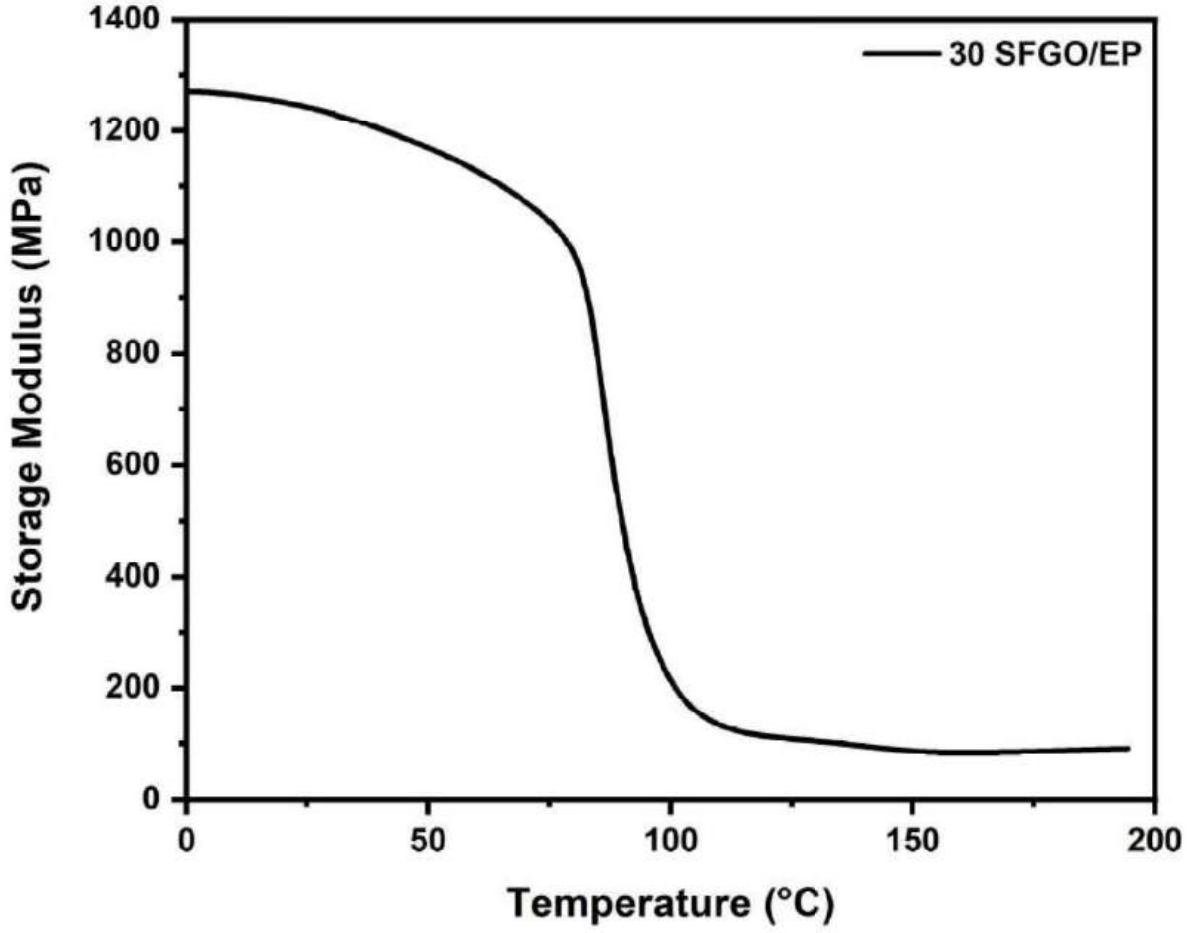

Figura 4.40 – Storage modulus variation with temperature for the 30 SFGO/EP nanocomposite.

Tabela 4.24 – Main Parameters for DMA storage modulus (E'), loss modulus (E") and tangent delta (Tan δ) for the investigated materials.

Composites	**E' at -50 °C (MPa)**	**E' at 25 °C (MPa)**	**E" (MPa)**	**Tan δ**	**T_g (°C)**
EP	3066	2380	200	0.458	129
10 SF/EP	1956	1766	188.5	0.579	117
20 SF/EP	1579	1441	168	0.602	106.5
30 SF/EP	1967	1832	201	0.737	99
30 SFGO/EP	-	1244	128.2	0.413	100.5

FIG. 4.41 displays the E"curve as a function of temperature for the SFGO/EP condition. It can be observed in the E"curve that it reached a maximum peak in the T_g region, at around 89 °C. Additionally, it can be seen that the T_g region started around 78

°C. Therefore, below this latter value, the region represents the material as hard and rigid, consequently, the loss modulus is low and constant. High energy dissipation, with the modulus reaching a maximum peak (around 128 MPa), represents the T_g of the system. This condition presents the lowest value when compared to the nanocomposite 30 SF/EP-GO E"(145 MPa) and EP (200 MPa), for example. Therefore, it can be deduced that, similar to E', the GO structure acted as a filler, further restricting molecular movement and reducing the viscoelastic friction capacity of the matrix.

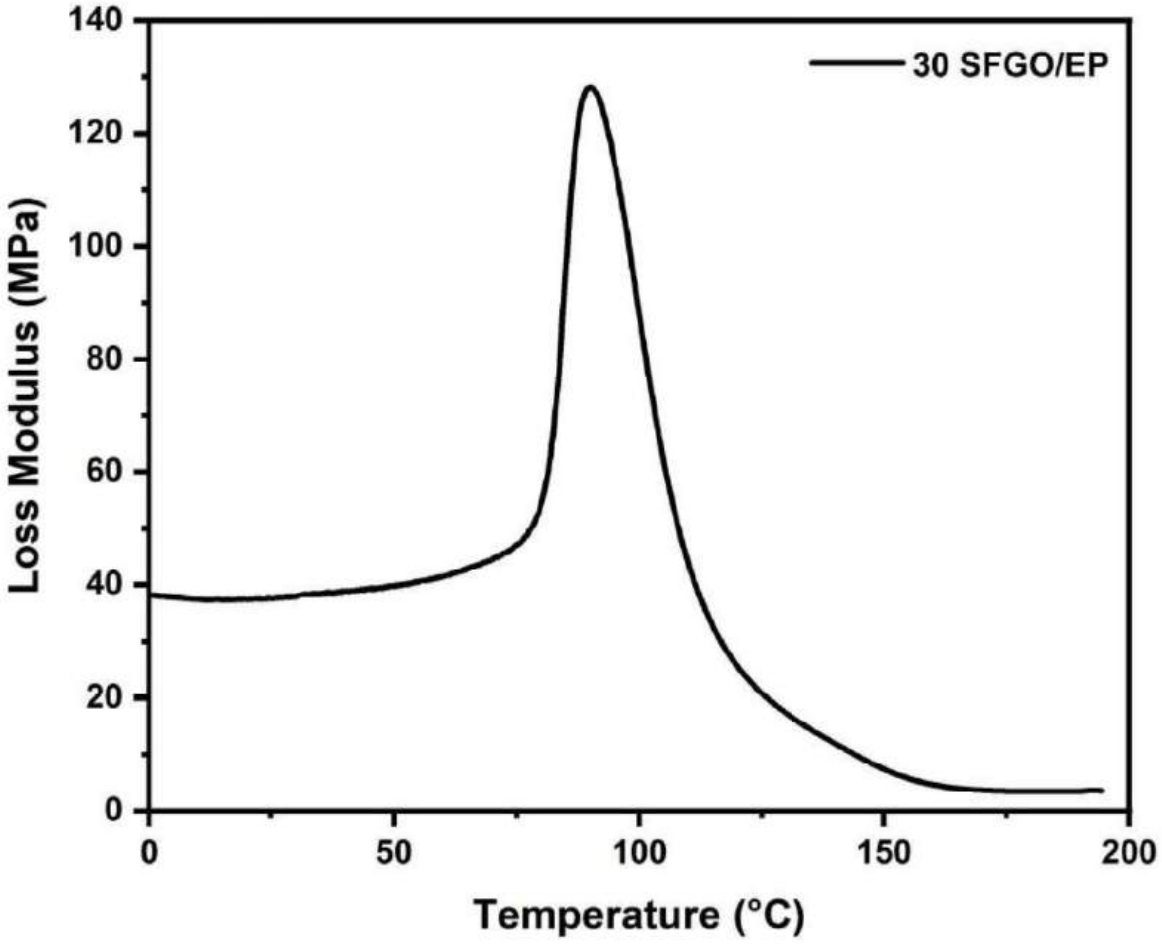

Figura 4.41 – Loss modulus variation with temperature for the 30 SFGO/EP nanocomposite.

FIG. 4.42 illustrates the damping property's behavior as a function of temperature for the SFGO/EP condition. The Tan δ value was approximately 0.41, contrasting with all Tan δ values of the composites (0.55-0.75) and EP (0.46). The reduced peak height of the EP and SFGO/EP conditions can be attributed to a polymer chain with restricted movement (JESUAROCKIAM et al., 2019). Indicating that the present nanocomposite has a strong interfacial interaction, similar to the control group, resulting in lower energy dissipation at the interface (HAZARIKA; MANDAL; MAJI, 2014; NAVEEN et al., 2019). Furthermore, it can be noted that Tan δ decreased when GO was incorporated into the

30 SF/EP condition from 0.75 to 0.41. This may be related to the fact that GO acted as nanoparticles interfering with the movement of EP molecules more intensively than in the 30 SF/EP-GO nanocomposite, as suggested by the E"results. Moreover, the final T_g range occurred at a higher temperature (around 158 °C) compared to 30 SF/EP (98 °C) and EP (131 °C).

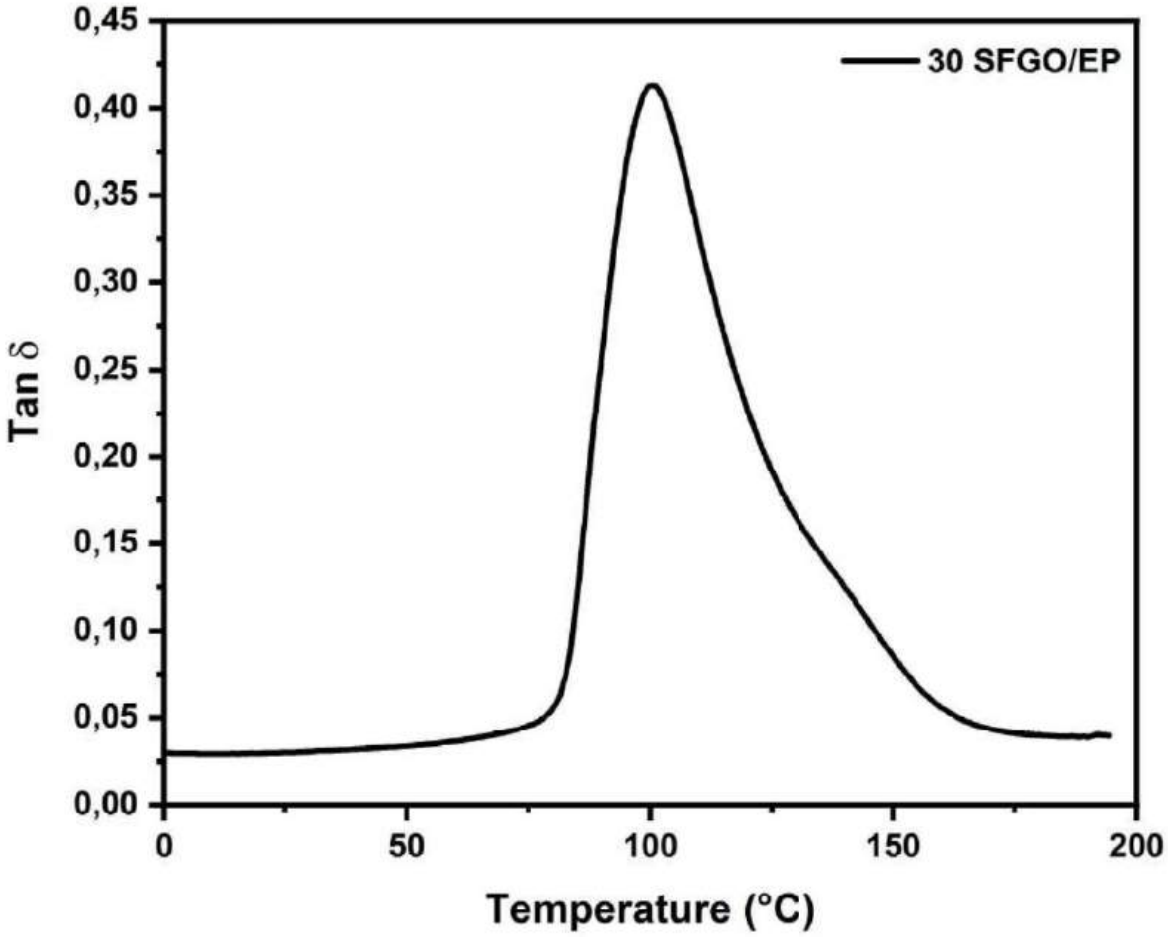

Figura 4.42 – Tan δ variation with temperature for the 30 SFGO/EP nanocomposite.

FIG. 4.43 illustrates a much less irregular curve when compared to the EP, 10 to 30 SF/EP, and 30 SF/EP-GO conditions analyzed. It can be inferred that the curve of the SFGO/EP condition presents a more homogeneous dispersion compared to EP. Particularly, the effect of GO functionalizing SF promoted an opposite behavior to the Cole-Cole curve of 30 SF/EP-GO, indicating that the nanoreinforcement did not show significant heterogeneous dispersions within the matrix.

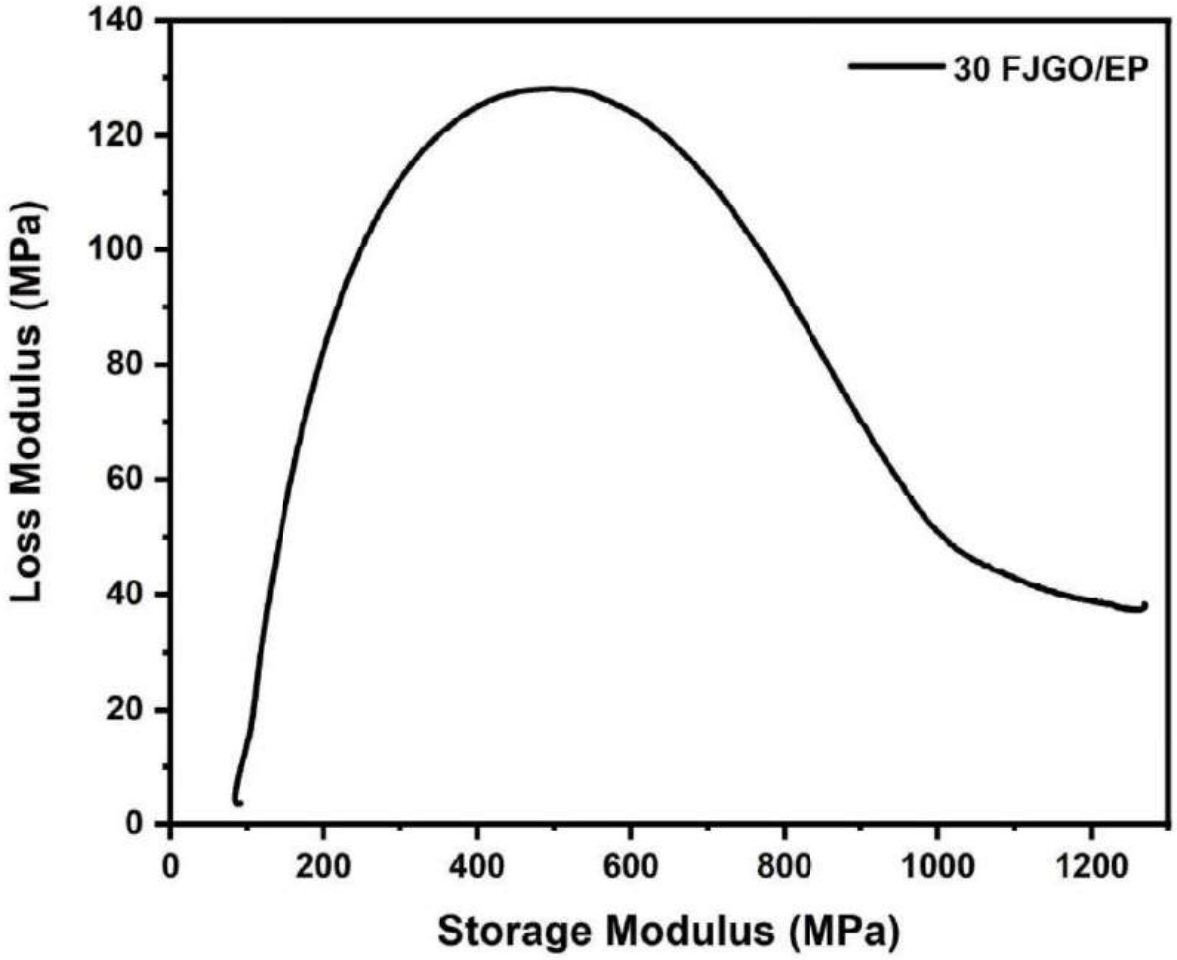

Figura 4.43 – Cole-Cole curve for the 30 SFGO/EP nanocomposite.

As can be seen from TAB. 4.25, the lowest value found for the effectiveness coefficient was in the nanocomposite 30 SFGO/EP, indicating a higher reinforcement efficiency compared to the other conditions. Therefore, the investigation aimed at verifying the effectiveness of GO in promoting a stronger interfacial bond was positively satisfactory. Furthermore, it became evident, compared to previous results, that GO functionalizing SF exhibited better performance than its incorporation into the EP matrix.

Tabela 4.25 – Effective coefficients (C) for all SF/EP composites, EP and the 30 SFGO/EP nanocomposite.

Conditions	**Tan δ (25 °C)**	**E' glassy (25 °C)**	**E"rubbery (165 °C)**	**C**
EP	0.03707	2380	31	-
10 SF/EP	0.04020	1766	48	0.479
20 SF/EP	0.03188	1441	45	0.417
30 SF/EP	0.03077	1832	44	0.542
30 SFGO/EP	0.03916	1244	85	0.191

4.4.2 THERMOMECHANICAL ANALYSIS (TMA)

The FIG. 4.44 shows the TMA curve for the condition 30 SFGO/EP, as well as the T_g. The latter was found at the value of 127 °C determined from the inflection of the TMA curve. The jute fibers coated with GO have a higher value than the other conditions of EP, 30 SF/EP, and 30 SF/EP-GO. Therefore, it can be inferred that the 30 SFGO/EP condition enhances the thermal stability of the material. This occurs because the GO incorporated into SF provides greater restriction to macromolecular mobility than functionalizing the epoxy resin.

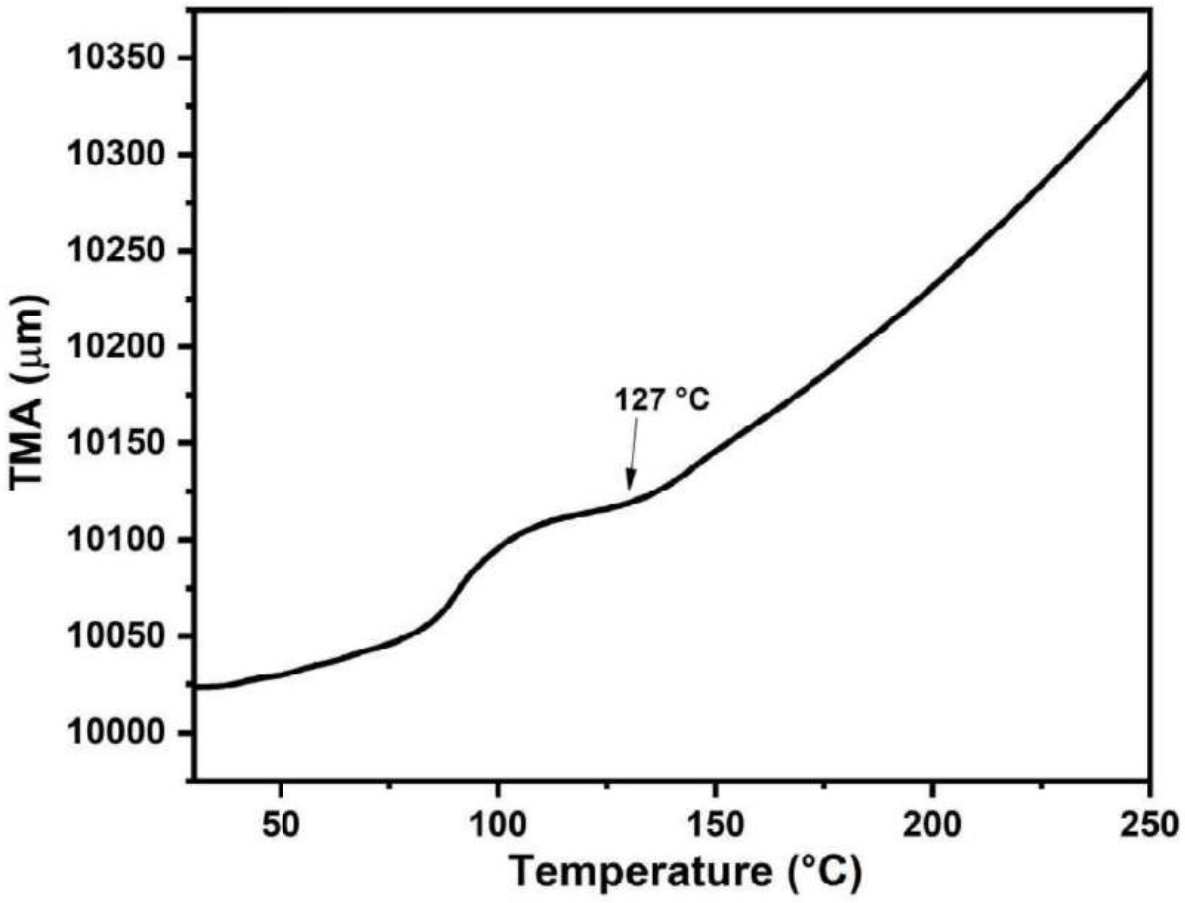

Figura 4.44 – Temperature dependence of the thermomechanical analysis for the 30 SFGO/EP nanocomposite.

In the TMA experiment, the linear thermal expansion coefficient found was 143.87 x 10^{-6}/°C. As previously mentioned, the increase in the coefficient is due to poor interfacial adhesion of the SF. Therefore, this treatment improved the fiber/matrix interface. Moreover, it proved to be slightly lower than the treatment of 30 SF/EP-G0 (168.03 x 10^{-6}/°C), indicating a higher effectiveness of GO coating the SF than when it is functionalizing the EP.

4.4.3 THERMOGRAVIMETRIC ANALYSIS (TGA/DTG)

The TG and DTG curves are presented in FIG. 4.45, for the 30 SFGO/EP condition. The TG curve highlights that a small mass loss was observed (2.07%) at low temperatures up to 200 °C, associated with moisture removal. The mass loss at this stage was slightly higher than the EP condition (1.63%) while being lower than 30 SF/EP (3.23%) and 30 SF/EP-GO (5.37%). Additionally, the T_{onset} found was 280 °C, and the maximum degradation rate was 309 °C. Both results are lower than all the other conditions investigated. Thus, it can be stated that the thermal stability of the 30 SFGO/EP condition has poorer thermal stability. A possible reason for this reduction is that GO acts by reducing the density of crosslinks, as inferred for the 30 SF/EP-GO condition. The second degradation stage ended with a mass loss of 66.27%, while the last stage concluded with 7.52%. Finally, the final percentage is associated with ash content and structures that did not degrade in the investigated temperature range.

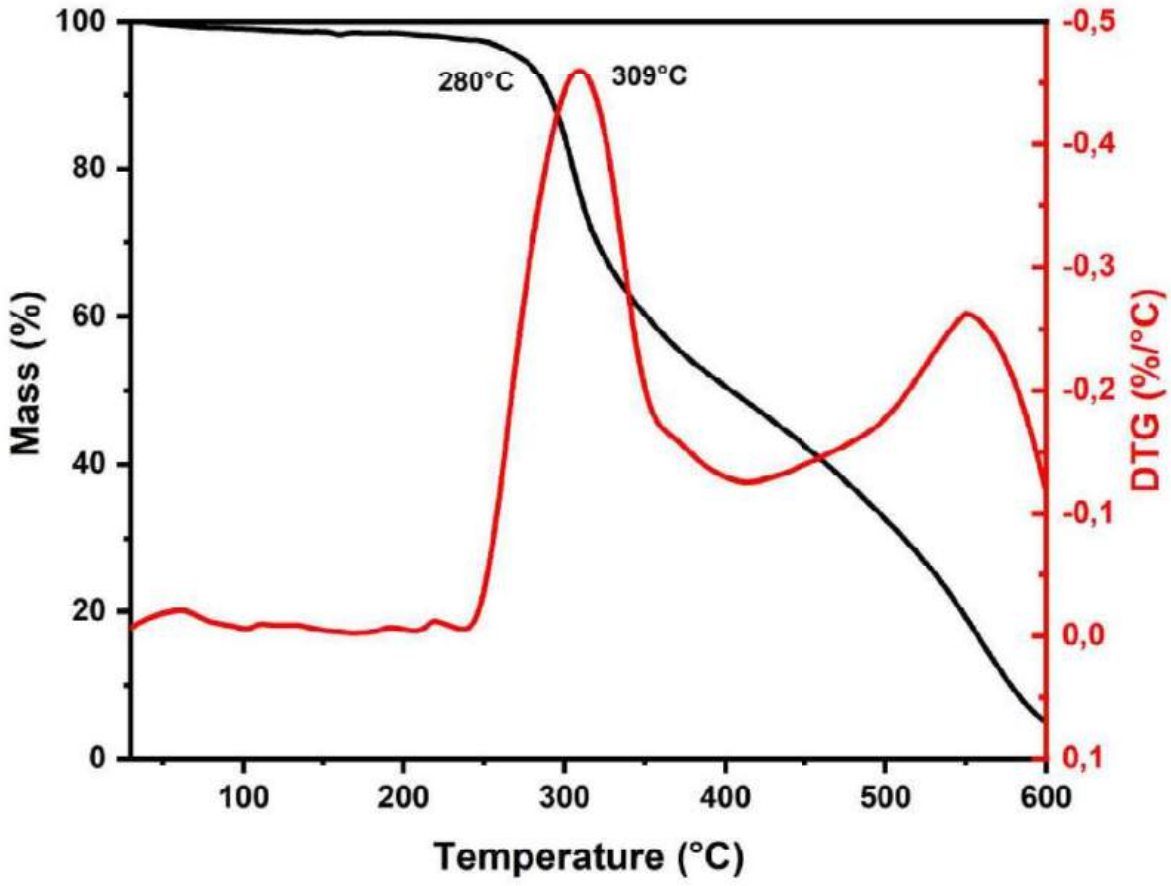

Figura 4.45 – Thermogravimetric curves for the present investigated 30 SFGO/EP nanocomposite.

4.4.4 DIFFERENTIAL SCANNING CALORIMETRY ANALYSIS (DSC)

FIG. 4.46 displays the DSC curve obtained for the 30 SFGO/EP condition. It is possible to observe an endothermic peak at 45 °C, associated with the T_g and release of moisture present on the surface of SF. The following exothermic peak at 75 °C may be associated with the post-curing process. As observed by (NEUBA et al., 2020), all SF/EP conditions presented a higher value for the T_g and post-curing range. The same phenomenon was observed in other studies (XUE et al., 2019; UMER et al., 2015). According to the authors, this occurred because hydroxyl groups present in the basal plane participate in the opening of epoxy rings as a curing agent, acting as a catalyst and accelerating the curing reaction (UMER et al., 2015; ACOCELLA et al., 2016). Additionally, two exothermic peaks related to the degradation of NLFs constituents are present. The first exhibits a peak at 349 °C and can be associated with the degradation of α cellulose (SEKI et al., 2013). The last one at 498 °C refers to the final decomposition of lignin and part of cellulose I (NARAYANASAMY et al., 2020; VRINCEANU et al., 2013).

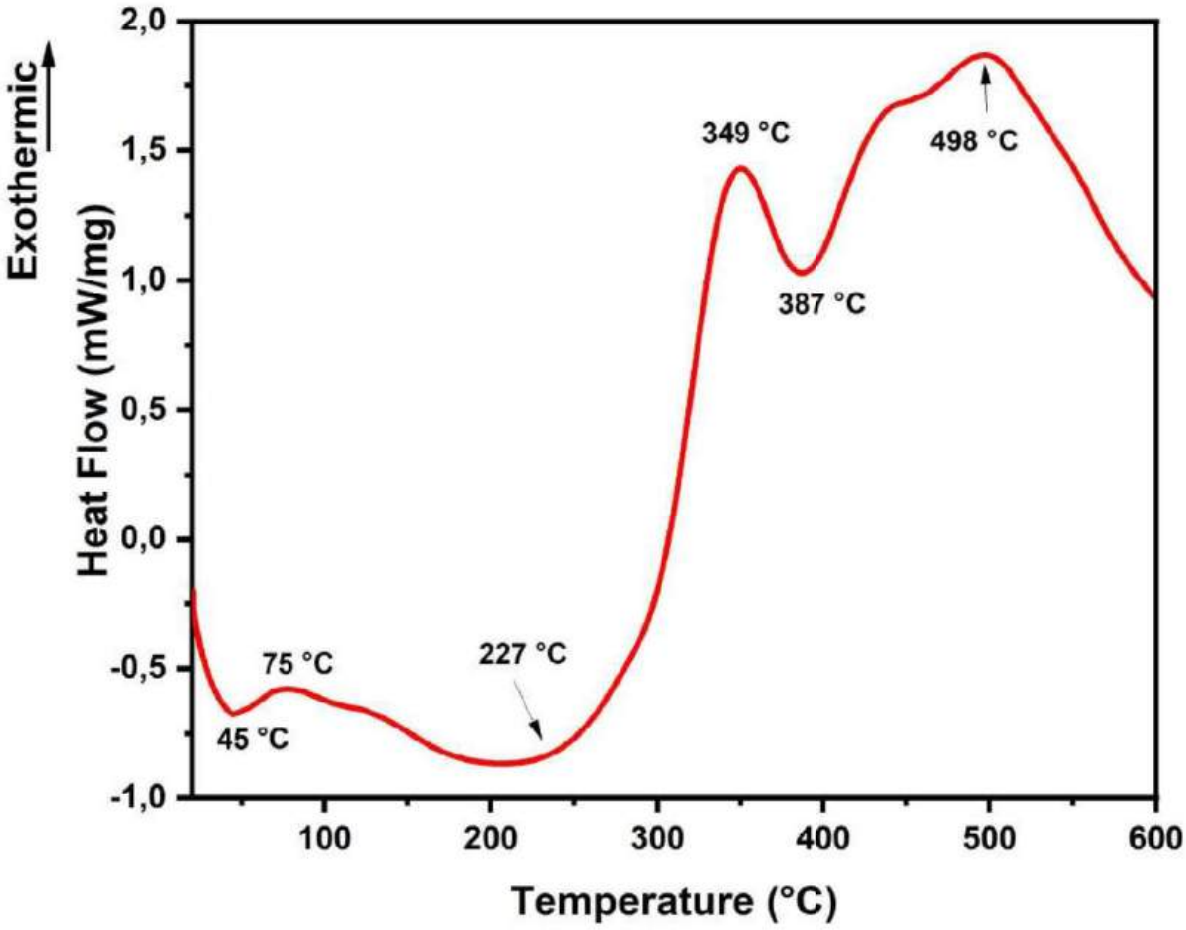

Figura 4.46 – DSC curve for the 30 SFGO/EP condition.

4.4.5 FOURIER TRANSFORM INFRARED SPECTROSCOPY (FTIR)

The FIG. 4.25 displays the spectrum for the 30 SFGO/EP condition. The O-H stretching and functional groups present in the GO nanostructure can be observed at 3422 cm^{-1}. Meanwhile, the C-H stretching is found in the absorption band at 2922 cm^{-1}. The band at 2358 cm^{-1} corresponds to the linkage between organic molecules. In the case of aromatic C=O groups present in the GO nanostructure, the band at 1608 cm^{-1} is directly associated. The aromatic rings appear at 1499 cm^{-1}, indicating that no chemical interaction occurred between them and SF. The vibration at 1461 cm^{-1} is related to the asymmetric bending of the methyl group (CECEN et al., 2008). Additionally, at 1249 cm^{-1}, it is attributed to the CH_2 twisting, and the C-O stretching occurs at 1025 cm^{-1}. The latter is associated with the GO nanosheets and the composite macromolecules. The peak at 826 cm^{-1} is associated with the vibration of C-H linked to the benzene ring (LI et al., 2021; SONG et al., 2020). At 563 cm^{-1}, the C-C stretching occurs. Finally, no significant changes were observed in the nanocomposite spectra.

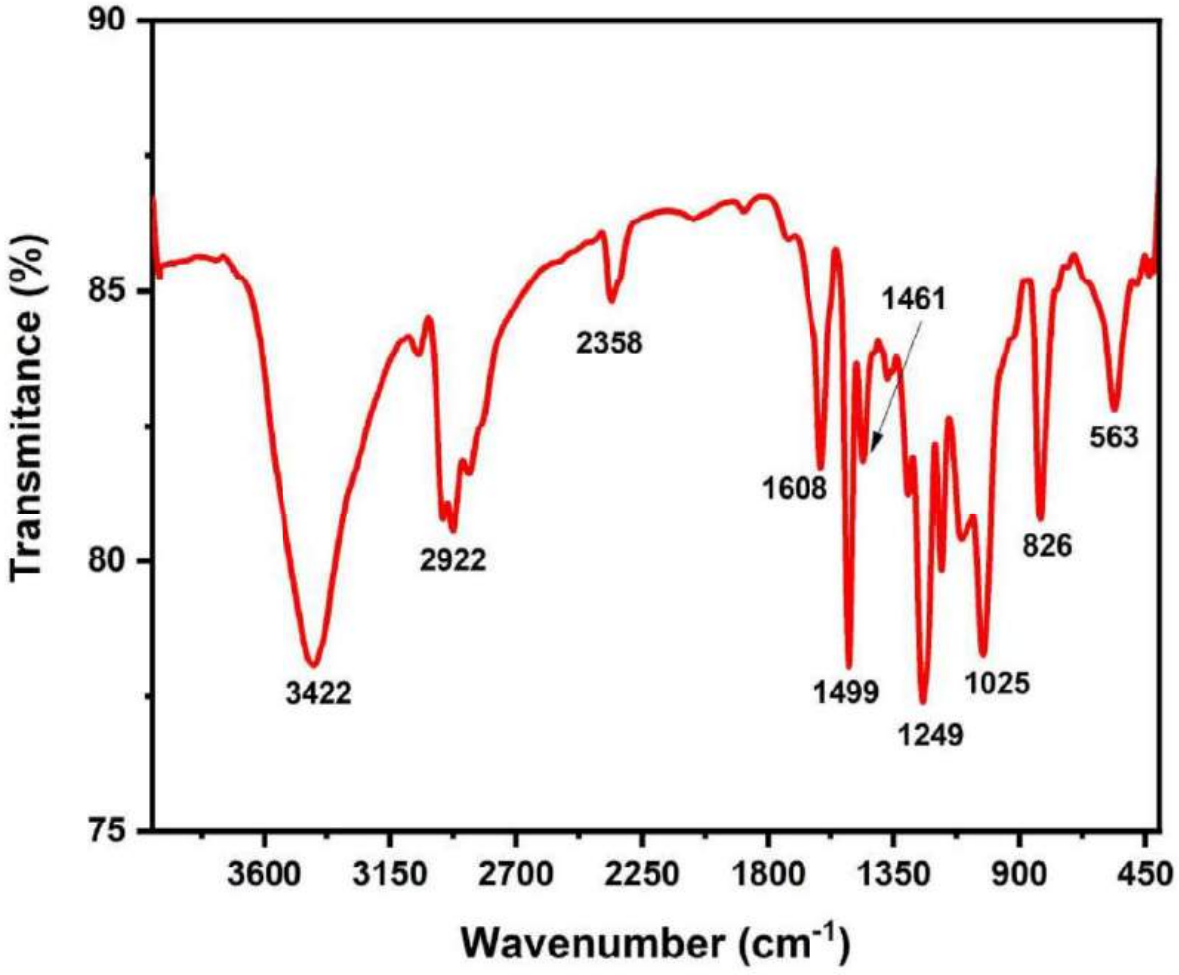

Figura 4.47 – FTIR Spectrum for the 30 SFGO/EP condition.

4.4.6 CHARPY IMPACT TEST

The results obtained for the Charpy impact test of the 30 SFGO/EP condition are presented in TAB. 4.26. The nanocomposite provided a comparatively higher energy absorption compared to the EP, SF/EP, and 30 SF/EP-GO conditions.

Tabela 4.26 – Charpy Impact Energy for samples of the 30 SFGO/EP group.

30 SFGO/EP condition	
Samples	**Impact Energy (J/m)**
1	129.49
2	128.23
3	207.61
4	147.89
5	139.89
6	196.85
7	128.98
Mean	**154.12**
Standard Deviation	**33.77**

A graphical comparison among the current condition, EP, and SF/EP allowed for a better understanding of the increasing trend in Charpy impact energy. Coating SF with GO proved to be considerably beneficial, showing a 1341.12% increase compared to the EP value. Meanwhile, enhancements of 71.95% and 10.74% were achieved compared to the 30 SF/EP and 30 SF/EP-GO conditions, respectively. Thus, the incorporation of GO on the SF surface promoted a better enhancement of energy absorption when compared to the same nanomaterial functionalizing the EP.

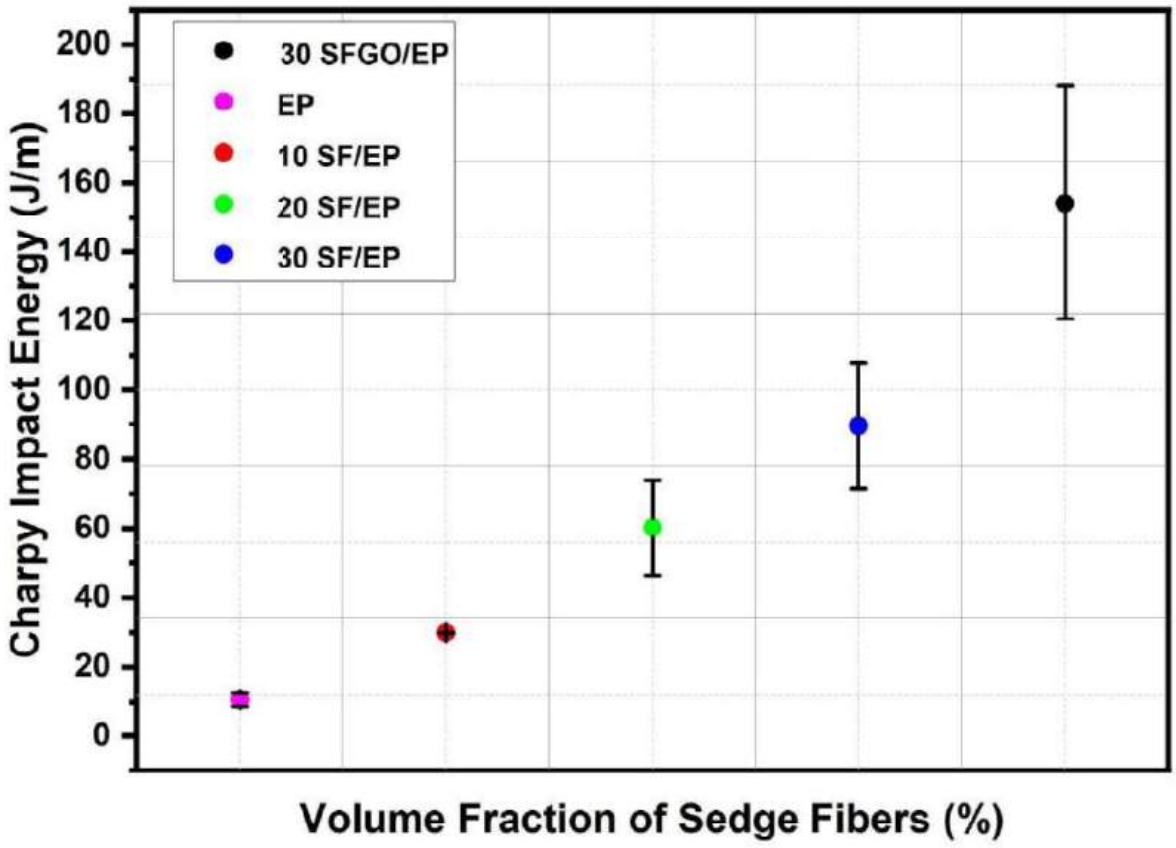

Figura 4.48 – Comparison of impact energy obtained in the Charpy test for EP, 10 to 30 SF/EP, and 30 SFGO/EP conditions.

All samples were completely fractured, as expected, validating the conducted test. Fracture mechanisms were observed through SEM micrographs. Thus, FIG. 4.49 displays the fracture surface of a sample from the 30 SFGO/EP group. It is possible to observe in FIG. 4.49(a) the presence of all expected mechanisms, as per the literature, such as fiber and fibril rupture, initiation and propagation of river marks, *pullout*. Although the *pullout* mechanism occurred, it was not observed in large quantities. These are the main failure mechanisms contributing to energy absorption. Indeed, the material showed good adhesion between the interfaces, with a slight displacement of SF at the interface, as shown in FIG. 4.49(b). This is relevant as it indicates that the incorporation of GO as a coupling agent fulfilled its main function sought in this research, i.e., enhancing the interface. Therefore, it is another alternative for this purpose, in addition to the 30SF/EP-GO condition.

Another crucial experimental observation is the folding of the fiber at the interface under 400x magnification. Possibly, this occurred because the fiber is very hollow, as various micrographs have demonstrated. Furthermore, even with the fiber folding, *pullout* did not occur. The other channels were compressed, and a hypothesis for this phenomenon is the pressing action of the fibers during the composite manufacturing process. Indeed, the presence of strong porosity in SF is in line with what (NEUBA et al., 2022a) reported,

where the authors found a density of 0.46 g/cm^3. Therefore, the air trapped inside the fiber channels will produce a low-density composite and possibly a high-specific-strength nanocomposite.

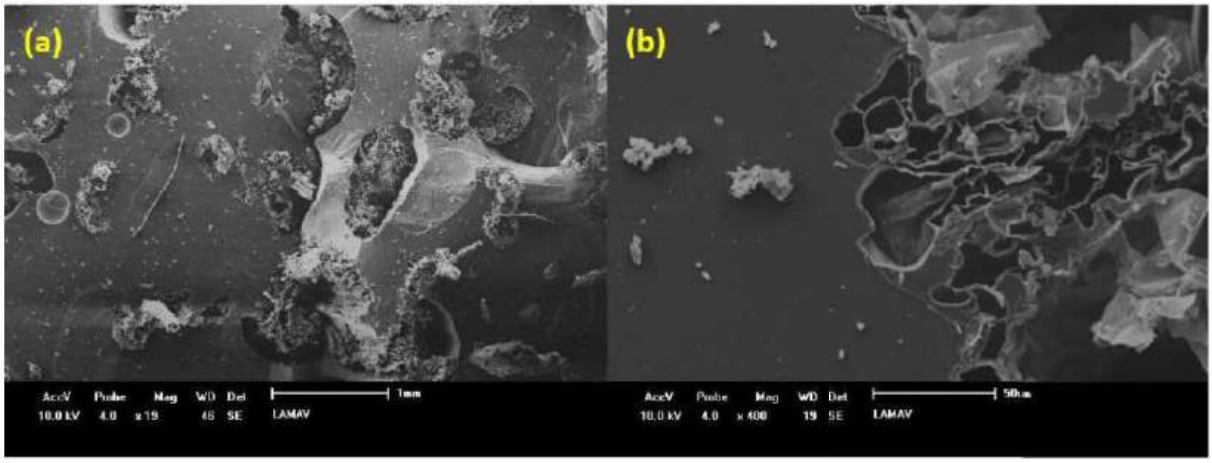

Figura 4.49 – SEM micrographs obtained with magnifications of (a) 19x and (b) 400x.

An ANOVA analysis was conducted to confirm if there is a significant difference between the mean Charpy impact energy results of the investigated conditions. As TAB. 4.27 illustrates, the hypothesis that the means are equal was rejected with a confidence level of 5%. This occurred because the calculated F parameter was higher than the critical F_c. Thus, the existence of a significant difference in the mean Charpy impact energy between the different sample groups was confirmed.

Tabela 4.27 – Analysis of variance of the mean impact energy obtained by the Charpy test for EP, 10 to 30 SF/EP, and 30 SFGO/EP.

Causes of Variation	Sums of squares	Degrees of freedom	Mean Square	F (calculated)	Fc (tabulated)
Treatments	4	72421.6	18105.4	**38.9**	**2.87**
Residue	20	9307.8	465.39		
Total	24	81729.4			

The results for the Tukey test are presented in TAB. 4.28. Differences above the HSD value (28.46) were considered significant. These values are marked in bold and indicate that the 30 SFGO/EP condition was the only one that showed significant differences among all the tested groups.

Tabela 4.28 – Results for the differences between the mean values of impact energy after applying the Tukey's test.

Conditions	EP	10 SF/EP	20 SF/EP	30 SF/EP	30 SFGO/EP
EP	0	17.35	**46.93**	**72.09**	**153.64**
10 SF/EP	17.35	0	**29.57**	**54.74**	**136.28**
20 SF/EP	**46.93**	**29.57**	0	25.17	**106.71**
30 SF/EP	**72.09**	**54.74**	25.17	0	**81.54**
30 SFGO/EP	**153.64**	**136.28**	**106.71**	**81.54**	0

4.4.7 IZOD IMPACT TEST

The TAB. 4.29 presents the average and individual Izod impact energy for each tested sample of the 30 SFGO/EP condition.

Tabela 4.29 – Izod Impact Energy for samples of the 30 SFGO/EP group.

	30 SFGO/EP condition
Samples	**Impact Energy (J/m)**
1	159.15
2	98.13
3	113.02
4	97.15
5	163.49
6	103.98
7	88.89
Mean	**117.68 ± 30.71**

The average Izod impact energy of the 30 SFGO/EP condition was graphically compared with the SF/EP and EP conditions. A considerable increase in energy was observed, highlighting that the incorporation of GO on the SF surface efficiently contributes to the enhancement of energy absorption. This increase was equivalent to 8.46% compared to the 30 SF/EPGO condition, indicating that the effect of GO functionalizing the EP was not as effective as the SF coating. Meanwhile, an increase of 426.06% and 86.79% was achieved compared to EP and 30 SF/EP, respectively. Although the standard deviation is relatively high, the enhancement of the average Izod impact energy was noteworthy.

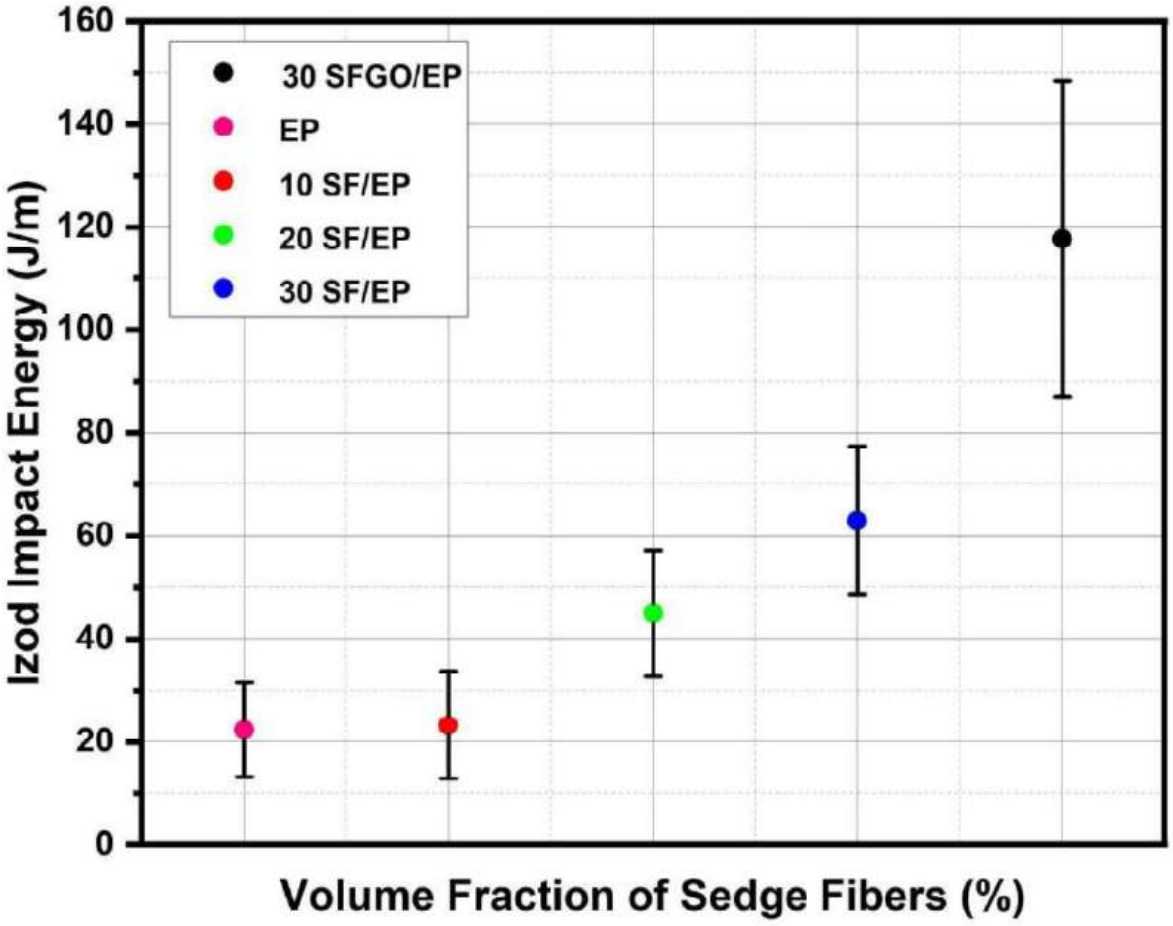

Figura 4.50 – Comparison of the impact energy obtained in the Izod test for EP, 10 to 30 SF/EP, and 30 SFGO/EP conditions.

All tested samples were completely fractured, indicating the validity of the test. An ANOVA analysis was performed to check for a significant mean difference between the average Izod impact energy results of the investigated conditions, as reported earlier in the literature. Thus, TAB. 4.30 reveals that the hypothesis of equivalent means was rejected, with a significance level of 5%. This is because the calculated F parameter was higher than the critical F_c. Therefore, it is confirmed that there is indeed a significant difference in the average Izod impact energy among the analyzed conditions.

Tabela 4.30 – Analysis of variance of the mean impact energy obtained by the Izod test for EP, 10 to 30 SF/EP, and 30 SFGO/EP.

Causes of Variation	Sums of squares	Degrees of freedom	Mean Square	F (calculated)	Fc (tabulated)
Treatments	4	41570.91	10393.73	**40.77**	**2.87**
Residue	20	5097.74	254.88		
Total	24	46668.65			

The results for the Tukey test are presented in TAB. 4.31. The calculated HSD value was 21.06 J/m, and differences above this value are considered significant. These values are shown in bold and indicated that only the 30 SFGO/EP condition had values above the HSD in all comparisons with the other conditions. Thus, the 30 SFGO/EP condition showed the best performance among all groups.

Tabela 4.31 – Results for the differences between the mean values of the average Izod impact energy after applying the Tukey test.

Conditions	**EP**	**10 SF/EP**	**20 SF/EP**	**30 SF/EP**	**30 SFGO/EP**
EP	0	1.97	**35.03**	**54.29**	**110.99**
10 SF/EP	1.97	0	**33.06**	**52.32**	**109.02**
20 SF/EP	**35.03**	**33.07**	0	19.27	**75.96**
30 SF/EP	**54.29**	**52.32**	19.27	0	**56.69**
30 SFGO/EP	**110.99**	**109.02**	**75.96**	**56.69**	0

4.4.8 BENDING TEST

TAB. 4.32 presents the results of the flexural mechanical properties for the EP, 10 to 30 SF/EP, and 30 SFGO/EP conditions.

Tabela 4.32 – Flexural strength properties of the test specimens for EP, 10 to 30 SF/EP, as well as 30 SFGO/EP conditions.

Conditions	**Flexural Strength (MPa)**	**Total Strain (%)**	**Elastic Modulus (GPa)**
EP	41.38 ± 7.02	2.75 ± 0.19	1.19 ± 0.14
10 SF/EP	22.27 ± 6.02	3.02 ± 0.62	0.68 ± 0.18
20 SF/EP	20.78 ± 5.06	2.86 ± 0.56	0.66 ± 0.09
30 SF/EP	24.63 ± 6.75	3.1 ± 0.35	0.83 ± 0,24
30 SFGO/EP	50.51 ± 3.12	1.56 ± 0.24	4.11 ± 0.40

FIG. 4.51 shows a comparison of the average flexural strength for different reinforcement conditions of EP. A considerable improvement in the flexural properties of the 30 SFGO/EP condition was observed compared to 30 SF/EP. Moreover, it was the only condition capable of exhibiting superior mechanical performance to the control group (EP). It showed an increase of 22.06% compared to EP, while in comparison to 30 SF/EP, it showed an increase of 104.99%. Thus, demonstrating better effectiveness in using GO to coat the fiber, as the 30 SF/EP-GO condition exhibited lower mechanical performance than EP. The improvement in mechanical performance can be justified by GO acting as a coupling agent between the hydrophilic fiber and the hydrophobic EP, enhancing the interface.

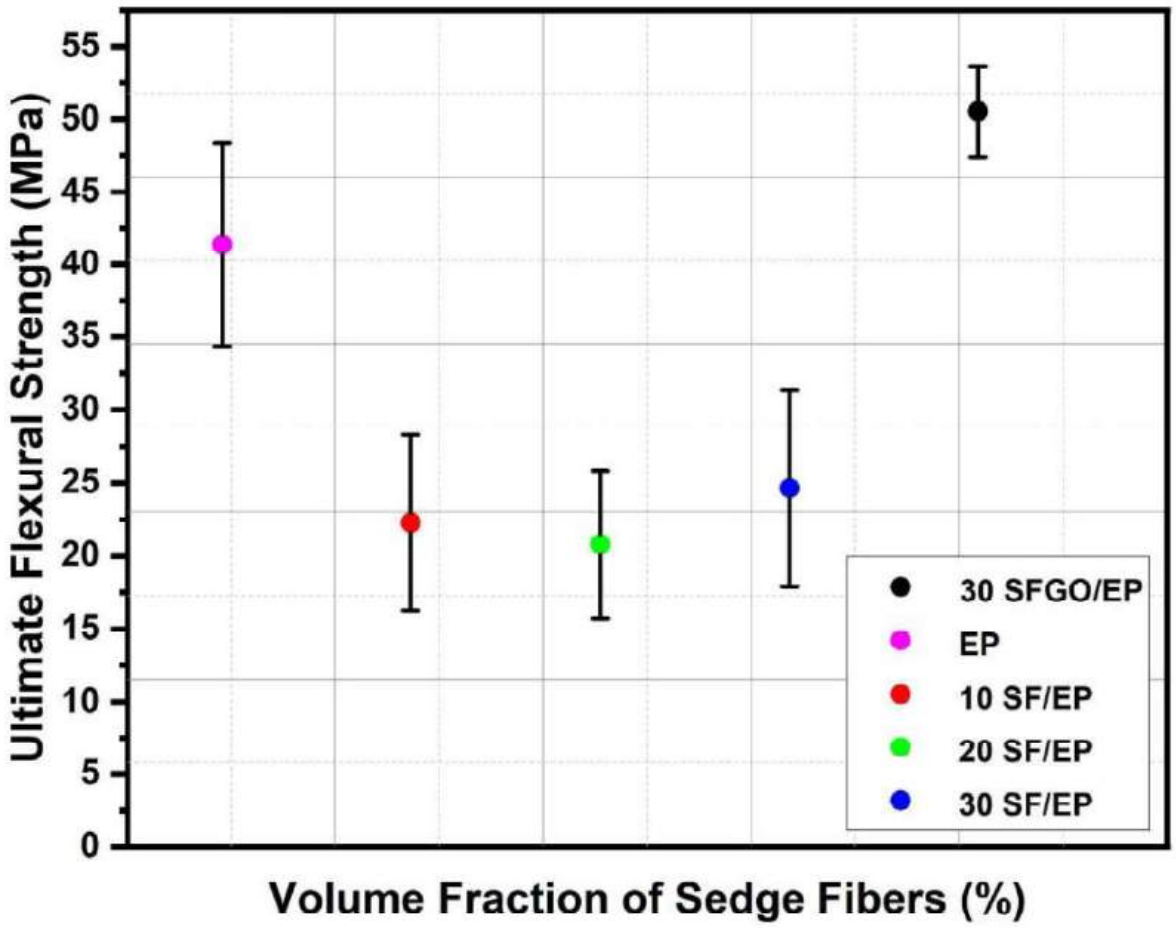

Figura 4.51 – Comparison of flexural strength among EP, 10 to 30 SF/EP, and 30 SFGO/EP conditions.

According to FIG. 4.52(a), it is possible to observe that the modulus of elasticity is significantly increased, being the only condition that exhibited this mechanical property superior to EP. Thus, the substantial increase compared to the latter condition was 345.38%. However, FIG. 4.52(b) revealed that the total strain presented by the investigated condition was lower than all others. Therefore, it can be deduced that toughness was considerably reduced.

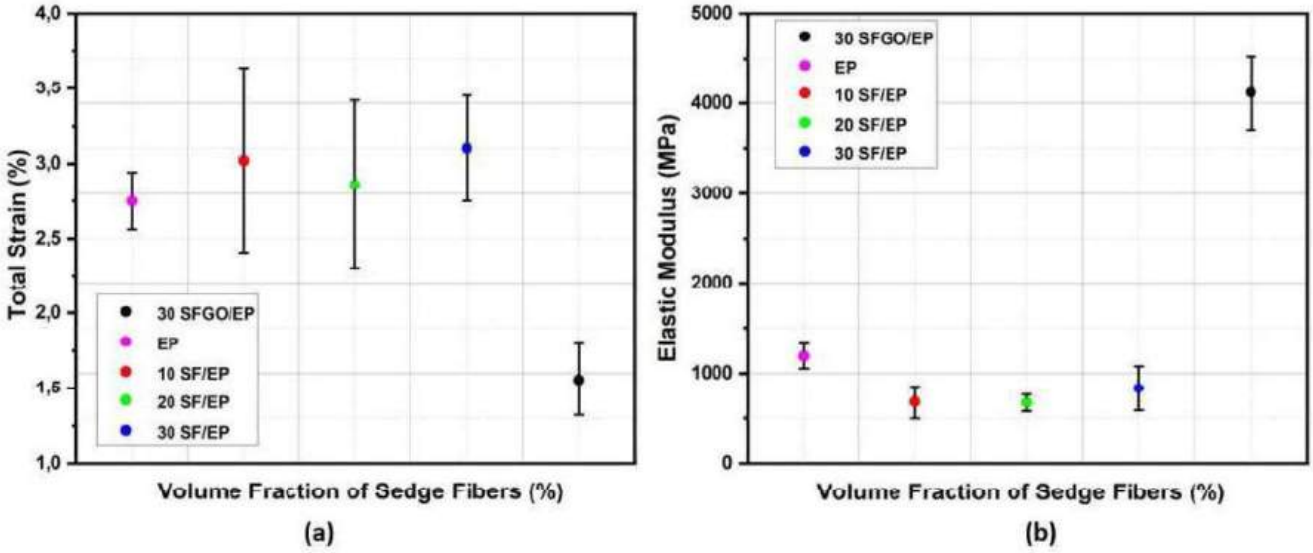

Figura 4.52 – (a) strain and (b) elastic modulus of EP, 10 to 30 SF/EP, and 30 SFGO/EP conditions.

In an attempt to verify failure mechanisms and how they contributed to the flexural mechanical property, SEM analyses were conducted. The micrograph in FIG. 4.53(a) revealed river marks, fiber rupture, and a considerable decrease in delamination between the fiber/matrix interface. This latter mechanism is considered detrimental to the enhancement of mechanical performance, so the addition of GO was considered positive. Meanwhile, Figure 4.53(b) presents the pullout mechanism, fibril rupture, and good adhesion between the fiber/matrix interface. Additionally, in both micrographs, there is no presence of GO clusters near the matrix interface, which could reduce the mechanical performance of the nanocomposite.

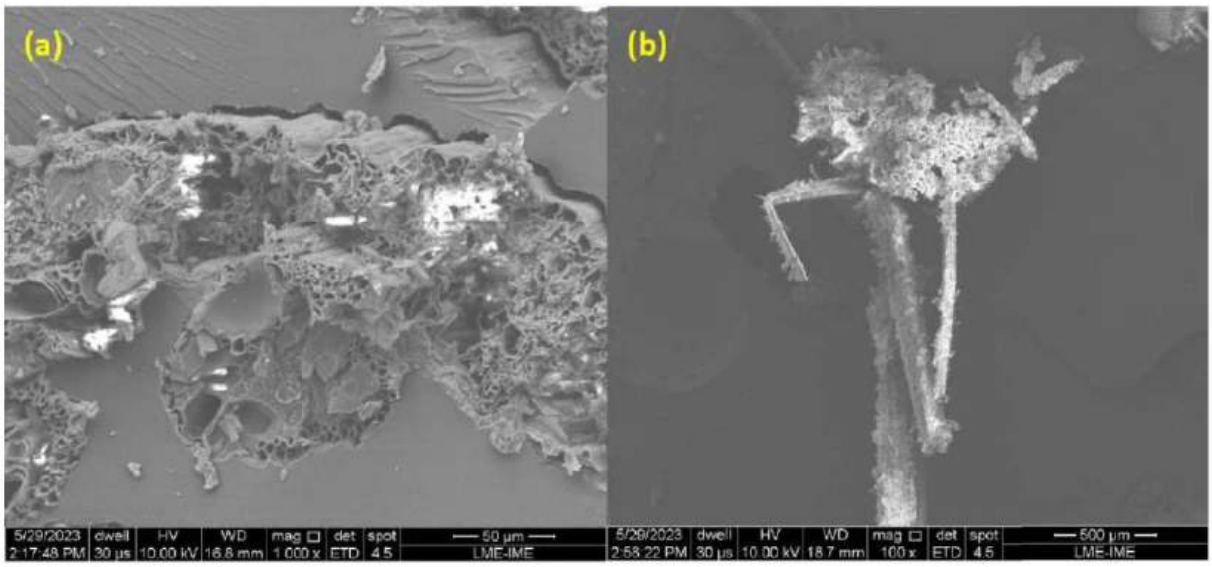

Figura 4.53 – Fracture mechanisms observed microscopically for the 30 SFGO/EP nanocomposite.

In order to understand if there is a significant difference between the average flexural strength, an ANOVA analysis was performed. According to TAB. 4.33, it can be seen that the hypothesis of equal means was rejected, considering a significance level of 5%. This is because the calculated F value (23.04) is greater than the critical F_c. Therefore, the existence of a significant difference in the flexural strength among the different reinforcement conditions was confirmed.

Tabela 4.33 – Analysis of variance of maximum flexural strength for EP, 10 to 30 SF/EP, and 30 SFGO/EP.

Causes of Variation	Sums of squares	Degrees of freedom	Mean Square	F (calculated)	Fc (tabulated)
Treatments	4	2389.98	597.49	**23.04**	**3.05**
Residue	15	388.90	25.92		
Total	19	2778.88			

The Tukey test was conducted to assess which groups exhibit significant differences when compared in pairs. TAB. 4.34 indicated that the 30 SFGO/EP condition was the only composite group that showed a value above the HSD (6.16). Thus, an indication that the 30 SFGO/EP condition differed from the other groups, the same was observed for the EP condition.

Tabela 4.34 – Results for the differences between the mean values of maximum flexural strength after applying the Tukey's test.

Conditions	EP	10 SF/EP	20 SF/EP	30 SF/EP	30 SFGO/EP
EP	0	**12.50**	**14.89**	**16.47**	**12.49**
10 SF/EP	**12.50**	0	2.38	3.97	**24.99**
20 SF/EP	**14.89**	2.38	0	1.58	**27.8**
30 SF/EP	**16.47**	3.97	1.58	0	**28.96**
30 SFGO/EP	**12.49**	**24.99**	**27.38**	**28.96**	0

4.4.9 TENSILE TEST

TAB. 4.35 highlights the mechanical properties obtained from the tensile test of the 30 SFGO/EP condition and compares them with results previously reported in the literature for the EP condition and 10 to 30 SF/EP conditions. These results refer to the mean values and standard deviations of the sample groups.

Tabela 4.35 – Tensile strength properties of test specimens for EP, 10 to 30 SF/EP, as well as 30 SFGO/EP conditions.

Conditions	Tensile Strength (MPa)	Total Strain (%)	Elastic Modulus (GPa)
10 SF/EP	7.0079 ± 3.1	4.04 ± 1.23	0.56 ± 0.19
20 SF/EP	12.4072 ± 5.5	4.3 ± 0.63	1.32 ± 0.40
30 SF/EP	15.1705 ± 3.6	4.66 ± 1.13	3.77 ± 0.05
30 SFGO/EP	35.35 ± 3.04	5.36 ± 2.29	0.67 ± 0.19

Through the graphical comparison shown in FIG. 4.54, it became clearer to observe that the 30 SFGO/EP condition significantly increased performance compared to 30 SF/EP. This increase was equivalent to 133.03%. Meanwhile, compared to the EP resin, there was a slight increase of 3.06%. Additionally, in comparison to the 30 SF/EP-GO condition, the increase was about 96.4%. Therefore, it can be deduced that the incorporation of GO coating on the surface was more effective than the functionalization of EP by the nanomaterial.

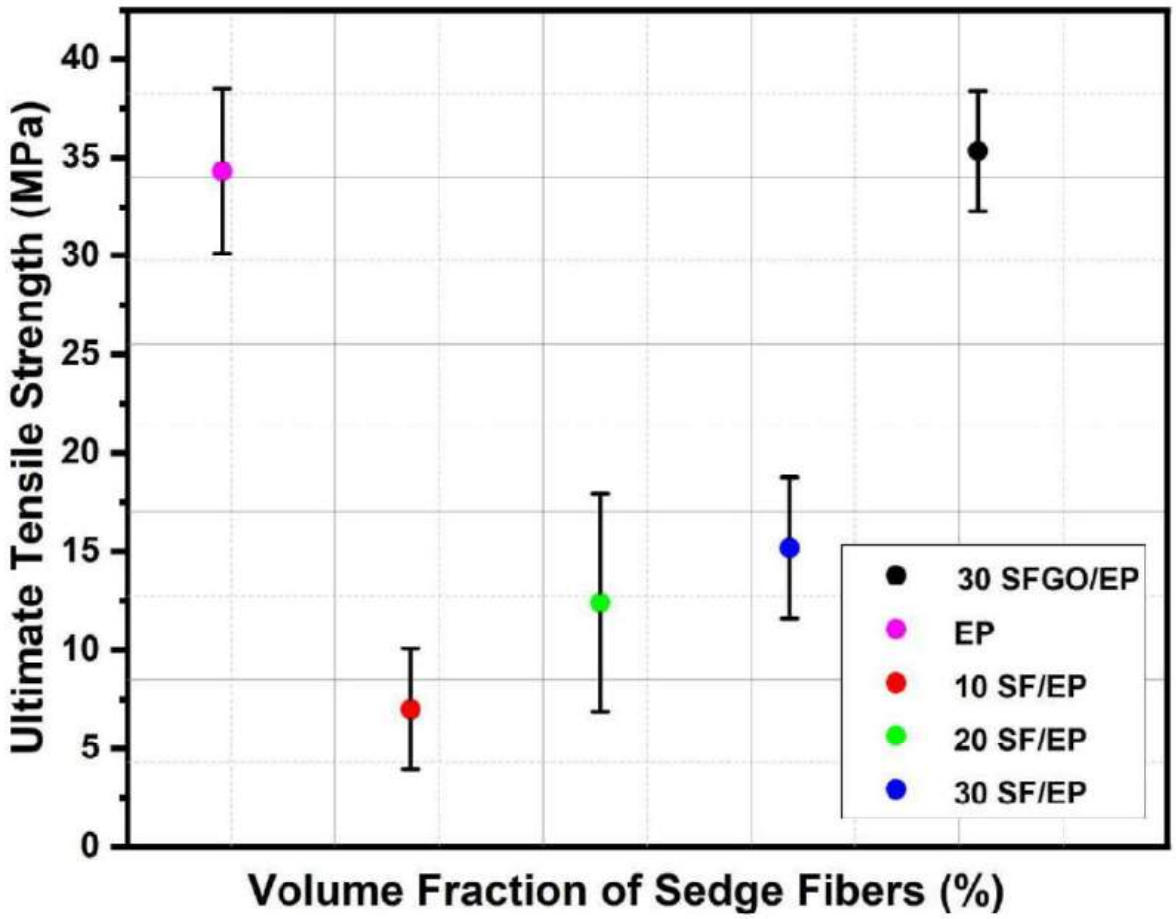

Figura 4.54 – Tensile strength comparison among EP, 10 to 30 SF/EP, and 30 SFGO/EP conditions.

FIG. 4.55(a) highlights the comparison of the modulus of elasticity among the previously mentioned conditions. It was observed that the 30 SFGO/EP condition had the worst performance, negatively impacting the material's toughness. Additionally, this may have been caused by the presence of voids acting as stress concentrators, formed during the curing reaction, leading to premature material failure. Meanwhile, the strain before rupture presented in FIG. 4.55(b) shows a trend of increasing average values. However, the investigated 30 SFGO/EP condition showed a high standard deviation. Once again, the difference in values may be due to premature failures caused by the appearance of voids.

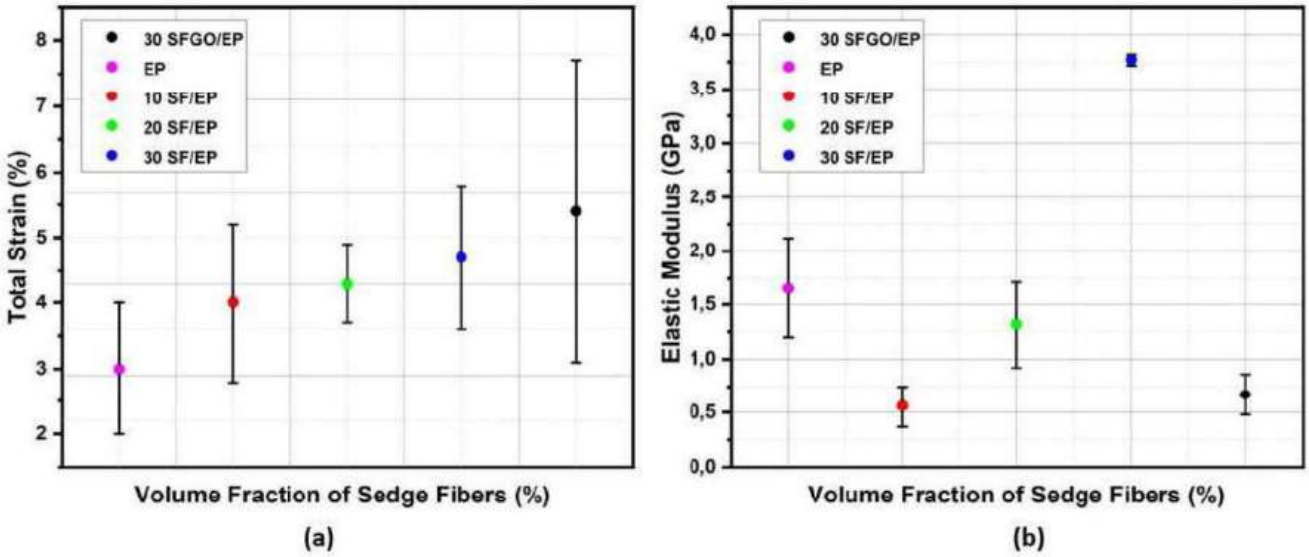

Figura 4.55 – (a) strain and (b) elastic modulus of EP, 10 to 30 SF/EP, and 30 SFGO/EP conditions.

The micrograph represented in FIG. 4.56(a) confirmed the presence of four voids formed near the microregions of the fiber-matrix interface. The existence of these voids negatively impacts the mechanical performance, and possibly without the absence of stress concentrators, the mechanical performance would be significantly superior to the EP condition. Additionally, mechanisms such as river marks, fiber rupture, and pullout were observed, contributing synergistically to the improvement of mechanical performance. In both micrographs, as shown in FIG. 4.56(a) and (b), it can be observed that the delamination of the interface was considerably reduced, and there is no presence of GO clusters near the interface.

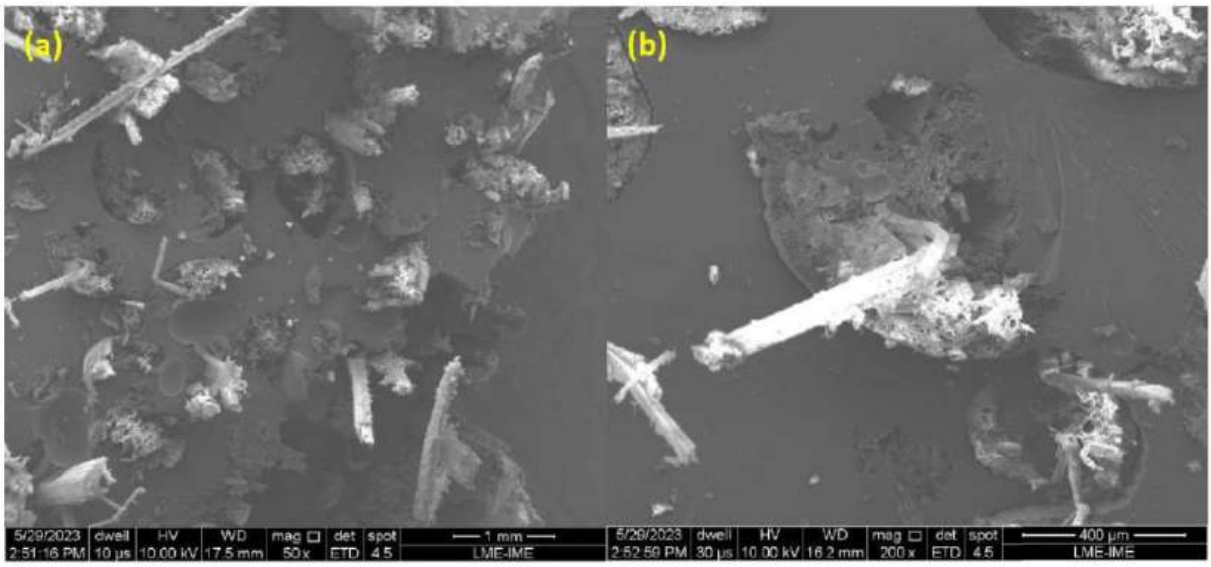

Figura 4.56 – Microscopic fracture mechanisms observed for the 30 SFGO/EP nanocomposite.

In an effort to verify if there were indeed significant differences between the compared conditions, an ANOVA analysis was conducted. The calculated F-value (55.47) was higher than the critical F_c value. Therefore, the hypothesis of mean equivalence was rejected with a significance level of 5%.

Tabela 4.36 – Analysis of variance of the maximum tensile strength for EP, 10 to 30 SF/EP, and 30 SFGO/EP.

Causes of Variation	**Sums of squares**	**Degrees of freedom**	**Mean Square**	**F (calculated)**	**Fc (tabulated)**
Treatments	3	1794.86	598.28	**55.47**	**3.49**
Residue	12	129.43	10.79		
Total	15	1924.29			

The Tukey test was performed to verify which conditions showed significant differences between the groups of 10 to 30 SF/EP and 30 SFGO/EP. The calculated HSD value was 5.07. Thus, the 30 SF/EP and 30 SFGO/EP conditions were the ones that presented significant differences among all composite groups.

Tabela 4.37 – Results for the differences between the mean values of maximum tensile strength after applying the Tukey's test.

Conditions	10 SF/EP	20 SF/EP	30 SF/EP	30 SFGO/EP
10 SF/EP	0	4.42	**10.54**	**29.26**
20 SF/EP	4.42	0	**6.12**	**24.84**
30 SF/EP	**10.54**	**6.12**	0	**18.72**
30 SFGO/EP	**29.26**	**24.84**	18.72	0

4.4.10 COMPRESSION TEST

TAB. 4.38 displays the results of compressive strength and percent strain at break for the 30 SFGO/EP condition and compares them with the 10 to 30 SF/EP conditions.

Tabela 4.38 – Compressive strength and total strain at break obtained from the compression test for the EP, 10 to 30 SF/EP, and 30 SFGO/EP conditions.

Composites	Compressive Strength (MPa)	Total Strain (%)
10 SF/EP	18.51 ± 1.50	25.71 ± 10.36
20 SF/EP	20.44 ± 2.49	13.81 ± 4.45
30 SF/EP	21.21 ± 1.45	15.19 ± 4.69
30 SFGO/EP	41.41 ± 10.19	33.40 ± 8.23

Through FIG. 4.57(a), it is possible to clearly observe the trend of increasing average compressive strength as the reinforcement fraction is increased. Compared to the 30 SF/EP condition, there was an equivalent increase of 95.23%. Meanwhile, in relation to the 30 SF/EP-GO condition, the increase was 86.61%. This indicates that only the coating of GO on the surface of SF was effective in enhancing the mechanical performance when the nanocomposite is subjected to compressive loads. FIG. 4.57(b) illustrates the comparison between the average values of percent strain at rupture. Thus, it was observed that the 30 SFGO/EP condition showed a higher value before the occurrence of rupture.

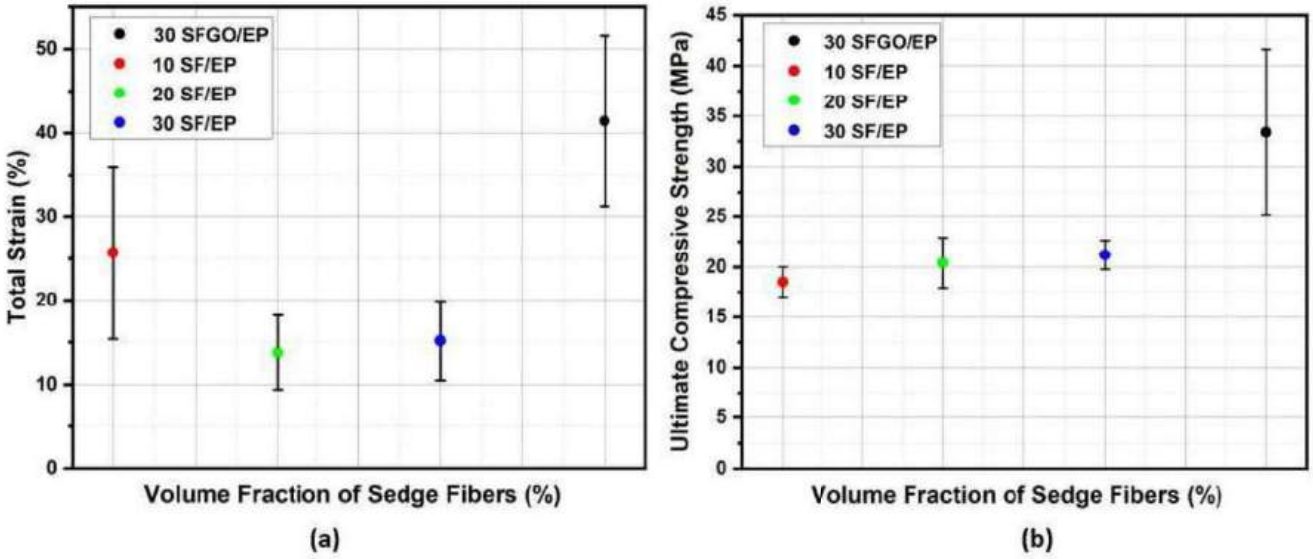

Figura 4.57 – (a) total strain and (b) compressive strength for the EP, 10 to 30 SF/EP, and 30 SFGO/EP conditions.

The micrographs shown in FIG. 4.58(a) and (b) display the fracture mechanisms caused by compressive loads. It can be noted that GO effectively promoted strong interfacial adhesion, as evidenced by the absence of delamination at the interface. Additionally, it was observed that fiber pullout occurred through the impression of the fiber in the matrix. Regarding fiber rupture, it occurs along the length, associated with cracks formed when the perpendicular load was applied. Moreover, the SF were also crushed. In relation to EP, the present mechanisms were river markings.

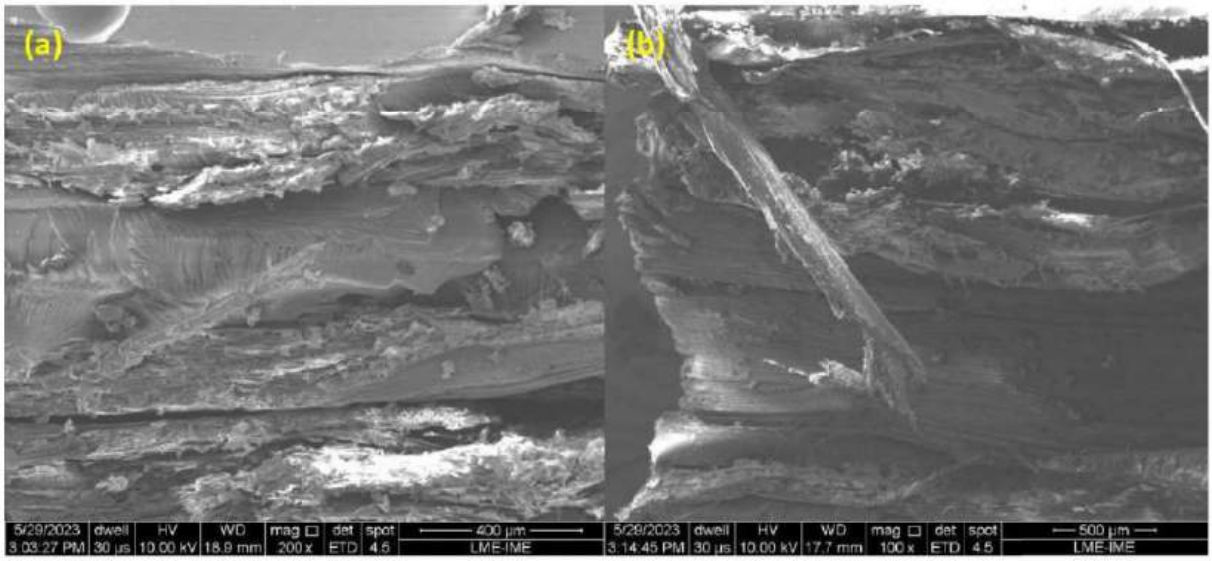

Figura 4.58 – Fracture mechanisms microscopically observed for the 30 SFGO/EP nanocomposite.

An ANOVA analysis was carried out to determine if there is a significant difference between the compared conditions. According to TAB. 4.39, the calculated F-value (17.26) was higher than the critical F-value at a significance level of 5%. Therefore, the hypothesis that the means are equal was rejected, confirming that there was a significant difference between the compression strength values for the different conditions.

Tabela 4.39 – Analysis of variance of the maximum compression stress for EP, 10 to 30 SF/EP, and 30 SFGO/EP.

Causes of Variation	**Sums of squares**	**Degrees of freedom**	**Mean Square**	**F (calculated)**	**Fc (tabulated)**
Treatments	3	1965.77	655.26	**17.26**	**3.49**
Residue	12	455.59	37.96		
Total	15	2421.36			

The Tukey's test, shown in TAB. 4.40, was conducted to understand which conditions exhibit differences greater than the calculated HSD (7.77). The only condition compared with the others that showed differences exceeding this value was 30 SFGO/EP. Therefore, this indicates that the current condition performed better than the other tested groups.

Tabela 4.40 – Results for the differences between the average values of maximum compression strength after the application of the Tukey's test.

Conditions	**10 SF/EP**	**20 SF/EP**	**30 SF/EP**	**30 SFGO/EP**
10 SF/EP	0	1.13	2.24	**25.22**
20 SF/EP	1.13	0	1.10	**24.08**
30 SF/EP	2.24	1.10	0	**22.98**
30 SFGO/EP	**25.22**	**24.08**	22.98	0

4.5 EPOXY MATRIX COMPOSITES REINFORCED WITH ALKALI TREATED SEDGE FIBERS

4.5.1 DYNAMIC MECHANICAL ANALYSIS (DMA)

FIG. 4.59 shows the E' curve as a function of temperature up to 200 °C for the 30 SFM/EP condition. It can be inferred that an increase in temperature induced a decrease in E', occurring from 50 to 150 °C. While the drop in the E' curve began at 76 °C for the 30 SFM/EP condition, being quite similar to the behavior exhibited by 30 SF/EP-GO, 30 SFGO/EP, and 10 to 30 SF/EP. Therefore, it can be inferred that the new treatment

condition investigated did not show a significant change for the E' value. Moreover, TAB. 4.41 illustrates values for E', loss modulus (E"), and Tan δ for the 30 SFM/EP condition compared to the EP, 10 to 30 SF/EP conditions.

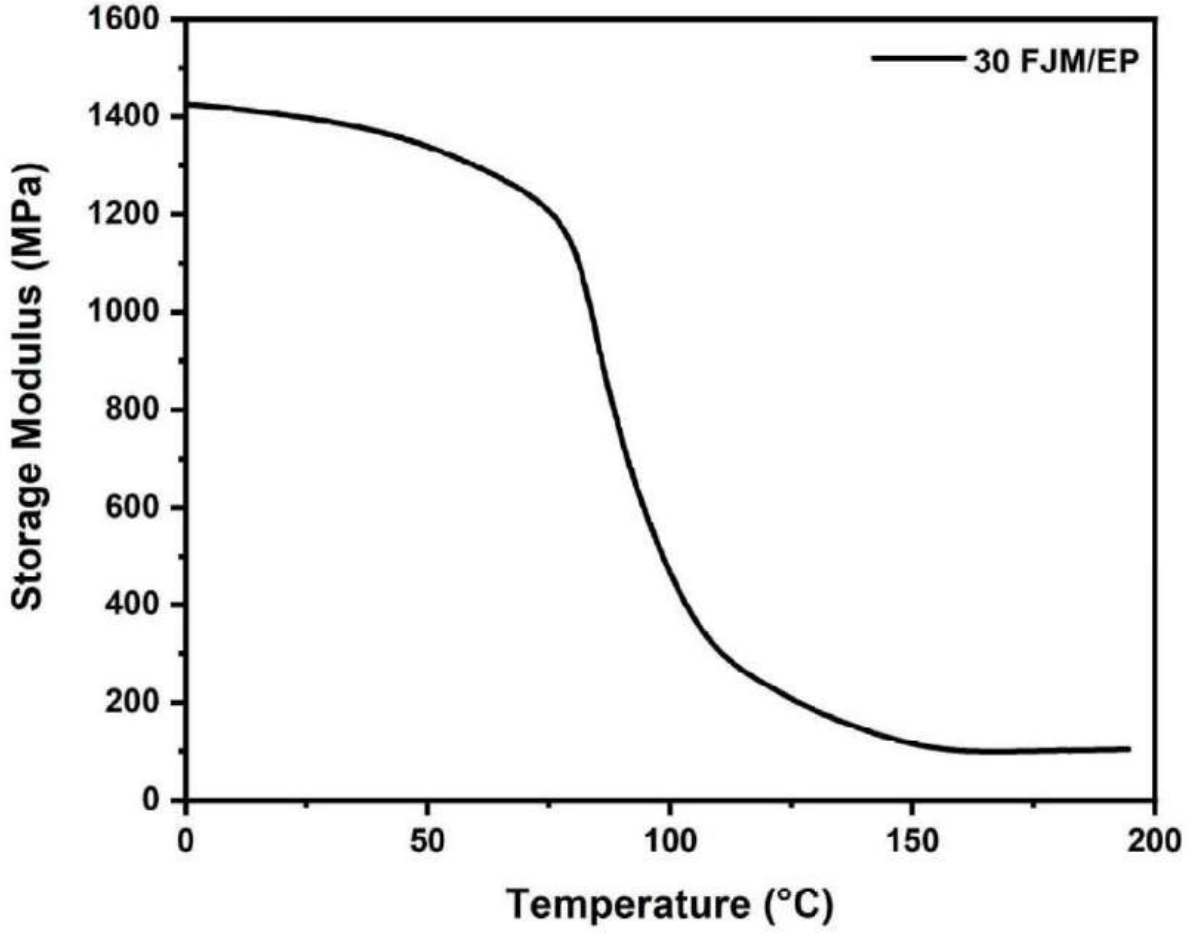

Figura 4.59 – Storage modulus variation with temperature for the 30 SFM/EP composite.

Tabela 4.41 – Main Parameters for DMA storage modulus (E'), loss modulus (E") and tangent delta (Tan δ) for the investigated materials: EP, 10 to 30 SF/EP and 30 SFM/EP.

Conditions	**E' at -50 °C (MPa)**	**E' at 25 °C (MPa)**	**E" (MPa)**	**Tan δ**	**T_g (°C)**
EP	3066	2380	200	0.458	129
10 SF/EP	1956	1766	188.5	0.579	117
20 SF/EP	1579	1441	168	0.602	106.5
30 SF/EP	1967	1832	201	0.737	99
30 SFM/EP	-	1399	132.9	0.3907	117.6

FIG. 4.60 displays the E"curve as a function of temperature for the SFM/EP condition. It can be noted on the E"curve that it reached a maximum peak in the T_g

region, at about 96 °C, slightly higher than the 30 SFGO/EP condition (89 °C). Besides, it can be seen that the T_g region started at around 76 °C. Therefore, below this latter value, the region represents the material as hard and rigid, consequently, the loss modulus is low and constant. A high energy dissipation, with the modulus reaching a maximum peak (about 132 MPa), represents the T_g of the system. The present condition shows the lowest value when compared to the nanocomposite 30 SF/EP-GO E"(145 MPa) and EP (200 MPa), but very similar to the 30 SFGO/EP condition (128 MPa). Therefore, it can be deduced that the alkaline treatment was effective in increasing the hydrophobicity of the SF and contributing to a stronger interfacial bond, further restricting molecular movement and reducing the viscoelastic friction capacity of the matrix. This is particularly interesting, as alkaline treatment has so far proved to be as effective as the functionalization of SF. Thus one of the treatment selection criteria could become the lower cost of the treatment, in case both have similar physical and mechanical property performance.

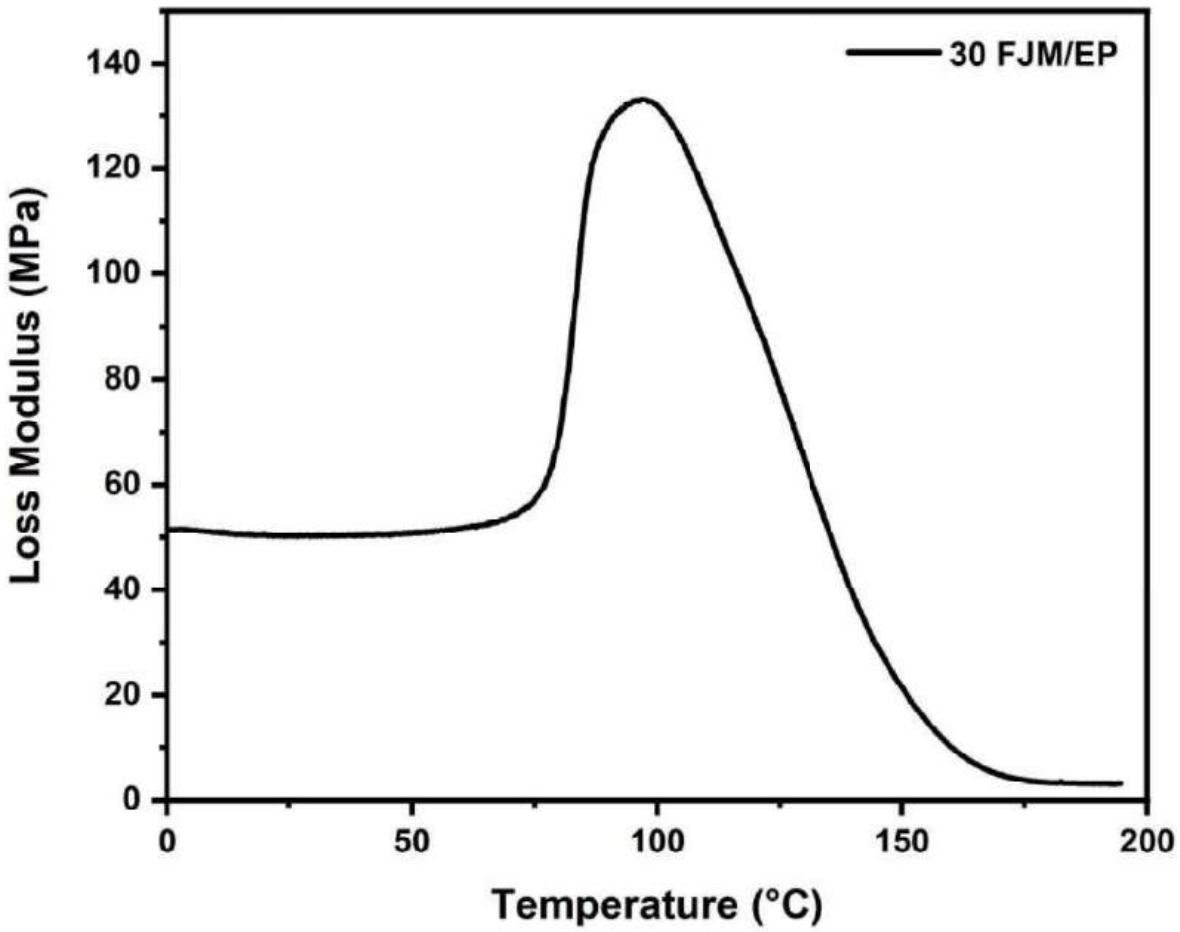

Figura 4.60 – Loss modulus variation with temperature for the 30 SFM/EP composite.

FIG. 4.61 illustrates the damping property behavior as a function of temperature for the 30 SFM/EP condition. The Tan δ value was approximately 0.39, quite similar to the 30 SFGO/EP condition (0.41) and contrasting with all Tan δ values of the composites

(0.55-0.75) and EP (0.46). The reduced peak height of the EP condition, 30 SFGO/EP, and 30 SFM/EP can be attributed to a polymer chain with restricted movement. This indicates that the current alkaline treatment produces a composite with a strong interfacial interaction, similar to the control group, resulting in lower energy dissipation at the interface. Furthermore, this result corroborates the findings presented in the E"curve. Moreover, the final range of the T_g occurred at a higher temperature (about 166 °C) compared to 30 SF/EP (98 °C) and EP (131 °C), however, very similar to the 30 SFGO/EP condition.

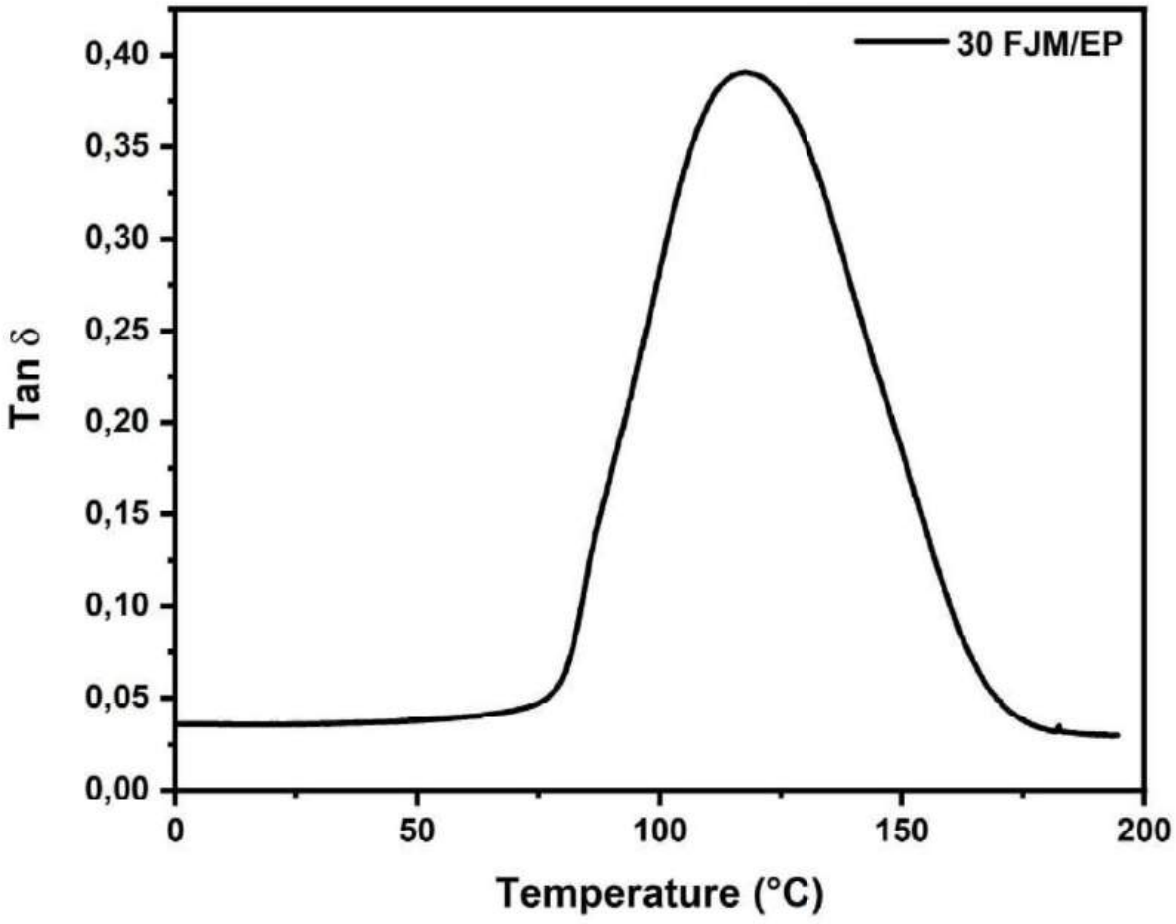

Figura 4.61 – Tan δ variation with temperature for the 30 SFM/EP composite.

FIG. 4.62 presents a much less irregular curve when compared to the analyzed conditions EP, 10 to 30 SF/EP, and 30 SF/EP-GO. It can be inferred that the curve of the 30 SFM/EP condition shows a more homogeneous dispersion compared to EP. Particularly, the effect of alkaline treatment significantly reduces heterogeneous dispersions within the matrix. The same behavior was observed for the nanocomposite 30 SFGO/EP, highlighting that both conditions improved the interfacial bonds of the composite.

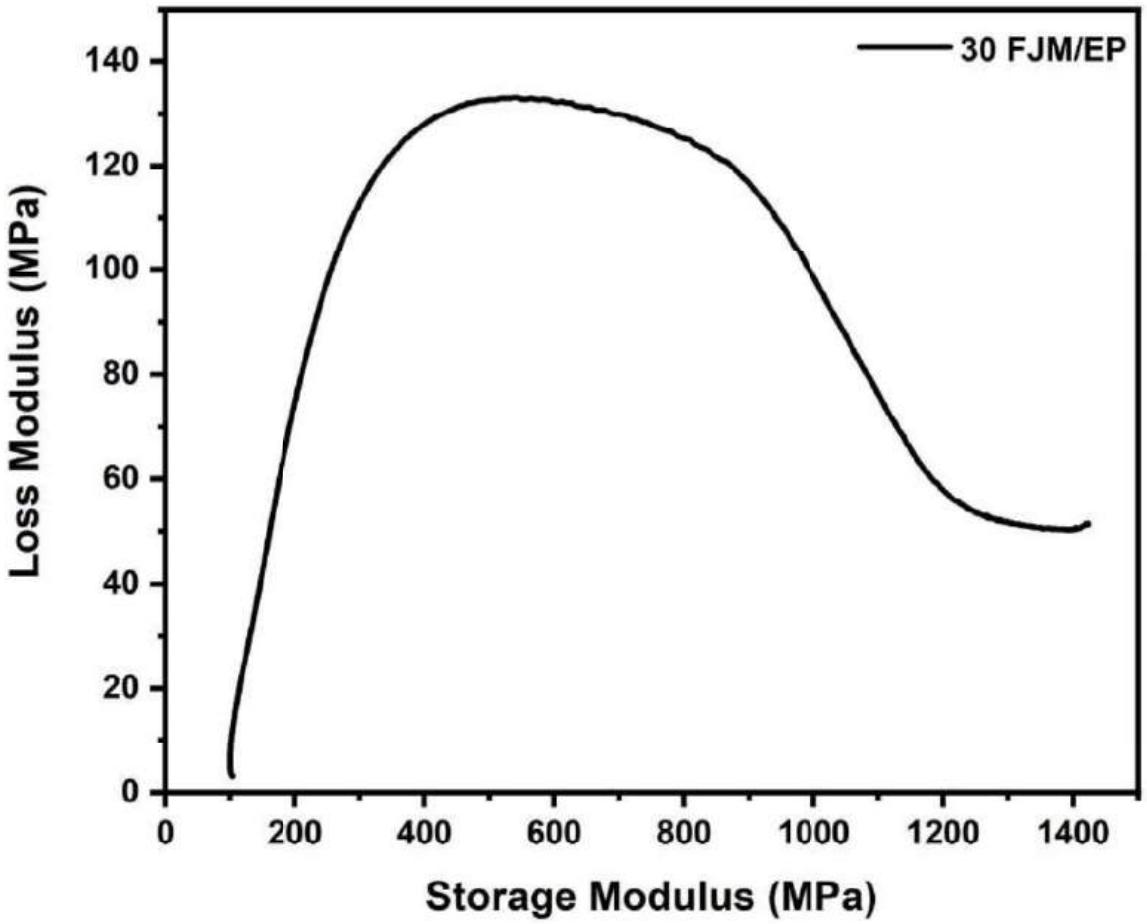

Figura 4.62 – Cole-Cole curve for the 30 SFM/EP composite.

TAB. 4.25 indicates that the investigated condition presented the lowest value (0.108) found for the coefficient of effectiveness, even lower than that reported for 30 SFGO/EP (0.191), showing the highest reinforcement efficiency compared to the other conditions. Therefore, the investigation aimed at verifying the effectiveness of the alkaline treatment in promoting a stronger interfacial bond was positively satisfactory and very similar to the performance of 30 SFGO/EP. Both treatment groups exhibited results that support the enhancement of the interfacial bond when comparing the loss modulus, damping coefficient, Cole-Cole curves, and the calculation of C.

Tabela 4.42 – Effective coefficient (C) for all SF/EP composites, EP and the 30 SFM/GO composite

Conditions	**Tan δ (25 °C)**	**E' glassy (25 °C)**	**E"rubbery (165 °C)**	**C**
EP	0.03707	2380	31	-
10 SF/EP	0.04020	1766	48	0.479
20 SF/EP	0.03188	1441	45	0.417
30 SF/EP	0.03077	1832	44	0.542
30 SFM/EP	0.03776	1399	168	0.108

4.5.2 THERMOMECHANICAL ANALYSIS (TMA)

FIG. 4.63 displays the TMA curve for the 30 SFM/EP condition, along with the glass transition temperature (T_g). The latter was found to be 131 °C, determined from the inflection point of the TMA curve. The jute fibers coated with GO have a higher value than the other EP conditions, 30 SF/EP, and 30 SF/EP-GO. Therefore, it can be inferred that the 30 SFM/EP condition enhances the thermal stability of the material. This occurs because alkaline treatment promotes better adhesion and interfacial shear strength, providing greater restraint to macromolecular mobility than GO functionalizing the epoxy resin.

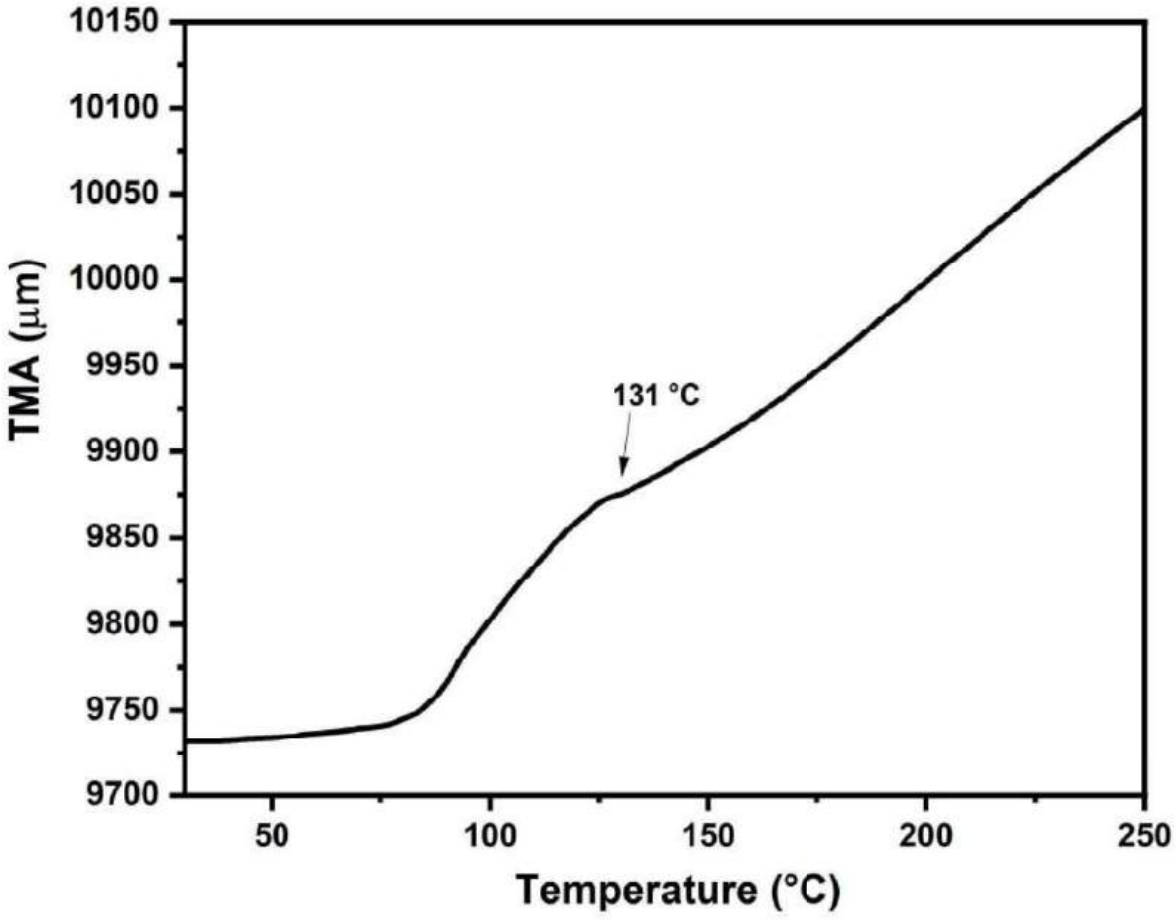

Figura 4.63 – Temperature dependence of the thermomechanical analysis for 30 SFM/EP composite.

In the TMA experiment, the linear thermal expansion coefficient found was 170.68 x 10^{-6}/°C. The present treatment improved the fiber/matrix interface compared to 30 SF/EP and EP. However, it showed a result close to the treatment of 30 SF/EP-G0 (168.03 x 10^{-6}/°C) and slightly lower than the 30 SFGO/EP condition (143.87 x 10^{-6}/°C). Therefore, it can be inferred that the use of GO acting through a mechanism similar to a compatibilizing agent, in which chemical bonding bridges are formed, proved to be more

effective than increasing surface roughness and hydrophobicity.

4.5.3 THERMOGRAVIMETRIC ANALYSIS (TGA/DTG)

The TG and DTG curves are presented in FIG. 4.64 for the 30 SFM/EP condition. The TG curve highlights that a small mass loss was observed (1.28%) at low temperatures up to 200 °C, associated with moisture removal. The mass loss at this stage was slightly lower than the EP condition (1.63%) and 30 SFGO/EP (2.07%), while being lower than 30 SF/EP (3.23%) and 30 SF/EP-GO (5.37%). Furthermore, the T_{onset} found was 263 °C, and the maximum degradation rate was at 314 °C. Both results are lower than all the other investigated conditions. Therefore, it can be stated that the thermal stability of the 30 SFM/EP condition has poorer thermal stability. Thus, alkaline treatment was able to act positively by reducing the hydrophilic character, as evidenced by a lower initial mass loss. However, a reduction in thermal stability occurred when compared to untreated fibers and EP. This behavior has been observed in the literature (ARRAKHIZ et al., 2013; KAUSHIK; KUMAR; KALIA, 2012), associated with the fiber becoming more amorphous. The second degradation stage concluded with a mass loss equivalent to 62.09%, while the last stage ended with 2.09% mass loss.

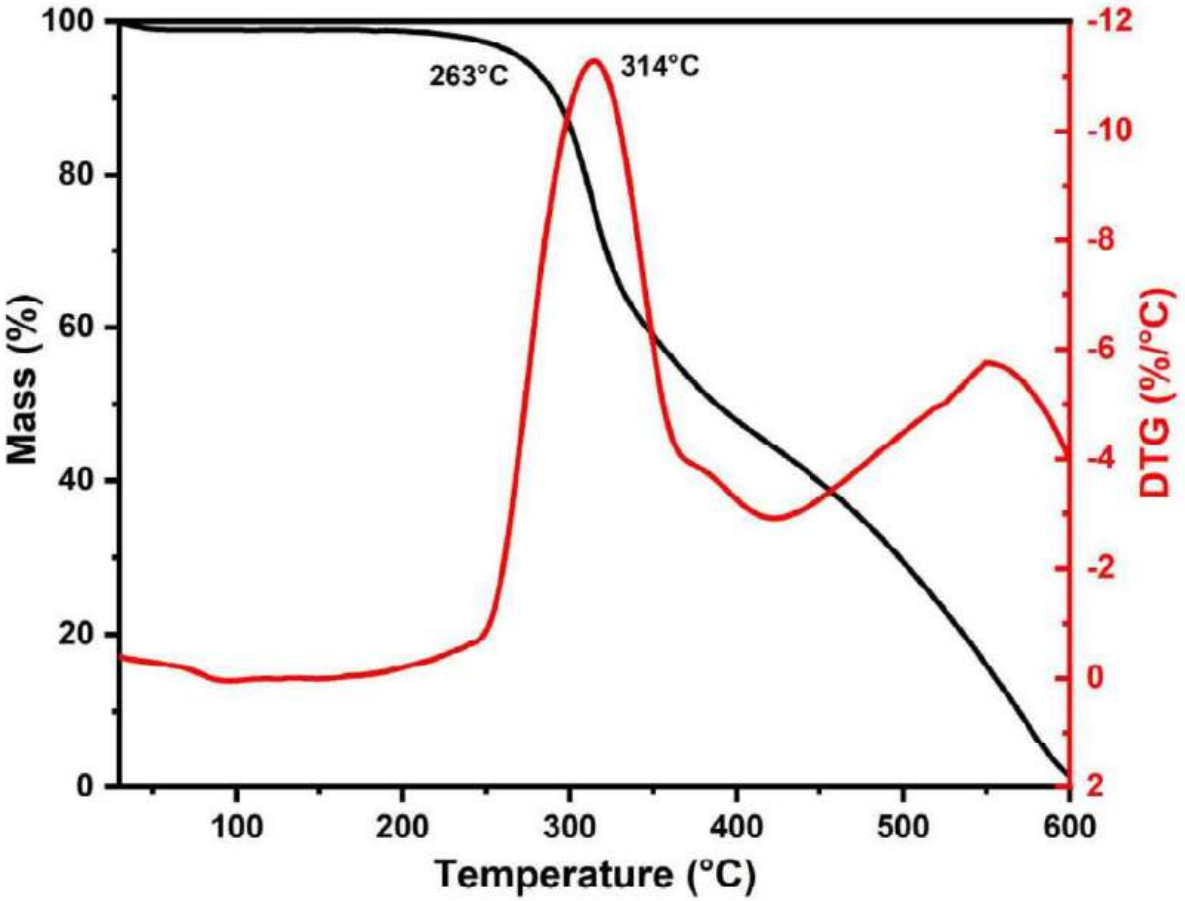

Figura 4.64 – Thermogravimetric curves for the present investigated 30 SFM/EP composite.

4.5.4 DIFFERENTIAL SCANNING CALORIMETRY (DSC)

The FIG. 4.46 displays the DSC curve obtained for the 30 SFGO/EP condition. An endothermic peak at 59 °C can be observed, associated with T_g and the release of moisture present on the surface of the SF. The subsequent exothermic peak at 120 °C may be associated with the post-curing process. As observed by (NEUBA et al., 2020), all SF/EP conditions showed a higher value for the T_g range. Additionally, an exothermic peak at 405 °C was observed, indicating that the hemicellulose and cellulose content were fully decomposed (SELVAN et al., 2023).

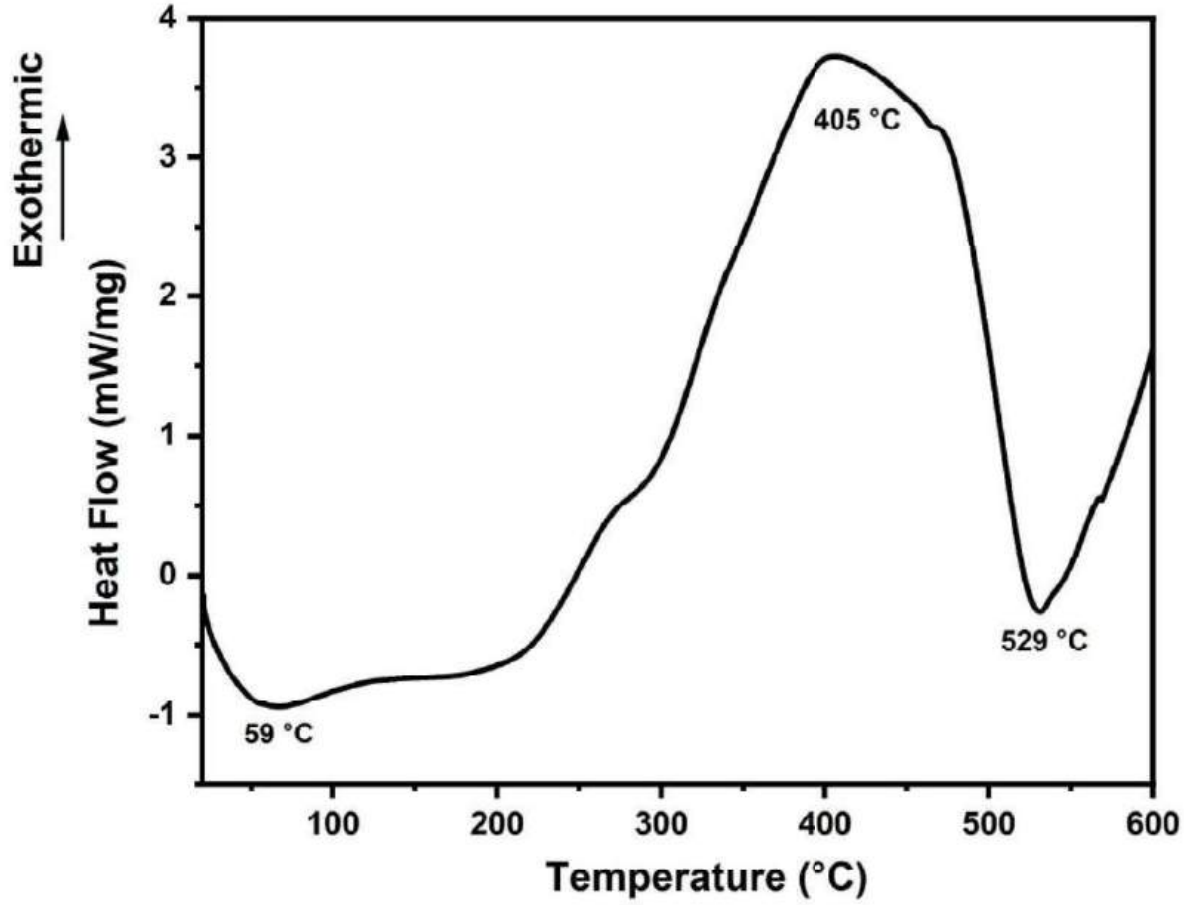

Figura 4.65 – DSC curve for the 30 SFM/EP condition.

4.5.5 FOURIER TRANSFORM INFRARED SPECTROSCOPY (FTIR)

FIG. 4.25 displays the spectrum for the 30 SFM/EP condition. The O-H stretching and functional groups can be observed at 3423 cm^{-1}. The C-H stretching is found in the absorption band at 2929 cm^{-1}. The band at 2349 cm^{-1} is related to the linkage between organic molecules and wax compounds on the fiber's surface. In the case of the present aromatic C=O groups, the band at 1603 cm^{-1} is directly associated. The aromatic rings appear at 1500 cm^{-1}, indicating that there was no chemical interaction between them and the SF. Additionally, at 1236 cm^{-1}, it is attributed to CH_2 twisting, and the C-O stretching occurs at 1024 cm^{-1}. The peak at 825 cm^{-1} is associated with the vibration of C-H linked to the benzene ring (LI et al., 2021; SONG et al., 2020). When compared to the 30 SFGO/EP condition, the bands at 1024 and 825 cm^{-1} decreased in intensity. This can be explained by the reduction in the amount of lignin due to the employed chemical treatment (BERAM; YASAR, 2020). The band at 657 cm^{-1} is related to C-C stretching, and at 554 cm^{-1}, the C-C stretching occurs. Moreover, there is an absence of the band at 1731 cm^{-1}, indicating the removal of hemicellulose. Finally, no significant changes were observed in the composite spectra.

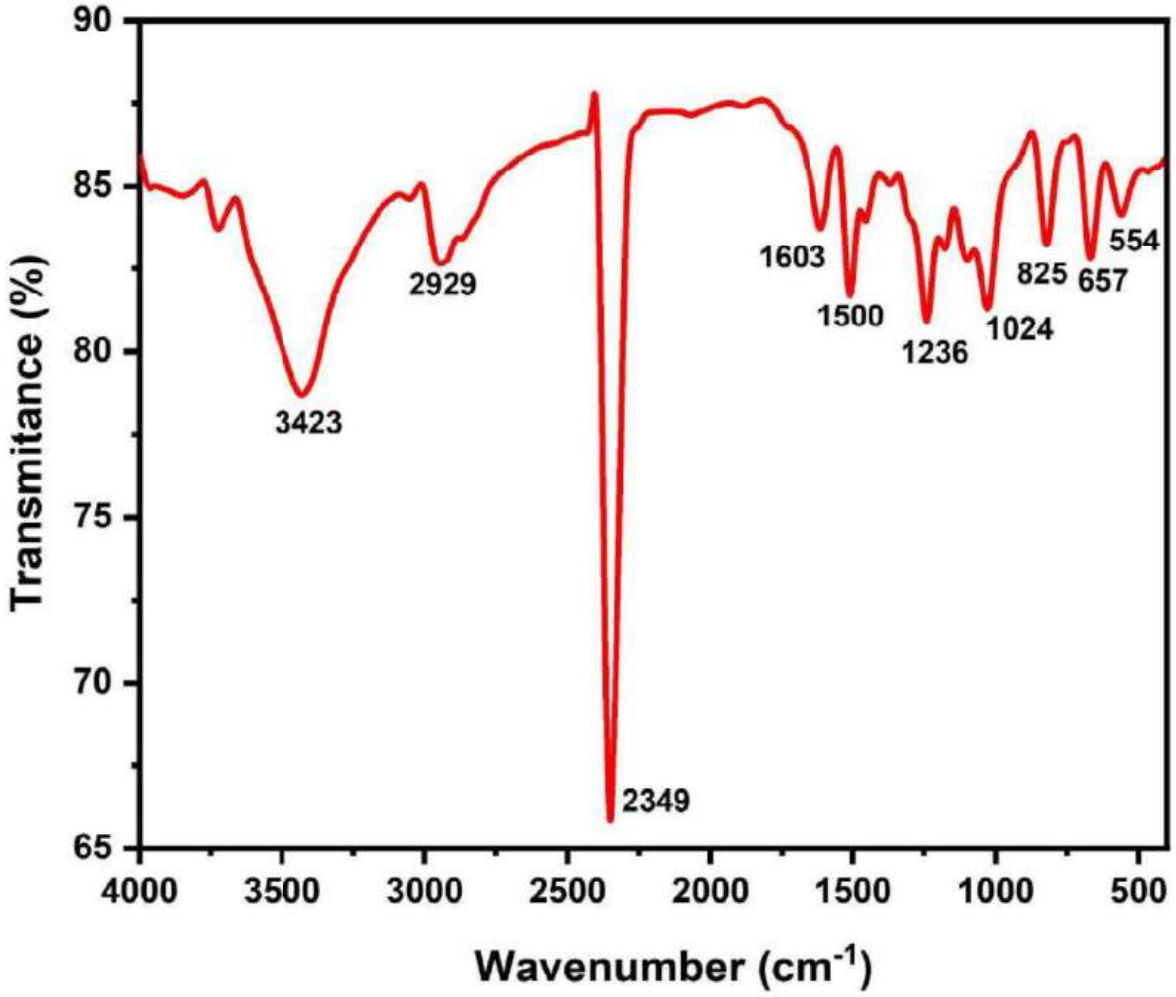

Figura 4.66 – FTIR spectrum for the 30 SFM/EP condition.

4.5.6 CHARPY IMPACT TEST

The TAB.4.43 presents the average absorbed Charpy impact energy and individual values for each tested sample in the 30 SFM/EP group.

Tabela 4.43 – Values of absorbed impact energy in the Charpy test for some samples from the 30 SFM/EP group.

30 SFM/EP Conditions	
Samples	**Impact Energy (J/m)**
1	103.45
2	137.44
3	107.75
4	122.03
5	156.93
6	117.93
7	108.35
Mean	**121.98**
Standard Deviation	**19.18**

The 30 SFM/EP condition was compared with EP and SF/EP through a graph, allowing the visualization of the increasing trend in energy absorption as reinforcements were added to the resin. An increase of 1041.06% and 36.09% was achieved compared to EP and 30 SF/EP, respectively. However, it experienced a decrease of 14.85% and 27.19% when compared to the 30 SF/EP-GO and 30 SFGO/EP conditions, respectively. Therefore, the investigated condition containing SFM was able to enhance the performance of 30 SF/EP and showed less efficiency when GO acted to increase the toughness of the EP resin or as a coating for SF.

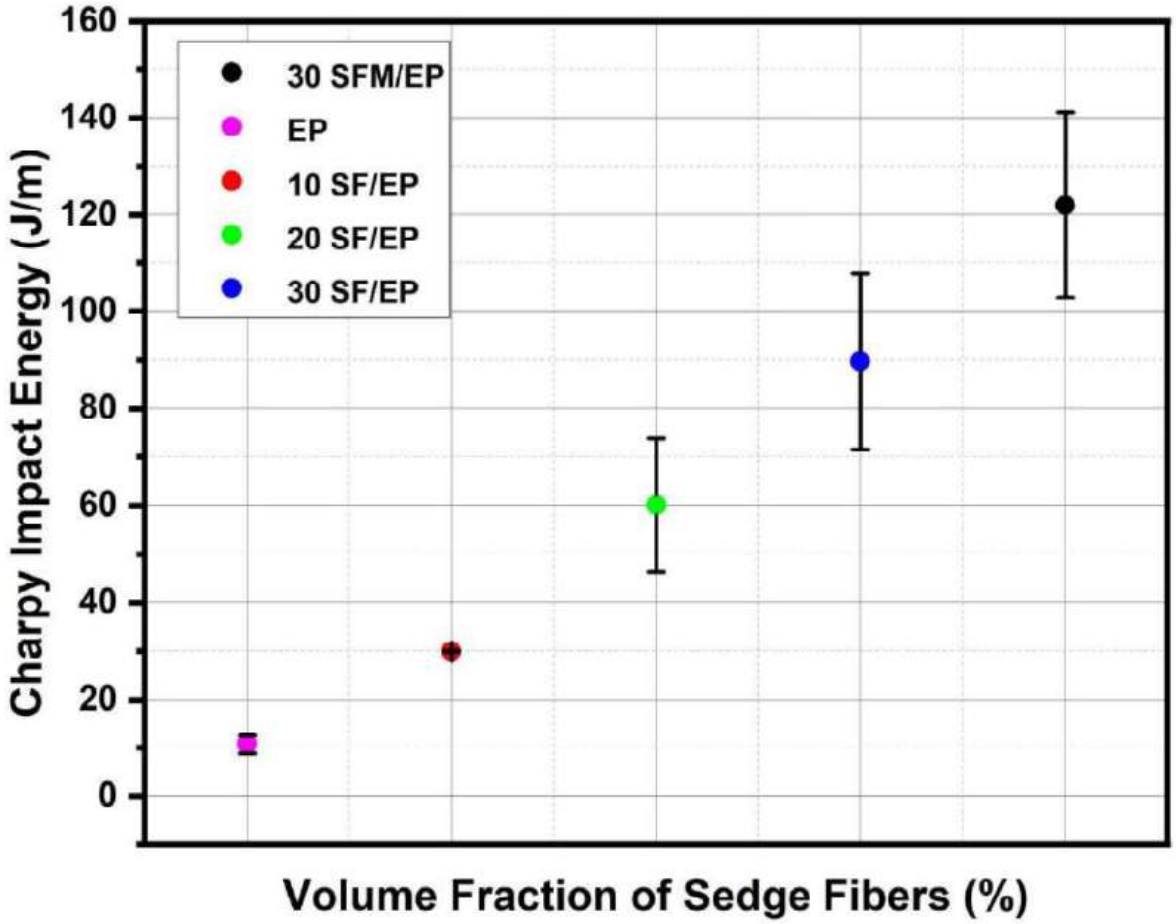

Figura 4.67 – Comparison of impact energy obtained in the Charpy test for the EP, 10 to 30 SF/EP, and 30 SFM/EP conditions.

All samples were completely fractured, validating the test. ANOVA analysis was conducted to confirm if there is a significant difference in the average Charpy impact energy results between the EP, 10 to 30 SF/EP, and 30 SFM/EP conditions. TAB. 4.44 clarifies that the hypothesis of equivalent means was rejected, with a significance level of 5%. This occurred because the calculated F parameter was higher than F_c. Therefore, it was confirmed that there is indeed a significant difference in Charpy impact energies between the different sample groups.

Tabela 4.44 – Analysis of variance of the average impact energy obtained by the Charpy test for EP, 10 to 30 SF/EP, and 30 SFM/EP.

Causes of Variation	Sums of squares	Degrees of freedom	Mean Square	F (calculated)	Fc (tabulated)
Treatments	4	43314.08	10828.52	**37.74**	**2.87**
Residue	20	5738.81	286.94		
Total	24	49052.89			

The results of the Tukey's test are shown in TAB. 4.45. Values highlighted in bold are higher than the calculated HSD (22.35). It was observed that 30 SFM/EP was the only condition that showed all comparisons between groups higher than the HSD value. This highlights that this group was the best among all others previously reported in the literature.

Tabela 4.45 – Results for the differences between the average values of the impact energy after applying the Tukey's test.

Conditions	**EP**	**10 SF/EP**	**20 SF/EP**	**30 SF/EP**	**30 SFM/EP**
EP	0	17.35	**46.93**	**72.09**	**117.84**
10 SF/EP	17.35	0	**29.57**	**54.74**	**100.49**
20 SF/EP	**46.93**	**29.57**	0	**25.17**	**70.91**
30 SF/EP	**72.09**	**54.74**	**25.17**	0	**45.74**
30 SFM/EP	**117.84**	**100.49**	**70.91**	**45.74**	0

4.5.7 IZOD IMPACT TEST

TAB. 4.46 displays the average and individual Izod impact energy absorbed for each sample tested under the condition 30 SFM/EP.

Tabela 4.46 – Izod impact energy for samples from the 30 SFM/EP group.

30 SFM/EP condition	
Samples	**Impact Energy (J/m)**
1	149.23
2	108.60
3	149.12
4	113.83
5	174.67
6	106.19
7	109.61
Mean	**130.18**
Standard Deviation	**27.18**

A graphical comparison, shown in FIG.4.68, was conducted among the conditions EP, 10 to 30 SF/EP, and 30 SFM/EP. It was noted that the trend of increased energy absorption persisted with the new condition investigated. Thus, the value showed an increase of 461.64% and 99.43% in relation to EP and 30 SF/EP, respectively. Meanwhile, it exhibited an increase of 15.79% and 6.74% related to 30 SF/GO-EP and SFGO/EP, respectively. Therefore, the investigated condition containing SFM showed better performance than all other conditions investigated.

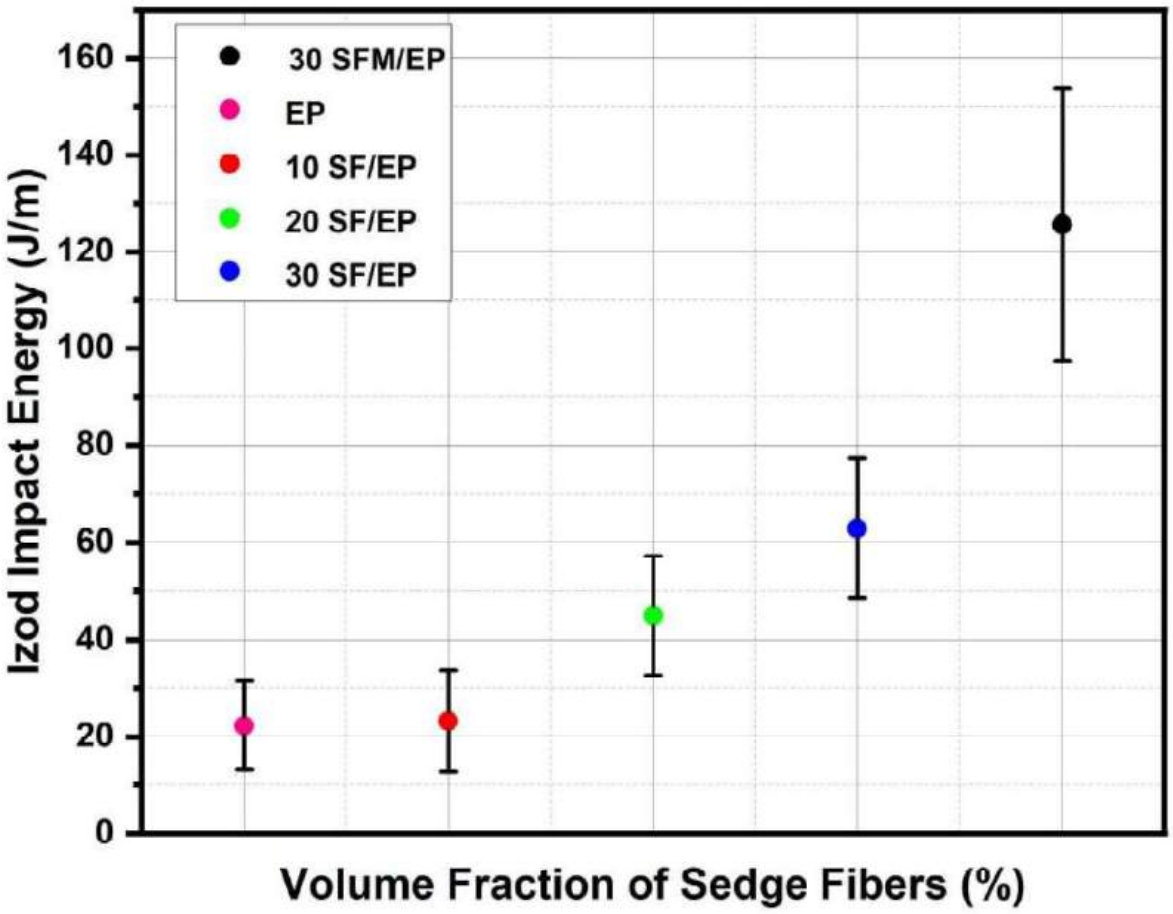

Figura 4.68 – Comparison of the impact energy obtained in the Izod test for the conditions EP, 10 to 30 SF/EP, and 30 SFM/EP

All specimens were completely fractured, demonstrating the validity of the test conducted. Thus, in an effort to evaluate the failure mechanisms that contribute synergistically to enhancing the absorbed energy of the material, a fractured region from a specimen of the 30 SFM/EP condition was selected.

The microscopies illustrated in FIG.4.69(a-f) revealed that the primary objective of interface improvement was achieved through the alkaline treatment. In the microscopies FIG.4.69(a-c), even with crack propagation up to the interface surfaces, there was no displacement of the SFs. While in (d) and (e) there was only a slight displacement. Therefore, as with the 30 SFGO/EP and 30 SF/EPGO conditions, the treatment was effective.

FIG.4.69(f) is actually the same region observed in (a), but with a lower magnification. An interesting experimental observation is the presence of very high porosity, highlighting once again, the presence of trapped air, which contributes to a low mechanical resistance of the composite, in general. Moreover, it is possible to observe the propagation of river marks on the surface of the EP resin and the presence of voids, which in turn, can act as stress concentrators due to the geometric discontinuity formed.

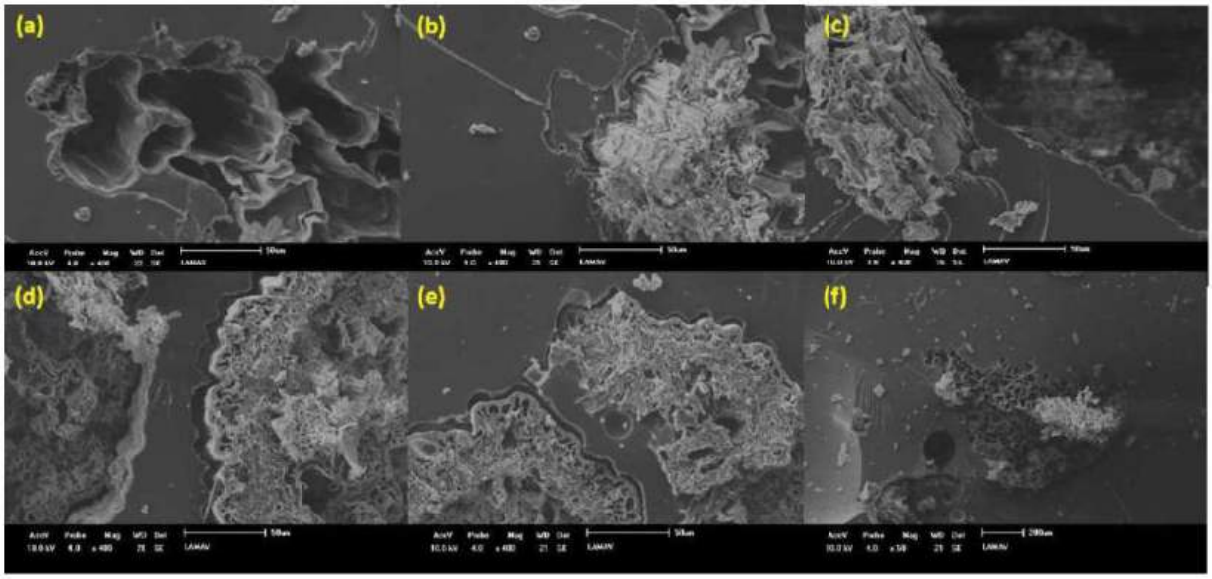

Figura 4.69 – Micrographs of the fractured surface at a magnification of (a-e) 400x and (f) 50x.

The ANOVA analysis was conducted to verify if there is a significant difference between the EP conditions, 10 to 30 SF/EP, and 30 SFM/EP. As per TAB. 4.47, it can be stated that the hypothesis that the means are equal was rejected, with a significance level of 5%. This was evidenced by the fact that the calculated F (55.83) was greater than the F_c. Therefore, it was confirmed that there is a significant difference between the Izod impact energies for the different groups analyzed.

Tabela 4.47 – Analysis of variance of the average impact energy obtained by the Izod test for EP, 10 to 30 SF/EP, and 30 SFM/EP.

Causes of Variation	Sums of squares	Degrees of freedom	Mean Square	F (calculated)	Fc (tabulated)
Treatments	4	49575.99	12394	**55.83**	**2.87**
Residue	20	4440.18	222.00		
Total	24	54016.17			

Through the Tukey's test, shown in TAB.4.48, it was possible to visualize through the bold values the comparisons that have significant differences. These highlighted values are higher than the calculated HSD (19.65). Thus, it was demonstrated that the 30 SFM/EP condition was the only one that showed a significant difference among all other groups. Therefore, indicating that the 30 SFM/EP sample group exhibited better performance.

Tabela 4.48 – Results for the differences between the average values of the Izod impact energy after applying the Tukey's test.

Conditions	EP	10 SF/EP	20 SF/EP	30 SF/EP	30 SFM/EP
EP	0	1.97	**35.03**	**54.29**	**121.69**
10 SF/EP	1.97	0	**33.06**	**52.32**	**119.72**
20 SF/EP	**35.03**	**33.07**	0	19.27	**86.66**
30 SF/EP	**54.29**	**52.32**	19.27	0	**67.39**
30 SFM/EP	**121.69**	**119.72**	**86.66**	**67.39**	0

4.5.8 BENDING TEST

TAB.4.49 illustrates the results related to the bending mechanical properties of the 30 SFM/EP group compared to the EP conditions and 10 to 30 SF/EP. The values presented refer to the averages and standard deviations found for samples within the same reinforcement condition.

Tabela 4.49 – Bending strength properties of the specimens for the EP, 10 to 30 SF/EP, as well as 30 SFM/EP.

Conditions	Flexural Strength (MPa)	Total Strain (%)	Elastic Modulus (GPa)
EP	41.38 ± 7.02	2.75 ± 0.19	1.19 ± 0.14
10 SF/EP	22.27 ± 6.02	3.02 ± 0.62	0.68 ± 0.18
20 SF/EP	20.78 ± 5.06	2.86 ± 0.56	0.66 ± 0.09
30 SF/EP	24.63 ± 6.75	3.1 ± 0.35	0.83 ± 0.24
30 SFM/EP	48.38 ± 11.97	2.19 ± 0.49	3.23 ± 0.49

With the help of the graphical comparison in FIG.4.70, it was observed that the 30 SFM/EP condition was the only composite group capable of exhibiting superior performance to EP. This improvement was about 16.9%. Meanwhile, there was an increase of 96.5% compared to the 30 SF/EP condition. However, alkaline treatment proved to be a slightly inferior treatment compared to the 30 SFGO/EP condition, as there was a decrease of 3.9%.

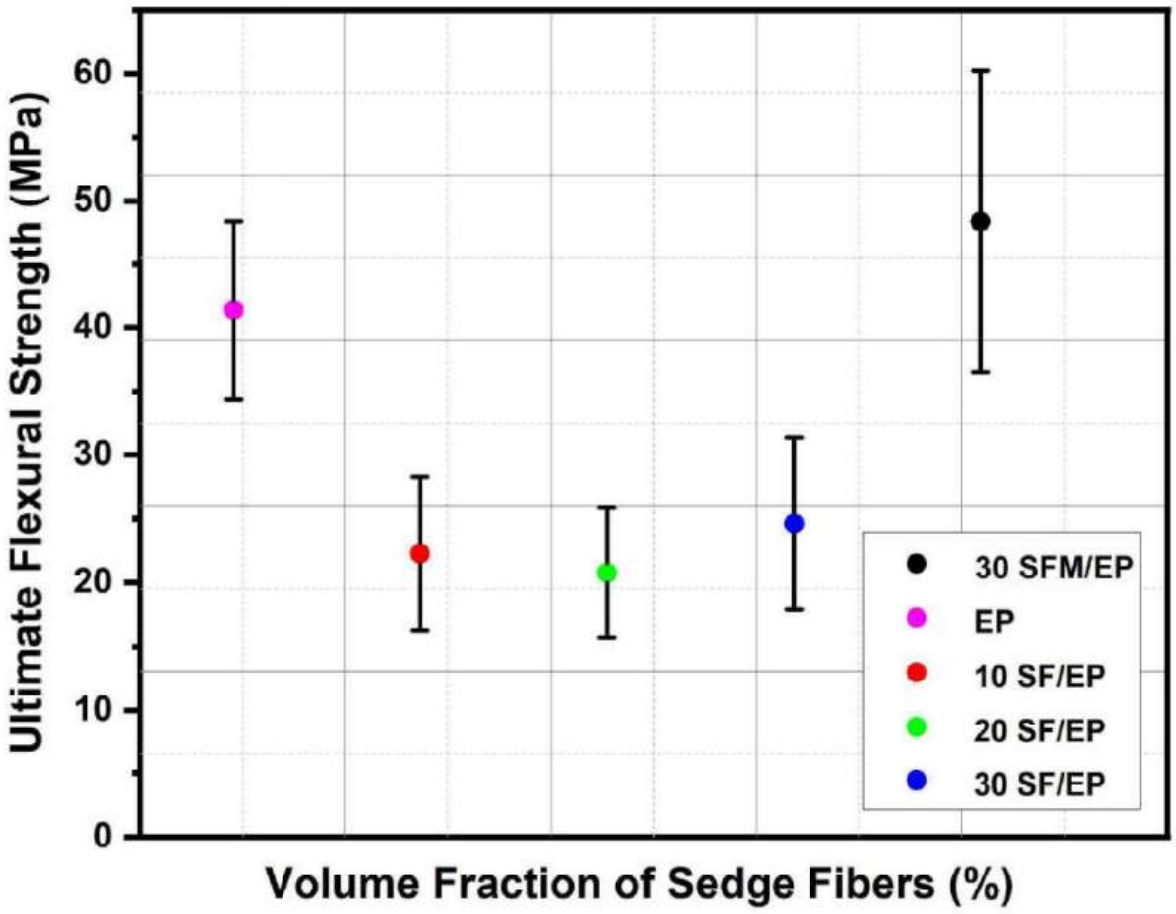

Figura 4.70 – Comparison of the flexural strength of the conditions EP, 10 to 30 SF/EP, and 30 SFM/EP.

The comparison of the modulus of elasticity, presented in FIG.4.71(a), revealed that the 30 SFM/EP condition was the only composite group that exhibited superior performance to the EP resin. Meanwhile, FIG.4.71(b) highlighted that the condition containing alkaline treated fibers showed a strain before failure lower than the other groups, indicating that toughness was reduced. This behavior, as reported in the literature (YAN; CHOUW; YUAN, 2012), can be due to the alkaline treatment negatively impacting some mechanical properties of the composites.

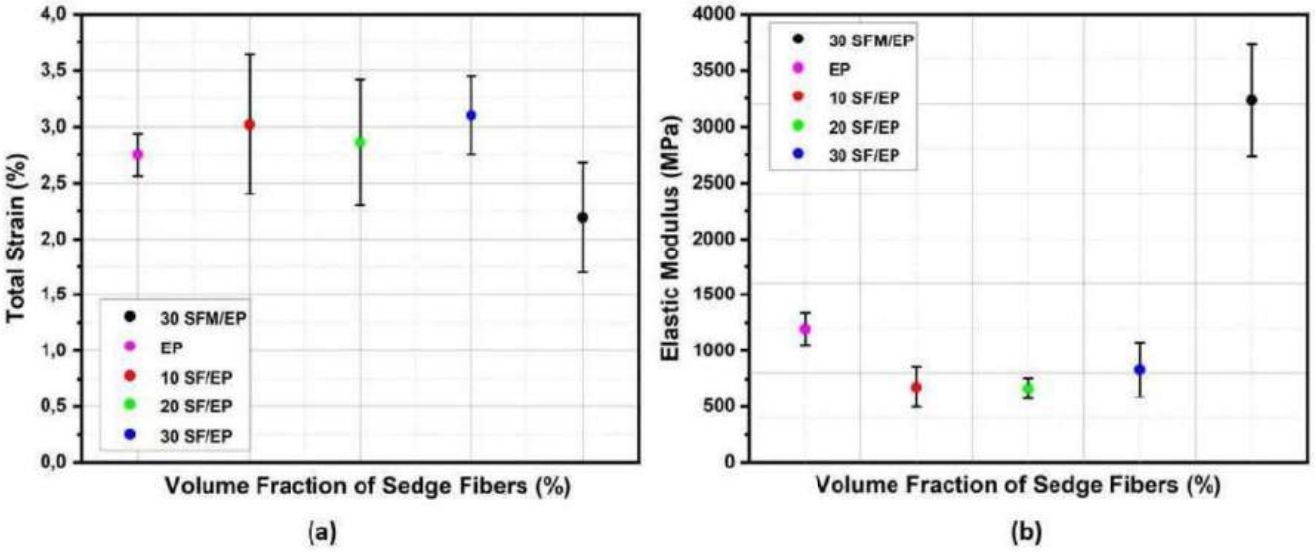

Figura 4.71 – (a) modulus of elasticity and (b) strain of EP, 10 to 30 SF/EP, and 30 SFM/EP.

The micrograph presented in FIG.4.72(a) highlighted failure mechanisms that synergistically contribute to the improvement of mechanical performance, such as fiber rupture, *pullout*, and river marks. Additionally, through FIG.4.72(a) and (b), it was possible to observe that interface delamination was significantly reduced. Thus, alkaline treatment was effective in promoting a strong interface between the fiber and matrix.

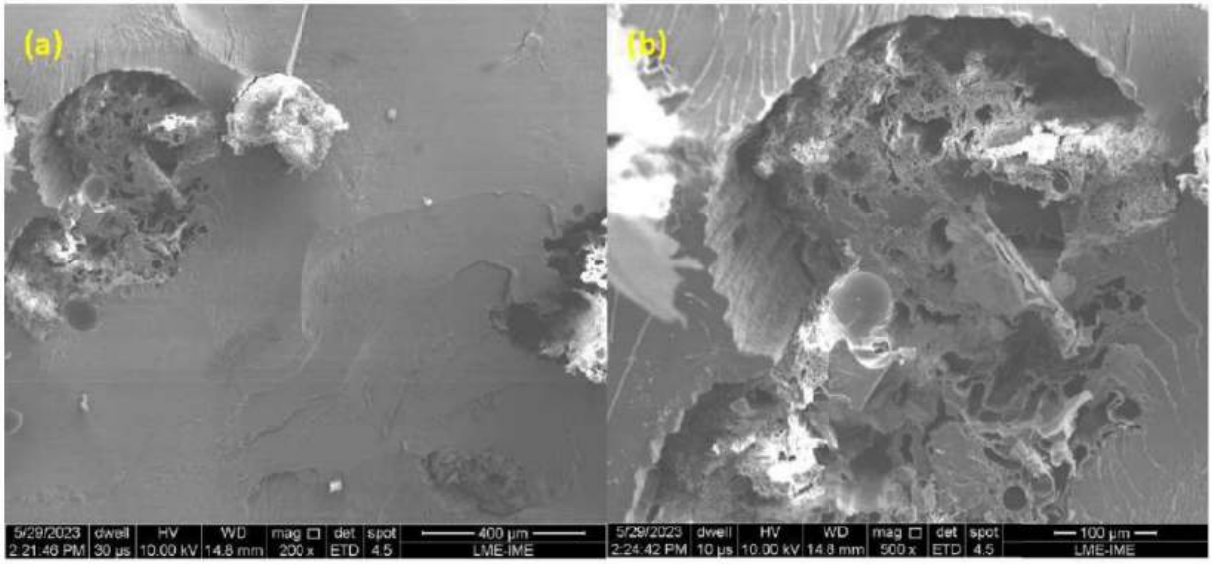

Figura 4.72 – Fracture mechanisms observed microscopically for the 30SFM/EP composite.

In order to assess whether there is a significant difference in flexural strength, an ANOVA analysis was performed. The conditions analyzed were EP, 10 to 30 SF/EP, and

30 SFM/EP. Therefore, TAB.4.50 revealed that the hypothesis that the means are equal was rejected, with a significance level of 5%. This is due to the calculated F (23.29) being higher than F_c, confirming that there is a significant difference between the groups.

Tabela 4.50 – Analysis of variance of the maximum flexural strength for EP, 10 to 30 SF/EP, and 30 SFM/EP.

Causes of Variation	Sums of squares	Degrees of freedom	Mean Square	F (calculated)	Fc (tabulated)
Treatments	4	3592.79	889.19	**23.29**	**3.05**
Residue	15	578.28	38.55		
Total	19	4171.08			

Through the Tukey's test, it was possible to observe which conditions had a value higher than the calculated HSD (7.55). According to TAB.4.51, the EP and 30 SFM/EP conditions showed a significant difference from all groups, as the value highlighted in bold exceeded the HSD. Thus, the alkaline treatment of SF proved to be very effective in improving the mechanical performance.

Tabela 4.51 – Results for the differences between the mean values of maximum flexural strength after applying the Tukey's test.

Condition	EP	10 SF/EP	20 SF/EP	30 SF/EP	30 SFM/EP
EP	0	**12.50**	**14.89**	**16.47**	**20.52**
10 SF/EP	**12.50**	0	2.38	3.97	**33.03**
20 SF/EP	**14.89**	2.38	0	1.58	**35.41**
30 SF/EP	**16.47**	3.97	1.58	0	**36.99**
30 SFM/EP	**20.52**	**33.03**	**35.41**	**36.99**	0

4.5.9 TENSILE TEST

TAB. 4.52 illustrates the mechanical properties obtained from the tensile test of the 30 SFM/EP condition and compares them with previous literature results from the EP and 10 to 30 SF/EP groups. The investigated mechanical properties include elastic modulus, strain, and tensile strength at rupture.

Tabela 4.52 – Tensile strength properties for EP, 10 to 30 SF/EP, as well as 30 SFM/EP conditions.

Conditions	**Tensile Strength (MPa)**	**Total Strain (%)**	**Elastic Modulus (GPa)**
10 SF/EP	7.0079 ± 3.1	4.04 ± 1.23	0.56 ± 0.19
20 SF/EP	12.4072 ± 5.5	4.3 ± 0.63	1.32 ± 0.40
30 SF/EP	15.1705 ± 3.6	4.66 ± 1.13	3.77 ± 0.05
30 SFM/EP	26.66 ± 2.39	7.99 ± 1.81	0.28 ± 0.06

A graphical comparison between the previously mentioned conditions is shown in FIG. 4.73. It can be observed that the alkaline treatment was effective in improving mechanical performance when compared to the 30 SF/EP condition, exhibiting an increase of 76%. However, this treatment was not effective in surpassing the EP condition, showing a decrease of 28.5%. Meanwhile, the decrease compared to the 30 SFGO/EP condition was 32.4%. According to the literature, alkaline treatment in some natural fibers leads to more fragile fibers, negatively impacting mechanical performance (ISMAIL et al., 2021). Thus, this factor may be one of the reasons why the alkaline treatment was not as effective as the GO coating on the fiber surface. However, there was an increase of 48.3% when compared to the result obtained for 30 SF/EP-GO, indicating that the EP functionalized with GO did not exhibit very satisfactory performance.

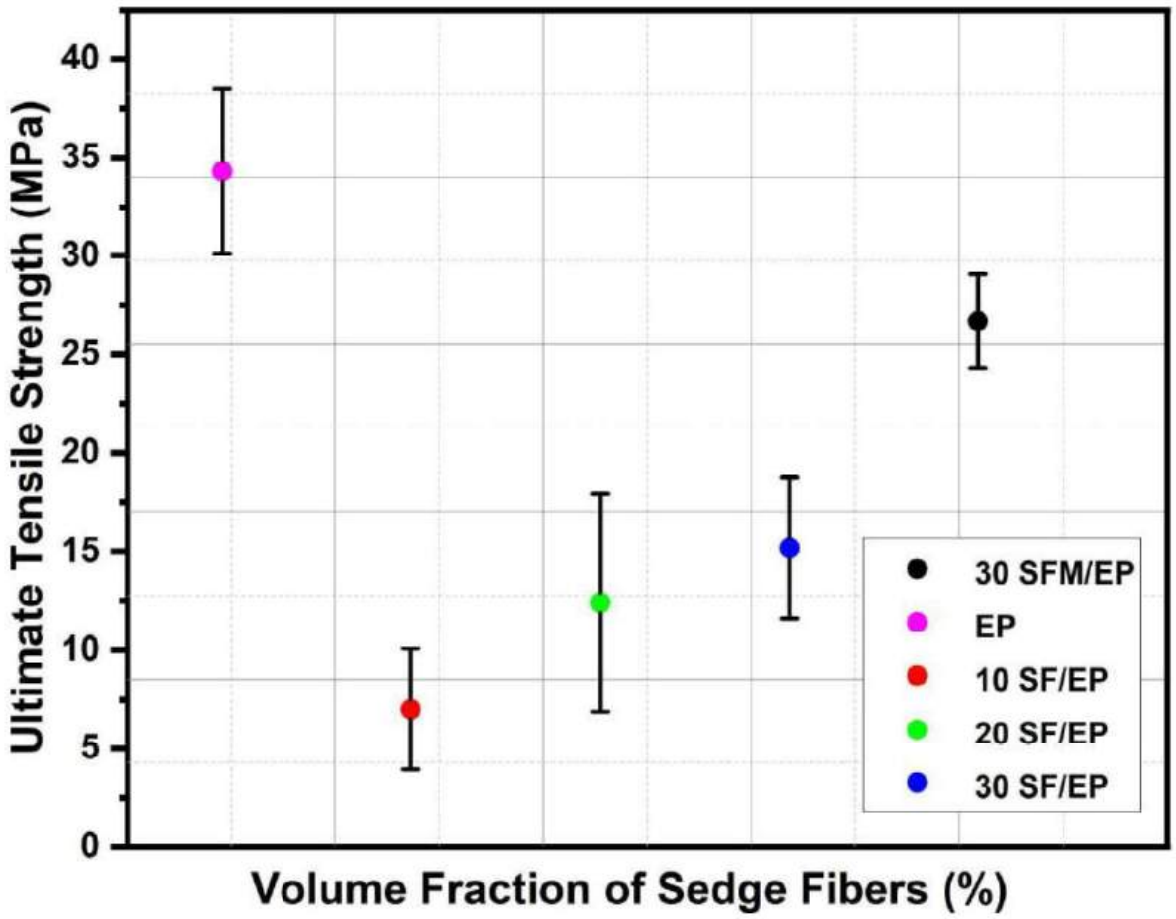

Figura 4.73 – Comparison of the tensile strength among EP, 10 to 30 SF/EP, and 30 SFM/EP conditions.

The modulus of elasticity revealed that the 30 SFM/EP condition has the worst performance among the compared conditions, as shown in FIG.4.74(a). This fact can be associated with factors such as stress concentrators leading to premature material failure and the fragility of SFM caused by the chemical treatment. While FIG.4.74(b) indicated the comparison of the strain at rupture, it can be observed that there was an increasing trend, and the 30 SFM/EP condition presented the highest value.

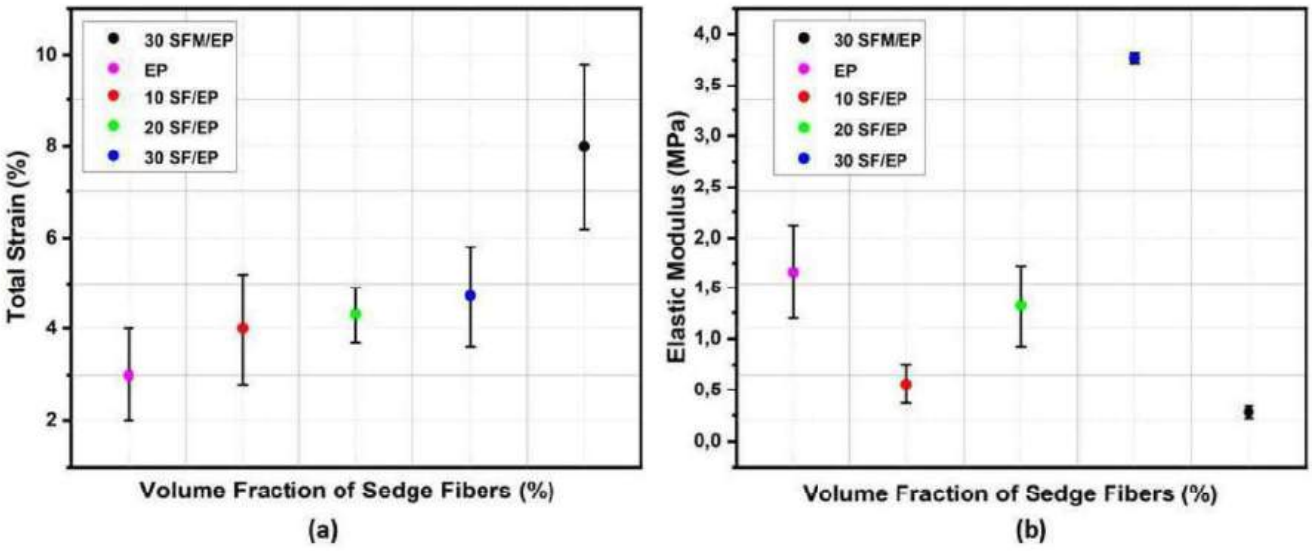

Figura 4.74 – (a) strain and (b) elastic modulus of the EP, 10 to 30 SF/EP, and 30 SFM/EP conditions.

The micrographs presented in FIG.4.75(a) and (b) show failure mechanisms that help increase the material's resistance, such as fiber rupture, river marks, *pullout*, and the presence of strong interfacial adhesion. The latter is justified by the reduced occurrence of delamination between the fiber and matrix interface. Therefore, an improvement in mechanical properties is evidenced by the efficient transfer of mechanical loads. However, in both figures, the presence of voids was observed, acting as stress concentrators. Therefore, due to this formation, the composite was possibly weakened, negatively impacting the material's mechanical performance.

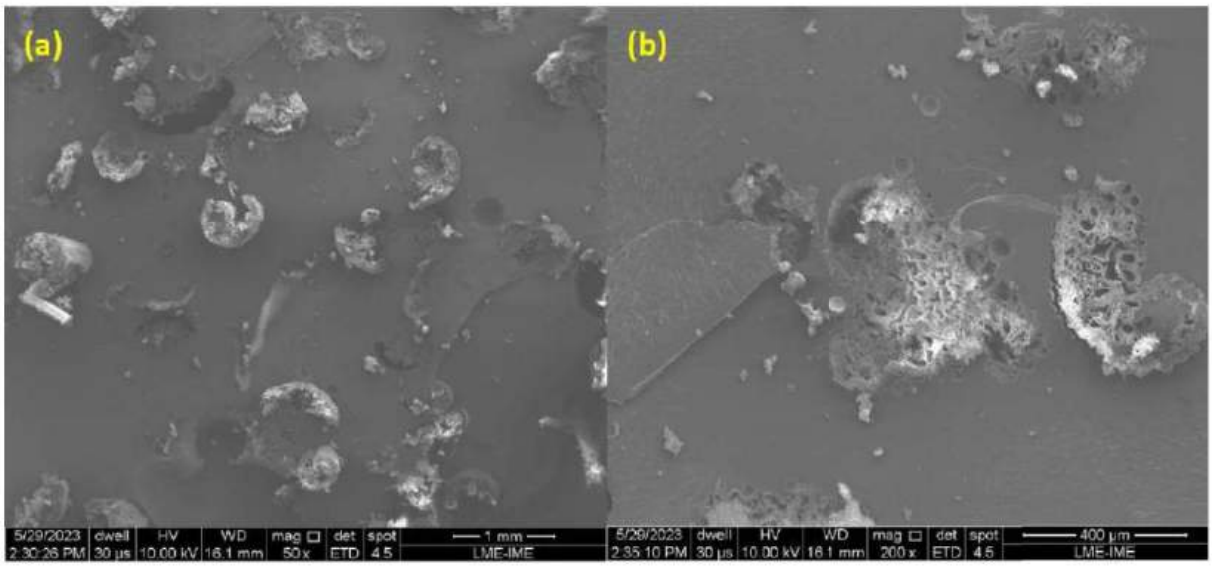

Figura 4.75 – Fracture mechanisms observed microscopically for the 30SFM/EP composite.

An ANOVA analysis was performed to check if there is a significant difference in the tensile strength at rupture between the 10 to 30 SF/EP and 30 SFM/EP conditions. As shown in TAB.4.53, the calculated F value (35.46) was much higher than the F_c at a significance level of 5%. Therefore, the hypothesis that the means are equal was rejected, indicating that there are conditions with significant differences.

Tabela 4.53 – Analysis of variance of the maximum tensile strength for 10 to 30 SF/EP and 30 SFM/EP.

Causes of Variation	Sums of squares	Degrees of freedom	Mean Square	F (calculated)	Fc (tabulated)
Treatments	3	996.09	332.03	**35.46**	**3.49**
Residue	12	112.37	9.36		
Total	15	1108.47			

The Tukey's test was performed to check which conditions have significant differences. This is validated when the values are higher than the calculated HSD (4.88). Thus, for this analysis, the conditions of 30 SF/EP and 30 SFM/EP showed values higher than the HSD. Meanwhile, the 20 SF/EP condition did not show a significant improvement compared to the 10 SF/EP group, although it showed a trend of increase in tensile strength at rupture.

Tabela 4.54 – Results for the differences between the mean values of maximum tensile strength after applying the Tukey's test.

Conditions	10 SF/EP	20 SF/EP	30 SF/EP	30 SFM/EP
10 SF/EP	0	4.42	**10.54**	**20.8**
20 SF/EP	4.42	0	**6.12**	**16.38**
30 SF/EP	**10.54**	**6.12**	0	**10.26**
30 SFM/EP	**20.8**	**16.38**	10.26	0

4.5.10 COMPRESSION TEST

The TAB.4.55 presents a comparison of compressive strength and strain at rupture for the conditions 10 to 30 SF/EP and 30 SFM/EP.

Tabela 4.55 – Average compressive strength (MPa) and total strain (%) obtained from the compression test for the EP, 10 to 30 SF/EP, and 30 SFM/EP conditions.

Conditions	Compressive Strength (MPa)	Total Strain (%)
10 SF/EP	18.51 ± 1.50	25.71 ± 10.36
20 SF/EP	20.44 ± 2.49	13.81 ± 4.45
30 SF/EP	21.21 ± 1.45	15.19 ± 4.69
30 SFM/EP	39.35 ± 11.24	41.44 ± 10.81

A graphical comparison of compressive strength for the aforementioned reinforcement conditions was conducted, as shown in FIG.4.76(a). This allowed observing the increasing trend as the amount of reinforcement increased. The alkaline treatment proved to be very effective, showing an increase of 85.52% compared to the 30 SF/EP condition. Furthermore, it performed better than the 30 SF/EP-GO condition (77.33%). However, the 30 SFGO/EP group was slightly superior, showing an increase of 5.23% compared to the present investigated condition.

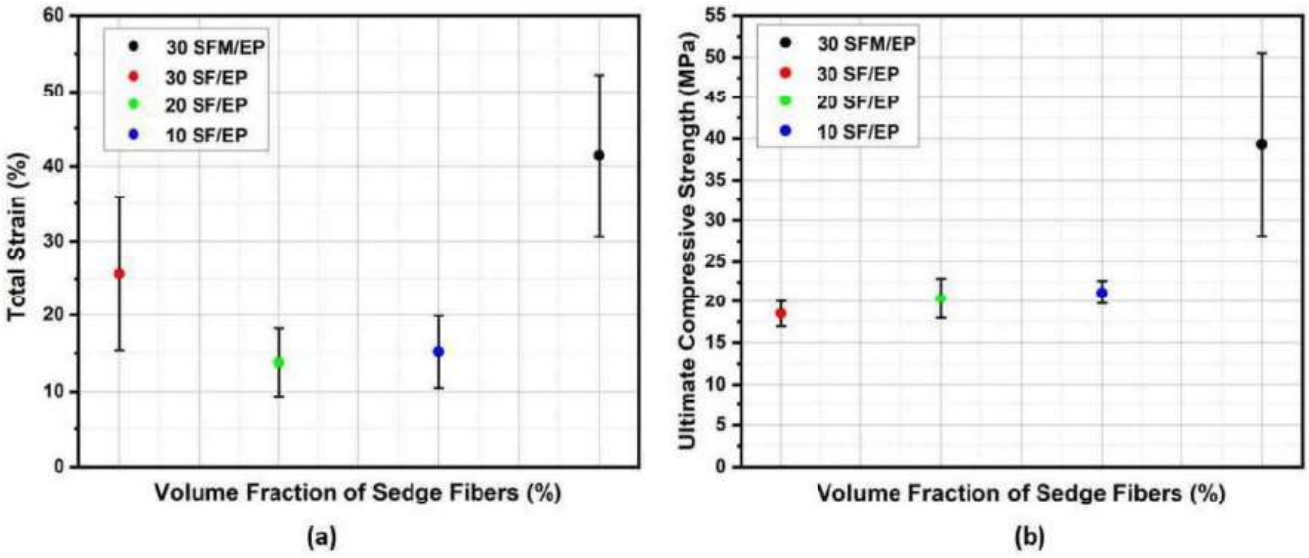

Figura 4.76 – (a) total strain and (b) compressive strength for the EP, 10 to 30 SF/EP, and 30 SFM/EP conditions.

The analyzed fracture mechanisms are illustrated in FIG.4.77 (a) and (b). In both micrographs, it is possible to observe the fiber surface impression in the matrix, indicating the pullout mechanism. Furthermore, river marks are present on the EP surface, indicating a brittle fracture mechanism. Meanwhile, the SF showed ruptures, bending and longitudinal fractures. There was an absence of delamination between the fiber-matrix interface, indicating that the alkaline treatment was effective and contributed to an efficient transfer of mechanical loads. Therefore, these were the main mechanisms that contributed to the increased material strength.

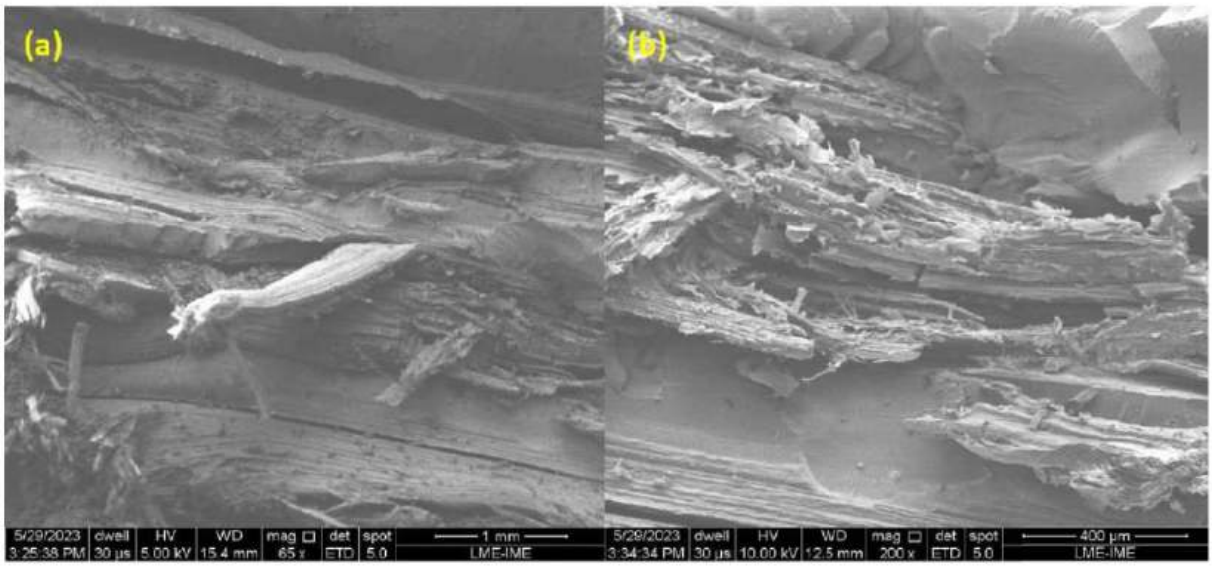

Figura 4.77 – Fracture mechanisms observed microscopically for the 30 SFM/EP composite.

ANOVA analysis was performed to investigate if there was a significant difference between the compared conditions. According to TAB.4.56, the hypothesis that the means are equal was rejected at a significance level of 5%. This was confirmed because the calculated F value (35.74) was higher than the tabulated F_c. Therefore, it was confirmed that there is a significant difference in compressive strength among the different reinforcement conditions.

Tabela 4.56 – Analysis of variance for the maximum compression stress for EP, 10 to 30 SF/EP, and 30 SFM/EP.

Causes of Variation	Sums of squares	Degrees of freedom	Mean Square	F (calculated)	Fc (tabulated)
Treatments	3	1833.27	611.09	**35.74**	**3.49**
Residue	12	205.15	17.09		
Total	15	2038.43			

The Tukey's test was conducted to verify which possible conditions show differences. As shown in TAB.4.57, the highlighted values presented a higher value than the calculated HSD (6.45). Therefore, only the 30 SFM/EP condition showed differences superior to all groups, indicating that this was the group that exhibited better mechanical performance.

Tabela 4.57 – Results for the differences between the mean values of maximum compressive strength after applying the Tukey's test.

Conditions	10 SF/EP	20 SF/EP	30 SF/EP	30 SFM/EP
10 SF/EP	0	1.13	2.24	**28.69**
20 SF/EP	1.13	0	1.10	**27.55**
30 SF/EP	2.24	1.10	0	**26.45**
30 SFM/EP	**28.69**	**27.55**	26.45	0

4.6 BALLISTIC TESTS

4.6.1 EVALUATION OF THE MULTILAYER ARMOR SYSTEM (MAS)

Ballistic tests measuring trauma on clay witness were conducted for the conditions presented in TAB.4.58. A total of 6 MAS were used in each group. No complete projectile penetration occurred in any tested group for the 7.62 mm projectile. The average trauma value on the clay witness, obtained for conditions ranging from 10 to 30 SF/EP, was below 44 mm. This value is considered lethal to humans, as outlined by the NIJ 0101.06 standard. However, in the 10 SF/EP group, samples 1 and 4 showed values above 44 mm. Meanwhile, the 20 and 30 SF/EP groups had some samples close to but below the value. This would indicate compliance with the standard; however, all composite plates from all groups did not meet the physical integrity criterion after the shot. This is indicative of the invalidation of the investigated MAS as a ballistic shielding material.

Tabela 4.58 – Results of ballistic tests for MAS containing an intermediate layer of 10 to 30 SF/EP for measuring trauma on clay witness.

Average Trauma Value on Clay Witness			
Shot	**10 SF/EP**	**20 SF/EP**	**30 SF/EP**
1	57.1	43.2	33.8
2	37.8	21.5	20.8
3	36.3	30.4	38.6
4	45.8	41.7	31.6
5	27.5	29.9	35.6
6	27.2	28.2	43.2
Mean	**38.62**	**32.48**	**33.93**
Standard Deviation	**10.43**	**7.63**	**6.93**

ANOVA analysis was conducted to verify the occurrence of a significant difference between the means of traumas produced in the clay witness by conditions 10 to 30 SF/EP. The statistical parameters found are disclosed in TAB.4.59. Therefore, the hypothesis that the mean values are equal is accepted with a significance level of 5%. This occurred

because the calculated F (0.63) had a lower value than F_c (3.88), confirming that there is no difference between the traumas caused in the clay witness after the ballistic test.

Tabela 4.59 – Analysis of variance of the average depths produced in clay witness by the impact of the 7.62 mm projectile in MASs containing an intermediate layer of 10 to 30 SF/EP.

Causes of Variation	**Sums of squares**	**Degrees of freedom**	**Mean Square**	**F (calculated)**	**Fc (tabulated)**
Treatments	2	60.24	30.12	**0.63**	**3.88**
Residue	12	753.63	62.80		
Total	14	813.88			

Through visual analysis according to FIG.4.78, it was possible to verify that all conditions exhibited complete fragmentation of the SF/EP composite intermediate plate. This renders the MAS unable to withstand subsequent impacts beyond the first projectile. Therefore, in addition to the trauma indentation value, this behavior makes the material unsuitable for use in individual ballistic protection. Furthermore, the NIJ standard does not consider a material appropriate for use in armor if it completely fragments after the first shot. Additionally, as observed, it was verified that the third layer was completely deformed after the conducted shot. Therefore, a hypothesis for improving the reinforcement would be to alter the configuration of the fiber reinforcement, for example, with alternating layers oriented at 0 and 90°.

Figura 4.78 – Sample observed macroscopically after the test was conducted.

In FIG.4.79, it is possible to observe the presence of ceramic debris adhered to the fragments of SF/EP composites. The micrographs shown in FIG.4.79 (a)-(f) revealed the presence of particles adhered to the SF/EP composites. Additionally, FIG.4.79 (d) exhibits the presence of river marks and delamination between the fiber and matrix interface.

Meanwhile, 4.79 (f) shows the pullout mechanism through the impression of the rough surface of SF in the matrix.

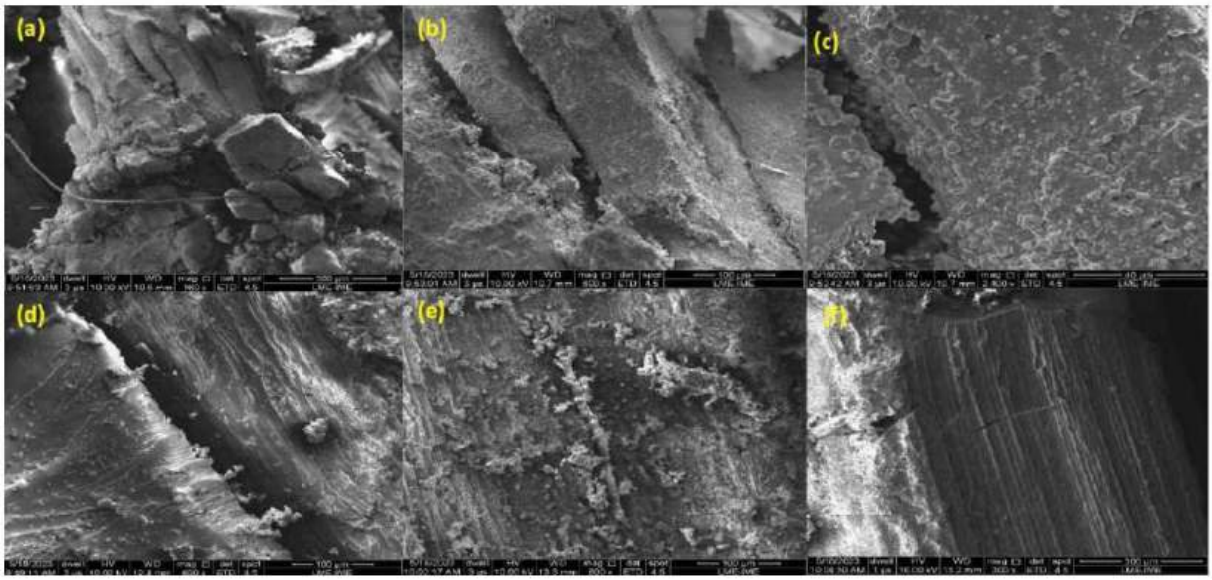

Figura 4.79 – Mechanisms observed microscopically for 10 to 30 SF/EP conditions.

Energy Dispersive Spectroscopy (EDS) was used to verify whether the particles are ceramic, as illustrated in FIG.4.80. It is possible to observe that the punctually analyzed region has an intense peak corresponding to the chemical element Al. This element is part of the chemical composition of alumina (Al_2O_3). Meanwhile, the Au (gold) peak is related to the deposition of gold to assist in electron conduction. Therefore, it is confirmed that the particles captured by the composites came from the ceramic front layer.

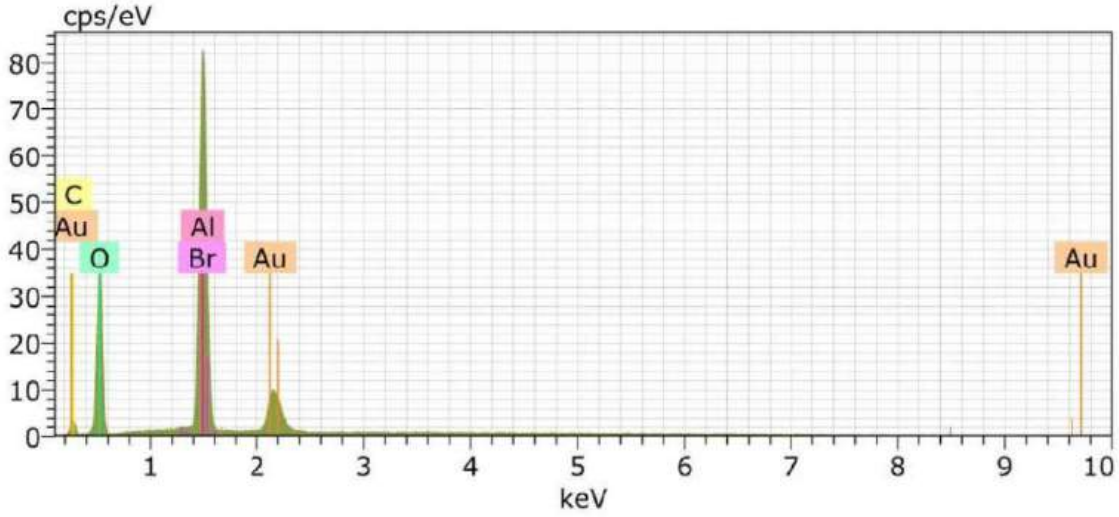

Figura 4.80 – Energy Dispersive Spectroscopy (EDS).

As shown in TAB.4.60, it is possible to observe that other fabrics, mats, or natural fibers reinforcing thermosetting matrices presented acceptable average values for trauma on

the clay witness. These values are considerably lower than 30 mm in trauma depth, which was not the case for the investigated conditions. Thus, SF acting as a reinforcement was not effective in producing an efficient reinforcement with physical integrity, even though it synergistically captured fragments of fractured ceramic debris.

Tabela 4.60 – Comparison between measured traumas for MASs reinforced with NLFs in different reinforcement configurations and the investigated conditions of 10 to 30 SF/EP.

Intermediary layer	**Average trauma value on clay witness reinforced (mm)**	**Reference**
10 SF/EP	38.6 ± 10.4	PT
20 SF/EP	32.5 ± 7.6	PT
30/SF/EP	33.9 ± 6.93	PT
Polyester reinforced with fique fiber 10% volume	17 ± 2	(LUZ et al., 2017)
Polyester reinforced with fique fiber 20% volume	16 ± 1	
Polyester reinforced with fique fiber 30% volume	17 ± 3	
Polyester reinforced with sisal fiber 10% volume	22 ± 3	(MONTEIRO et al., 2016)
Polyester reinforced with sisal fiber 20% volume	26 ± 4	
Polyester reinforced with sisal fiber 30% volume	26 ± 2	
Epoxy reinforced with curaua fiber 30% volume	25.6 ± 0.2	(COSTA et al., 2019)
Epoxy reinforced with curaua mat 30% volume	28 ± 3	(BRAGA et al., 2017b)
Epoxy reinforced with jute fabric 30% volume	21 ± 3	(LUZ et al., 2015)
Polyester reinforced with jute mat 30% volume	24 ± 7	(ASSIS et al., 2018)
Kevlar	23 ± 3	(MONTEIRO et al., 2016)

4.6.2 RESIDUAL VELOCITY BALLISTIC TEST FOR EPOXY COMPOSITE REINFORCED WITH SEDGE FIBERS

In the ballistic tests, the values of V_i and V_R were determined through EQ. 2.10, which allows the calculation of energy absorption. The E_{abs} for the samples of each group condition are shown in TAB. 4.61. The influence of fibers percentage used as reinforcement can be seen by the mean results and their respective standard deviations. However, the reliability of the results will depend on the statistical analyses.

Tabela 4.61 – The results of energy absorption for different composite plates conditions.

Conditions	**10 SF/EP**	**20 SF/EP**	**30 SF/EP**
Absorbed Energy (J)	189.95	272.99	199.49
	228.44	228.79	163.74
	188.48	189.12	232.83
	203.17	214.44	204.99
	181.76	218.47	129.91
	278.47	220.49	129.91
	246.22	224.69	169.11
	202.26	207.84	116.45
Mean	**214.85**	**222.11**	**167.18**
Standard Deviation	**31.46**	**22.38**	**39.05**

ANOVA analyses have been performed. In the ANOVA analysis, there are statistical parameters that interfere with its reliability, as shown in TAB.4.62. Confirmation occurred that F is greater than F_c because the value of F is 6.2 and F_c (3.47). For this reason, it can be concluded that the mean values are equal in the hypothesis of being rejected with 95% confidence. The different amounts of fibers in the composites influenced the energy absorption (E_{abs}), which was confirmed by ANOVA.

Tabela 4.62 – ANOVA analysis to obtain energy absorption results.

Causes of variation	**Degrees of freedom**	**Sums of squares**	**Mean square**	**F (calculated)**	**Fc (tabulated)**
Treatment	2	14244.28	7122.14	6.19	3.47
Residue	21	24126.34	1148.87		
Total	23	38379.63			

Furthermore, the Tukey test, as depicted in Table 5, was used in order to associate the mean values. The result of q was found to be 2.94 for 3 treatments and 21 of freedom. Therefore, the 35.2 J value of the honestly significant difference (HSD) was calculated

using EQ. 3.8. TAB. 4.63 shows the relationship between the mean values using HSD. It is worth mentioning that the highlighted disparities between mean values were superior to the HSD and are present in this table. The use of the present material is recommended as one of the layers of the multilayer armor system (MAS), as mentioned in the literature (REIS et al., 2021; OLIVEIRA et al., 2021; BHAT et al., 2021).

Tabela 4.63 – Mean values of the Tukey's test for absorption by composite plates.

Conditons	**10 SF/EP**	**20 SF/EP**	**30 SF/EP**
10 SF/EP	0	7.26	**47.66**
20 SF/EP	7.26	0	**54.93**
30 SF/EP	**47.66**	**54.93**	0

EQ. 2.11 was used to determine the limit velocity values (V_L) and the results are disclosed in TAB.4.64. In addition, this shows a comparison of the limit velocity for composites, whether reinforced with natural fibers or reinforced by synthetic fibers of Twaron and Kevlar™. When applied to an autonomous target, investigation has shown hat the sedge fiber reinforced epoxy matrix composite proved unsatisfactory with a protection against 7.62 mm ammunition. As a consequence of the impact velocity for this type of ammunition exceeding 800 m/s. While the composite manages to stop the bullet only on a range of 180-215 m/s with the present conditions tested.

Tabela 4.64 – Limit, residual and impact velocity for the composite plates reinforced with sedge fibers tested.

Conditions	$\mathbf{V_i}$	$\mathbf{V_R}$	$\mathbf{V_L}$	$\mathbf{E_{abs}}$	**References**
10 SF/EP	837.17 ± 2.73	810.27 ± 5.07	209.93 ± 15.02	214.85 ± 31.36	PT*
20 SF/EP	832.22 ± 4.96	808.37 ± 5.26	213.74 ± 10.56	222.11 ± 22.38	PT*
30 SF/EP	805.64 ± 29.37	784.07 ± 25.97	184.40 ± 21.58	167.18 ± 39.05	PT*
Epoxy/ 30% piassava fibers	-	-	202 ± 7	200 ± 15	Filho et al. (2020a)
Kevlar™	-	-	212 ± 23	-	Braga et al. (2017a)

*PT = Present Work.

Based on the results acquired and calculated, it is possible to observe that the condition containing 20 SF/EP presents the highest energy absorption. Although it is very similar to the value obtained for the condition of 10 SF/EP. The behavior of these samples could be correlated with the brittle fracture of the epoxy matrix that tends to dissolve the energy by the production of fractured surfaces. Thus, it could be considered an indicative that the reinforcement has not been done in an effective way. It became evident by the HSD that the group 30 SF/EP exhibited the lowest values of energy absorption.

FIG. 4.81 (a) and (b) depict the macroscopic fracture aspect of the conditions of 30 and 20 SF/EP after the ballistic tests have been performed. FIG. 4.81 (b) shows a rupture pattern of a specimen containing 20 SF/EP without a preferential direction that resulted in the absolute fragmentation of the specimen into the specimen. It is worth mentioning that the same behavior occurred for the groups containing 10 SF/EP acting as a reinforcement. Furthermore, this behavior is not desirable in terms of ballistic armor application that should be subjected to multiple hits from gun ammunition. However, the physical integrity of the targets reinforced with 30 SF/EP stands out as the most integer group condition. Although, when set against the amount of energy absorbed by the Kevlar^{TM} laminate (220 $\pm$ 17 J) (BRAGA et al., 2017a), it is clear to observe that only the conditions of 10 and 20 SF/EP present values are similar or just a bit lower.

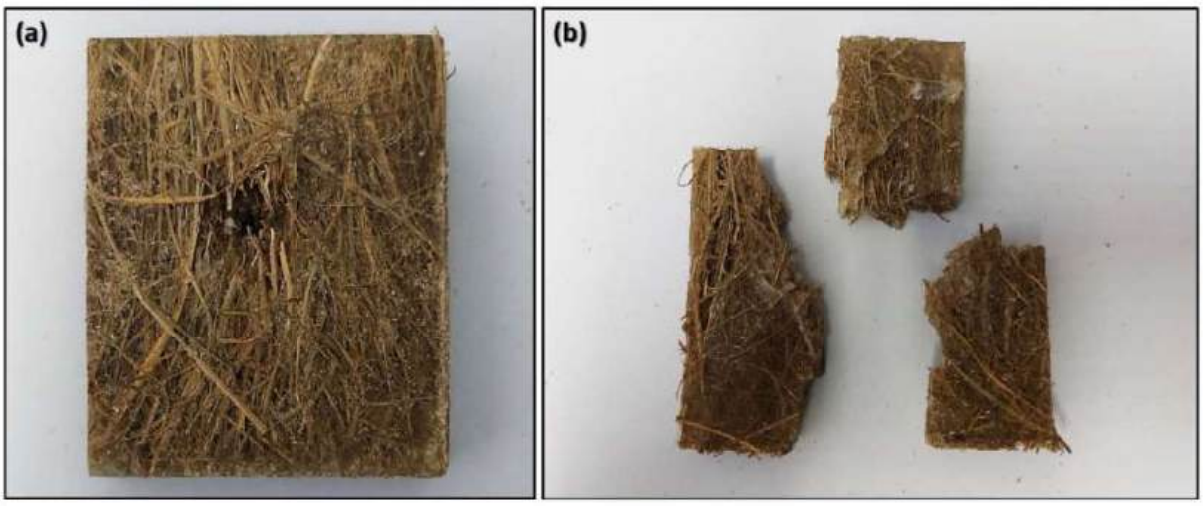

Figura 4.81 – Visual analysis after the ballistic impact of the composite plates for the percentages of (a) 30 SF/EP and (b) 20 SF/EP.

Considering the application of the composite plates as an intermediate layer for the multilayer armor system (MAS) against a multi-hit standard ballistic test (LUZ et al., 2017; MONTEIRO et al., 2018; ASSIS et al., 2018; PEREIRA et al., 2019), the physical integrity of this material after multiple impacts plays is of great importance for the material selection. Another important factor that stimulates the use of the 30 SF/EP condition is the relationship between the quantity of fiber used and the reduction in the final cost of

the composite. Even so, the results of the absorbed energy did not show a satisfactory increase when compared to other conditions.

The complete rupture of the composites reinforced with 10 and 20 SF/EP is due to the brittle characteristic displayed by the epoxy matrix for the main mechanism of failure. These conditions not only have a lower amount of sedge fiber acting as a reinforcement but may be due to an ineffective percentage of reinforcement. Recent researchers in literature report that the composite material becomes more resistant to the impact when matrix reinforcement is increased by adding more fibers (COSTA et al., 2020; PRASAD et al., 2021; PEREIRA et al., 2022). Hence, other complex fracture mechanisms are present, such as fiber bridging, fiber *pullout*, fracture of matrix and fiber and delamination (MONTEIRO et al., 2009).

These mechanisms can be better understood and investigated by depicting the various failure mechanisms that provide ballistic impact. As an example, FIG. 4.82 (a) portrays a fiber breakage, including the microfibril rupture after the ballistic impact. It is important to note that fiber fracture that discloses fragile characteristics, is verified through the internal rupture of the channels relating to a structural cell. In literature, these channels are described as microfibrils arrangements (AL-MAHARMA; AL-HUNITI, 2019). In 4.82 (a), the epoxy matrix presented brittle fracture. This is associated with the appearance of river mark patterns on the epoxy matrix surface.

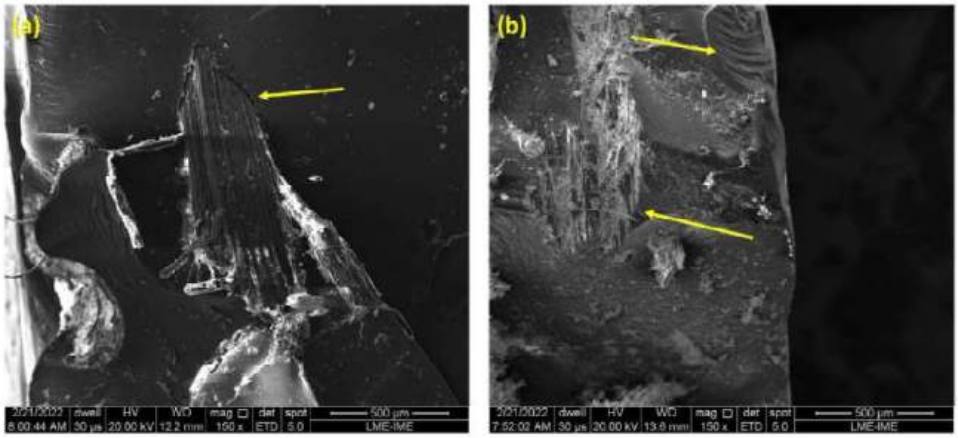

Figura 4.82 – During the ballistic impact, the failure mechanisms are observed: (a) fracture of fiber and microfibrils rupture; (b) river marks and printed surface of sedge fiber in epoxy matrix after complete fiber/matrix separations.

In FIG. 4.83 (a), also shown brittle behavior of the epoxy matrix. It was noted that the fracture of the fiber presented fragile characteristics , due to the internal voids breakage associated with the cellular structure. In literature, the voids are described as the microfibrillar arrangement (AHMED; ULVEN, 2018; SHAKER; NAWAB, 2022). It was observed that in all conditions tested that the failure of the epoxy matrix showed

mechanisms typical of brittle fracture. While mechanisms associated with the fibers were also present, as it is shown in the figures aforementioned. FIG. 4.83 (b) shows the fiber extraction mechanism which is identified as the *pullout* hole. The impression caused on the surface of the fiber in the matrix is due to the mechanism of removal of the fiber from the epoxy matrix with the same direction as the loading. When composites are subjected to static loads or after dynamic events, they suffer a type of failure that is considered a low fiber/matrix interfacial adhesion mechanism (FILHO et al., 2020a).

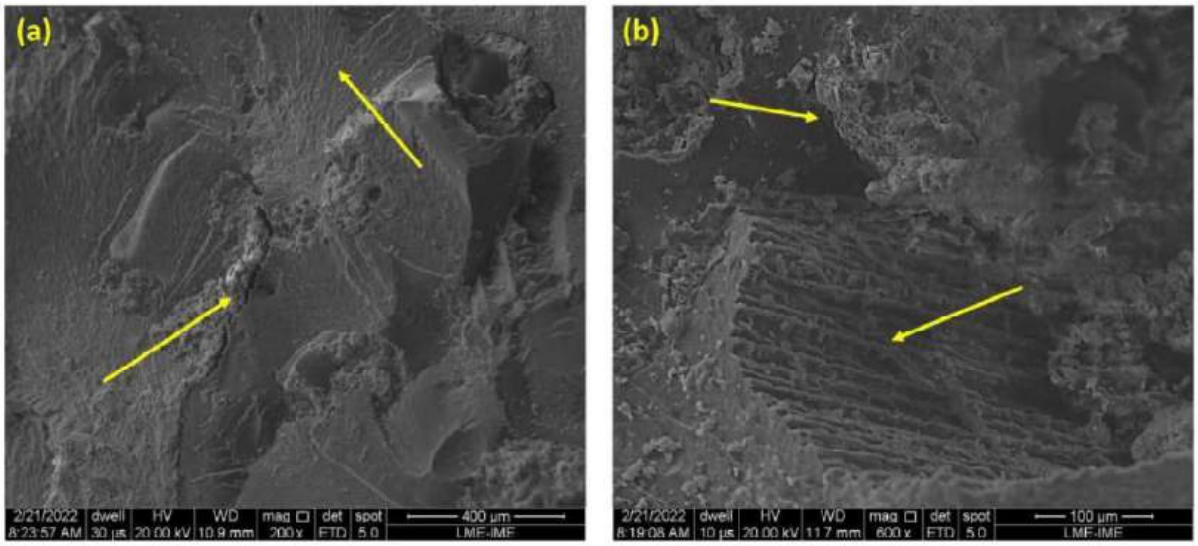

Figura 4.83 – Microscopic aspect of the composite plate after the ballistic impact: (a) cracks, river marks, and matrix brittle failure;(b) pullout hole and fiber rupture.

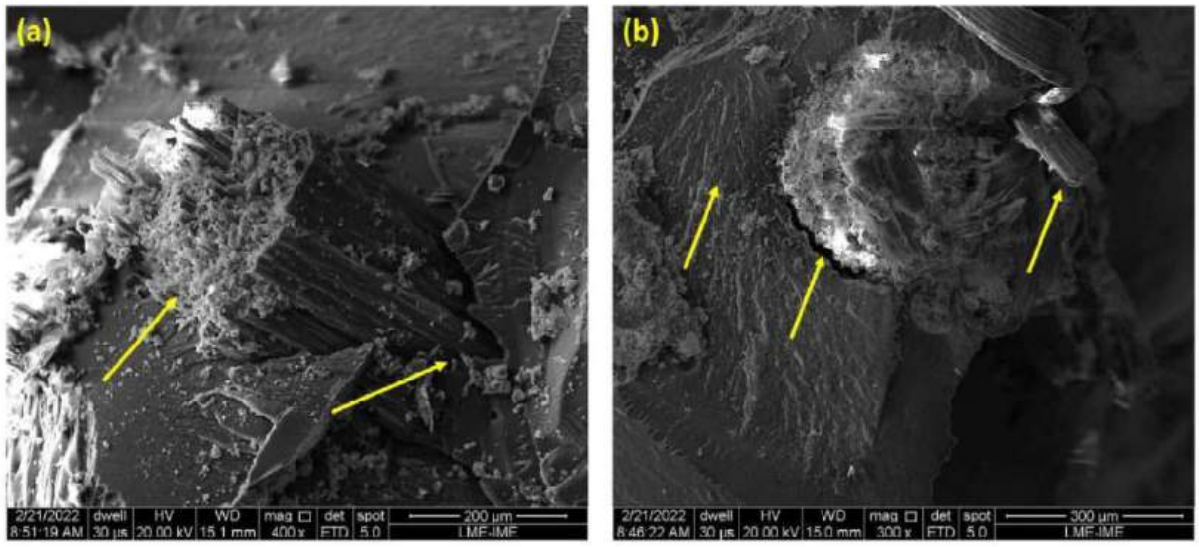

Figura 4.84 – Delamination mechanism: (a) fiber rupture and a low fiber/matrix interfacial adhesion; (b) river marks, microfibril rupture, and delamination.

The crack present in FIG. 4.84 (a) tends to occur and when it spreads near the interface delamination takes place. Additionally, in FIG. 4.84 (a), it is possible to observe a rupture of the epoxy matrix. While FIG. 4.84 (b) shows in detail the delamination mechanisms, which is a behavior associated with the preexisting characteristics of the epoxy matrix and natural fiber. Because the epoxy matrix has a hydrophobic characteristic, in contrast, sedge fibers display a hydrophilic characteristic as well as other NLFs. Regarding the sedge fibers, it was previously reported (NEUBA et al., 2020) that they presents a moisture content present equal to 15.2%. This is even higher than other NLFs. For this reason, even the drying process may not be effective to ensure good adhesion. Although, some chemical treatments should be worthier for reaching this desired characteristic. Thus, the matrix does not acquire structural quality with its reinforcement due to poor interfacial adhesion, which is not desirable.

4.6.3 RESIDUAL VELOCITY TEST OF COMPOSITES REINFORCED WITH SEDGE FIBERS COATED WITH GRAPHENE OXIDE (GO)

The parameters of V_i, V_r, V_L and E_{abs} for the samples belonging to the 30 SFGO/EP condition are presented in TAB. 4.65. Similar to the conditions of 10 to 30 SF/EP, the investigated group is not effective in providing sufficient protection against 7.62 mm ammunition when used as a standalone target. This is because this type of ammunition has a ballistic impact velocity above 800 m/s. While the projectile stopped by the 30 SFGO/EP composite has an average speed of 172 m/s, according to the calculated limit speed.

Tabela 4.65 – Impact velocity, residual velocity, limit velocity, and absorbed energy for the 30 SFGO/EP condition.

30 SFGO/EP Condition				
Shots	$\mathbf{V_i}$	$\mathbf{V_r}$	$\mathbf{V_L}$	$\mathbf{E_{abs}}$
1	869.32	851.05	177.31	152.48
2	876.15	858.00	177.38	152.59
3	871.43	857.31	156.24	118.39
4	872.55	855.37	172.29	143.97
5	870.94	853.24	174,67	147.97
6	880.72	865.86	161.10	125.87
7	872.51	852.99	183.53	163.36
8	872.22	854.31	175.89	150.04
Mean	**873.23**	**856.02**	**172.30**	**144.33**
Standard Deviation	**3.36**	**4.29**	**8.51**	**13.95**

Additionally, it can be observed that the current 30 SFGO/EP condition has a

lower value of energy absorption compared to the other SF/EP conditions. This may be an indicative of effective reinforcement, as the 10 and 20 SF/EP conditions show higher absorption values due to the complete rupture of the brittle material. Furthermore, it showed a lower value than the 30 SF/EP condition, possibly because GO enhances interfacial strength and promotes greater physical integrity with lower percentages of cracks.

A graphical comparison was conducted and presented in FIG. 4.85 between the averages of the absorbed energies of 10 to 30 SF/EP and 30 SFGO/EP conditions. Therefore, it was possible to observe that the standard deviation proved to be lower than the other previously investigated conditions (NEUBA et al., 2023b), indicating that the current condition presents greater homogeneity and similar energy absorption performance among the tested plates. Additionally, a slight reduction in E_{abs} was observed compared to the 30 SF/EP condition and a lower value compared to Kevlar™.

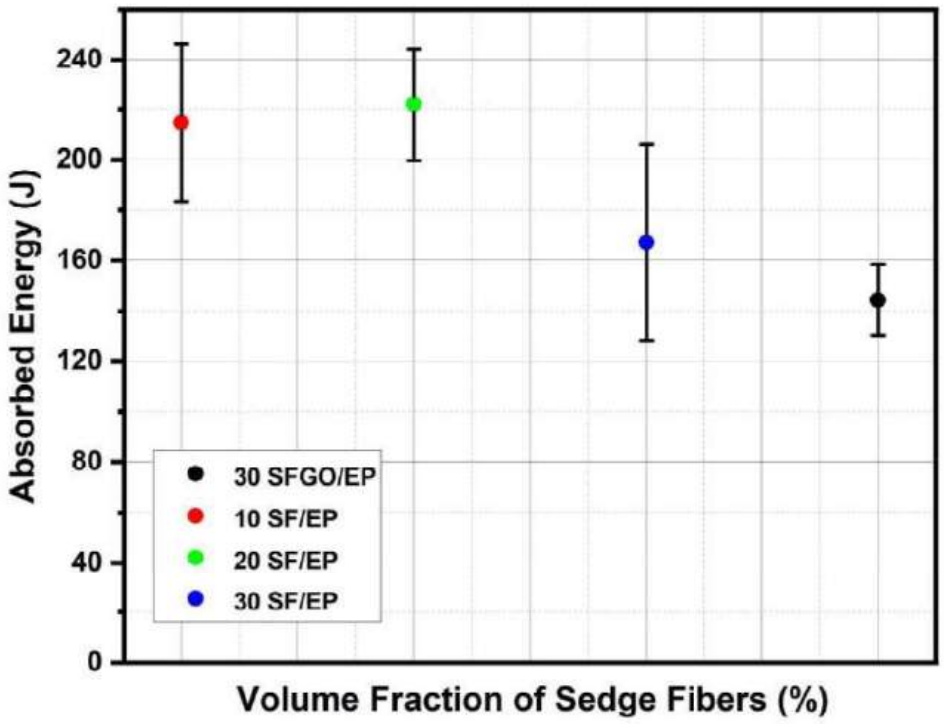

Figura 4.85 – Comparison of absorbed energy for different SF/EP reinforcement conditions and 30 SFGO/EP.

ANOVA analysis was performed to check for significant differences among the mean absorbed energies. As shown in TAB. 4.66, the comparison between the calculated F (6.04) and the tabulated F_c (3.24) indicated that the calculated F is higher. Thus, the hypothesis that the mean values are equivalent can be rejected with 95% confidence, corroborating that the difference in reinforcements in the test specimens did indeed affect E_{abs}.

Tabela 4.66 – ANOVA treatment for the absorbed energy data from the 10 to 30 SF/EP conditions and 30 SFGO/EP.

Causes of Variation	**Sums of squares**	**Degrees of freedom**	**Mean Square**	**F (calculated)**	**Fc (tabulated)**
Treatament	3	13194.24	11650.55	6.04	3.24
Residue	16	11650.55	728.16		
Total	19	24844.79			

The Tukey's test was conducted to compare mean values and identify conditions with significant differences. The calculated HSD value was 36.18. Differences between mean values greater than the HSD are highlighted in TAB. 4.67. As indicated, the 30 SFGO/EP condition only shows significant differences with the groups of 10 and 30 SF/EP. Meanwhile, the 30 SF/EP condition exhibits differences only with 20 SF/EP. Therefore, it can be affirmed that the reduction in absorbed energy was not drastic for the 30 SFGO/EP and 30 SF/EP conditions.

Tabela 4.67 – Results for differences between mean absorbed energy values after applying the Tukey's test.

Conditions	**10 SF/EP**	**20 SF/EP**	**30 SF/EP**	**30 SFGO/EP**
10 SF/EP	0	26.40	12.17	**45.07**
20 SF/EP	26.40	0	**38.57**	**71.47**
30 SF/EP	12.17	**38.57**	0	32,90
30 SFGO/EP	**45.07**	**71.47**	32.90	0

FIG. 4.86 illustrates the macroscopic fracture appearance of the 30 SFGO/EP condition after the ballistic test. The observed physical integrity of the composite plate highlights a desirable behavior for ballistic armor applications subjected to multiple shots. However, structural integrity needs to be verified when inserted into a MAS.

Figura 4.86 – condition 30 SFGO/EP seen macroscopically after the test has been performed.

The fracture mechanisms of the matrix and fiber were investigated through microscopic images presented in FIG.4.87(a) to (f), aiming for a better understanding of the material's fracture behavior. In FIG.4.87(e), the microfibril rupture mechanism is evident. Additionally, in all micrographs, except for FIG.4.87(e), the appearance and propagation of river marks to the fiber/matrix interface regions are observed, which is characteristic of a material exhibiting brittle behavior. Furthermore, other fiber-related failure modes are associated, such as FIG.4.87(f), highlighting the presence of a hole with the impression of the SF's rough surface, indicative of the pullout mechanism. Additionally, FIG.4.87(a) to (c) indicate partial pullout extraction of the SFs near the interface regions. Lastly, the absence of delamination effects is observed in all micrographs. This failure mechanism

contributes negatively to the material's performance. Therefore, this is indicative that GO effectively acted as a coupling agent, providing a strong interface for the nanocomposite.

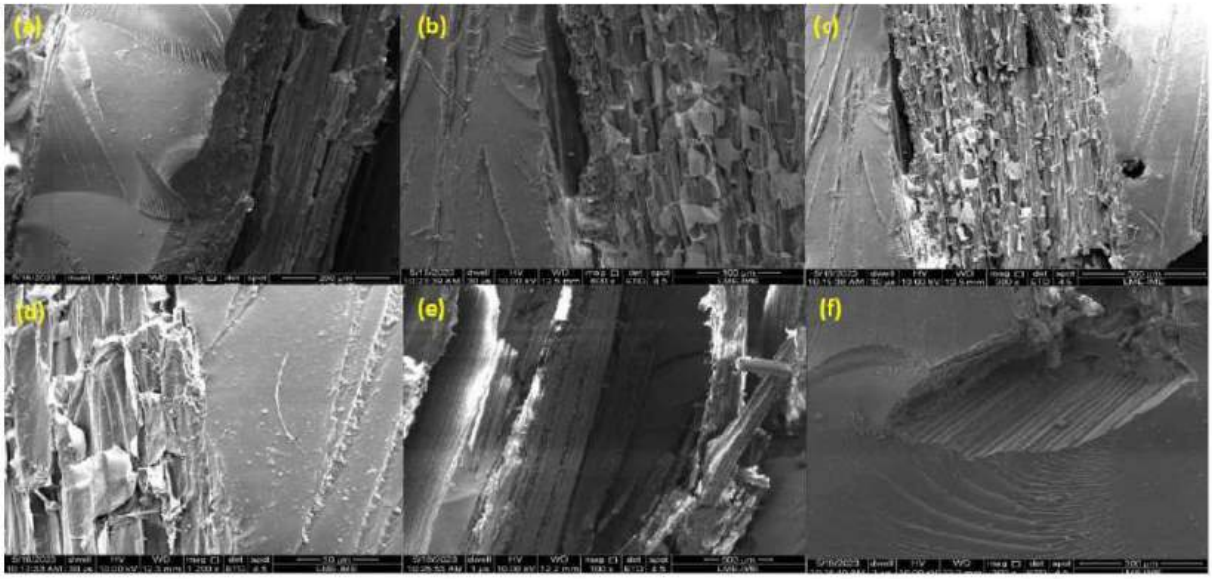

Figura 4.87 – Microscopically observed mechanisms for the 30 SFGO/EP nanocomposite.

4.6.4 RESIDUAL VELOCITY TEST OF COMPOSITES REINFORCED WITH ALKALINE TREATED SEDGE FIBERS

The parameters of V_i, V_r, V_L, and E_{abs} for the samples belonging to the 30 SFM/EP condition are presented in TAB. 4.68. Similar to the conditions of 10 to 30 SF/EP and 30 SFGO/EP, the investigated group is not effective in providing enough protection against 7.62 mm ammunition when employed as a standalone target. This is due to this type of ammunition having a ballistic impact velocity above 800 m/s. While the projectile stopped by the 30 SFM/EP composite has an average velocity of 185 m/s, according to the calculated limit speed.

Tabela 4.68 – Impact velocity, residual velocity, limit, and absorbed energy for the 30 SFM/EP condition.

Condition SFM/EP				
Shots	$\mathbf{V_i}$	$\mathbf{V_r}$	$\mathbf{V_L}$	$\mathbf{E_{abs}}$
1	854.38	839	160.71	125
2	851.58	836.35	160.38	124.74
3	853.13	828.69	202.73	199.33
4	845.00	826.38	176.42	150.33
5	852.85	831.37	190.18	175.42
6	861.49	842.25	181.06	158.99
7	847.28	826.77	185.29	166.52
8	862.60	833.12	223.58	242.45
Mean	**853.54**	**833.00**	**185.05**	**167.96**
Standard Deviation	**5.73**	**5.46**	**19.73**	**36.49**

Additionally, it can be observed that the current condition, 30 SFM/EP, has a lower value of energy absorption compared to the conditions of 10 to 20 SF/EP, similar to the 30 SF/EP condition, and higher than the 30 SFGO/EP condition. This may indicate that the reinforcement was effective, as the 10 and 20 SF/EP conditions exhibit higher absorption values due to the complete rupture of the brittle material. The lower performance compared to the 30 SF/EP condition is likely associated with the embrittlement of SF through the alkaline treatment. Thus, the complete rupture of the material would contribute to the increased energy absorption.

A graphical comparison was conducted and presented in FIG. 4.88 between the averages of absorbed energies of composites 10 to 30 SF/EP and the 30 SFM/EP condition. Therefore, it was observed that the standard deviation proved to be higher than the previously investigated conditions of 10 and 20 SF/EP (NEUBA et al., 2023b), indicating that the current condition exhibits greater heterogeneity and divergent energy absorption performance among the tested plates. Additionally, an increase in E_{abs} was observed compared to the 30 SFGO/EP condition, and similar performance to 30 SF/EP.

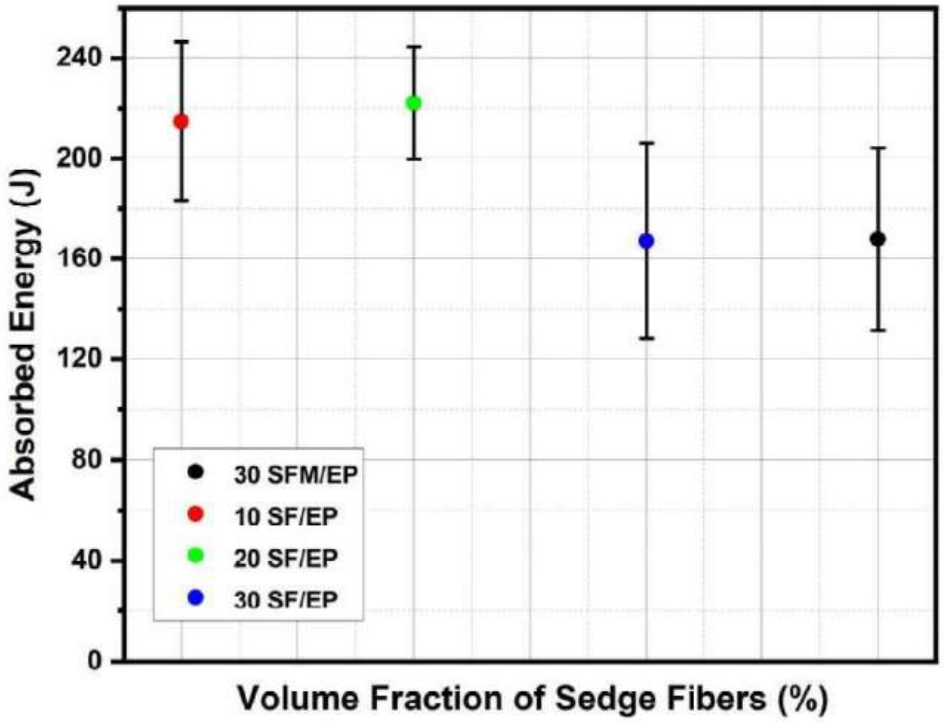

Figura 4.88 – Comparison of energy absorption for different SF/EP reinforcement conditions and 30 SFM/EP.

ANOVA analysis was conducted to verify if there is a significant difference between the average absorbed energies of the groups. As shown in TAB. 4.69, the comparison between the calculated F (4.25) and the critical F_c (3.24) indicated that the calculated F is higher. Thus, the hypothesis that the mean values are equal can be rejected with a 95% confidence level, indicating that the difference in reinforcements in the test specimens indeed affected E_{abs}.

Tabela 4.69 – ANOVA treatment for the data related to absorbed energy of conditions 10 to 30 SF/EP and 30 SFM/EP.

Causes of Variation	Sums of squares	Degrees of freedom	Mean Square	F (calculated)	Fc (tabulated)
Treatment	3	12514.18	4171.39	4.25	3.24
Residue	16	15706.59	981.66		
Total	19	28220.76			

The Tukey's test was conducted to compare mean values and identify which conditions have significant differences. The calculated HSD value was equivalent to 42. Differences between mean values greater than the HSD are highlighted in TAB. 4.70. As indicated, the current condition 30 SFM/EP only has significant differences between the groups of 10 and 20 SF/EP. Therefore, it can be stated that the reduction in absorbed

energy was not drastic for the 30 SFM/EP condition, and both 30 SFM/EP and 30 SF/EP have relatively close mean values.

Tabela 4.70 – Results for the differences between mean values of absorbed energy after applying the Tukey's test.

Conditions	10 SF/EP	20 SF/EP	30 SF/EP	30 SFM/EP
10 SF/EP	0	26.40	12.17	**43.22**
20 SF/EP	26.40	0	38.57	**69.61**
30 SF/EP	12.17	38.57	0	31.05
30 SFM/EP	**43.22**	**69.62**	31.05	0

The compromised physical integrity observed in some composite plates highlights an undesirable behavior for ballistic protection applications that should be subjected to multiple shots. In fact, alkaline treatment affected the physical integrity of the composite, as the 30 SF/EP condition statistically presented higher physical integrity in the tested samples. This may be due to the weakening of the sedge fiber due to the chemical treatment. As observed earlier, SFM presented regions with voids associated with the removal of lignin content, responsible for binding microfibrils. However, structural integrity verification is necessary when inserted into an MAS. In this case, SFM might not be effective for MAS in the unidirectional reinforcement condition. Checking different reinforcement configurations would be necessary for the 30 SF/EP, 30 SFGO/EP, and 30 SFM/EP conditions.

4.7 PERSPECTIVE OF ENGINEERING APPLICATIONS

According to Al-Oqla et al. (2016), Holbery e Houston (2006) automotive industry sector is continuously concerned about the governmental, societal and the environmental needs and responsibilities in improving their products. Natural fibers with polymer-based composites were strongly enhanced and developed for automobile industries in European countries. It can be found that the bio-based commercial vehicles—which are rich with interior parts made from recyclable natural fiber composites—are more economic and lighter alternatives for consumers. Several works had addressed the potential and capabilities in different applications. The mechanical properties, manufacturing processes, constituents compatibility as well as chemical modifications of natural fiber reinforcing polymer composites to improve their performance were extensively addressed (ABDAL-HAY et al., 2012; SAPUAN et al., 2013; THAKUR; VENNERBERG; KESSLER, 2014).

Asim et al. (2018) and Mansor et al. (2019) affirmed that since its inception, the aerospace industry has actively pioneered the use of advanced materials, especially polymer composites for aircraft construction. The key objectives are to gain lightweight advantages, so that aircraft can burn less fuel, and hence travel longer distances or carry higher payload

over the same distance. In line with the current drive toward improving sustainability performance the in aerospace industry, environmentally friendly materials are steadily being introduced as substitute materials for aircraft component construction, such as natural fiber polymer composites. The authors are in accordance with several aircraft industries are currently using composite materials for aircraft components to reduce weight such as in blade, secondary structures as aircraft radome and interior cabin components, and in other machinery parts. Many defense aircraft industries are also looking at the potential of fiber composite in camouflaging their aircraft from radar signals. Therefore, the epoxy sedge composites investigated are highly valuable options of environmentally friendly materials, as well as, possessing the advantage of low specific density and weight. At last, certainly are promising composites to be applied on ballistic vests, but require further investigation in order to clarify the ballistic behavior of fabric, mat and specific sedge fiber orientation reinforcing epoxy matrix

5 CONCLUSIONS

The work evaluated the effect of chemical treatment with NaOH on natural sedge fibers. Different NaOH solution concentrations of 3%, 5%, and 10% with different periods of 24, 48, and 72 h presented parameters that can be applied for obtaining better properties of the sedge fiber in polymeric composites. Furthermore, This work evaluated the GO coating effect on the surface of sedge fibers (SFGO). The GO concentration used was equivalent to 0.1 wt.% of the sedge fibers (SF).

1) The increase in crystallite size was observed for all nine alkali treated sedge conditions. Thus, favored resistance to moisture absorption and chemical reactivity of sedge fibers. Besides, a higher concentration of NaOH could lower the content of α cellulose, since strong degradation occurred by intracrystalline swelling. SEM images for the fibers treated with alkali showed that there was not as much presence of hemicellulose, wax, impurities, and lignin as shown for the fibers treated with 3% NaOH in different periods of time. Under conditions of 5% and 10% NaOH, damages on the surface of the fiber and greater extension of voids were present.

2) The crystallite size and crystallinity index of the SFGO were obtained by the XRD analysis. The increase in the crystallite size discloses a better resistance against moisture absorption and chemical reactivity of the sedge fiber. This ensures good adhesion of the interface. Furthermore, the GO is amphiphilic by nature, acting as a coupling agent. SEM images for the SF and SFGO showed that the GO has a thinner layer coating the sedge fiber, possessing nanometer thickness. Thus, the mechanical interlocking remains the same since the roughness was not significantly changed. While, the plain and uniform GO coating is similar to other observations in the literature. As expected, the amorphous content was not removed and coated by GO as well. In addition, is possible to observe some dashes with a higher, saturation which might be a sign of the GO coating. Therefore, the investigation has presented parameters that contribute for attaining the best interfacial adhesion when sedge fibers are to be applied as a reinforcement for polymer composites.

3) For all treatments of different concentrations and times, the disappearance of the 1731 cm^{-1} band stood out in comparison with the untreated fiber. This band is associated to the stretching of ester and carboxyl groups (C-O compound) present in hemicellulose. Thus, it is an indicative that amorphous content was removed. As for the SFGO, it was observed in the FTIR that the chemical bonding provided by the functional groups of GO caused a changed on the intensities of the spectra. Furthermore, according to the bands observed in the SFGO spectrum the presence of oxygen bonds is abundant.

4) TGA/DTG analysis revealed mass loss type results up to 200 °C, at the end

of the second stage, and up to 600 °C, in addition to the initial degradation and the maximum degradation rate. Comparing all the tests, the sedge fibers treated with NaOH at a concentration of 3% obtained the lower values of the thermal curves when compared with those under 5% and 10% NaOH treatments. In addition, the untreated fibers showed lower values than those with the 3% NaOH treatment. Under the time of 48 h, better thermal stability with a decay of the thermal curves was shown for all treatment conditions. DSC analysis showed the endothermic and exothermic peaks that better clarified the degradation of cellulose and hemicellulose and volatilization of lignin and wax present in the structure of the sedge fiber. Although, the 48 h condition presented a better stability, the same disclosed a higher intracrystalline swelling. Moreover, concentrations of 5% and 10% in all periods of time presented a damage on the surface integrity of the fiber. For the stated reasons, the lowest (3%) NaOH concentration has the potential to enhance composites reinforced by this fiber. The SFGO TGA/DTG analysis showed that the first thermal stability limit, represented by T_{onset}, was slightly lower than the untreated condition. However, the maximum degradation rate was increased from 300.95 to 321.14 °C. Thus, affirming that the GO effectively enhances the thermal stability of the sedge fibers. The third and final stage of degradation, associated with the lignin decomposition, reached its end at approximately 500 °C. The DSC analysis supported the comprehension of the endothermic and exothermic peaks regarding the cellulose, hemicellulose, volatilization of lignin and waxes. In addition, it was possible to observe the peaks associated with cellulose I (135 °C) and α cellulose (342 °C). Besides, presented a significantly change for the endothermic and exothermic of the unfunctionalized sedge fiber. Therefore, the investigation has presented parameters that contribute for attaining the best interfacial adhesion when sedge fibers are to be applied as a reinforcement for polymer composites

5) E' for all materials decreased around 73-78 °C, where movement occurs in the polymer chains and changes the material to a rubbery state. At 25 °C, the value of 2380 MPa for EP shows a higher value of E' compared to the composites. The E"of 30 SF/EP showed similar results to EP, with values of 201 and 200 MPa, respectively. Tan δ peak increased with the incorporation of the SFs into the EP. This may be linked to a decrease in adhesion between the fiber and the matrix. The Cole-Cole curves for each group showed irregular semicircles, which may be associated with greater material heterogeneity. The coefficient of effectiveness suggests an effective contribution by the SFs to the transition from the glassy to the rubbery state of the EP. E' for the nanocomposite was around 75 °C, where movement occurs in the polymer chains and changes the material to the rubbery state. At E", the 30 SF/EP-GO nanocomposite showed a relatively lower value (145 MPa). In Tan δ the GO acted as a filler for the limits of movement of the PE macromolecules, reducing viscoelastic friction. In relation to the incorporation of GO, a relatively lower Tan δ peak can be associated with the nanoparticles interfering with the macromolecular movement of EP as also found for E' and E". The Cole-Cole curve showed an irregular

semicircle, which may be associated with greater heterogeneity of the material. Particularly, the addition of GO promotes a more pronounced semicircular distortion, which can be interpreted as a heterogeneous distribution in the matrix. The effectiveness coefficient suggests an effective contribution from SF and GO to the transition from the glassy to the rubbery state of PE, with a comparatively more effective participation from GO. Regarding the 30 SFGO/EP nanocomposite, the drop of E' curve began in 79 °C. The E"curve reached a maximum peak in the T_g region around 89 °C. In addition, the T_g region began around 78 °C. The modulus reached a maximum peak of 128 MPa, indicating that the GO acted more strongly restricting the movement of the matrix macromolecules compared to the 30 SF/EP-GO nanocomposite. The Tan δ value was approximately 0.41, the reduced peak height of the 30 SFGO/EP condition can be attributed to a polymer chain with restricted movement. Meanwhile, the final T_g interval occurred at a higher temperature (around 158 °C) compared to the other conditions. It can be inferred from the Cole-Cole curve that 30 SFGO/EP presents a more homogeneous dispersion compared to EP. In particular, the effect of GO functionalizing SF promoted a behavior opposite to that of the Cole-Cole curve of 30 SF/EP-GO. The lowest value found for the effectiveness coefficient was for the 30 SFGO/EP nanocomposite, showing greater reinforcement efficiency compared to the other conditions. Furthermore, it is clear from the previous results that GO functionalizing SF performed better than incorporating it into the EP matrix. The drop in the E' curve began at 76 °C for the 30 SFM/EP condition, which is very similar to the behavior exhibited by 30 SF/EP-GO, 30 SFGO/EP and 10 to 30 SF/EP. In curve E"a maximum peak in the T_g region, at around 96 °C was reached, slightly higher than the 30 SFGO/EP condition (89 °C). Moreover, it can be seen that the T_g region began at 76 °C. A high energy dissipation, with the modulus reaching a maximum peak (around 132 MPa), represents the T_g of the system. The Tan δ value was approximately 0.39, very similar to condition 30 SFGO/EP (0.41), indicating that the present alkaline treatment produced a composite with a strong interfacial interaction, and similar to the control group, resulting in a lower energy dissipation at the interface. This result corroborates that presented in E". Furthermore, the final T_g interval occurred at a higher temperature (around 166 °C). The Cole-Cole curve of the 30 SFM/EP condition showed the same behavior as 30 SFGO/EP, where a more homogeneous dispersion was noted compared to EP. In particular, the effect of alkali treatment significantly reduces heterogeneous dispersion within the matrix. The 30 SFM/EP condition investigated presented the lowest value (0.108) found for the effectiveness coefficient, even lower than that exposed for 30SFGO/EP (0.191), exhibiting the highest reinforcement efficiency compared to the other conditions. Therefore, the investigation to verify the effectiveness of the alkali treatment and GO in promoting a stronger interfacial bond was positively satisfactory.

6) The TMA shows that the SF increased the T_g and the coefficient of linear thermal expansion (TEC). The incorporation of GO increased the TEC from 208.52 x 10^{-6}/°C to

248.95 x 10^{-6}/°C, but did not change due to the restriction of EP macromolecules. T_g found at 127 °C for the 30 SFGO/EP condition was higher than the other EP conditions, 30 SF/EP and 30 SF/EP-GO. It can therefore be inferred that the 30 SFGO/EP condition improves the material's thermal stability. Meanwhile, the TEC of 143.87 x 10^{-6}/°C proved to be slightly lower than the 30 SF/EP-GO treatment (168.03 x 10^{-6}/°C). This indicates that the GO coating the SF was more effective than the GO functionalizing the EP, corroborating the DMA results and providing an improved interface. While 30 SFM/EP showed a value of 131 °C for T_g. This is due to alkaline treatment promoting better adhesion and interfacial shear strength, providing greater restriction on macromolecular mobility. The alkaline treatment condition showed a TEC of 170.68 x 10^{-6}/°C. This treatment improved the fiber/matrix interface when compared to 30 SF/EP and EP. However, it showed a result close to the 30 SF/EP-G0 treatment (168.03 x 10^{-6}/°C) and slightly lower than the 30 SFGO/EP condition (143.87 x 10^{-6}/°C). Therefore it can be inferred that the use of GO, acting by a mechanism similar to a compatibilizing agent, proved to be more effective than increasing surface roughness and hydrophobicity. TGA and DTG analysis showed a lower thermal stability limit for the 30 SF/EP-GO nanocomposite when compared to the SF/EP conditions reported in the literature. Regarding the TGA/DTG analysis, it was observed that the addition of the nanofiller decreased the thermal stability when compared to the SF/EP and EP. According to the literature, the worse thermal stability may be caused by the GO reinforcement decreasing the cross-link density of the epoxy. The mass loss for the 30 SFGO/EP condition in the first stage was slightly higher than the EP condition (1.63%), while it was lower than 30 SF/EP (3.23%) and 30 SF/EP-GO (5.37%). T_{onset} found was 280 °C and the maximum degradation rate was 309 °C. Both results are lower than all the other conditions investigated. Thus, it can be inferred that the thermal stability of condition 30 SFGO/EP has a worse thermal stability. One possible reason for this reduction is that GO acts by reducing the density of cross-links, as inferred for 30 SF/EP-GO. Regarding the 30 SFM/EP condition, the T_{onset} found was 263 °C and the maximum degradation rate was 314 °C. Thus, it can be inferred that the thermal stability of condition 30 SFM/EP has the worst thermal stability. Therefore, alkali treatment was able to act positively by reducing the hydrophilic character, as evidenced by a lower initial mass loss. However, there was a reduction in thermal stability. The literature indicates that this behavior is associated with the fiber becoming more amorphous. The DSC analysis showed that the hydroxyl groups present in the basal plane of EP-GO participated in the opening of the epoxy rings as a curing agent. Acting as a catalyst and accelerating the curing reaction. This justifies the exothermic peak associated with the post-curing process occurring at lower temperatures than the EP and SF/EP conditions. Moreover, 30 SFGO/EP also showed the same behavior as the opening of the epoxy rings, due to the GO incorporated into the SF. In addition, an exothermic peak observed at 349 °C can be associated with the degradation of α cellulose

(SEKI et al., 2013). Another exothermic peak at 498 °C refers to the final decomposition of lignin and part of cellulose I. Regarding 30 SFM/EP, an endothermic peak was observed at 59 °C, associated with the T_g and release of the moisture present on the surface of the SF. The following exothermic peak at 120 °C may be associated with the post-curing process. Finally, an exothermic peak at 405 °C was observed, indicating that the hemicellulose and cellulose content had been completely decomposed.

7) In the FTIR spectra, bands associated with the 30 SF/EP-GO nanomaterial were observed, such as 1032 cm^{-1}. The O-H stretching and functional groups present in the GO nanostructure can be observed at 3433 cm^{-1}. Aromatic C=O groups present in the GO nanostructure are associated with the band at 1618 cm^{-1}. For 30 SFGO/EP the O-H stretch and functional groups present in the GO nanostructure can be observed at 3422 cm^{-1}. While the band at 1608 cm^{-1} is related to the aromatic group of the GO nanostructure and the C-O stretch, associated with GO, occurred at 1025 cm^{-1}. The values found for 30 SFGO/EP are very close to the 30 SF/EP-GO condition. Regarding the 30 SFM/EP composite, when compared to the 30 SFGO/EP condition, the 1024 and 825 cm^{-1} bands decreased in intensity. This can be explained by the reduction in the amount of lignin due to the chemical treatment used. Additionally, there is the absence of the band at 1731 cm^{-1}, indicating the removal of hemicellulose.

8) The Charpy and Izod impact tests were the only ones in which the 30 SF/EP-GO condition outperformed the control group. However, with the exception of the tensile test, the others showed a significant difference compared to the 30 SF/EP group, as observed by the Tukey test. The SEM micrographs showed some agglomerations of the nanoreinforcement. Interface delamination has been drastically reduced, indicating that the interface has become stronger. This possibly contributes to the increased mechanical performance of the material as a whole. Agglomerations, on the other hand, may have had the opposite effect. The literature extensively reports superior mechanical performance when mGO is applied as a reinforcement in polymeric matrices. Therefore, it could be a possible alternative to avoid the need to add more material and agglomeration. This makes the chemical modification of GO more economically attractive. Furthermore, the ANOVA analysis showed that there was a significant difference between the different conditions for all the mechanical tests. The Charpy and IZOD impact tests of the 30 SFGO/EP nanocomposite provided comparatively higher energy absorption compared to the EP, SF/EP and 30 SF/EP-GO conditions. This shows that the incorporation of GO into the surface of SF contributes efficiently to improving energy absorption. The hypotheses of equivalent means were rejected by ANOVA analysis of the Charpy impact, Izod, bending, tensile and compression tests. There was a considerable improvement in the flexural properties of the 30 SFGO/EP condition compared to 30 SF/EP. Furthermore, it was the only condition capable of showing superior mechanical performance to the control group. The same behavior occurred for the modulus of elasticity. The tensile test revealed

that, the 30 SFGO/EP condition, had considerably increased performance compared to 30 SF/EP and a slight increase in the EP condition. Therefore, it is possible to deduce that the incorporation of GO coating the surface was more effective than the functionalization of EP by the nanomaterial. Regarding the compression test, it was found that only the GO coating on the SF surface was effective in improving the mechanical performance when the nanocomposite is subjected to compressive stresses compared to the control group, when compared to the 30 SF/EP-GO condition. The Charpy impact test revealed that the 30 SFM/EP condition was able to improve the performance of the 30 SF/EP and proved to be less efficient when the GO acted by increasing the toughness of the EP resin or as a coating for the SF. On the other hand, the investigated condition containing SFM performed better than all the other conditions investigated. The hypotheses of equivalent means were again rejected by ANOVA analysis of the Charpy impact, Izod, bending, tensile and compression tests. The tensile test revealed that the alkali treatment was effective in improving mechanical performance when compared to the 30 SF/EP condition. However, it was ineffective in outperforming EP and 30 SFGO/EP. The literature investigated, have reported that the alkali treatment of some NLFs produces more fragile fibers, which has a negative impact on mechanical performance. The performance of the modulus of elasticity was also unsatisfactory, associated with some factors such as stress concentrators leading to premature rupture of the material and the SFM fragile behavior caused by the chemical treatment. Moreover, the microscopies investigated revealed some mechanisms for 30 SFGO/EP and 30 SFM/EP conditions : fiber and fibril rupture, fiber rupture along the length, fiber crushing, initiation and propagation of river marks, pullout, fiber surface imprinting on the matrix, absence of GO agglomerations, presence of voids formed near the fiber-matrix interface micro-regions. Although the pullout mechanism occurred, it was not observed in large quantities. The presence of voids was observed for the 30 SFGO/EP and 30 SFM/EP conditions, in the micrographs of the samples referring to the tensile test of the 30 SFGO/EP condition, corroborating the hypothesis that they acted as stress concentrators and had a negative impact on the toughness of the material. These are the main failure mechanisms that contribute to energy absorption. In fact, it was observed that the material showed good adhesion between the interfaces, with a slight displacement of the SF at the interface. This is relevant, as it is an indicative that the incorporation of GO as a coupling agent has fulfilled its main function sought in this research. This function is to improve the interface between SF and EP resin. Additionally, the delamination mechanism was also drastically reduced for the 30 SFM/EP condition, indicating that the alkali treatment was effective in fulfilling its main purpose. Another very important experimental observation is the bending of the fiber at the interface. This may have occurred because the fiber is very hollow, as many micrographs have shown. Furthermore, even though the fiber bent, it did not undergo pullout. One hypothesis for the occurrence of this phenomenon is the action of compressing the SF during the

composite manufacturing process. Therefore, the air trapped inside the fiber channels will produce a low-density composite and possibly a nanocomposite with high specific strength. While only the mechanical strength of the composite is low. Regarding the bending test, the 30 SFM/EP condition was the only composite group capable of outperforming EP. However, the alkali treatment was inferior to 30 SFGO/EP.

9) In none of the groups tested there was complete penetration by the 7.62 mm projectile. The average value of the trauma to the clay witness, obtained for 10 to 30 SF/EP, was less than 44 mm. However, in the 10 SF/EP group, samples 1 and 4 showed values higher than 44 mm. Meanwhile, the 20 and 30 SF/EP groups had some samples close to the value, but lower. This would indicate approval by the standard. However, all the composite plates in all the groups did not meet the criteria for physical integrity after firing, i.e. they fragmented completely. This indicates that the MASs investigated have been invalidated as a ballistic armor material by the standard. A possible future investigation would be to investigate the effect of using different geometric configurations of the reinforcements, such as multidirectional or bidirectional reinforcement.

10) According to the ANOVA analysis carried out, the hypothesis that the mean values are equal is accepted, thus confirming that there is no difference between the traumas caused to the clay witness after the ballistic test. The mechanisms identified in the microscopic analysis were the presence of delamination between the fiber/matrix interface, pullout, river marks and the presence of particles adhered to the SF. In fact, the confirmation of the particles in the alumina front layer was corroborated by EDS, confirming the chemical elements associated with the chemical composition (Al_2O_3) of the ceramic material. Based on the comparison, it was observed that other fabrics, mats or natural fibers reinforcing polymer matrices showed acceptable average trauma values on clay witness. Furthermore, they showed average trauma values of less than 30 mm in indentation depth. Although SF/EP composites acted synergistically by capturing the ceramic debris in the current unidirectional reinforcement configuration, they did not perform as well as fique and sisal fibers, for example. Therefore, an investigation of different SF reinforcement configurations becomes pertinent to investigate whether there is a more effective performance of the new composite material.

11) Epoxy matrix composites reinforced with 20 SF/EP the highest value for energy absorption for the tested samples. Although, the mechanism responsible for this was in the composite to fragment that is mostly attributed to the fragility of the epoxy matrix, which resulted in a complete rupture of the composite plates. Therefore, the condition of no integrity after the ballistic impact is evaluated as inappropriate for applicability in ballistic armor, referring to more than one shot to have standard conditioning.The composite plates reinforced with 30 SF/EP have disclosed a suitable ballistic performance, by mixing the energy absorption and a considerably adequate physical integrity. However,

the absorbed energy disclosed by them is not similar to Twaron and Kevlar^{TM} applying the same test parameters. Results of limit velocities showed similarity to ballistic parameters when compared to composite materials, both reinforced with natural or synthetic fibers. SEM micrographs investigation have shown that the epoxy matrix has a brittle fracture mechanism as well as sedge fiber ruptures, pullout and delamination are present on the fractured surface. The present epoxy composites reinforced with sedge fibers were evaluated with great applicability for individual ballistic protection of a multilayer armor, considering the specific use as an intermediate layer. Reduced manufacturing costs, and lightweight are one of the reasons for this novel material selection.

12) According to the results of 30 SFGO/EP, the projectile stopped by the nanocomposite has a mean speed of 172 m/s, based on the calculated speed limit. As this type of ammunition has a ballistic impact velocity of over 800 m/s, it is not effective in providing sufficient protection if used as a standalone target. In addition, it has a lower energy absorption value when compared to other SF/EP conditions, which may be an indicative that the reinforcement was done effectively. This is possibly associated with the GO improving interfacial resistance and promoting greater physical integrity with lower crack percentages. The standard deviation of the absorbed energy was lower than that other conditions, indicating greater homogeneity and similar energy absorption performance between the plates tested. This was corroborated by the physical integrity of all plates tested, which is a desirable behavior for ballistic armor applications. ANOVA analysis indicated a significant difference between the groups. Regarding the fracture mechanisms investigated by SEM, the following were found: rupture of the microfibril, initiation and propagation of river marks up to the fiber/matrix interface regions, an extraction mechanism known as pullout, partial pullout of the SFs and the absence of the delamination effect. The latter makes a detrimental contribution to the material's performance. This is therefore an indicative that the GO acted effectively, providing a strong interface for the nanocomposite. The 30 SFM/EP condition was also not effective in promoting efficient protection, the mean limit speed shown being 185 m/s. Although it showed a lower mean energy absorption value than 10 and 20 SF/EP conditions, the lower performance related to 30 SFM/EP condition is probably associated with the embrittlement of the SF by the alkali treatment. Moreover, as indicated by the standard deviation, there was greater heterogeneity in the results. This was corroborated by a greater number of samples that fragmented after the ballistic test was conducted, when compared to the 30 SFGO/EP and 30 SF/EP conditions, which is an undesirable behavior. Thus, the alkali treatment impaired the material's ballistic performance due to the embrittlement caused. In this case, it is possible that SFM would not be effective for MAS in the unidirectional reinforcement condition. The ANOVA analysis also indicated a significant difference between the groups.

6 FUTURE WORK

Based on the study carried out, suggestions for future work can be proposed, such as:

• Investigate other fractions of sedge fibers in the composite in conditions of 40, 50 and 60% by volume, in order to define the maximum percentage at which the composite shows an improvement in mechanical properties.

• Study the effect of the mGO treatment when used to coat the sedge fiber or functionalized the epoxy matrix.

• Study the effect of alkali treatment, followed by GO coating, when used to coat the sedge fiber or functionalized the epoxy matrix.

• Verify the performance of the GO-functionalized epoxy matrix composite reinforced with seven-island sedge fibers as an intermediate layer in a multilayer armor system (MAS).

• Verify the performance of the epoxy matrix composite reinforced with GO-coated sedge fibers (SFGO) as an intermediate layer in a multilayer armor system (MAS).

• Verify the performance of the epoxy matrix composite reinforced with alkali sedge fibers as an intermediate layer in a multilayer armor system (MAS).

• Evaluate the mechanical performance of composites made of another polymeric matrix, such as polyester, when reinforced with sedge fibers.

• Investigate the ballistic behavior and mechanical properties of a hybrid composite using another natural fiber as reinforcement combined with sedge fibers.

• Study the influence of reinforcement in the form of sedge fabric or mat on the mechanical properties of a composite.

REFERENCES

ABDAL-HAY, A.; SUARDANA, N. P. G.; JUNG, D. Y.; CHOI, K.-S.; LIM, J. K. Effect of diameters and alkali treatment on the tensile properties of date palm fiber reinforced epoxy composites. *International Journal of Precision Engineering and Manufacturing*, Springer, v. 13, p. 1199–1206, 2012.

ABERNETHY, R. B.; BRENEMAN, J.; MEDLIN, C.; REINMAN, G. L. *Weibull analysis handbook*. [S.l.], 1983.

ABNT, N. 15000. *Blindagens para impactos balísticos-classificação e critérios de avaliação*, 2005.

ACHABY, M. E.; ARRAKHIZ, F.-E.; VAUDREUIL, S.; QAISS, A. el K.; BOUSMINA, M.; FASSI-FEHRI, O. Mechanical, thermal, and rheological properties of graphene-based polypropylene nanocomposites prepared by melt mixing. *Polymer composites*, Wiley Online Library, v. 33, n. 5, p. 733–744, 2012.

ACOCELLA, M. R.; CORCIONE, C. E.; GIURI, A.; MAGGIO, M.; MAFFEZZOLI, A.; GUERRA, G. Graphene oxide as a catalyst for ring opening reactions in amine crosslinking of epoxy resins. *RSC advances*, Royal Society of Chemistry, v. 6, n. 28, p. 23858–23865, 2016.

AFROJ, S.; TAN, S.; ABDELKADER, A. M.; NOVOSELOV, K. S.; KARIM, N. Highly conductive, scalable, and machine washable graphene-based e-textiles for multifunctional wearable electronic applications. *Advanced Functional Materials*, Wiley Online Library, v. 30, n. 23, p. 2000293, 2020.

AHMED, S.; ULVEN, C. A. Dynamic in-situ observation on the failure mechanism of flax fiber through scanning electron microscopy. *Fibers*, Multidisciplinary Digital Publishing Institute, v. 6, n. 1, p. 17, 2018.

AL-MAHARMA, A. Y.; AL-HUNITI, N. Critical review of the parameters affecting the effectiveness of moisture absorption treatments used for natural composites. *Journal of Composites Science*, Multidisciplinary Digital Publishing Institute, v. 3, n. 1, p. 27, 2019.

AL-OQLA, F. M.; SAPUAN, S.; ISHAK, M.; NURAINI, A. A decision-making model for selecting the most appropriate natural fiber–polypropylene-based composites for automotive applications. *Journal of Composite Materials*, SAGE Publications Sage UK: London, England, v. 50, n. 4, p. 543–556, 2016.

ALHIJAZI, M.; SAFAEI, B.; ZEESHAN, Q.; ASMAEL, M.; EYVAZIAN, A.; QIN, Z. Recent developments in luffa natural fiber composites. *Sustainability*, Multidisciplinary Digital Publishing Institute, v. 12, n. 18, p. 7683, 2020.

AMIANDAMHEN, S.; MEINCKEN, M.; TYHODA, L. Natural fibre modification and its influence on fibre-matrix interfacial properties in biocomposite materials. *Fibers and polymers*, The Korean Fiber Society, v. 21, n. 4, p. 677–689, 2020.

ARRAKHIZ, F.; ACHABY, M. E.; MALHA, M.; BENSALAH, M.; FASSI-FEHRI, O.; BOUHFID, R.; BENMOUSSA, K.; QAISS, A. Mechanical and thermal properties of natural fibers reinforced polymer composites: Doum/low density polyethylene. *Materials & Design*, Elsevier, v. 43, p. 200–205, 2013.

ARTHANARIESWARAN, V.; KUMARAVEL, A.; SARAVANAKUMAR, S. Physico-chemical properties of alkali-treated acacia leucophloea fibers. *International Journal of Polymer Analysis and Characterization*, Taylor & Francis, v. 20, n. 8, p. 704–713, 2015.

ASIM, M.; SABA, N.; JAWAID, M.; NASIR, M. Potential of natural fiber/biomass filler-reinforced polymer composites in aerospace applications. In: *Sustainable composites for aerospace applications*. [S.l.]: Elsevier, 2018. p. 253–268.

ASKELAND, D. R.; PHULÉ, P. P. *Ciência e engenharia dos materiais*. [S.l.]: Cengage Learning, 2008.

ASSIS, F. S. de; PEREIRA, A. C.; FILHO, F. da C. G.; JR, E. P. L.; MONTEIRO, S. N.; WEBER, R. P. Performance of jute non-woven mat reinforced polyester matrix composite in multilayered armor. *Journal of materials research and technology*, Elsevier, v. 7, n. 4, p. 535–540, 2018.

ASTM-D256. *Standard Test Methods for Determining the Izod Pendulum Impact Resistance of Plastics*. 2006.

ASTM-D3039. *Standard Test Method for Tensile Properties of Polymers Matrix Composite Materials*. 1995.

ASTM-D6110. *Standard Test Methods for Determining the Charpy Impact Resistance of Notched Specimens of Plastics*. 1997.

ASTM-D790. *Standard Test Method for Flexural Properties of Unreinforced and Reinforced Plastics and Electrical Insulating*. 2007.

ASYRAF, M.; ISHAK, M.; NORRRAHIM, M.; NURAZZI, N.; SHAZLEEN, S.; ILYAS, R.; RAFIDAH, M.; RAZMAN, M. Recent advances of thermal properties of sugar palm lignocellulosic fibre reinforced polymer composites. *International journal of biological macromolecules*, Elsevier, v. 193, p. 1587–1599, 2021.

BABU, G. D.; GUDAPATI, S. K.; PRASAD, A. R.; BABU, K. S. Experimental investigation on mechanical and thermal properties of esculentus cyperus fiber reinforced polypropylene composites. *Materials Today: Proceedings*, Elsevier, v. 23, p. 557–560, 2020.

BALLA, V. K.; KATE, K. H.; SATYAVOLU, J.; SINGH, P.; TADIMETI, J. G. D. Additive manufacturing of natural fiber reinforced polymer composites: Processing and prospects. *Composites Part B: Engineering*, Elsevier, v. 174, p. 106956, 2019.

BENAZIR, J. A. F.; MANIMEKALAI, V.; RAVICHANDRAN, P.; SUGANTHI, R.; DINESH, D. C. Properties of fibres/culm strands from mat sedge–cyperus pangorei rottb. *BioResources*, v. 5, n. 2, p. 951–967, 2010.

BENITEZ, T.; GÓMEZ, Y. S., de oliveira, a., travitzky, n., & hotza, d.(2017). transparent ceramic and glass-ceramic materials for armor applications. *Ceramics International*, v. 43, n. 16, p. 13031–13046.

BENZAIT, Z.; TRABZON, L. A review of recent research on materials used in polymer–matrix composites for body armor application. *Journal of Composite Materials*, SAGE Publications Sage UK: London, England, v. 52, n. 23, p. 3241–3263, 2018.

BERAM, A.; YASAR, S. Performance of brutian pine (pinus brutia ten.) fibers modified with low concentration naoh solutions in fiberboard production. *Fresenius Environmental Bulletin*, v. 29, n. 1, p. 70–78, 2020.

BEZERRA, W. B. A. *Caracterização dos Materiais Precursores e Comportamento Balístico Preliminar de Compósitos de Resina Epóxi Reforçada com Escamas de Pirarucu.* 92 p. Mestrado em Ciência dos Materiais — Instituto Militar de Engenharia, Rio de Janeiro, 2020. Disponível em: <http://www.comp.ime.eb.br/images/repositorio-dissertacoes/2020-Wendell_Bezerra.pdf>.

BHAT, A.; NAVEEN, J.; JAWAID, M.; NORRRAHIM, M.; RASHEDI, A.; KHAN, A. Advancement in fiber reinforced polymer, metal alloys and multi-layered armour systems for ballistic applications–a review. *Journal of Materials Research and Technology*, Elsevier, v. 15, p. 1300–1317, 2021.

BHAWAL, P.; GANGULY, S.; DAS, T. K.; MONDAL, S.; CHOUDHURY, S.; DAS, N. Superior electromagnetic interference shielding effectiveness and electro-mechanical properties of ema-irgo nanocomposites through the in-situ reduction of go from melt blended ema-go composites. *Composites Part B: Engineering*, Elsevier, v. 134, p. 46–60, 2018.

BLEDZKI, A.; GASSAN, J. Composites reinforced with cellulose based fibres. *Progress in polymer science*, Elsevier, v. 24, n. 2, p. 221–274, 1999.

BLEDZKI, A.; REIHMANE, S.; GASSAN, J. The effect of alkaline treatment on mechanical properties of kenaf fibers and their epoxy composites. *J. Appl. Polym. Sci*, v. 59, p. 1329–1336, 1996.

BORA, C.; BHARALI, P.; BAGLARI, S.; DOLUI, S. K.; KONWAR, B. K. Strong and conductive reduced graphene oxide/polyester resin composite films with improved mechanical strength, thermal stability and its antibacterial activity. *Composites Science and Technology*, Elsevier, v. 87, p. 1–7, 2013.

BOURMAUD, A.; BEAUGRAND, J.; SHAH, D. U.; PLACET, V.; BALEY, C. Towards the design of high-performance plant fibre composites. *Progress in Materials Science*, Elsevier, v. 97, p. 347–408, 2018.

BOUTIN, M.; ROGEON, A.; AUFRAY, M.; PIQUET, R.; ROUILLY, A. Influence of flax fibers on network formation of dgeba/deta matrix. *Composite Interfaces*, Taylor & Francis, p. 1–18, 2020.

BRAGA, F. de O.; BOLZAN, L. T.; JR, É. P. L.; MONTEIRO, S. N. Performance of natural curaua fiber-reinforced polyester composites under 7.62 mm bullet impact as a stand-alone ballistic armor. *Journal of Materials Research and Technology*, Elsevier, v. 6, n. 4, p. 323–328, 2017.

BRAGA, F. de O.; BOLZAN, L. T.; LUZ, F. S. da; LOPES, P. H. L. M.; JR, É. P. L.; MONTEIRO, S. N. High energy ballistic and fracture comparison between multilayered

armor systems using non-woven curaua fabric composites and aramid laminates. *Journal of Materials Research and Technology*, Elsevier, v. 6, n. 4, p. 417–422, 2017.

BRAGA, F. O.

Comportamento Balístico de uma Blindagem Multicamada Utilizando Compósito Poliéster-Curauá como Camada Intermediária — Dissertação de Mestrado do Curso de Pós-Graduação em Ciência dos Materiais ..., 2015.

BRYDSON, J. A. *Handbook of plastics Materials*. London: Van Nostrand Co, 1966.

CAI, C.; SANG, N.; SHEN, Z.; ZHAO, X. Facile and size-controllable preparation of graphene oxide nanosheets using high shear method and ultrasonic method. *Journal of Experimental Nanoscience*, Taylor & Francis, v. 12, n. 1, p. 247–262, 2017.

CAMINERO, M.; CHACÓN, J.; GARCÍA-MORENO, I.; RODRÍGUEZ, G. Impact damage resistance of 3d printed continuous fibre reinforced thermoplastic composites using fused deposition modelling. *Composites Part B: Engineering*, Elsevier, v. 148, p. 93–103, 2018.

CANDIDO, V. S.; SILVA, A. C. R. da; SIMONASSI, N. T.; LUZ, F. S. da; MONTEIRO, S. N. Toughness of polyester matrix composites reinforced with sugarcane bagasse fibers evaluated by charpy impact tests. *Journal of Materials Research and Technology*, Elsevier, v. 6, n. 4, p. 334–338, 2017.

CECEN, V.; SEKI, Y.; SARIKANAT, M.; TAVMAN, I. H. Ftir and sem analysis of polyester-and epoxy-based composites manufactured by vartm process. *Journal of Applied Polymer Science*, Wiley Online Library, v. 108, n. 4, p. 2163–2170, 2008.

CHAIYAKUN, S.; WITIT-ANUN, N.; NUNTAWONG, N.; CHINDAUDOM, P.; OAEW, S.; KEDKEAW, C.; LIMSUWAN, P. et al. Preparation and characterization of graphene oxide nanosheets. *Procedia Engineering*, Elsevier, v. 32, p. 759–764, 2012.

CHAWLA, K. K. *Composite materials: science and engineering*. [S.l.]: Springer Science & Business Media, 2012.

CHEE, S. S.; JAWAID, M.; ALOTHMAN, O. Y.; FOUAD, H. Effects of nanoclay on mechanical and dynamic mechanical properties of bamboo/kenaf reinforced epoxy hybrid composites. *Polymers*, MDPI, v. 13, n. 3, p. 395, 2021.

CHEE, S. S.; JAWAID, M.; SULTAN, M.; ALOTHMAN, O. Y.; ABDULLAH, L. C. Thermomechanical and dynamic mechanical properties of bamboo/woven kenaf mat reinforced epoxy hybrid composites. *Composites Part B: Engineering*, Elsevier, v. 163, p. 165–174, 2019.

CHEN, C.; CHEN, Y.; LI, K.; YANG, S.; WANG, J.; WANG, S.; MAO, Y.; LUO, L.; WU, Y. The ductile-brittle transition behaviors of w/ta multilayer composites. *Journal of Alloys and Compounds*, Elsevier, v. 946, p. 169377, 2023.

CHEN, H.; MIAO, M.; DING, X. Influence of moisture absorption on the interfacial strength of bamboo/vinyl ester composites. *Composites Part A: Applied Science and Manufacturing*, Elsevier, v. 40, n. 12, p. 2013–2019, 2009.

CHEN, H.; WU, J.; SHI, J.; ZHANG, W.; WANG, H. Effect of alkali treatment on microstructure and thermal stability of parenchyma cell compared with bamboo fiber. *Industrial Crops and Products*, Elsevier, v. 164, p. 113380, 2021.

CHEN, J.; HUANG, Z.; LV, W.; WANG, C. Graphene oxide decorated sisal fiber/mapp modified pp composites: Toward high-performance biocomposites. *Polymer Composites*, Wiley Online Library, v. 39, p. E113–E121, 2018.

CHEN, Q.; GUO, Z.; CHENG, F.; CHAI, G. B.; LI, Y.; LUAN, Y.; LIANG, J. Effect of go agglomeration on the mechanical properties of graphene oxide and nylon 66 composites and micromechanical analysis. *Polymer Composites*, Wiley Online Library, v. 43, n. 11, p. 8356–8367, 2022.

CLYNE, T.; HULL, D. *An introduction to composite materials*. [S.l.]: Cambridge university press, 2019.

COMPTON, O. C.; CRANFORD, S. W.; PUTZ, K. W.; AN, Z.; BRINSON, L. C.; BUEHLER, M. J.; NGUYEN, S. T. Tuning the mechanical properties of graphene oxide paper and its associated polymer nanocomposites by controlling cooperative intersheet hydrogen bonding. *ACS nano*, ACS Publications, v. 6, n. 3, p. 2008–2019, 2012.

CORRO, E. D.; TARAVILLO, M.; BAONZA, V. G. Nonlinear strain effects in double-resonance raman bands of graphite, graphene, and related materials. *Physical Review B*, APS, v. 85, n. 3, p. 033407, 2012.

COSTA, U. O.; NASCIMENTO, L. F. C.; BEZERRA, W. B. A.; AGUIAR, V. de O.; PEREIRA, A. C.; MONTEIRO, S. N.; PINHEIRO, W. A. Dynamic mechanical behavior of graphene oxide functionalized curaua fiber-reinforced epoxy composites: A brief report. *Polymers*, Multidisciplinary Digital Publishing Institute, v. 13, n. 11, p. 1897, 2021.

COSTA, U. O.; NASCIMENTO, L. F. C.; GARCIA, J. M.; MONTEIRO, S. N.; LUZ, F. S. d.; PINHEIRO, W. A.; FILHO, F. d. C. G. Effect of graphene oxide coating on natural fiber composite for multilayered ballistic armor. *Polymers*, Multidisciplinary Digital Publishing Institute, v. 11, n. 8, p. 1356, 2019.

COSTA, U. O.; NASCIMENTO, L. F. C.; GARCIA, J. M.; BEZERRA, W. B. A.; MONTEIRO, S. N. Evaluation of izod impact and bend properties of epoxy composites reinforced with mallow fibers. *Journal of Materials Research and Technology*, Elsevier, v. 9, n. 1, p. 373–382, 2020.

DEVI, L. U.; BHAGAWAN, S.; THOMAS, S. Dynamic mechanical analysis of pineapple leaf/glass hybrid fiber reinforced polyester composites. *Polymer composites*, Wiley Online Library, v. 31, n. 6, p. 956–965, 2010.

DIKIN, D. A.; STANKOVICH, S.; ZIMNEY, E. J.; PINER, R. D.; DOMMETT, G. H.; EVMENENKO, G.; NGUYEN, S. T.; RUOFF, R. S. Preparation and characterization of graphene oxide paper. *Nature*, Nature Publishing Group, v. 448, n. 7152, p. 457–460, 2007.

DIMIEV, A. M.; TOUR, J. M. Mechanism of graphene oxide formation. *ACS nano*, ACS Publications, v. 8, n. 3, p. 3060–3068, 2014.

DIVAKARAN, N.; ZHANG, X.; KALE, M. B.; SENTHIL, T.; MUBARAK, S.; DHAMODHARAN, D.; WU, L.; WANG, J. Fabrication of surface modified graphene oxide/unsaturated polyester nanocomposites via in-situ polymerization: Comprehensive property enhancement. *Applied Surface Science*, Elsevier, v. 502, p. 144164, 2020.

DONA, D. G. G.; WANG, M.; LIU, M.; MOTTA, N.; WACLAWIK, E.; YAN, C. Recent advances in fabrication and characterization of graphene-polymer nanocomposites. *Graphene*, Scientific Research Publishing, Inc., v. 1, n. 2, p. 30–49, 2012.

DRESCH, A. B.; VENTURINI, J.; ARCARO, S.; MONTEDO, O. R.; BERGMANN, C. P. Ballistic ceramics and analysis of their mechanical properties for armour applications: A review. *Ceramics International*, Elsevier, v. 47, n. 7, p. 8743–8761, 2021.

D'APUZZO, F.; NUCCI, L.; DELFINO, I.; PORTACCIO, M.; MINERVINI, G.; ISOLA, G.; SERINO, I.; CAMERLINGO, C.; LEPORE, M. Application of vibrational spectroscopies in the qualitative analysis of gingival crevicular fluid and periodontal ligament during orthodontic tooth movement. *Journal of Clinical Medicine*, MDPI, v. 10, n. 7, p. 1405, 2021.

EBNESAJJAD, S.; KHALADKAR, P. 10-failure analysis of fluoropolymer parts. *Fluoropolymer Applications in the Chemical Processing Industries*, Plastics Design Library, p. 357–400, 2018.

ELANCHEZHIAN, C.; RAMNATH, B. V.; RAMAKRISHNAN, G.; RAJENDRAKUMAR, M.; NAVEENKUMAR, V.; SARAVANAKUMAR, M. Review on mechanical properties of natural fiber composites. *Materials Today: Proceedings*, Elsevier, v. 5, n. 1, p. 1785–1790, 2018.

ELMARAKBI, A.; AZOTI, W. State of the art on graphene lightweighting nanocomposites for automotive applications. In: *Experimental Characterization, Predictive Mechanical and Thermal Modeling of Nanostructures and their Polymer Composites*. [S.l.]: Elsevier, 2018. p. 1–23.

FABBRI, P.; BASSOLI, E.; BON, S. B.; VALENTINI, L. Preparation and characterization of poly (butylene terephthalate)/graphene composites by in-situ polymerization of cyclic butylene terephthalate. *Polymer*, Elsevier, v. 53, n. 4, p. 897–902, 2012.

FARUK, O.; BLEDZKI, A. K.; FINK, H.-P.; SAIN, M. Biocomposites reinforced with natural fibers: 2000–2010. *Progress in polymer science*, Elsevier, v. 37, n. 11, p. 1552–1596, 2012.

FARUK, O.; BLEDZKI, A. K.; FINK, H.-P.; SAIN, M. Progress report on natural fiber reinforced composites. *Macromolecular Materials and Engineering*, Wiley Online Library, v. 299, n. 1, p. 9–26, 2014.

FERREIRA, M. V. F.; NEVES, A. C. C.; OLIVEIRA, C. G. de; LOPES, F. P. D.; MARGEM, F. M.; VIEIRA, C. M. F.; MONTEIRO, S. N. Thermogravimetric characterization of polyester matrix composites reinforced with eucalyptus fibers. *Journal of Materials Research and Technology*, Elsevier, v. 6, n. 4, p. 396–400, 2017.

FILHO, F. C. G.; LUZ, F. S.; OLIVEIRA, M. S.; BEZERRA, W.; BARBOSA, J. D.; MONTEIRO, S. N. Influence of rigid brazilian natural fiber arrangements in polymer composites: Energy absorption and ballistic efficiency. *Journal of Composites Science*, Multidisciplinary Digital Publishing Institute, v. 5, n. 8, p. 201, 2021.

FILHO, F. D. C. G.; OLIVEIRA, M. S.; PEREIRA, A. C.; NASCIMENTO, L. F. C.; MATHEUS, J. R. G.; MONTEIRO, S. N. Ballistic behavior of epoxy matrix composites

reinforced with piassava fiber against high energy ammunition. *Journal of Materials Research and Technology*, Elsevier, v. 9, n. 2, p. 1734–1741, 2020.

FILHO, F. da C. G.; LUZ, F. S. da; OLIVEIRA, M. S.; PEREIRA, A. C.; COSTA, U. O.; MONTEIRO, S. N. Thermal behavior of graphene oxide-coated piassava fiber and their epoxy composites. *Journal of Materials Research and Technology*, Elsevier, v. 9, n. 3, p. 5343–5351, 2020.

FU, S.; SONG, P.; LIU, X. Thermal and flame retardancy properties of thermoplastics/natural fiber biocomposites. In: *Advanced High Strength Natural Fibre Composites in Construction*. [S.l.]: Elsevier, 2017. p. 479–508.

GAFSI, N.; VERDEJO, R.; KHARRAT, M.; BARLETTA, M.; LÓPEZ-MANCHADO, M. Á.; DAMMAK, M. Effect of filler content on scratch behavior and tribological performance of polyester/graphene oxide nanocomposite coating. *Journal of Coatings Technology and Research*, Springer, v. 18, n. 5, p. 1269–1280, 2021.

GANAPATHY, T.; SATHISKUMAR, R.; SENTHAMARAIKANNAN, P.; SARAVANAKUMAR, S.; KHAN, A. Characterization of raw and alkali treated new natural cellulosic fibres extracted from the aerial roots of banyan tree. *International journal of biological macromolecules*, Elsevier, v. 138, p. 573–581, 2019.

GBIF. *Pesquisas de ocorrência - 2020*. 2020. 7 mai. de 2021. Disponível em: <https://www.gbif.org/pt/occurrence/map?taxon_key=2738262>.

GHASEMNEJAD, H.; SOROUSH, V.; MASON, P.; WEAGER, B. To improve impact damage response of single and multi-delaminated frp composites using natural flax yarn. *Materials & Design (1980-2015)*, Elsevier, v. 36, p. 865–873, 2012.

GHOLAMPOUR, A.; OZBAKKALOGLU, T. A review of natural fiber composites: Properties, modification and processing techniques, characterization, applications. *Journal of Materials Science*, Springer, p. 1–64, 2020.

GOLISZEK, M.; PODKOŚCIELNA, B.; KLEPKA, T.; SEVASTYANOVA, O. Preparation, thermal, and mechanical characterization of uv-cured polymer biocomposites with lignin. *Polymers*, MDPI, v. 12, n. 5, p. 1159, 2020.

GOMES, A.; LOURO, L.; COSTA, C. Ballistic behavior of alumina with niobia additions. In: EDP SCIENCES. *Journal de Physique IV (Proceedings)*. [S.l.], 2006. v. 134, p. 1009–1014.

GÜVEN, O.; MONTEIRO, S. N.; MOURA, E. A.; DRELICH, J. W. Re-emerging field of lignocellulosic fiber–polymer composites and ionizing radiation technology in their formulation. *Polymer Reviews*, Taylor & Francis, v. 56, n. 4, p. 702–736, 2016.

HAN, S.; ZHANG, T.; GUO, Y.; LI, C.; WU, H.; GUO, S. Brittle-ductile transition behavior of the polypropylene/ultra-high molecular weight polyethylene/olefin block copolymers ternary blends: Dispersion and interface design. *Polymer*, Elsevier, v. 182, p. 121819, 2019.

HARIS, N. I. N.; HASSAN, M. Z.; ILYAS, R.; SUHOT, M. A.; SAPUAN, S.; DOLAH, R.; MOHAMMAD, R.; ASYRAF, M. Dynamic mechanical properties of natural fiber reinforced hybrid polymer composites: A review. *Journal of Materials Research and Technology*, Elsevier, 2022.

HASSANI, F. O.; MERBAHI, N.; OUSHABI, A.; ELFADILI, M.; KAMMOUNI, A.; OUELDNA, N. Effects of corona discharge treatment on surface and mechanical properties of aloe vera fibers. *Materials Today: Proceedings*, Elsevier, v. 24, p. 46–51, 2020.

HAZARIKA, A.; MANDAL, M.; MAJI, T. K. Dynamic mechanical analysis, biodegradability and thermal stability of wood polymer nanocomposites. *Composites Part B: Engineering*, Elsevier, v. 60, p. 568–576, 2014.

HAZARIKA, D.; GUPTA, K.; MANDAL, M.; KARAK, N. High-performing biodegradable waterborne polyester/functionalized graphene oxide nanocomposites as an eco-friendly material. *ACS omega*, ACS Publications, v. 3, n. 2, p. 2292–2303, 2018.

HE, S.; LIU, K.; MACOSKO, C. W.; STEIN, A. Effect of primary particle size and aggregate size of modified graphene oxide on toughening of unsaturated polyester resin. *Polymer Composites*, Wiley Online Library, v. 40, n. 10, p. 3886–3894, 2019.

HE, S.; PETKOVICH, N. D.; LIU, K.; QIAN, Y.; MACOSKO, C. W.; STEIN, A. Unsaturated polyester resin toughening with very low loadings of go derivatives. *Polymer*, Elsevier, v. 110, p. 149–157, 2017.

HE, S.; QIAN, Y.; LIU, K.; MACOSKO, C. W.; STEIN, A. Modified-graphene-oxide-containing styrene masterbatches for thermosets. *Industrial & Engineering Chemistry Research*, ACS Publications, v. 56, n. 40, p. 11443–11450, 2017.

HEIDARY, H.; KARIMI, N. Z.; MINAK, G. Investigation on delamination and flexural properties in drilling of carbon nanotube/polymer composites. *Composite Structures*, Elsevier, v. 201, p. 112–120, 2018.

HEMNATH, A.; ANBUCHEZHIYAN, G.; NANTHAKUMAR, P.; SENTHILKUMAR, N. Tensile and flexural behaviour of rice husk and sugarcane bagasse reinforced polyester composites. *Materials Today: Proceedings*, Elsevier, v. 46, p. 3451–3454, 2021.

HIROCE, R.; JÚNIOR, R. B.; FEITOSA, C. T. Estudos nutricionais em junco: adubação e calagem. *Bragantia*, SciELO Brasil, v. 47, n. 2, p. 313–323, 1988.

HOLBERY, J.; HOUSTON, D. Natural-fiber-reinforced polymer composites in automotive applications. *Jom*, Springer, v. 58, n. 11, p. 80–86, 2006.

HOU, J.-r.; HUANG, S.-s.; ZHANG, N.; LIU, D.-y.; ZHANG, Z.-j.; YANG, H.-s.; ZONG, L.; DUAN, Y.-x.; ZHANG, J.-m. Reinforcing natural rubber by amphiphilic graphene oxide for high-performance catheters. *Polymer*, Elsevier, v. 232, p. 124142, 2021.

HU, K.; KULKARNI, D. D.; CHOI, I.; TSUKRUK, V. V. Graphene-polymer nanocomposites for structural and functional applications. *Progress in polymer science*, Elsevier, v. 39, n. 11, p. 1934–1972, 2014.

HUANG, X.; LIU, F.; JIANG, P.; TANAKA, T. Is graphene oxide an insulating material? In: IEEE. *2013 IEEE International Conference on Solid Dielectrics (ICSD)*. [S.l.], 2013. p. 904–907.

ISMAIL, N. F.; RADZUAN, N. A. M.; SULONG, A. B.; MUHAMAD, N.; HARON, C. H. C. The effect of alkali treatment on physical, mechanical and thermal properties of kenaf fiber and polymer epoxy composites. *Polymers*, MDPI, v. 13, n. 12, p. 2005, 2021.

ISO-604. *Plastics - Determination of Compressive Properties*. 2002.

ISTRATE, O. M.; PATON, K. R.; KHAN, U.; O'NEILL, A.; BELL, A. P.; COLEMAN, J. N. Reinforcement in melt-processed polymer–graphene composites at extremely low graphene loading level. *Carbon*, Elsevier, v. 78, p. 243–249, 2014.

JAAFAR, J.; SIREGAR, J. P.; SALLEH, S. M.; HAMDAN, M. H. M.; CIONITA, T.; RIHAYAT, T. Important considerations in manufacturing of natural fiber composites: a review. *International Journal of Precision Engineering and Manufacturing-Green Technology*, Springer, v. 6, n. 3, p. 647–664, 2019.

JACOB, M.; THOMAS, S.; VARUGHESE, K. T. Mechanical properties of sisal/oil palm hybrid fiber reinforced natural rubber composites. *Composites science and Technology*, Elsevier, v. 64, n. 7-8, p. 955–965, 2004.

JENA, P. K.; MOHANTY, J. R.; NAYAK, S. Effect of surface modification of vetiver fibers on their physical and thermal properties. *Journal of Natural Fibers*, Taylor & Francis, p. 1–12, 2020.

JEONG, H.; JIN, M.; SO, K.; LIM, S.; LEE, Y. Tailoring the characteristics of graphite oxides by different oxidation times. *Journal of Physics D: Applied Physics*, IOP Publishing, v. 42, n. 6, p. 065418, 2009.

JESUAROCKIAM, N.; JAWAID, M.; ZAINUDIN, E.; SULTAN, M.; YAHAYA, R. *Enhanced thermal and dynamic mechanical properties of synthetic/natural hybrid composites with graphene nanoplatelets*. [S.l.]: Polymers, 2019.

JHA, K.; KATARIA, R.; VERMA, J.; PRADHAN, S. Potential biodegradable matrices and fiber treatment for green composites: A review. *AIMS Mater. Sci*, v. 6, p. 119–138, 2019.

JI, X.; XU, Y.; ZHANG, W.; CUI, L.; LIU, J. Review of functionalization, structure and properties of graphene/polymer composite fibers. *Composites Part A: Applied Science and Manufacturing*, Elsevier, v. 87, p. 29–45, 2016.

JOHN, M. J.; THOMAS, S. Biofibres and biocomposites. *Carbohydrate polymers*, Elsevier, v. 71, n. 3, p. 343–364, 2008.

JR, W. D. C.; RETHWISCH, D. G. *Callister's Materials Science and Engineering*. [S.l.]: John Wiley & Sons, 2016.

JR, W. D. C.; RETHWISCH, D. G. *Callister's materials science and engineering*. [S.l.]: John Wiley & Sons, 2020.

JR, W. S. H.; OFFEMAN, R. E. Preparation of graphitic oxide. *Journal of the american chemical society*, ACS Publications, v. 80, n. 6, p. 1339–1339, 1958.

JUNIO, R. F. P.; NASCIMENTO, L. F. C.; NEUBA, L. d. M.; SOUZA, A. T.; MOURA, J. V. B.; FILHO, F. d. C. G.; MONTEIRO, S. N. Copernicia prunifera leaf fiber: A promising new reinforcement for epoxy composites. *Polymers*, Multidisciplinary Digital Publishing Institute, v. 12, n. 9, p. 2090, 2020.

JUSTICE, . N. I. o. J. National Criminal Justice Reference Service; US Department of. *NIJ 0101.04. Ballistic Resistance of Body Armor*. 2000. 14 fev. de 2022. Disponível em: <https://nij.ojp.gov/library/publications/ballistic-resistance-personal-body-armor-nij-standard-010104>.

JUSTICE, . N. I. o. J. National Criminal Justice Reference Service; US Department of. *Ballistic Resistance of Body Armor NIJ Standard-0101.06*. 2008. 18 fev. de 2022. Disponível em: <https://nij.ojp.gov/library/publications/ballistic-resistance-body-armor-nij-standard-010106>.

KALIA, S.; KAITH, B.; KAUR, I. Pretreatments of natural fibers and their application as reinforcing material in polymer composites—a review. *Polymer Engineering & Science*, Wiley Online Library, v. 49, n. 7, p. 1253–1272, 2009.

KANNAN, G.; THANGARAJU, R. Recent progress on natural lignocellulosic fiber reinforced polymer composites: A review. *Journal of Natural Fibers*, Taylor & Francis, p. 1–32, 2021.

KANNAN, G.; THANGARAJU, R. Recent progress on natural lignocellulosic fiber reinforced polymer composites: A review. *Journal of Natural Fibers*, Taylor & Francis, v. 19, n. 13, p. 7100–7131, 2022.

KARTHIKEYAN, A.; BALAMURUGAN, K.; KALPANA, A. The new approach to improve the impact property of coconut fiber reinforced epoxy composites using sodium laulryl sulfate treatment. NISCAIR-CSIR, India, 2013.

KATHIRSELVAM, M.; KUMARAVEL, A.; ARTHANARIESWARAN, V.; SARAVANAKUMAR, S. Characterization of cellulose fibers in thespesia populnea barks: Influence of alkali treatment. *Carbohydrate polymers*, Elsevier, v. 217, p. 178–189, 2019.

KAUSHIK, V. K.; KUMAR, A.; KALIA, S. Effect of mercerization and benzoyl peroxide treatment on morphology, thermal stability and crystallinity of sisal fibers. *International Journal of Textile Science*, v. 1, n. 6, p. 101–105, 2012.

KERN, W. T.; KIM, W.; ARGENTO, A.; LEE, E. C.; MIELEWSKI, D. F. Finite element analysis and microscopy of natural fiber composites containing microcellular voids. *Materials & Design*, Elsevier, v. 106, p. 285–294, 2016.

KHALID, M. Y.; ARIF, Z. U.; RASHID, A. A. Investigation of tensile and flexural behavior of green composites along with their impact response at different energies. *International Journal of Precision Engineering and Manufacturing-Green Technology*, Springer, v. 9, n. 5, p. 1399–1410, 2022.

KHAN, M. Z.; SRIVASTAVA, S. K.; GUPTA, M. Tensile and flexural properties of natural fiber reinforced polymer composites: A review. *Journal of Reinforced Plastics and Composites*, SAGE Publications Sage UK: London, England, v. 37, n. 24, p. 1435–1455, 2018.

KIM, H.; ABDALA, A. A.; MACOSKO, C. W. Graphene/polymer nanocomposites. *Macromolecules*, ACS Publications, v. 43, n. 16, p. 6515–6530, 2010.

KONG, J.-Y.; CHOI, M.-C.; KIM, G. Y.; PARK, J. J.; SELVARAJ, M.; HAN, M.; HA, C.-S. Preparation and properties of polyimide/graphene oxide nanocomposite films with mg ion crosslinker. *European polymer journal*, Elsevier, v. 48, n. 8, p. 1394–1405, 2012.

KOOHESTANI, B.; DARBAN, A.; MOKHTARI, P.; YILMAZ, E.; DAREZERESHKI, E. Comparison of different natural fiber treatments: A literature review. *International Journal of Environmental Science and Technology*, Springer, v. 16, n. 1, p. 629–642, 2019.

KU, H.; WANG, H.; PATTARACHAIYAKOOP, N.; TRADA, M. A review on the tensile properties of natural fiber reinforced polymer composites. *Composites Part B: Engineering*, Elsevier, v. 42, n. 4, p. 856–873, 2011.

KUDIN, K. N.; OZBAS, B.; SCHNIEPP, H. C.; PRUD'HOMME, R. K.; AKSAY, I. A.; CAR, R. Raman spectra of graphite oxide and functionalized graphene sheets. *Nano letters*, ACS Publications, v. 8, n. 1, p. 36–41, 2008.

KUMAR, S.; MALEK, A.; BABU, R.; MATHUR, S. Ballistic efficiency of multilayered armor system reinforced with jute-kevlar epoxy composite against high-energy steel core projectile. *Journal of Materials Engineering and Performance*, Springer, v. 30, n. 11, p. 8447–8464, 2021.

KUMAR, S.; SAMAL, S. K.; MOHANTY, S.; NAYAK, S. K. Curing kinetics of bio-based epoxy resin-toughened dgeba epoxy resin blend. *Journal of Thermal Analysis and Calorimetry*, Springer, v. 137, n. 5, p. 1567–1578, 2019.

KUNUSA, W. R.; ISA, I.; LALIYO, L. A.; IYABU, H. Ftir, xrd and sem analysis of microcrystalline cellulose (mcc) fibers from corncorbs in alkaline treatment. In: IOP PUBLISHING. *Journal of Physics: Conference Series*. [S.l.], 2018. v. 1028, n. 1, p. 012199.

LAKHDAR, Y.; TUCK, C.; TERRY, A.; SPADACCINI, C.; GOODRIDGE, R. Direct ink writing of boron carbide monoliths. *Journal of the European Ceramic Society*, Elsevier, v. 41, n. 16, p. 76–92, 2021.

LATIF, R.; WAKEEL, S.; KHAN, N. Z.; SIDDIQUEE, A. N.; VERMA, S. L.; KHAN, Z. A. Surface treatments of plant fibers and their effects on mechanical properties of fiber-reinforced composites: A review. *Journal of Reinforced Plastics and Composites*, SAGE Publications Sage UK: London, England, v. 38, n. 1, p. 15–30, 2019.

LEE, W.; LEE, J. U.; JUNG, B. M.; BYUN, J.-H.; YI, J.-W.; LEE, S.-B.; KIM, B.-S. Simultaneous enhancement of mechanical, electrical and thermal properties of graphene oxide paper by embedding dopamine. *Carbon*, Elsevier, v. 65, p. 296–304, 2013.

LERF, A.; HE, H.; FORSTER, M.; KLINOWSKI, J. Structure of graphite oxide revisited. *The Journal of Physical Chemistry B*, ACS Publications, v. 102, n. 23, p. 4477–4482, 1998.

LI, C.; HUANG, C.; ZHAO, Y.; ZHENG, C.; SU, H.; ZHANG, L.; LUO, W.; ZHAO, H.; WANG, S.; HUANG, L.-J. Effect of choline-based deep eutectic solvent pretreatment on the structure of cellulose and lignin in bagasse. *Processes*, MDPI, v. 9, n. 2, p. 384, 2021.

LI, P.; WANG, B.; LIU, Y.-Y.; XU, Y.-J.; JIANG, Z.-M.; DONG, C.-H.; ZHANG, L.; LIU, Y.; ZHU, P. Fully bio-based coating from chitosan and phytate for fire-safety and antibacterial cotton fabrics. *Carbohydrate polymers*, Elsevier, v. 237, p. 116173, 2020.

LI, X.; LIU, Y. M.; LI, W. G.; LI, C. Y.; SANJAYAN, J. G.; DUAN, W. H.; LI, Z. Effects of graphene oxide agglomerates on workability, hydration, microstructure and compressive strength of cement paste. *Construction and Building Materials*, Elsevier, v. 145, p. 402–410, 2017.

LI, X.; SUN, Z.; TIAN, L.; HE, T.; LI, J.; WANG, J.; WANG, H.; CHEN, B. Effects of spatial expansion between phragmites australis and cyperus malaccensis on variations of arsenic and heavy metals in decomposing litters in a typical subtropical estuary (min river), china. *Chemosphere*, Elsevier, v. 240, p. 124965, 2020.

LI, X.; TABIL, L. G.; PANIGRAHI, S. Chemical treatments of natural fiber for use in natural fiber-reinforced composites: a review. *Journal of Polymers and the Environment*, Springer, v. 15, p. 25–33, 2007.

LI, Y.; FENG, Z.; HUANG, L.; ESSA, K.; BILOTTI, E.; ZHANG, H.; PEIJS, T.; HAO, L. Additive manufacturing high performance graphene-based composites: A review. *Composites Part A: Applied Science and Manufacturing*, Elsevier, v. 124, p. 105483, 2019.

LI, Z.; KINLOCH, I. A.; YOUNG, R. J. The role of interlayer adhesion in graphene oxide upon its reinforcement of nanocomposites. *Philosophical Transactions of the Royal Society A: Mathematical, Physical and Engineering Sciences*, The Royal Society Publishing, v. 374, n. 2071, p. 20150283, 2016.

LIAO, K.-H.; PARK, Y. T.; ABDALA, A.; MACOSKO, C. Aqueous reduced graphene/thermoplastic polyurethane nanocomposites. *Polymer*, Elsevier, v. 54, n. 17, p. 4555–4559, 2013.

LIU, K.; HE, S.; QIAN, Y.; AN, Q.; STEIN, A.; MACOSKO, C. W. Nanoparticles in glass fiber-reinforced polyester composites: comparing toughening effects of modified graphene oxide and core-shell rubber. *Polymer Composites*, Wiley Online Library, v. 40, n. S2, p. E1512–E1524, 2019.

LIU, L.; ZHANG, J.; ZHAO, J.; LIU, F. Mechanical properties of graphene oxides. *Nanoscale*, Royal Society of Chemistry, v. 4, n. 19, p. 5910–5916, 2012.

LIU, P.; STRANO, M. S. Toward ambient armor: can new materials change longstanding concepts of projectile protection? *Advanced Functional Materials*, Wiley Online Library, v. 26, n. 6, p. 943–954, 2016.

LIU, R.; GAO, S.; PENG, Q.; PU, W.; SHI, P.; HE, Y.; ZHANG, T.; DU, D.; SHENG, J. J. Experimental and molecular dynamic studies of amphiphilic graphene oxide for promising nanofluid flooding. *Fuel*, Elsevier, v. 330, p. 125567, 2022.

LOGANATHAN, T. M.; SULTAN, M. T. H.; AHSAN, Q.; JAWAID, M.; NAVEEN, J.; SHAH, A. U. M.; HUA, L. S. Characterization of alkali treated new cellulosic fibre from cyrtostachys renda. *Journal of Materials Research and technology*, Elsevier, v. 9, n. 3, p. 3537–3546, 2020.

LOH, K. P.; BAO, Q.; EDA, G.; CHHOWALLA, M. Graphene oxide as a chemically tunable platform for optical applications. *Nature chemistry*, Nature Publishing Group, v. 2, n. 12, p. 1015–1024, 2010.

LOTFI, A.; LI, H.; DAO, D. V.; PRUSTY, G. Natural fiber–reinforced composites: A review on material, manufacturing, and machinability. *Journal of Thermoplastic Composite Materials*, SAGE Publications Sage UK: London, England, p. 0892705719844546, 2019.

LUO, M.; ZENG, C.-S.; TONG, C.; HUANG, J.-F.; CHEN, K.; LIU, F.-Q. Iron reduction along an inundation gradient in a tidal sedge (cyperus malaccensis) marsh: the rates, pathways, and contributions to anaerobic organic matter mineralization. *Estuaries and Coasts*, Springer, v. 39, n. 6, p. 1679–1693, 2016.

LUZ, F. S. d.; FILHO, F. d. C. G.; COSTA, U. O.; OLIVEIRA, M. S.; MONTEIRO, S. N. Graphene oxide surface treatment on piassava fiber attalea funifera to improve adhesion in epoxy matrix. *Journal of Natural Fibers*, Taylor & Francis, p. 1–14, 2021.

LUZ, F. S. d.; FILHO, F. d. C. G.; COSTA, U. O.; OLIVEIRA, M. S.; MONTEIRO, S. N. Graphene oxide surface treatment on piassava fiber attalea funifera to improve adhesion in epoxy matrix. *Journal of Natural Fibers*, Taylor & Francis, v. 19, n. 14, p. 8568–8581, 2022.

LUZ, F. S. d.; FILHO, F. d. C. G.; OLIVEIRA, M. S.; NASCIMENTO, L. F. C.; MONTEIRO, S. N. Composites with natural fibers and conventional materials applied in a hard armor: A comparison. *Polymers*, Multidisciplinary Digital Publishing Institute, v. 12, n. 9, p. 1920, 2020.

LUZ, F. S. d.; JUNIOR, E. P. L.; LOURO, L. H. L.; MONTEIRO, S. N. Ballistic test of multilayered armor with intermediate epoxy composite reinforced with jute fabric. *Materials Research*, SciELO Brasil, v. 18, p. 170–177, 2015.

LUZ, F. S. d.; MONTEIRO, S. N.; LIMA, E. S.; LIMA, É. P. Ballistic application of coir fiber reinforced epoxy composite in multilayered armor. *Materials Research*, SciELO Brasil, v. 20, p. 23–28, 2017.

LUZ, F. S. da; FILHO, F. d. C. G.; DEL-RIO, M. T. G.; NASCIMENTO, L. F. C.; PINHEIRO, W. A.; MONTEIRO, S. N. Graphene-incorporated natural fiber polymer composites: A first overview. *Polymers*, Multidisciplinary Digital Publishing Institute, v. 12, n. 7, p. 1601, 2020.

MAHMOUD, W. E. Morphology and physical properties of poly (ethylene oxide) loaded graphene nanocomposites prepared by two different techniques. *European Polymer Journal*, Elsevier, v. 47, n. 8, p. 1534–1540, 2011.

MANALO, A. C.; WANI, E.; ZUKARNAIN, N. A.; KARUNASENA, W.; LAU, K.-t. Effects of alkali treatment and elevated temperature on the mechanical properties of bamboo fibre–polyester composites. *Composites Part B: Engineering*, Elsevier, v. 80, p. 73–83, 2015.

MANIMARAN, P.; SANJAY, M.; SENTHAMARAIKANNAN, P.; SARAVANAKUMAR, S.; SIENGCHIN, S.; PITCHAYYAPILLAI, G.; KHAN, A. Physico-chemical properties of fiber extracted from the flower of celosia argentea plant. *Journal of Natural Fibers*, Taylor & Francis, v. 18, n. 3, p. 464–473, 2021.

MANNA, S.; MUKHERJEE, S.; ROY, A. Contribution of three sedges of cyperus in the rural economy of sundarbans, india. *Global Journal of Science Frontier Research: C Biological Science*, v. 16, n. 1, p. 32–41, 2016.

MANO, E. B. *Introdução a polímeros*. [S.l.]: Edgar Blücher, 2001.

MANSOR, M.; NURFAIZEY, A.; TAMALDIN, N.; NORDIN, M. Natural fiber polymer composites: utilization in aerospace engineering. In: *Biomass, biopolymer-based materials, and bioenergy*. [S.l.]: Elsevier, 2019. p. 203–224.

MATHAPATI, V. C.; MURALIDHAR, N.; TULASIRAM, B.; BALREDDY, M. S. Experimental study on dynamic mechanical properties of arecanut husk fiber composite. *Materials Today: Proceedings*, Elsevier, v. 66, p. 858–865, 2022.

MAYANDI, K.; RAJINI, N.; PITCHIPOO, P.; JAPPES, J. W.; RAJULU, A. V. Extraction and characterization of new natural lignocellulosic fiber cyperus pangorei. *International Journal of Polymer Analysis and Characterization*, Taylor & Francis, v. 21, n. 2, p. 175–183, 2016.

MCCOY, T. M.; TURPIN, G.; TEO, B. M.; TABOR, R. F. Graphene oxide: a surfactant or particle? *Current Opinion in Colloid & Interface Science*, Elsevier, v. 39, p. 98–109, 2019.

MCCREARY, A.; AN, Q.; FORSTER, A. M.; LIU, K.; HE, S.; MACOSKO, C. W.; STEIN, A.; WALKER, A. R. H. Raman imaging of surface and sub-surface graphene oxide in fiber reinforced polymer nanocomposites. *Carbon*, Elsevier, v. 143, p. 793–801, 2019.

MEDVEDOVSKI, E. Lightweight ceramic composite armour system. *Advances in Applied Ceramics*, Taylor & Francis, v. 105, n. 5, p. 241–245, 2006.

MEYERS, M. A. *Dynamic behavior of materials*. [S.l.]: John wiley & sons, 1994.

MICHELLETI, M. *Produto regional produção de esteiras*. 2021. 7 mai. de 2021. Disponível em: <http://regionaljornal.blogspot.com/2011/08/produto-regional-producao-deesteiras.>

MISHRA, S.; MOHANTY, A.; DRZAL, L.; MISRA, M.; PARIJA, S.; NAYAK, S.; TRIPATHY, S. Studies on mechanical performance of biofibre/glass reinforced polyester hybrid composites. *Composites science and technology*, Elsevier, v. 63, n. 10, p. 1377–1385, 2003.

MOHANTY, A.; MISRA, M.; ; HINRICHSEN, G. Biofibres, biodegradable polymers and biocomposites: An overview. *Macromolecular materials and Engineering*, Wiley Online Library, v. 276, n. 1, p. 1–24, 2000.

MOHANTY, A. K.; MISRA, M.; DRZAL, L. Sustainable bio-composites from renewable resources: opportunities and challenges in the green materials world. *Journal of Polymers and the Environment*, Springer, v. 10, n. 1-2, p. 19–26, 2002.

MOHANTY, A. K.; MISRA, M.; DRZAL, L. T. *Natural fibers, biopolymers, and biocomposites*. [S.l.]: CRC press, 2005.

MOKALOBA, N.; BATANE, R. The effects of mercerization and acetylation treatments on the properties of sisal fiber and its interfacial adhesion characteristics on polypropylene. *International Journal of Engineering Science and Technology*, v. 6, n. 4, p. 83–97, 2014.

MONTEIRO, S. N.; ASSIS, F. Salgado de; FERREIRA, C. L.; SIMONASSI, N. T.; WEBER, R. P.; OLIVEIRA, M. S.; COLORADO, H. A.; PEREIRA, A. C. Fique fabric: a promising reinforcement for polymer composites. *Polymers*, Multidisciplinary Digital Publishing Institute, v. 10, n. 3, p. 246, 2018.

MONTEIRO, S. N.; CANDIDO, V. S.; BRAGA, F. O.; BOLZAN, L. T.; WEBER, R. P.; DRELICH, J. W. Sugarcane bagasse waste in composites for multilayered armor. *European Polymer Journal*, Elsevier, v. 78, p. 173–185, 2016.

MONTEIRO, S. N.; DRELICH, J. W.; LOPERA, H. A. C.; NASCIMENTO, L. F. C.; LUZ, F. S. da; SILVA, L. C. da; SANTOS, J. L. dos; FILHO, F. da C. G.; ASSIS, F. S. de; LIMA, É. P. et al. Natural fibers reinforced polymer composites applied in ballistic multilayered armor for personal protection—an overview. *Green materials engineering*, Springer, p. 33–47, 2019.

MONTEIRO, S. N.; LOPES, F. P. D.; BARBOSA, A. P.; BEVITORI, A. B.; SILVA, I. L. A. D.; COSTA, L. L. D. Natural lignocellulosic fibers as engineering materials—an overview. *Metallurgical and Materials Transactions A*, Springer, v. 42, n. 10, p. 2963–2974, 2011.

MONTEIRO, S. N.; LOPES, F. P. D.; FERREIRA, A. S.; NASCIMENTO, D. C. O. Natural-fiber polymer-matrix composites: cheaper, tougher, and environmentally friendly. *Jom*, Springer, v. 61, n. 1, p. 17–22, 2009.

MONTEIRO, S. N.; MILANEZI, T. L.; LOURO, L. H. L.; JR, É. P. L.; BRAGA, F. O.; GOMES, A. V.; DRELICH, J. W. Novel ballistic ramie fabric composite competing with kevlar^{TM} fabric in multilayered armor. *Materials & Design*, Elsevier, v. 96, p. 263–269, 2016.

MORAIS, A. P.; MARTINS, Y. B.; CARVALHO, B. E. O.; FURTUOSO, G. D.; SCHEEREN, G. V.; SANTOS, J. L.; COSTA, P. H.; JORGE, V. D.; GOMES, A. V. Estudo da densificação da alumina com adição de nióbia e fluoreto de lítio com variação do tempo de sinterização. *Revista Militar de Ciência e Tecnologia*, v. 34, n. especial, p. 8–9, 2017.

MORIANA, R.; VILAPLANA, F.; KARLSSON, S.; RIBES, A. Correlation of chemical, structural and thermal properties of natural fibres for their sustainable exploitation. *Carbohydrate polymers*, Elsevier, v. 112, p. 422–431, 2014.

MORYE, S.; HINE, P.; DUCKETT, R.; CARR, D.; WARD, I. Modelling of the energy absorption by polymer composites upon ballistic impact. *Composites science and technology*, Elsevier, v. 60, n. 14, p. 2631–2642, 2000.

MU, X.; WU, X.; ZHANG, T.; GO, D. B.; LUO, T. Thermal transport in graphene oxide–from ballistic extreme to amorphous limit. *Scientific reports*, Nature Publishing Group, v. 4, n. 1, p. 1–9, 2014.

MURALIDHAR, N.; VADIVUCHEZHIAN, K.; ARUMUGAM, V.; REDDY, I. S. Flexural modulus of epoxy composite reinforced with arecanut husk fibre (ahf): A mechanics approach. *Materials Today: Proceedings*, Elsevier, v. 27, p. 2265–2268, 2020.

MUTHUKUMAR, C.; KRISHNASAMY, S.; THIAGAMANI, S. M. K.; NAGARAJAN, R.; SIENGCHIN, S. Thermal characterization of the natural fiber-based hybrid composites: An overview. *Natural Fiber-Reinforced Composites: Thermal Properties and Applications*, Wiley Online Library, p. 1–15, 2022.

MUZYKA, R.; KWOKA, M.; SMĘDOWSKI, Ł.; DÍEZ, N.; GRYGLEWICZ, G. Oxidation of graphite by different modified hummers methods. *New Carbon Materials*, Elsevier, v. 32, n. 1, p. 15–20, 2017.

MWAIKAMBO, L. Y.; ANSELL, M. P. Chemical modification of hemp, sisal, jute, and kapok fibers by alkalization. *Journal of applied polymer science*, Wiley Online Library, v. 84, n. 12, p. 2222–2234, 2002.

NARAYANASAMY, P.; BALASUNDAR, P.; SENTHIL, S.; SANJAY, M.; SIENGCHIN, S.; KHAN, A.; ASIRI, A. M. Characterization of a novel natural cellulosic fiber from calotropis gigantea fruit bunch for ecofriendly polymer composites. *International journal of biological macromolecules*, Elsevier, v. 150, p. 793–801, 2020.

NASCIMENTO, L. F. C.; HOLANDA, L. I. F.; LOURO, L. H. L.; MONTEIRO, S. N.; GOMES, A. V.; LIMA, É. P. Natural mallow fiber-reinforced epoxy composite for ballistic armor against class iii-a ammunition. *Metallurgical and Materials Transactions A*, Springer, v. 48, n. 10, p. 4425–4431, 2017.

NASCIMENTO, L. F. C.; MONTEIRO, S. N.; LOURO, L. H. L.; LUZ, F. S. da; SANTOS, J. L. dos; BRAGA, F. de O.; MARÇAL, R. L. S. B. Charpy impact test of epoxy composites reinforced with untreated and mercerized mallow fibers. *Journal of materials research and technology*, Elsevier, v. 7, n. 4, p. 520–527, 2018.

NAVEEN, J.; JAWAID, M.; ZAINUDIN, E.; SULTAN, M. T.; YAHAYA, R.; MAJID, M. A. Thermal degradation and viscoelastic properties of kevlar/cocos nucifera sheath reinforced epoxy hybrid composites. *Composite Structures*, Elsevier, v. 219, p. 194–202, 2019.

NAYAK, S. Y.; SULTAN, M. T. H.; SHENOY, S. B.; KINI, C. R.; SAMANT, R.; SHAH, A. U. M.; AMUTHAKKANNAN, P. Potential of natural fibers in composites for ballistic applications–a review. *Journal of Natural Fibers*, Taylor & Francis, p. 1–11, 2020.

NEUBA, L. d. M.; JUNIO, R. F. P.; SOUZA, A. T.; RIBEIRO, M. P.; SILVEIRA, P. H. P. M. da; SILVA, T. T. da; PEREIRA, A. C.; MONTEIRO, S. N. Evaluation of the change in density with the diameter and thermal analysis of the seven-islands-sedge fiber. *Polymers*, MDPI, v. 14, n. 17, p. 3687, 2022.

NEUBA, L. d. M.; JUNIO, R. F. P.; SOUZA, A. T.; RIBEIRO, M. P.; SILVEIRA, P. H. P. M. da; SILVA, T. T. da; PEREIRA, A. C.; MONTEIRO, S. N. Mechanical properties, critical length, and interfacial strength of seven-islands-sedge fibers (cyperus malaccensis) for possible epoxy matrix reinforcement. *Polymers*, MDPI, v. 14, n. 18, p. 3807, 2022.

NEUBA, L. d. M.; JUNIO, R. F. P.; SOUZA, A. T.; CHAVES, Y. S.; TAVARES, S.; PALMEIRA, A. A.; MONTEIRO, S. N.; PEREIRA, A. C. Alkaline treatment investigation for sedge fibers (cyperus malaccensis): a promising enhancement. *Polymers*, MDPI, v. 15, n. 9, p. 2153, 2023.

NEUBA, L. de M.; JUNIO, R. F. P.; RIBEIRO, M. P.; SOUZA, A. T.; LIMA, E. de S.; FILHO, F. d. C. G.; FIGUEIREDO, A. B.-H. d. S.; BRAGA, F. d. O.; AZEVEDO, A. R. G. d.; MONTEIRO, S. N. Promising mechanical, thermal, and ballistic properties of novel epoxy composites reinforced with cyperus malaccensis sedge fiber. *Polymers*, Multidisciplinary Digital Publishing Institute, v. 12, n. 8, p. 1776, 2020.

NEUBA, L. de M.; JUNIO, R. F. P.; SOUZA, A. T.; CARVALHO, M. T.; RIBEIRO, M. E. A.; LAZARUS, B. S.; PEREIRA, A. C.; MONTEIRO, S. N. Dynamic mechanical and thermal mechanical analysis of cyperus malaccensis sedge fiber reinforced go-incorporated

epoxy nanocomposites: a short communication. *Journal of Materials Research and Technology*, Elsevier, v. 24, p. 1653–1662, 2023.

NEUBA, L. de M.; PEREIRA, A. C.; JUNIO, R. F. P.; SOUZA, A. T.; CHAVES, Y. S.; OLIVEIRA, M. P.; MONTEIRO, S. N. Ballistic performance of cyperus malaccensis sedge fibers reinforcing epoxy matrix as a standalone target. *Journal of Materials Research and Technology*, Elsevier, v. 23, p. 4367–4375, 2023.

NURAZZI, N.; ASYRAF, M.; KHALINA, A.; ABDULLAH, N.; AISYAH, H.; RAFIQAH, S.; SABARUDDIN, F.; KAMARUDIN, S.; NORRRAHIM, M.; ILYAS, R. et al. A review on natural fiber reinforced polymer composite for bullet proof and ballistic applications. *Polymers*, Multidisciplinary Digital Publishing Institute, v. 13, n. 4, p. 646, 2021.

O'CONNOR, P.; KLEYNER, A. *Practical reliability engineering*. [S.l.]: John Wiley & Sons, 2012.

OHIJEAGBON, I.; BELLO-OCHENDE, M.; ADELEKE, A.; IKUBANNI, P.; SAMUEL, A.; LASODE, O.; ATOYEBI, O. Physico-mechanical properties of cement bonded ceiling board developed from teak and african locust bean tree wood residue. *Materials Today: Proceedings*, Elsevier, v. 44, p. 2865–2873, 2021.

(OLES), O. of L. E. S.; AMERICA, U. S. of. Ballistic resistance of body armor nij standard-0101.06. 2008.

OLIVEIRA, M. S.; LUZ, F. S. d.; LOPERA, H. A. C.; NASCIMENTO, L. F. C.; FILHO, F. d. C. G.; MONTEIRO, S. N. Energy absorption and limit velocity of epoxy composites incorporated with fique fabric as ballistic armor—a brief report. *Polymers*, Multidisciplinary Digital Publishing Institute, v. 13, n. 16, p. 2727, 2021.

OUSHABI, A. The pull-out behavior of chemically treated lignocellulosic fibers/polymeric matrix interface (lf/pm): a review. *Composites Part B: Engineering*, Elsevier, v. 174, p. 107059, 2019.

OUSHABI, A.; SAIR, S.; HASSANI, F. O.; ABBOUD, Y.; TANANE, O.; BOUARI, A. E. The effect of alkali treatment on mechanical, morphological and thermal properties of date palm fibers (dpfs): Study of the interface of dpf–polyurethane composite. *South African Journal of Chemical Engineering*, Elsevier, v. 23, p. 116–123, 2017.

PANAITESCU, D. M.; FRONE, A. N.; CHIULAN, I.; GABOR, R. A.; SPATARU, I. C.; CĂŞĂRICĂ, A. Biocomposites from polylactic acid and bacterial cellulose nanofibers obtained by mechanical treatment. *BioResources*, v. 12, n. 1, p. 662–672, 2017.

PANAITESCU, D. M.; NICOLAE, C. A.; GABOR, A. R.; TRUSCA, R. Thermal and mechanical properties of poly (3-hydroxybutyrate) reinforced with cellulose fibers from wood waste. *Industrial crops and products*, Elsevier, v. 145, p. 112071, 2020.

PANDELE, A. M.; IONITA, M.; CRICA, L.; DINESCU, S.; COSTACHE, M.; IOVU, H. Synthesis, characterization, and in vitro studies of graphene oxide/chitosan–polyvinyl alcohol films. *Carbohydrate polymers*, Elsevier, v. 102, p. 813–820, 2014.

PANZAVOLTA, S.; BRACCI, B.; GUALANDI, C.; FOCARETE, M. L.; TREOSSI, E.; KOUROUPIS-AGALOU, K.; RUBINI, K.; BOSIA, F.; BRELY, L.; PUGNO, N. M. et al. Structural reinforcement and failure analysis in composite nanofibers of graphene oxide and gelatin. *Carbon*, Elsevier, v. 78, p. 566–577, 2014.

PAOLI, M. A. D. *Degradação e estabilização de polímeros*. [S.l.]: Artliber São Paulo, 2009.

PAPAGEORGIOU, D. G.; KINLOCH, I. A.; YOUNG, R. J. Mechanical properties of graphene and graphene-based nanocomposites. *Progress in Materials Science*, Elsevier, v. 90, p. 75–127, 2017.

PARK, J.-M.; SON, T. Q.; JUNG, J.-G.; HWANG, B.-S. Interfacial evaluation of single ramie and kenaf fiber/epoxy resin composites using micromechanical test and nondestructive acoustic emission. *Composite Interfaces*, Taylor & Francis, v. 13, n. 2-3, p. 105–129, 2006.

PARK, S.; LEE, K.-S.; BOZOKLU, G.; CAI, W.; NGUYEN, S. T.; RUOFF, R. S. Graphene oxide papers modified by divalent ions—enhancing mechanical properties via chemical cross-linking. *ACS nano*, ACS Publications, v. 2, n. 3, p. 572–578, 2008.

PAULA, A. C. de; ULIANA, F.; FILHO, E. A. da S.; SOARES, K.; LUZ, P. P. Use of dma-material pocket to determine the glass transition temperature of nitrocellulose blends in film form. *Carbohydrate polymers*, Elsevier, v. 226, p. 115288, 2019.

PEÇAS, P.; CARVALHO, H.; SALMAN, H.; LEITE, M. Natural fibre composites and their applications: a review. *Journal of Composites Science*, Multidisciplinary Digital Publishing Institute, v. 2, n. 4, p. 66, 2018.

PEREIRA, A.; ASSIS, F. D. Filho, fdcg; oliveira, ms; demosthenes, lcdc; lopera, hac; monteiro, sn ballistic performance of multilayered armor with intermediate polyester composite reinforced with fique natural fabric and fibers. *J. Mater. Res. Technol*, v. 8, p. 4221–4226, 2019.

PEREIRA, A. C.; ASSIS, F. S. de; FILHO, F. da C. G.; OLIVEIRA, M. S.; DEMOSTHENES, L. C. da C.; LOPERA, H. A. C.; MONTEIRO, S. N. Ballistic performance of multilayered armor with intermediate polyester composite reinforced with fique natural fabric and fibers. *Journal of Materials Research and Technology*, Elsevier, v. 8, n. 5, p. 4221–4226, 2019.

PEREIRA, A. C.; LIMA, A. M.; DEMOSTHENES, L. C. d. C.; OLIVEIRA, M. S.; COSTA, U. O.; BEZERRA, W. B. A.; MONTEIRO, S. N.; RODRIGUEZ, R. J. S.; DEUS, J. F. d.; PINHEIRO, W. A. Ballistic performance of ramie fabric reinforcing graphene oxide-incorporated epoxy matrix composite. *Polymers*, Multidisciplinary Digital Publishing Institute, v. 12, n. 11, p. 2711, 2020.

PEREIRA, A. C.; MONTEIRO, S. N.; ASSIS, F. S. de; MARGEM, F. M.; LUZ, F. S. da; BRAGA, F. de O. Charpy impact tenacity of epoxy matrix composites reinforced with aligned jute fibers. *Journal of Materials Research and Technology*, Elsevier, v. 6, n. 4, p. 312–316, 2017.

PEREIRA, A. C.; MONTEIRO, S. N.; SIMONASSI, N. T.; VIEIRA, C. M. F.; LIMA, A. M.; COSTA, U. O.; PINHEIRO, W. A.; OLIVEIRA, M. S.; FIGUEIREDO, A. B.-H. da S. Enhancement of impact toughness using graphene oxide in epoxy composite reinforced with ramie fabric. *Composite Structures*, Elsevier, v. 282, p. 115023, 2022.

PICKERING, K. L.; EFENDY, M. A.; LE, T. M. A review of recent developments in natural fibre composites and their mechanical performance. *Composites Part A: Applied Science and Manufacturing*, Elsevier, v. 83, p. 98–112, 2016.

PIRES, G.; PEREIRA, D.; FILHO, N. D.; VECCHIA, G. Caracterização físico-química e mecânica do sistema éster de silsexquioxano/resina epóxi dgeba/dietilenotriamina. *Revista Matéria*, v. 10, n. 2, p. 317–330, 2005.

POTTS, J. R.; LEE, S. H.; ALAM, T. M.; AN, J.; STOLLER, M. D.; PINER, R. D.; RUOFF, R. S. Thermomechanical properties of chemically modified graphene/poly (methyl methacrylate) composites made by in situ polymerization. *Carbon*, Elsevier, v. 49, n. 8, p. 2615–2623, 2011.

PRASAD, L.; SINGH, V.; PATEL, R. V.; YADAV, A.; KUMAR, V.; WINCZEK, J. Physical and mechanical properties of rambans (agave) fiber reinforced with polyester composite materials. *Journal of Natural Fibers*, Taylor & Francis, p. 1–15, 2021.

RAFIEE, M. A.; RAFIEE, J.; SRIVASTAVA, I.; WANG, Z.; SONG, H.; YU, Z.-Z.; KORATKAR, N. Fracture and fatigue in graphene nanocomposites. *small*, Wiley Online Library, v. 6, n. 2, p. 179–183, 2010.

RAFIQ, A.; MERAH, N.; BOUKHILI, R.; AL-QADHI, M. Impact resistance of hybrid glass fiber reinforced epoxy/nanoclay composite. *Polymer Testing*, Elsevier, v. 57, p. 1–11, 2017.

RAHMAN, M. Z. Mechanical and damping performances of flax fibre composites–a review. *Composites Part C: Open Access*, Elsevier, v. 4, p. 100081, 2021.

RAJA, T.; MOHANAVEL, V.; RAVICHANDRAN, M.; KUMAR, S. S.; ALBAQAMI, M. D.; ALOTABI, R. G.; MURUGESAN, M. Dynamic mechanical analysis of banyan/ramie fibers reinforced with nanoparticle hybrid polymer composite. *Advances in Polymer Technology*, Hindawi, v. 2022, 2022.

RAJESH, G.; PRASAD, A. R.; GUPTA, A. Water absorption characteristics of successive alkali treated jute/polylactic acid composites. *Materials Today: Proceedings*, Elsevier, v. 5, n. 11, p. 24414–24421, 2018.

RAY, S. *Applications of graphene and graphene-oxide based nanomaterials*. [S.l.]: William Andrew, 2015.

REDDY, R. A.; YOGANANDAM, K.; MOHANAVEL, V. Effect of chemical treatment on natural fiber for use in fiber reinforced composites–review. *Materials Today: Proceedings*, Elsevier, v. 33, p. 2996–2999, 2020.

REED, J. S. Principles of ceramics processing. Wiley New York, 1995.

REIS, R. H. M.; NUNES, L. F.; LUZ, F. S. da; CANDIDO, V. S.; SILVA, A. C. R. da; MONTEIRO, S. N. Ballistic performance of guaruman fiber composites in multilayered armor system and as single target. *Polymers*, Multidisciplinary Digital Publishing Institute, v. 13, n. 8, p. 1203, 2021.

REIS, R. H. M.; NUNES, L. F.; OLIVEIRA, M. S.; JUNIOR, V. F. de V.; FILHO, F. D. C. G.; PINHEIRO, M. A.; CANDIDO, V. S.; MONTEIRO, S. N. Guaruman fiber: another possible reinforcement in composites. *Journal of Materials Research and Technology*, Elsevier, v. 9, n. 1, p. 622–628, 2020.

RICHERSON, D. W.; LEE, W. E. *Modern ceramic engineering: properties, processing, and use in design*. [S.l.]: CRC press, 2018.

ROURKE, J. P.; PANDEY, P. A.; MOORE, J. J.; BATES, M.; KINLOCH, I. A.; YOUNG, R. J.; WILSON, N. R. The real graphene oxide revealed: stripping the oxidative debris from the graphene-like sheets. *Angewandte Chemie International Edition*, Wiley Online Library, v. 50, n. 14, p. 3173–3177, 2011.

RUSHING, R. A.; THOMPSON, C.; CASSIDY, P. E. Investigation of polyamine quinones as hydrophobic curatives for epoxy resins. *Journal of applied polymer science*, Wiley Online Library, v. 53, n. 9, p. 1211–1219, 1994.

SABA, N.; JAWAID, M.; ALOTHMAN, O.; PARIDAH, M. A review on dynamic mechanical properties of natural fibre reinforced. vol. 106. *Polym Compos Constr Build Mater*, p. 149–159, 2016.

SABA, N.; JAWAID, M.; ALOTHMAN, O. Y.; PARIDAH, M. A review on dynamic mechanical properties of natural fibre reinforced polymer composites. *Construction and Building Materials*, Elsevier, v. 106, p. 149–159, 2016.

SAHEB, D. N.; JOG, J. P. Natural fiber polymer composites: a review. *Advances in Polymer Technology: Journal of the Polymer Processing Institute*, Wiley Online Library, v. 18, n. 4, p. 351–363, 1999.

SALIH, A. A.; ZULKIFLI, R.; AZHARI, C. H. Tensile properties and microstructure of single-cellulosic bamboo fiber strips after alkali treatment. *Fibers*, MDPI, v. 8, n. 5, p. 26, 2020.

SAM, M.; JOJITH, R.; RADHIKA, N. Progression in manufacturing of functionally graded materials and impact of thermal treatment—a critical review. *Journal of Manufacturing Processes*, Elsevier, v. 68, p. 1339–1377, 2021.

SANJAY, M.; MADHU, P.; JAWAID, M.; SENTHAMARAIKANNAN, P.; SENTHIL, S.; PRADEEP, S. Characterization and properties of natural fiber polymer composites: A comprehensive review. *Journal of Cleaner Production*, Elsevier, v. 172, p. 566–581, 2018.

SANJAY, M.; SIENGCHIN, S.; PARAMESWARANPILLAI, J.; JAWAID, M.; PRUNCU, C. I.; KHAN, A. A comprehensive review of techniques for natural fibers as reinforcement in composites: Preparation, processing and characterization. *Carbohydrate polymers*, Elsevier, v. 207, p. 108–121, 2019.

SANTOS, P. A.; SPINACÉ, M. A.; FERMOSELLI, K. K.; PAOLI, M.-A. D. Polyamide-6/vegetal fiber composite prepared by extrusion and injection molding. *Composites Part A: Applied Science and Manufacturing*, Elsevier, v. 38, n. 12, p. 2404–2411, 2007.

SAPUAN, S.; PUA, F.-l.; EL-SHEKEIL, Y.; AL-OQLA, F. M. Mechanical properties of soil buried kenaf fibre reinforced thermoplastic polyurethane composites. *Materials & Design*, Elsevier, v. 50, p. 467–470, 2013.

SARKER, F.; KARIM, N.; AFROJ, S.; KONCHERRY, V.; NOVOSELOV, K. S.; POTLURI, P. High-performance graphene-based natural fiber composites. *ACS applied materials & interfaces*, ACS Publications, v. 10, n. 40, p. 34502–34512, 2018.

SATYANARAYANA, K.; GUIMARÃES, J.; WYPYCH, F. Studies on lignocellulosic fibers of brazil. part i: Source, production, morphology, properties and applications. *Composites Part A: Applied Science and Manufacturing*, Elsevier, v. 38, n. 7, p. 1694–1709, 2007.

SATYANARAYANA, K. G.; ARIZAGA, G. G.; WYPYCH, F. Biodegradable composites based on lignocellulosic fibers—an overview. *Progress in polymer science*, Elsevier, v. 34, n. 9, p. 982–1021, 2009.

SCAZZOSI, R.; SOUZA, S. D. B. de; AMICO, S. C.; GIGLIO, M.; MANES, A. Experimental and numerical evaluation of the perforation resistance of multi-layered alumina/aramid fiber ballistic shield impacted by an armor piercing projectile. *Composites Part B: Engineering*, Elsevier, v. 230, p. 109488, 2022.

SCIFONI, S. IdentificaÇÃo e proteÇÃo da paisagem agroindustrial da imigraÇÃo japonesa no vale do ribeira/sÃo paulo. p. 1–26, 2008.

SCOPUS. *pesquisa sobre o termo 'cyperus malaccensis' AND 'composites'*. 2024. 15 jun. de 2024. Disponível em: <www.scopus.com/search/form.uri#basic>.

SEGAL, L.; CREELY, J.; JR, A. M.; CONRAD, C. An empirical method for estimating the degree of crystallinity of native cellulose using the x-ray diffractometer. *Textile research journal*, Sage Publications Sage CA: Thousand Oaks, CA, v. 29, n. 10, p. 786–794, 1959.

SEKI, Y.; SARIKANAT, M.; SEVER, K.; DURMUŞKAHYA, C. Extraction and properties of ferula communis (chakshir) fibers as novel reinforcement for composites materials. *Composites Part B: Engineering*, Elsevier, v. 44, n. 1, p. 517–523, 2013.

SELEZNEVA, M.; SWOLFS, Y.; KATALAGARIANAKIS, A.; ICHIKAWA, T.; HIRANO, N.; TAKETA, I.; KARAKI, T.; VERPOEST, I.; GORBATIKH, L. The brittle-to-ductile transition in tensile and impact behavior of hybrid carbon fibre/self-reinforced polypropylene composites. *Composites Part A: Applied Science and Manufacturing*, Elsevier, v. 109, p. 20–30, 2018.

SELVAN, M. T. G. A.; BINOJ, J. S.; MANSINGH, B. B.; SAJIN, J. A. B. Physico-chemical properties of alkali treated cellulosic fibers from fragrant screw pine prop root. *Journal of Natural Fibers*, Taylor & Francis, v. 20, n. 1, p. 2129897, 2023.

SHAH, D. U. Developing plant fibre composites for structural applications by optimising composite parameters: a critical review. *Journal of materials science*, Springer, v. 48, n. 18, p. 6083–6107, 2013.

SHAKER, K.; NAWAB, Y. Lignocellulosic fiber structure. In: *Lignocellulosic Fibers*. [S.l.]: Springer, 2022. p. 11–19.

SHAPCHENKOVA, O.; LOSKUTOV, S.; ANISKINA, A.; BÖRCSÖK, Z.; PÁSZTORY, Z. Thermal characterization of wood of nine european tree species: thermogravimetry and differential scanning calorimetry in an air atmosphere. *European Journal of Wood and Wood Products*, Springer, v. 80, n. 2, p. 409–417, 2022.

SHEKAR, H. S.; RAMACHANDRA, M. Green composites: a review. *Materials Today: Proceedings*, Elsevier, v. 5, n. 1, p. 2518–2526, 2018.

SHEN, B.; ZHAI, W.; TAO, M.; LU, D.; ZHENG, W. Chemical functionalization of graphene oxide toward the tailoring of the interface in polymer composites. *Composites Science and Technology*, Elsevier, v. 77, p. 87–94, 2013.

SHIOYA, M.; MYOGA, A.; KITAGAWA, A.; TOKUNAGA, Y.; HAYASHI, H.; KOGO, Y.; SHIMADA, H.; SATAKE, S.-i. Analysis of deflection and dynamic plant characteristics of cyperus malaccensis lam. *Plant Production Science*, Taylor & Francis, v. 22, n. 2, p. 242–249, 2019.

SHRIVASTAVA, A. Plastic properties and testing. *Introduction to plastics engineering*, William Andrew Publishing Amsterdam, The Netherlands, p. 49–110, 2018.

SILVA, M. da; STAINER, D.; AL-QURESHI, H.; HOTZA, D. Ceramic armors for ballistic applications: a review. *Cerâmica*, SciELO Brasil, v. 60, n. 355, p. 323–331, 2014.

SILVA, T. T. da; SILVEIRA, P. H. P. M. d.; FIGUEIREDO, A. B.-H. d. S.; MONTEIRO, S. N.; RIBEIRO, M. P.; NEUBA, L. d. M.; SIMONASSI, N. T.; FILHO, F. d. C. G.; NASCIMENTO, L. F. C. Dynamic mechanical analysis and ballistic performance of kenaf fiber-reinforced epoxy composites. *Polymers*, MDPI, v. 14, n. 17, p. 3629, 2022.

SILVEIRA, P.; SILVA, T.; RIBEIRO, M.; JESUS, P. Rodrigues de; CREDMANN, P.; GOMES, A. A brief review of alumina, silicon carbide and boron carbide ceramic materials for ballistic applications. *Academia Letters*, 2021.

SILVEIRA, P. H. P. da; RIBEIRO, M. P.; SILVA, T. T.; LIMA, A. M.; LEMOS, M. F.; OLIVEIRA, A. G.; NASCIMENTO, L. F. C.; GOMES, A. V.; MONTEIRO, S. N. Effect of alkaline treatment and graphene oxide coating on thermal and chemical properties of hemp (cannabis sativa l.) fibers. *Journal of Natural Fibers*, Taylor & Francis, v. 19, n. 15, p. 12168–12181, 2022.

SILVEIRA, P. H. P. M. da; JESUS, P. R. R. de; RIBEIRO, M. P.; MONTEIRO, S. N.; OLIVEIRA, J. C. S. D.; GOMES, A. V. Sintering behavior of al2o3 ceramics doped with pre-sintered nb2o5 and lif. In: TRANS TECH PUBL. *Materials Science Forum*. [S.l.], 2020. v. 1012, p. 190–195.

SONG, Y.; CHANDRA, R. P.; ZHANG, X.; SADDLER, J. N. Non-productive celluase binding onto deep eutectic solvent (des) extracted lignin from willow and corn stover with inhibitory effects on enzymatic hydrolysis of cellulose. *Carbohydrate polymers*, Elsevier, v. 250, p. 116956, 2020.

SOOD, M.; DWIVEDI, G. Effect of fiber treatment on flexural properties of natural fiber reinforced composites: A review. *Egyptian journal of petroleum*, Elsevier, v. 27, n. 4, p. 775–783, 2018.

SOUZA, A. T.; JUNIO, R. F. P.; NEUBA, L. d. M.; CANDIDO, V. S.; SILVA, A. C. R. da; AZEVEDO, A. R. G. de; MONTEIRO, S. N.; NASCIMENTO, L. F. C. Caranan fiber from mauritiella armata palm tree as novel reinforcement for epoxy composites. *Polymers*, Multidisciplinary Digital Publishing Institute, v. 12, n. 9, p. 2037, 2020.

SPINACÉ, M. A.; LAMBERT, C. S.; FERMOSELLI, K. K.; PAOLI, M.-A. D. Characterization of lignocellulosic curaua fibres. *Carbohydrate Polymers*, Elsevier, v. 77, n. 1, p. 47–53, 2009.

SRIDHAR, K. R.; KARAMCHAND, K. S.; SUMATHI, P. Fungal colonization and breakdown of sedge (cyperus malaccensis lam.) in an indian mangrove. *Botanica Marina*, De Gruyter, v. 53, n. 6, p. 525–533, 2010.

STANDARD, N. . 0101.04 (2000) ballistic resistance of personal body armor. *US Department of Justice, Office of Justice Programs, National Institute of Justice, Washington.*

STANKOVICH, S.; DIKIN, D. A.; COMPTON, O. C.; DOMMETT, G. H.; RUOFF, R. S.; NGUYEN, S. T. Systematic post-assembly modification of graphene oxide paper with primary alkylamines. *Chemistry of Materials*, ACS Publications, v. 22, n. 14, p. 4153–4157, 2010.

STANKOVICH, S.; DIKIN, D. A.; PINER, R. D.; KOHLHAAS, K. A.; KLEINHAMMES, A.; JIA, Y.; WU, Y.; NGUYEN, S. T.; RUOFF, R. S. Synthesis of graphene-based nanosheets via chemical reduction of exfoliated graphite oxide. *carbon*, Elsevier, v. 45, n. 7, p. 1558–1565, 2007.

STANKOVICH, S.; PINER, R. D.; NGUYEN, S. T.; RUOFF, R. S. Synthesis and exfoliation of isocyanate-treated graphene oxide nanoplatelets. *Carbon*, Elsevier, v. 44, n. 15, p. 3342–3347, 2006.

STOBINSKI, L.; LESIAK, B.; MALOLEPSZY, A.; MAZURKIEWICZ, M.; MIERZWA, B.; ZEMEK, J.; JIRICEK, P.; BIELOSHAPKA, I. Graphene oxide and reduced graphene oxide studied by the xrd, tem and electron spectroscopy methods. *Journal of Electron Spectroscopy and Related Phenomena*, Elsevier, v. 195, p. 145–154, 2014.

SUK, J. W.; PINER, R. D.; AN, J.; RUOFF, R. S. Mechanical properties of monolayer graphene oxide. *ACS nano*, ACS Publications, v. 4, n. 11, p. 6557–6564, 2010.

SUMMERSCALES, J.; DISSANAYAKE, N. P.; VIRK, A. S.; HALL, W. A review of bast fibres and their composites. part 1–fibres as reinforcements. *Composites Part A: Applied Science and Manufacturing*, Elsevier, v. 41, n. 10, p. 1329–1335, 2010.

SUN, Z.; LI, J.; HE, T.; TIAN, L.; LI, J.; LI, X. Bioaccumulation of heavy metals by cyperus malaccensis and spartina alterniflora in a typical subtropical estuary (min river) of southeast china. *Journal of Soils and Sediments*, Springer, v. 19, n. 4, p. 2061–2075, 2019.

TEIJIN. *Ballistic Materials Handbook*. [S.l.: s.n.], 2019.

TELI, M. D.; TEREGA, J. M. Effects of alkalization on the properties of ensete ventricosum plant fibre. *The Journal of The Textile Institute*, Taylor & Francis, v. 110, n. 4, p. 496–507, 2019.

THAKUR, V.; SINGHA, A.; THAKUR, M. Natural cellulosic polymers as potential reinforcement in composites: physicochemical and mechanical studies. *Advances in Polymer Technology*, Wiley Online Library, v. 32, n. S1, p. E427–E435, 2013.

THAKUR, V. K.; THAKUR, M. K.; GUPTA, R. K. raw natural fiber–based polymer composites. *International Journal of Polymer Analysis and Characterization*, Taylor & Francis, v. 19, n. 3, p. 256–271, 2014.

THAKUR, V. K.; VENNERBERG, D.; KESSLER, M. R. Green aqueous surface modification of polypropylene for novel polymer nanocomposites. *ACS applied materials & interfaces*, ACS Publications, v. 6, n. 12, p. 9349–9356, 2014.

TIAN, M.; QU, L.; ZHANG, X.; ZHANG, K.; ZHU, S.; GUO, X.; HAN, G.; TANG, X.; SUN, Y. Enhanced mechanical and thermal properties of regenerated cellulose/graphene composite fibers. *Carbohydrate polymers*, Elsevier, v. 111, p. 456–462, 2014.

TIAN, Y.; CAO, Y.; WANG, Y.; YANG, W.; FENG, J. Realizing ultrahigh modulus and high strength of macroscopic graphene oxide papers through crosslinking of mussel-inspired polymers. *Advanced materials*, Wiley Online Library, v. 25, n. 21, p. 2980–2983, 2013.

TISSERA, N. D.; WIJESENA, R. N.; PERERA, J. R.; SILVA, K. N. de; AMARATUNGE, G. A. Hydrophobic cotton textile surfaces using an amphiphilic graphene oxide (go) coating. *Applied Surface Science*, Elsevier, v. 324, p. 455–463, 2015.

UMASHANKARAN, M.; GOPALAKRISHNAN, S. Effect of sodium hydroxide treatment on physico-chemical, thermal, tensile and surface morphological properties of pongamia pinnata l. bark fiber. *Journal of Natural Fibers*, Taylor & Francis, v. 18, n. 12, p. 2063–2076, 2021.

UMER, R.; LI, Y.; DONG, Y.; HAROOSH, H.; LIAO, K. The effect of graphene oxide (go) nanoparticles on the processing of epoxy/glass fiber composites using resin infusion. *The International Journal of Advanced Manufacturing Technology*, Springer, v. 81, p. 2183–2192, 2015.

VALASEK, P.; MUELLER, M.; SLEGER, V. Influence of plasma treatment on mechanical properties of cellulose-based fibres and their interfacial interaction in composite systems. *BioResources*, NORTH CAROLINA STATE UNIV DEPT WOOD & PAPER SCI CAMPUS BOX 8005, RALEIGH, NC ..., v. 12, n. 3, p. 5449–5461, 2017.

VECA, L. M.; MEZIANI, M. J.; WANG, W.; WANG, X.; LU, F.; ZHANG, P.; LIN, Y.; FEE, R.; CONNELL, J. W.; SUN, Y.-P. Carbon nanosheets for polymeric nanocomposites with high thermal conductivity. *Advanced Materials*, Wiley Online Library, v. 21, n. 20, p. 2088–2092, 2009.

VENUGOPAL, A.; BOOMINATHAN, S. K. Physico-chemical, thermal and tensile properties of alkali-treated acacia concinna fiber. *Journal of Natural Fibers*, Taylor & Francis, v. 19, n. 8, p. 3093–3108, 2022.

VERDEJO, R.; BERNAL, M. M.; ROMASANTA, L. J.; LOPEZ-MANCHADO, M. A. Graphene filled polymer nanocomposites. *Journal of Materials Chemistry*, Royal Society of Chemistry, v. 21, n. 10, p. 3301–3310, 2011.

VIJAY, R.; SINGARAVELU, D. L. Influence of stacking sequence on mechanical characteristics of cyperus pangorei fibres based natural fibre composites. *Materials Today: Proceedings*, Elsevier, v. 5, n. 2, p. 8504–8513, 2018.

VRINCEANU, N.; PETRE, A. B.; HRISTODOR, C. M.; POPOVICI, E.; PUI, A.; COMAN, D.; TANASA, D. Zinc oxide—linen fibrous composites: Morphological, structural, chemical, humidity adsorptive and thermal barrier attributes. *Modern surface engineering treatments*, IntechOpen, n. 4, 2013.

WANG, C.; FROGLEY, M. D.; CINQUE, G.; LIU, L.-Q.; BARBER, A. H. Deformation and failure mechanisms in graphene oxide paper using in situ nanomechanical tensile testing. *Carbon*, Elsevier, v. 63, p. 471–477, 2013.

WANG, L.; KANESALINGAM, S.; NAYAK, R.; PADHYE, R. Recent trends in ballistic protection. *Textiles and Light Industrial Science and Technology*, Science and Engineering Publishing Company, v. 3, p. 37–47, 2014.

WANG, W. Q.; SARDANS, J.; WANG, C.; ZENG, C. S.; TONG, C.; ASENSIO, D.; PENUELAS, J. Ecological stoichiometry of c, n, and p of invasive phragmites australis and native cyperus malaccensis species in the minjiang river tidal estuarine wetlands of china. *Plant ecology*, Springer, v. 216, n. 6, p. 809–822, 2015.

WILLIAM, S.; HUMMERS, J.; OFFEMAN, R. E. et al. Preparation of graphitic oxide. *J. Am. Chem. Soc*, v. 80, n. 6, p. 1339–1339, 1958.

WILSON, N. R.; PANDEY, P. A.; BEANLAND, R.; YOUNG, R. J.; KINLOCH, I. A.; GONG, L.; LIU, Z.; SUENAGA, K.; ROURKE, J. P.; YORK, S. J. et al. Graphene oxide: structural analysis and application as a highly transparent support for electron microscopy. *ACS nano*, ACS Publications, v. 3, n. 9, p. 2547–2556, 2009.

XIAO, F.-X.; PAGLIARO, M.; XU, Y.-J.; LIU, B. Layer-by-layer assembly of versatile nanoarchitectures with diverse dimensionality: a new perspective for rational construction of multilayer assemblies. *Chemical Society Reviews*, Royal Society of Chemistry, v. 45, n. 11, p. 3088–3121, 2016.

XU, Z.; GAO, C. In situ polymerization approach to graphene-reinforced nylon-6 composites. *Macromolecules*, ACS Publications, v. 43, n. 16, p. 6716–6723, 2010.

XUE, G.; ZHANG, B.; XING, J.; SUN, M.; ZHANG, X.; LI, J.; WANG, L.; LIU, C. A facile approach to synthesize in situ functionalized graphene oxide/epoxy resin nanocomposites: mechanical and thermal properties. *Journal of Materials Science*, Springer, v. 54, n. 22, p. 13973–13989, 2019.

YAN, L.; CHOUW, N.; YUAN, X. Improving the mechanical properties of natural fibre fabric reinforced epoxy composites by alkali treatment. *Journal of Reinforced Plastics and Composites*, SAGE Publications Sage UK: London, England, v. 31, n. 6, p. 425–437, 2012.

YANG, P.; WANG, M.; LAI, D. Y.; CHUN, K.; HUANG, J.; WAN, S.; BASTVIKEN, D.; TONG, C. Methane dynamics in an estuarine brackish cyperus malaccensis marsh: Production and porewater concentration in soils, and net emissions to the atmosphere over five years. *Geoderma*, Elsevier, v. 337, p. 132–142, 2019.

YASIN, M.; TAUQEER, T.; ZAIDI, S. M.; SAN, S. E.; MAHMOOD, A.; KÖSE, M. E.; CANIMKURBEY, B.; OKUTAN, M. Synthesis and electrical characterization of graphene oxide films. *Thin Solid Films*, Elsevier, v. 590, p. 118–123, 2015.

YIN, Q.; ZHU, B.; ZENG, H. *Microstructure, property and processing of functional ceramics*. [S.l.]: Springer Science & Business Media, 2010.

ZHANG, H.; ZHU, P.; LIU, Z.; QI, S.; ZHU, Y. Research on prediction method of mechanical properties of open-hole laminated plain woven cfrp composites considering drilling-induced delamination damage. *Mechanics of Advanced Materials and Structures*, Taylor & Francis, v. 28, n. 24, p. 2515–2530, 2021.

ZHANG, W. L.; PARK, B. J.; CHOI, H. J. Colloidal graphene oxide/polyaniline nanocomposite and its electrorheology. *Chemical Communications*, Royal Society of Chemistry, v. 46, n. 30, p. 5596–5598, 2010.

ZHAO, X.; ZHANG, Q.; CHEN, D.; LU, P. Enhanced mechanical properties of graphene-based poly (vinyl alcohol) composites. *Macromolecules*, ACS Publications, v. 43, n. 5, p. 2357–2363, 2010.

ZHI, M.; LIU, Q.; CHEN, H.; CHEN, X.; FENG, S.; HE, Y. Thermal stability and flame retardancy properties of epoxy resin modified with functionalized graphene oxide containing phosphorus and silicon elements. *ACS omega*, ACS Publications, v. 4, n. 6, p. 10975–10984, 2019.

ZHOU, F.; CHENG, G.; JIANG, B. Effect of silane treatment on microstructure of sisal fibers. *Applied Surface Science*, Elsevier, v. 292, p. 806–812, 2014.

ZINI, E.; SCANDOLA, M. Green composites: an overview. *Polymer composites*, Wiley Online Library, v. 32, n. 12, p. 1905–1915, 2011.

ZUKAS, J. *Impact dynamics: theory and experiment*. [S.l.], 1980.